University of Strathclyde

Doctoral Thesis

Evolution of Residual Stress and Mechanical Properties During Forging and Ageing of Nickel-Based Superalloys IN718 and AD730

A thesis submitted to the University of Strathclyde in fulfilment of the requirements of the degree of Doctor of Philosophy (PhD)

2024

Michael King

Advanced Forming Research Centre

Declaration & Copyright

This thesis is the result of the author's original research. It has been composed by the author and has not been previously submitted for examination which has led to the award of a degree.

Signed: 

Date: 19/9/24

List of Papers

The following paper has been included in this thesis:

1. M. King and S. Rahimi, "Optimisation of sample geometry for thermo-mechanical testing of precipitation hardenable nickel-based superalloys with an ETMT machine," Strain, vol. 60, no. 1, p. e12458, doi: https://doi.org/10.1111/str.12458.

As the author of this thesis, I declare that it contains previously published work for which I hold responsibility. My contribution to the work included conducting all testing, post-processing, and analyses. I served as the primary author of the paper, with Dr. S. Rahimi, my co-author and main academic PhD supervisor, responsible for proofreading, amendments, and guidance.

Signed: 

Date: 19/9/24

Abstract

Nickel-based superalloys such as Inconel 718 (IN718) and AD730 are critical materials in high-temperature applications due to their exceptional mechanical properties and corrosion resistance. Optimising their thermo-mechanical processing is essential for enhancing performance and extending service life in demanding environments. This study aims to develop comprehensive predictive models to improve understanding and control over the thermo-mechanical processing of these alloys.

This research first examined the effects of quenching configuration and media on residual stress generation during water quenching of scaled IN718 discs. A novel methodology was created to determine heat transfer coefficients (HTCs), which were integrated into a finite element (FE) model to predict residual stresses. Experimental validation confirmed the model's accuracy and its effectiveness in predicting and mitigating residual stresses.

To facilitate precise mechanical characterisation at elevated temperatures, a new sample geometry was designed for miniaturised tensile testing using an electro-thermal mechanical testing system. This optimised geometry provides more reliable and accurate measurement of high-temperature mechanical properties compared to existing designs. Using this optimised geometry, stress relaxation tests were conducted on IN718 and AD730, leading to the formulation of Zener-Wert-Avrami and hyperbolic constitutive stress relaxation models. The hyperbolic model proved particularly effective in predicting stress relaxation behaviour during ageing, enhancing the understanding of material responses under service conditions.

The study culminated in the creation of a multi-process FE model to simulate the thermo-mechanical processing of AD730 during forging and ageing. This model integrated HTC values, stress relaxation data, and advanced constitutive material models. The model successfully predicted the hot deformation behaviour of AD730, with experimental validation confirming accuracy and underscoring potential as a powerful tool for optimising processing parameters and improving component performance.

Overall, this study provides significant advancements in predictive modelling of nickel-based superalloys, offering insights and methodologies for improving manufacturing processes and material performance in high-temperature applications

Acknowledgements

There are so many people I owe a huge thanks to for their support throughout my PhD journey. I'm sure there were days—especially when working on that ETMT—when I was a bit of a pain: manic, grumpy, and borderline unbearable. But the people around me—my colleagues, friends, family, and especially my partner—helped get me through. For that, I'm eternally grateful.

First and foremost, I want to thank my main academic supervisor, Dr. Salah Rahimi. From the moment you gave me my start at the AFRC, you have been a real mentor and a friend, helping me navigate the ups and downs of my career. So if this thesis doesn't hold up, well… we're both going down together! Jokes aside, your guidance and encouragement during the times I felt overwhelmed or unsure were invaluable. I couldn't have asked for a better supervisor.

A big thank you to Dr. Paul Blackwell and Dr. Ioannis Violatos, who stepped in as my second supervisors. When Salah was unavailable, you both provided much-needed assistance. Ioannis, your help with the modelling and those never-ending inverse HTC calculations was particularly appreciated—I'm pretty sure they're still running somewhere! I'm also grateful to my examiners, Professors Birosca and Vorontsov. Your thorough review and challenging questions during my viva were tough but made my thesis all the stronger. Thank you for your time and constructive feedback.

I want to extend a huge thank you to the amazing technical experts at the AFRC who played a crucial role in making this project a reality. A special shout-out to Dr. Paul Souza for keeping me right with my constitutive models and to Dr. Giribaskar Sivaswamy for ensuring my micrographs were on-point. I'm also deeply grateful to all the technicians: Kornelia Kondziolka, Ryan O'Neil, Jacqueline Schramm, Martin Ogilby, Liza Hall, and, of course, Duncan Rodgers. Your efforts were invaluable. A heartfelt thanks to the Materials Science and Residual Stress team, where I've spent 11 incredible years. I've learned so much from you, and it's been a privilege to work alongside such talented and supportive colleagues. Youse are no bad.

A special thanks to Dr. Dorothy Evans, who helped set me on my PhD journey and always looked out for me, even when it wasn't her job to. I'd also like to thank Professor Tatyana Konkova for her perfectly timed 'accidental' appearance in the waiting room just before my viva. Your presence really put me at ease and calmed my nerves—thank you, and yes, I see what you did there!

A special shout-out to my fellow members of the AFRC's 'late-night' Loser's Club. Thanks for the snacks and for sharing in the pain of working long, late hours. With my thesis wrapped up, I'm crossing my fingers for a lifetime ban, but I'm worried I might just be a Loser for life now.

I want to express my gratitude to Aubert & Duval for their guidance on the industrial aspects of this project. A special thanks to Christian Dumont for his kind words and genuine interest. Most of although, I'm incredibly grateful to Sebastien Nouveau. Your extensive knowledge and support throughout my PhD and time at the AFRC were invaluable and made a huge difference. You've shaped me as a researcher over the years, and I'm truly sad to see you leave the AFRC. Merci pour tout votre soutien - Hope I got that right!

Most importantly, I want to thank my family and friends. Completing this PhD while working at the AFRC has been a monumental effort for me, and I know I haven't been around as much as we'd have liked. I hope this thesis shows that it was all worth it.

A special shout-out to Elen Jump and Lyn Johnstone for being the most mischievous of pals—I'll never forget our prank war and really thought Paul Blackwell was going to sack us that day! Thanks to Stephen, Danny, Ashleigh, Natalie, Jade, Julie, and Connor for your constant encouragement and unwavering faith.

And of course, a big thanks to Gary McGarvey, my best mate of nearly 30 years. For that feat alone, you deserve a medal! From all the shenanigans we got up to growing up, to supporting me through this PhD, you've always been there. Your constant friendship, rock-solid support, and most importantly your knack for showing up with a pint when I need it most, mean the world to me. Thanks, mate. Not bad for a couple of guys from the Garngad, eh?

I'd also like to thank my parents for giving me the platform to be who I am today. You've both loved and accepted me (despite the obvious challenges!) and helped mould me into the person I am today. I hope I make you proud. To my mum, whose ear I could always bend when

things weren't going well and who always offered advice—even on matters of material science! Your positive words and occasional wee kicks up the backside kept me from getting too down on myself and helped me stay on track. Thank you for everything you've done and continue to do for me.

And to my dad, who has always been my biggest supporter. You gave me the confidence to pursue university when I was young and doubted myself. Your constant belief in me, even when I struggled to believe in myself, has been a source of great strength throughout my entire life. Thank you. I hope I've paid you back enough in pints over the years, but if not, I'll make sure to square you up come graduation. And by the way, just so you know, I'm going to be lording this over you and the rest of the family forever!

Lastly, and certainly not least, to John Michael. I don't know where to start. Your love, patience, and support have been my anchor throughout this journey. I want to thank you for being by my side through the long hours, the late nights, the self-doubt, and the many burnouts. You've let me rant, you've let me brood, but you've never let me lose faith. Your belief in me has been the cornerstone of my strength and determination. You've supported me in every way someone could, short of actually doing some forging trials yourself! For all of this and more, I'm deeply grateful and forever in your debt. I love you, Dummy.

Contents

1 Introduction

1.1 Research Area and Motivation

The processing of Ni-based superalloys involves several intricate steps such as multiple super-solvus and sub-solvus forging stages, various heat treatments (including homogenisation, solutioning, and ageing), and controlled cooling methods like quenching and furnace cooling. Each of these steps has the potential to influence the microstructure, which in turn can impact subsequent processing stages. Therefore, meticulous control and comprehensive understanding of each stage of the thermo-mechanical processing route are essential to achieve a tailored microstructure optimised for the intended application.

The challenges inherent in processing these materials for maximum performance underscore the necessity for advanced tools that can offer precise insights into their behaviour. In this context, the development of predictive Finite Element (FE) models emerges as a crucial research area. These models offer invaluable insights into the material's response to processing, leading to improved manufacturing efficiency and enhanced component performance. In industries where optimising manufacturing processes is crucial, FE models serve as indispensable tools for streamlining production workflows and tailoring material properties for specific applications, all while reducing manufacturing costs, offering clear and tangible benefits to industry. Through their application, manufacturers can achieve greater precision, efficiency, and reliability in the thermo-mechanical processing of Ni-based

superalloys and similar materials, ultimately driving innovation and competitiveness in the manufacturing sector.

1.2 Research Aims and Objectives

The aim of this research is to investigate the thermo-mechanical processing routes of two Ni-based superalloys, aiming to comprehend their mechanical behaviour and stress evolution through development of a predictive FE thermo-mechanical process model, validated against experimental tests and trials. There were three primary aims of the work carried out in this dissertation.

The first was to investigate the influence of quenching configuration and media on the residual stresses induced in a scaled disc fabricated from Inconel™ 718 (IN718)[1]. During the thermo-mechanical processing of IN718, multiple forging stages are required to tailor the microstructure for its intended use as a turbine disc in a jet engine. A crucial part of this process is water quenching post-solution annealing, necessary for controlling precipitate size, morphology, and distribution. Water quenching introduces substantial residual stress, which can affect subsequent operations like machining or in-service performance. Thus, understanding key factors influencing residual stress generation, such as quenching configuration and media, is crucial. The heat transfer coefficient (HTC) is pivotal in describing heat flow from a solid to a fluid, essential for characterising cooling behaviour and, consequently, residual stress generation and modelling during water quenching of parts. Therefore, seeking an accurate method to determine this coefficient, as well as assessing the method's precision, was a key driver alongside understanding the impact of quenching configuration and media the residual stresses.

The second aim of this work was to establish a method for conducting micro-mechanical testing of Ni-based superalloys at elevated temperatures required for ageing, using a resistive heating tensile rig. The Electro-Thermal Mechanical Testing (ETMT) system is a resistive heating micro-mechanical testing rig used for performing tensile tests on miniaturised samples. However, accurately determining mechanical properties in precipitation-hardenable materials at ageing temperatures using these rigs poses a known and proven challenge. This challenge arises from the non-uniform distribution of temperature resulting from heating

[1] Inconel™ is a registered trademark of Special Metals Corporation and its subsidiaries.

based on the joule effect (i.e., resistivity heating), which, in turn, leads to heterogeneous deformation along the gauge length of a tensile sample. Hence, designing a testing methodology, and potentially a new sample geometry, is crucial for testing precipitation hardenable materials such as Ni-based superalloys. This new testing approach and geometry are expected to facilitate the completion of tests related to the final aim of this project.

The third and final aim of this work was to develop a multi-process FE model for AD730™ [2], incorporating advanced constitutive models describing its deformation and stress relaxation behaviours, reflective of the forging process for this alloy. The challenges inherent in processing Ni-based superalloys for maximum performance underscore the necessity for advanced tools that can offer precise insights into their behaviour. In this context, the development of predictive FE models emerges as a crucial research area. These models offer invaluable insights into the material's response to processing, leading to improved manufacturing efficiency and enhanced component performance. In industries where optimising manufacturing processes is crucial, FE models serve as indispensable tools for streamlining production workflows and tailoring material properties for specific applications, all while reducing manufacturing costs, offering clear and tangible benefits to industry. Through their application, manufacturers can achieve greater precision, efficiency, and reliability in the thermo-mechanical processing of Ni-based superalloys and similar materials, ultimately driving innovation and competitiveness in the manufacturing sector.

1.3 Layout of Dissertation

The following chapter provides an introduction to Ni-based superalloys, with a particular focus on AD730 and IN718, the two alloys under investigation in this thesis. It also delves into residual stresses, exploring their significance in manufacturing processes, their origins, measurement techniques, and strategies for control. Additionally, it discusses the modelling of residual stresses and proposes methodologies for developing a thermo-mechanical model to predict residual stresses during forging and subsequent heat treatments. Following this, chapter 3 provides a brief overview of the overarching challenge addressed in this thesis, along with the specific challenges and motivations driving each subsequent chapter. It also lays out how each chapter is connected to the next.

[2] AD730™ is a registered trademark of Aubert & Duval.

Chapter 4 investigates the influence of quenching configuration on residual stress generation. This section presents the development of a FE model to predict residual stress generation in an IN718 scaled disc subjected to water quenching after solutioning at 980°C. The model's accuracy is verified through experimental trials.

Chapter 5 and 6 introduce a method for miniaturised testing of Ni-based superalloy materials using resistive heating micro-mechanical testing rigs. These chapters showcase the effectiveness of the methodology by capturing stress relaxation results for IN718 and AD730, which are then utilised to develop constitutive stress relaxation models.

In chapter 7, two constitutive material models describing the hot deformation behaviour of AD730 during forging are developed, with the most accurate model being integrated into a FE solver. Subsequently, the results are validated against experimental forging trials. Chapter 8 consolidates the findings from Chapters 4, 5, 6, and 7 to construct a comprehensive multi-step, multi-process predictive model capable of predicting the stress relaxation evolution of AD730 during forging and the subsequent heat treatments.

Finally this dissertation is concluded in chapter 9 with a summary of the conclusions, followed by intentions for future work and the bibliography in chapters 10 and 11, respectively.

2

Literature Review

A review of the relevant literature for this PhD thesis is presented in the following sections. It provides a brief overview of Ni-based superalloys, including basic microstructure, mechanical properties, and the industrial forging routes used to design the microstructure for the desired properties. This review then focuses on the two alloys of interest for the subject of this PhD project, IN718 and AD730. A short discussion on the unique properties of these alloys is then followed by a review of residual stress including the main causes, their evolution during thermo-mechanical processing, and how best to measure and control them. Particular attention is given to stress relaxation behaviour and the underlying mechanisms which drive it. The final section reviews numerical models used for different thermo-mechanical processes such as hot isothermal compression testing, water quenching, and stress relieving heat treatments.

2.1 Nickel-Based Superalloys

2.1.1 The Gas Turbine Engine

Gas turbine engines have been employed worldwide for over 80 years, serving as power sources for electricity generation and aircraft propulsion. While these engines are often perceived as large and complex systems as illustrated in Figure 2.1, their operation can be simplified to three main components, as demonstrated in Figure 2.2. The fundamental operation of a gas turbine engine is as follows:

The compressor - This initial component of the engine compresses incoming air to high pressure. Multiple rows of compressor blades, progressively decreasing in size, facilitate air compression as it traverses through the compressor.

The combustion chamber - Following compression, the air-fuel mixture ignites in this section, propelling the high-pressure air from the compressor to expand towards the rear of the engine.

The turbine - Here, the hot, high-velocity air exiting the combustion chamber drives the turbine, which extracts work and powers the compressor at the engine's forefront through a connecting shaft. The momentum exchange between the incoming and outgoing air generates the engine's thrust.

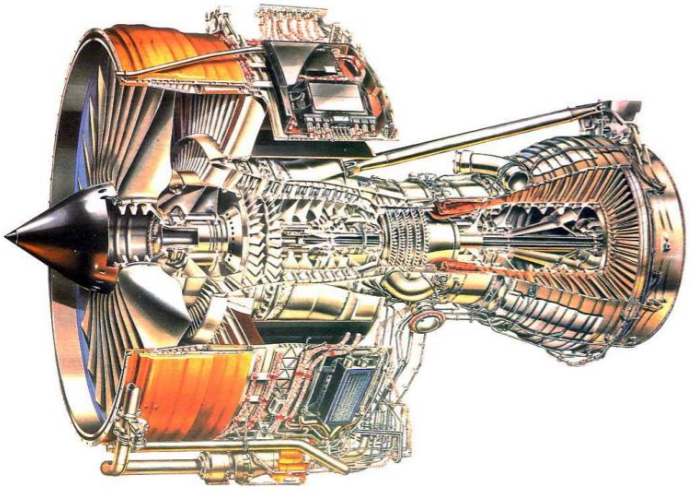

Figure 2.1: Rolls Royce Trent 800 gas turbine engine [1]

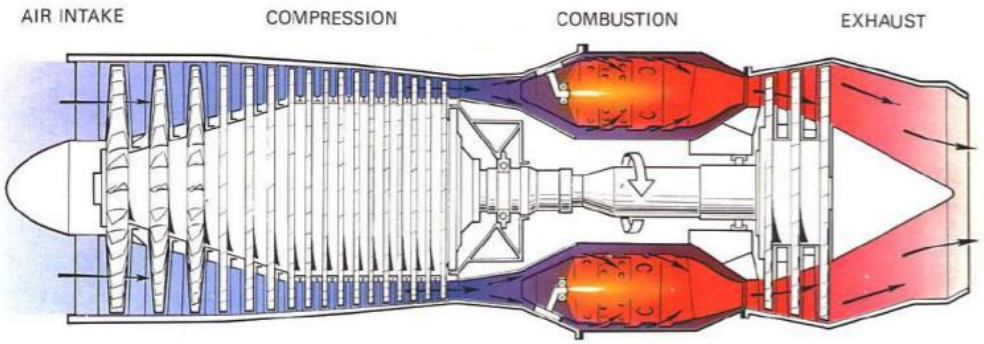

Figure 2.2: Diagram of classic gas turbine engine [1]

The operating conditions within a gas turbine engine therefore impose significant demands, particularly from a materials point-of-view. The high-pressure turbine, located immediately downstream of the combustion chamber, can encounter turbine entry temperatures exceeding 1400°C [2]. However, with turbine blade cooling and thermal barrier coatings, they often operate at temperatures closer to 700°C [3]. These elevated temperatures are essential for maximising engine efficiency by optimising the temperature difference between turbine inlet and outlet, as dictated by the second law of thermodynamics. The gas undergoes isentropic expansion through the turbine, and higher turbine inlet temperatures result in greater useful work being extracted. Consequently, there has been a continual effort to elevate turbine entry temperatures to enhance gas turbine engine efficiency. However, this endeavour presents challenges as the turbomachinery must withstand the ever-increasing temperatures and demanding stress conditions.

Ni-based superalloys have emerged as the preferred materials for gas turbine engines, particularly in critical components such as the turbine entry sections. Their widespread adoption can be attributed to a combination of exceptional mechanical properties at high temperatures, robust resistance to creep, fatigue, and oxidation. These attributes are critical for withstanding the extreme operating conditions within turbine entry sections, where temperatures and mechanical stresses are high. Despite their superior performance characteristics, the thermo-mechanical processing of these alloys poses considerable challenges, necessitating intricate processing techniques and meticulous control over microstructural evolution.

2.1.2 A History of Nickel-Based Superalloys

Nickel-Chromium alloys have been used since the turn of the nineteenth century when Albert L. Marsh was granted a patent for the electric resistance element in 1906 [4]. His patent showed that the alloying of nickel and chromium produced a metal that had high electrical resistivity properties, good resistance to oxidation, and good formability (i.e., it was able to be drawn). Formation of Cr_2O_3 was the reason for this good resistance to oxidation as it acts as a protective oxide for the material at high temperatures [5].

There is some debate as to when the very first nickel-chrome alloy containing aluminium or titanium was developed [6], [7], however it is widely credited that the first nickel-chrome alloy to contain sufficient amounts of both aluminium and titanium was designed by Bedford, Pilling and Merica in 1929 [8]. This can be seen on the timeline of Ni-based superalloy development in Figure 2.3.

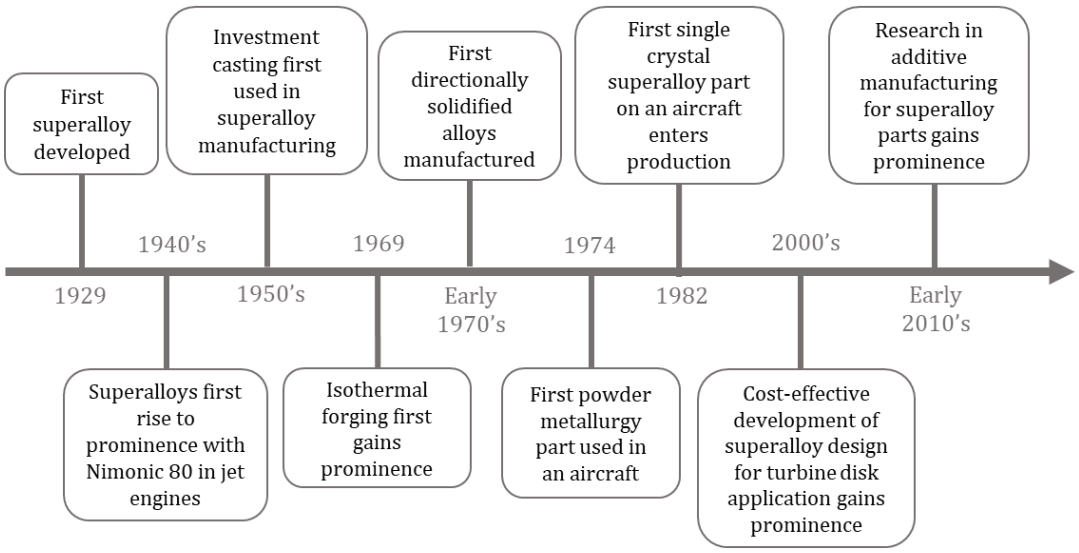

Figure 2.3: Timeline of Ni-based superalloy development [2], [7], [8], [9], [10], [11], [12], [13], [14], [15], [16].

It wasn't until the 1940's however when alloy design became more sophisticated when 0.1% carbon and 0.3% titanium were added to a nickel-chromium alloy to form one of the first Ni-based superalloys, Nimonic 75 [17], [18]. Soon after in 1940, a patent was filed by Leonard B. Pfeil of the Mond Nickel Company for an alloy with a base of at least 20% nickel, 1.5-5% titanium, 0-30% chromium, 0-60% iron, 0-0.25% carbon, 20% tungsten or molybdenum or

both, and 10% of other elements [12]. This alloy then named Nimonic 800, and later renamed to just Nimonic 80, was designed to be used for the turbine blades in Frank Whittles' gas turbine engine which flew as part of the Gloster Meteor in the early 1940's [19].

Nimonic 80A was developed a few years later when additional aluminium was added to further strengthen the material, which did so primarily because of the intermetallic $L1_2$ ordered $Ni_3(Al,Ti)$ phase known as the γ' phase [20]. It was unknown at that time, that this phase, precipitating coherently within the face-centred-cubic (FCC) structure, was the primary strengthening mechanism (this will be discussed in detail later). Similar to its Nimonic predecessors, Nimonic 80A had a sufficient amount of carbon that precipitated as secondary carbides at the grain boundaries acting as a grain boundary strengthener[2].

Further development of superalloys aimed to raise the fraction of the γ' phase to improve the alloys' strength at high temperatures. However, when the volume fraction of γ' exceeded 40%, the alloys became challenging to manufacture and process, particularly through forging, because of their increased high-temperature strength. Consequently, there existed a practical constraint on superalloy development, limiting the γ' volume fraction to approximately 40%, until advancements in investment casting technologies emerged [2].

The investment casting process gained prominence in the 1950s, particularly for superalloy development. This technique facilitated an increase in the volume fraction of the γ' phase from 40% to approximately 60% by adjusting alloy compositions, such as increasing the aluminium content and reducing chromium levels [11]. This adjustment is illustrated in Figure 2.4. Consequently, the γ' solvus temperature was raised, leading to enhanced mechanical properties at high temperatures. However, in alloys like IN100, this adjustment also decreased the alloys resistance to hot corrosion. As a response, a new trend emerged in superalloy design, exemplified by alloys like IN738LC, which maintained moderate chromium levels to preserve favourable high-temperature mechanical properties while improving resistance to hot corrosion [2].

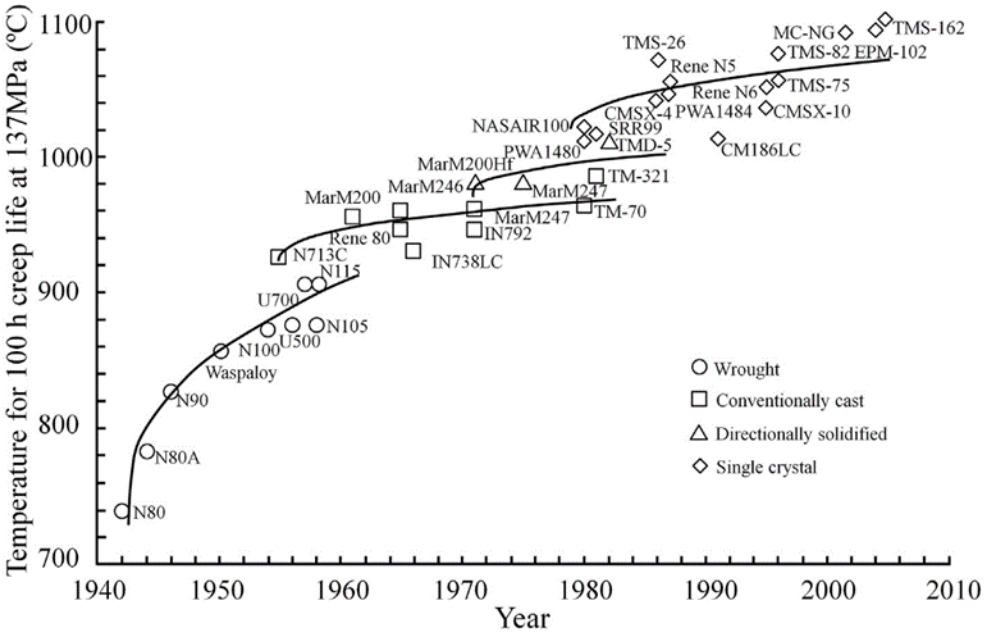

Figure 2.4: History of high temperature creep performance of Nickel based superalloys classified by manufacturing route [2].

Advancements in wrought superalloy manufacturing continued alongside the progress in conventional casting technologies. The evolution included the adoption of larger presses and die sizes, along with a transition towards closed-die press forging, enabling the production of larger and more intricate parts such as turbine discs [12]. Additionally, the emergence of isothermal forging gained traction around 1969 and later found application in manufacturing alloys through the powder metallurgy route. The suitability of powder metallurgy as a manufacturing method for superalloys became evident in 1974, demonstrated by its use in producing a component for the Pratt and Whitney F100 engine utilised in the F-15 Eagle fighter [2], [10].

Turbine discs made from Ni-based superalloys are subjected to vibrational loads during service and significant forces during the start and stop of turbine blades. This exposure makes them prone to high-cycle and low-cycle fatigue failures. Fatigue crack growth in blade and disc components can lead to part failure with potentially dangerous consequences. It has been found that the fatigue crack growth rate depends on the applied load, number of cycles, frequency of cycling, and environmental conditions such as temperature, material properties, and the presence of residual stresses. As a result, this area was identified as a key research focus for these alloys.

During the 1970's whilst working for the Pratt and Whitney company, Francis L Versnyder and colleagues began to apply the already pre-established method discovered by Percy W. Bridgman for growing crystals to superalloy development [2]. The alloys developed using this technique were called directionally solidified alloys. This technique manufactured alloys that had large, columnar grains and was initially used to form alloys like PWA 1422. The elimination of these perpendicular grain boundaries had resulted in better creep and rupture properties, particularly because the grain boundaries are susceptible to the initiation of creep [21].

In 1982, a significant advancement occurred in superalloy development with Pratt and Whitney's achievement of eliminating columnar grains in directionally solidified alloys. They introduced the first single crystal alloy, PWA 1480, for use in turbine aerofoils [9]. Single crystal alloys lacked grain boundaries, rendering grain boundary strengthening elements like boron, carbon, zirconium, and hafnium unnecessary in the chemical compositions. Consequently, subsequently developed alloys could undergo heat treatment at higher temperatures without encountering issues related to incipient melting at grain boundaries caused by these strengthening elements [22].

Carron et al. [23] have summarised the history of single crystals very well; they showed that single crystals without the grain boundary strengthening elements were typically referred to as first generation single crystals. These consisted of alloys such as CMSX-2, PWA 1480, and NASAIR100, the latter of which was developed from the earlier MAR-M247 alloy. First generation single crystals are characterised by the lack of boron, carbon, zirconium and hafnium, as well as their improved creep strength over conventionally cast or directionally solidified alloys. A timeline of single crystal alloys and their high temperature creep performance classified by generation can be seen in Figure 2.5.

They also showed that the second generation of single crystals included the addition of rhenium, typically up to about 3 % wt., which further improved the creep strength of these alloys. A drawback to this addition though is the emergence of topologically close packed (TCP) brittle phases which weaken the material mechanical properties. Some examples of second-generation single crystal superalloys are CMSX-4, SMP14, and PWA1484.

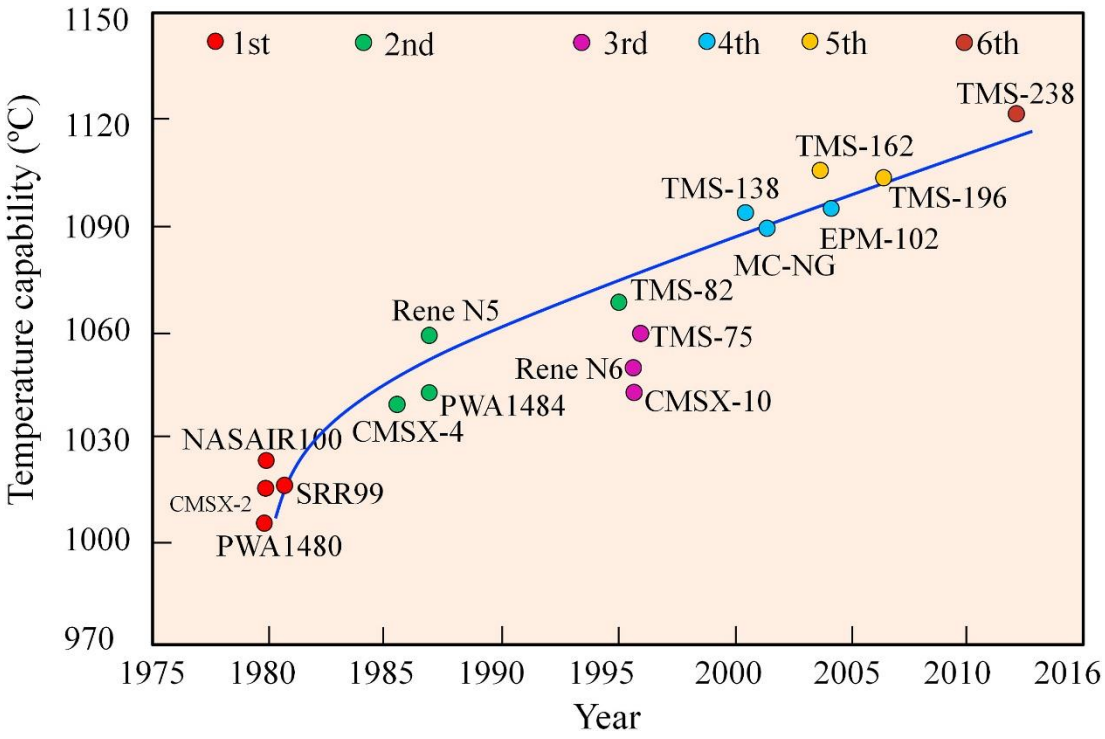

Figure 2.5: A selection of single crystal Nickel-based superalloys classified by generation, showing their temperature capability. Note temperature capability is the alloys capability in enduring 100 hrs of creep testing at 137 MPa tensile stress without cracking [2], [24], [25], [26].

Furthermore, Carron et al. [23] have also shown that the third-generation single crystal alloys can be easily characterised by the addition of yet more rhenium, up to 6 % wt.. Naturally, this leads to further problems with the deleterious TCP phases as the larger amount of refractory material increases the likelihood of precipitation. CMSX-10 and René N6 are both classic examples of third generation single crystal alloys.

Recently, ruthenium has been incorporated into alloys to preserve high creep strength properties while mitigating some adverse effects of TCP phase precipitation. These alloys are commonly known as fourth-generation single crystal superalloys, exemplified by TMS-138 and TMS-162. Additionally, fifth and sixth-generation alloys have emerged, featuring increased ruthenium content ranging from 3% to 5% for fifth-generation superalloys, along with various adjustments to the quantities of other elements distinguishing sixth-generation alloys [24].

Recent efforts have explored the application of additive manufacturing techniques such as binder jetting, laser metal deposition, and powder bed fusion for producing superalloy parts used in aircraft. These methods are favoured for their elimination of hard tooling

requirements, reduced post-processing needs, and minimised material usage compared to traditional methods [13]. However, these technologies still face several limitations, including slow production rates, restricted part sizes, subpar surface finishes, porosity issues, and challenges in achieving intricate details [13]. Moreover, a significant drawback lies in the microstructure of the fabricated parts, resembling that of as-cast ingots with elongated dendrites, resulting in anisotropic properties. There are also difficulties in controlling secondary phase precipitation [14]. Further advancements are needed before these techniques can be viable for mass-producing medium to large-scale parts made from Ni-based superalloys.

Finally, modern design of superalloys for turbine discs applications has taken a more focussed approach in tailoring the necessary high strength mechanical properties for the given application, whilst trying to keep the manufacturing costs down. Therefore, alloys like Udimet 720, ATI 718Plus, and AD730 have favoured the cast and wrought route of manufacturing as it is a cheaper method of manufacture than the powder metallurgy route [15]. These alloys, despite favouring the cheaper manufacturing route, are part of a continued effort to bridge the gap in terms of performance between IN718 and alloys developed using the powder metallurgy route [27].

2.1.3 Microstructure, Composition and Strengthening Mechanisms in Ni-Based Superalloys for Turbine Disc Application

Table 2.1 shows the nominal chemical composition of some Ni-based superalloys typically used for turbine disc applications. As can be seen, there is a large variety of alloying elements present in these alloys. The alloying elements partition to certain constituents of the alloy and help to stabilise microstructural phases necessary to achieve the desired mechanical properties. The main phases present in the microstructure of Ni-based superalloys were outlined well in [2] and [28], and are briefly discussed in the following section.

Table 2.1: Nominal chemical composition of selected Ni-based superalloys (% wt.) [27], [29]

Alloy	Ni	Cr	Mo	W	Co	Fe	Nb	Ti	Al	Other
AD730	Bal.	15.7	3.1	2.7	8.5	4	1.1	3.4	2.25	Zr, B, C
ATI 718 Plus	Bal.	18	2.8	1	9	10	5.4	0.7	1.45	B
Waspaloy	Bal.	19.4	4.25	-	13.2	-	-	3	1.3	Zr, B
Udimet 720	Bal.	16	3	1.25	15	-	-	5	2.5	Zr, B
Inconel 718	Bal.	18.1	2.9	-	-	18	5.4	1	0.45	-

The γ Matrix

The γ matrix is a continuous austenitic phase with FCC crystal structure where all other phases reside. This matrix is typically made up of nickel, cobalt, chromium, rhenium, ruthenium, molybdenum, and sometimes iron. The most dominant element in the alloy is nickel, with typically the next most plentiful alloy being chromium. The chromium content in Ni-based superalloys is usually in the region of 10-20 % weight percentage (% wt.) [30]. Chromium displays a body centred cubic (BCC) structure, however, as can be seen in the nickel-chromium phase diagram shown in Figure 2.6, at levels of 10-20 wt% chromium is an FCC stabiliser. The addition of chromium provides excellent hot corrosion and oxidation resistance to the material through the formation of a protective oxide layer (i.e., Cr_2O_3). This oxide layer protects the material by acting as a diffusion barrier on the surface. This oxide only forms when there is sufficient chromium in the material indicating that a lack of chromium in the alloy severely reduces the hot corrosion and oxidation properties. Conversely, excessive chromium content increases the likelihood of the TCP sigma (σ) phase precipitating [30].

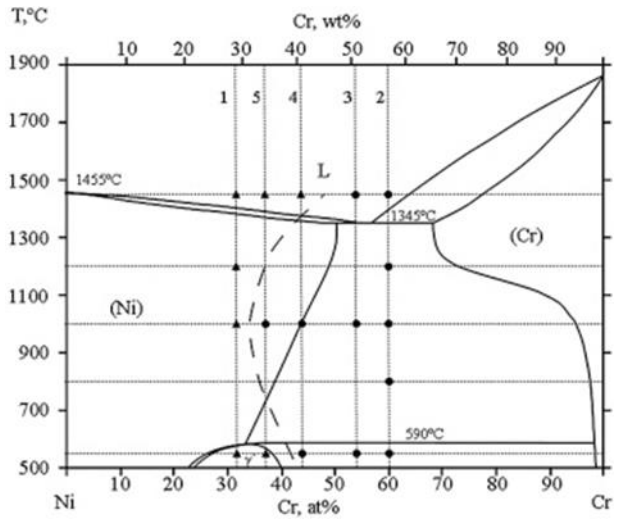

Figure 2.6: Binary Phase Diagram of Nickel-Chromium [29].

The addition of cobalt typically increases the cost of the material as this is a particularly expensive metal, however, it provides the alloy with better hot workability, better creep rupture life, and a reduced creep rate. For those superalloys which include iron, this typically reduces the net strength of the material but makes the cost of the superalloy more affordable [30]. Finally, molybdenum and tungsten, two of the other alloying elements which reside within the γ matrix, increase the solid solution strength of the material along with chromium and aluminium; this will be discussed in more details later.

The γ' Phase

γ' is the primary strengthening phase containing nickel and other alloying elements such as aluminium, titanium, and tantalum. The nickel-aluminium binary phase diagram in Figure 2.7 shows that there are solid phases for which the chemical structure of nickel-aluminium is ordered containing $NiAl_2$, Ni_2Al_3 etc. as well as the all-important Ni_3Al. Figure 2.8 shows the disordered FCC composition as well as the ordered γ' phase. The γ' phase has a cubic (Ll_2) crystal structure which is often coherent with the FCC γ matrix [2]. As can be seen in Figure 2.8, there are 3 nickel atoms for every 1 aluminium atom. As was previously mentioned, the γ' phase can form as Ni_3(Al, Ti, Ta) where the titanium and tantalum atoms substitute for the aluminium atoms in the structure shown in Figure 2.8.

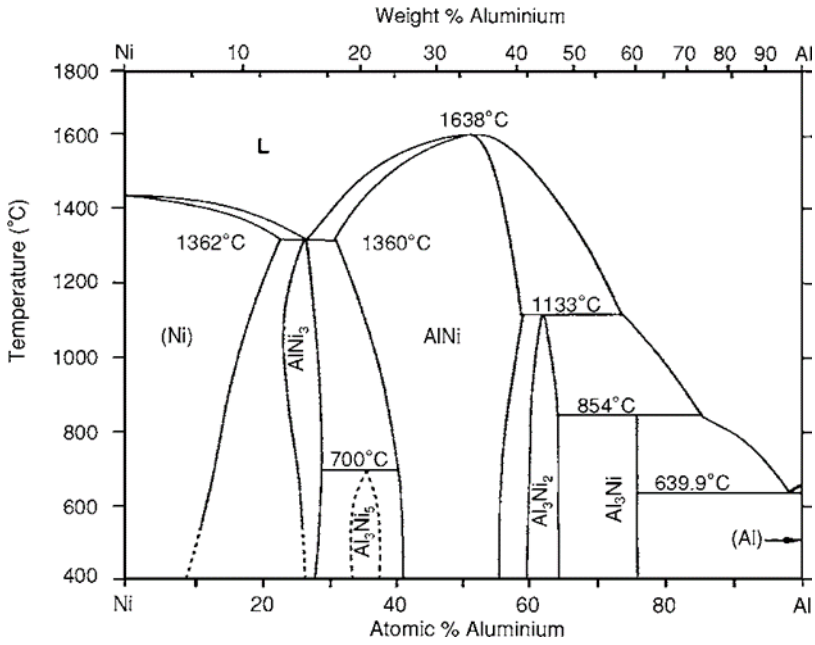

Figure 2.7: Binary Phase Diagrams of Nickel-Aluminium [31].

Analysis has been done using transmission electron microscopy (TEM) to understand the orientation relationship between the γ' precipitates and the γ matrix. It has been shown to have a cube-cube orientation relationship described in Equation 2.1, with the γ' aligning often along the <100> direction [2].

$$\{100\}_{\gamma}//\{100\}_{\gamma},$$

$$\{010\}_{\gamma}//\{010\}_{\gamma},$$

Equation 2.1

Not only can the composition of the γ' precipitates vary, but their size and morphology can also change too. It has been shown that as the size of the γ/γ' lattice misfit is increased, the morphology of the γ’ changes from spheroidal to cuboidal, to an array of cubes analogous to a butterfly shape (i.e., due to directional growth)[30]. Solution heat treatments, the cooling rates of the alloy from the heat treatments, and ageing heat treatments, have all been shown to impact the size and shape of the precipitates [2].

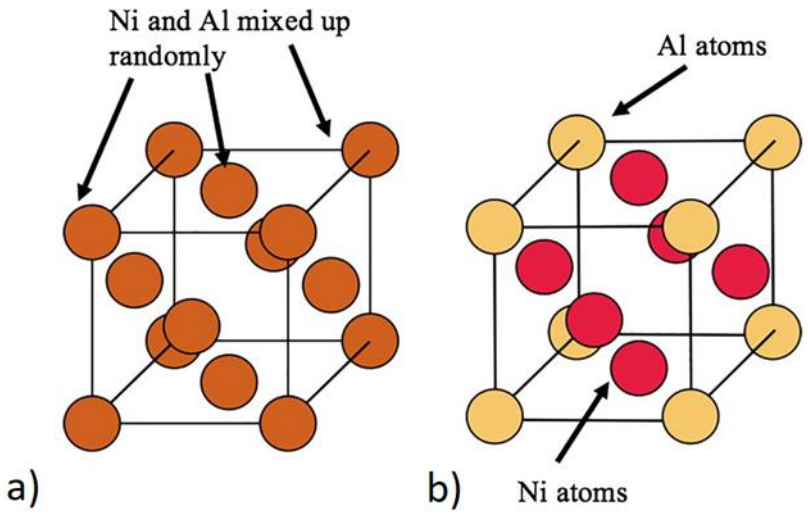

Figure 2.8: Face Centred Cubic (FCC) Unit Cell showing a) disordered Nickel-Aluminium atoms and b) L12 ordered Nickel-Aluminium atoms [32].

The γ' precipitates are often classified into three categories based on their size. These sizes often vary depending on the source, however a good guide is provided in literature and described in the following [2]. Figure 2.9 depicts the phases graphically.

Primary γ': These coarse precipitates, with diameters ranging between 1-10 µm, form during the casting and forging processes. These precipitates, which endure subsequent solution heat treatments, are primarily located at the grain boundaries, known as intergranular precipitates. They are the only size of γ' precipitate that is incoherent with the γ matrix. The γ' solvus temperature, determining the dissolution of γ' into the γ matrix, is heavily influenced by the chemical composition of the alloy. Typically, for superalloys utilised in turbine disc applications, the γ' solvus temperature falls within the range of 1050 ˚C - 1200 ˚C [2].

Secondary γ': These precipitates range in diameter from 70 nm to 120 nm, although in some cases, they are still considered secondary even at sizes up to 200 nm [33]. They are generally cuboidal in shape but can also take the form of a butterfly or an array of cubes, depending on their size. Unlike the primary γ' precipitates, the secondary and tertiary ones are coherent with the matrix.

Tertiary γ': Tertiary γ' precipitates are the smallest among the γ' precipitates, with a diameter ranging from 5 nm to 50 nm. These precipitates typically assume a spherical shape and are formed when the material is rapidly cooled from the solution heat treatment temperature,

such as during water quenching. If the sample is quenched immediately after the solution heat treatment, the precipitates will be in the range of 5 nm to 15 nm. However, after ageing, they grow to larger sizes, ranging between 15 nm and 50 nm

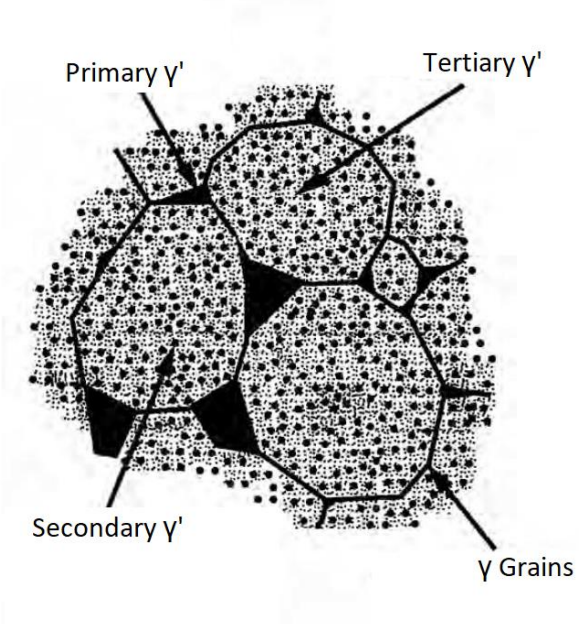

Figure 2.9: Schematic representation of a typical Ni-based superalloy microstructure labelling primary, secondary and tertiary γ' phases. Altered from [2].

The γ'' Phase

The γ" phase with body centred tetragonal (BCT) crystal structure is only present in nickel-iron rich superalloys which have high concentrations of niobium, or sometimes vanadium in the form of $Ni_3(Nb,V)$. The γ'' precipitates are typically coherent with the γ matrix and have the DO_{22} crystal structure as shown in Figure 2.10, like that present in IN718. IN718 contains both γ' and γ'', however the latter provides the primary strengthening mechanism for this material [34]. The morphology of this precipitate is different from that of the γ' phase. Unlike the spherical and cuboidal shapes present in γ', the γ'' precipitates have a disc or 'pancake' like morphology growing along {111} crystallographic planes.

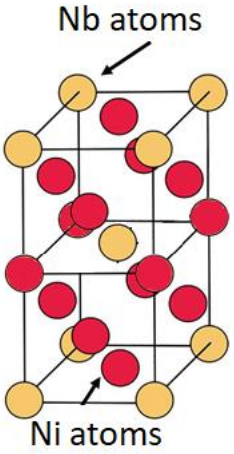

Figure 2.10: Body Centred Tetragonal (BCT) unit cell showing $D0_{22}$ ordered Nickel-Niobium atoms. Recreated from [2].

One of the notable characteristics of γ'' strengthened alloys is their susceptibility to the precipitation of the δ phase. This is discussed more later in this thesis.

Carbides

Different types of carbides form in superalloys depending on the carbon content, the types of alloying elements present in the composition, and the processing conditions of the material. Carbides can take on many forms including MC, M_6C, $M_{23}C_6$, and M_7C_3, where M is substituted by chromium, hafnium, molybdenum, tantalum, tungsten, or titanium. The primary MC carbide forms at higher temperatures when the alloy solidifies from the molten phase, with a coarse cubic morphology that often forms heterogeneously, and is rich mainly in titanium, hafnium or tantalum [35], [36]. This carbide has a FCC structure and is relatively stable. The primary MC carbide with molybdenum or tungsten however is less stable with weaker bond strength that makes it prone to decomposition to a reduced form such as $M_{23}C_6$ and lower carbides [36].

The primary MC carbides break down and decompose at higher temperatures, yielding carbon, which reacts with the γ matrix forming secondary carbides and γ' according to the chemical reactions shown in Equation 2.2 and Equation 2.3 [2], [37].

$$MC + \gamma \rightarrow M_6C + \gamma'$$

Equation 2.2

$$MC + \gamma \rightarrow M_{23}C_6 + \gamma'$$

Equation 2.3

The secondary $M_{23}C_6$ carbides often contain high levels of chromium and typically precipitates at the grain boundaries where they inhibit grain boundary sliding. The M_6C secondary carbide is more thermodynamically stable than the $M_{23}C_6$ carbide and often forms when there are higher levels of molybdenum and tungsten. These carbides precipitate at the grain boundary, pinning the boundaries and preventing further grain growth [36].

Borides

Like their carbide counterparts, borides typically form at grain boundaries and act as strengthening particles. They can form as M_5B_3, M_3B_2 and sometimes M_2B depending on the alloying elements and the applied processing conditions [38]. Boron usually combines with chromium or molybdenum to form borides which helps to improve the rupture life of superalloys. However, adding too much boron to the alloy composition can negatively impact the rupture life by the breakdown of borides into deleterious TCP phases [24].

Topologically Close Packed (TCP) Phases

TCP phases like mu (μ), sigma (σ), eta (η) and laves all form in different materials and have different structures [2]. These phases form at high temperatures during service, and form due to an excess of rhenium, chromium, tungsten or molybdenum [2]. They often have precise stoichiometry as well as a very high density and packing of atoms giving weight to their names. These phases are almost always undesirable and deleterious to the material in some way, whether that's through weakening of mechanical properties, facilitating crack propagation, reduction in ductility and causing low temperature brittle fracture of the material, or through weakening of the creep properties [24], [39]. A summary of some key phases and their microstructural characteristics such as crystallographic structure is given in the Appendix.

Strengthening

The creep strength of an alloy can be increased by the addition of solutes with high hardening coefficients and good solid solubility to the γ matrix. These solid solution forming elements impart strength to the material by resisting against the free movement of dislocations through grains. They do this by making cross slipping of atoms more difficult through several ways. Firstly, by introducing solute atoms with a higher shear modulus than the lattice thus

generating a higher local shear modulus creating a local stress field, and secondly, by the distortion of the lattice created by the solute atoms size [40]. Furthermore, as the distance between nickel's position and that of the solutes on the periodic table is increased, the stacking fault energy decreases and the lattice distortion is increased. This phenomenon results in solutes with larger atomic radii and position farther away from nickel in the periodic table, providing more strength to the material.

As has been mentioned previously, γ‘ is the primary strengthening mechanism in Ni-based superalloys. The size, morphology, volume fraction and distribution, all have an impact on the strengthening imparted to the material. The γ‘ volume fraction has been shown to positively impact the mechanical properties when it is greater. It was shown previously [41] that peak strength is reached when tertiary γ‘ is at its highest volume fraction before it coarsens. However, there is often a trade-off between mechanical properties and creep properties. The distribution of precipitates is also key to the materials strengthening. It is often the case that the creep deformation is restricted to the γ matrix as dislocations are unable to cut precipitates. When this is the case, small and uniformly dispersed precipitates are the optimal microstructure with a fine γ‘ channel between the precipitates. An example of this is shown in Figure 2.11 with the γ‘ being slightly coarser than tertiary γ‘ size.

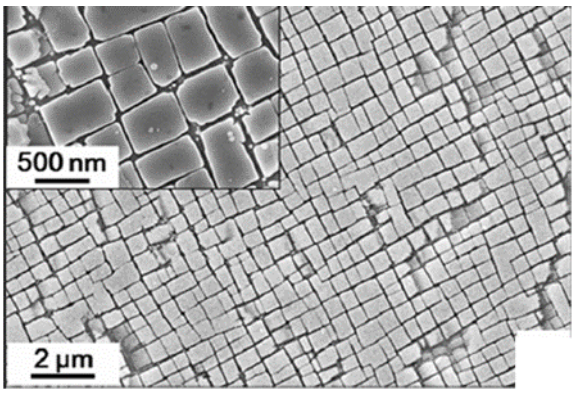

Figure 2.11: Small, uniformly dispersed γ‘ precipitates shown in a single crystal superalloy CMSX-4 with a small γ matrix channel [42].

The γ‘ precipitates are stronger than the γ matrix making them difficult, though not impossible, to be cut by dislocations. One of the main barriers to dislocations cutting the precipitates is whether the anti-phase boundary energy can be overcome. The anti-phase boundary is the point where the crystallographic order of the lattice is completely opposite to that of the perfectly ordered crystallographic lattice. Anti-phase boundary energy refers to the energy

needed to prevent this boundary from forming when a dislocation cuts through a precipitate [2].

If dislocations were to cut the precipitate, as can be seen in Figure 2.13, it would create an anti-phase boundary which would have considerable anti-phase boundary energy associated with it. It has been shown that dislocations do not travel through the γ/γ' microstructure singularly, but rather as a pair known as super dislocations. This was shown by Nembach *et al* [43] and can be seen in Figure 2.12. The particle cutting stress is shown to be significant and is the reason that γ' precipitates offer a substantial amount of strength to superalloys through what is known as order strengthening.

If the dislocations cannot penetrate and cut the particle, they will often bypass the precipitate in what is known as Orowan bowing, as can be seen in Figure 2.13 [2]. Orowan bowing occurs when the precipitate size increase past the critical size (r_c) meaning it is more likely for bowing to take place than cutting. This bypassing of the precipitates creates loops around the precipitates which act as entanglements and serve to further increase the strength much in the same way as work hardening [2].

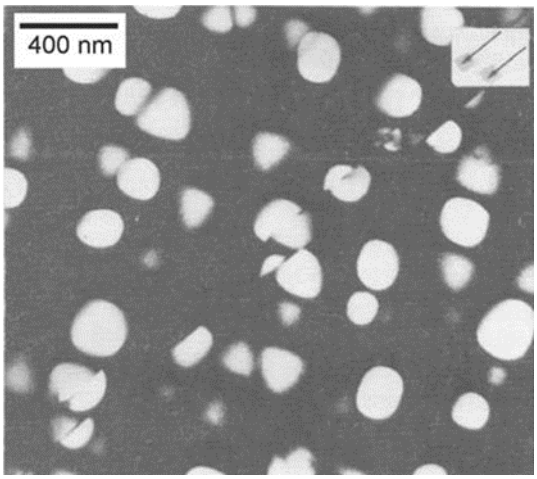

Figure 2.12: TEM micrograph supporting the idea that dislocations travel through the γ/γ' microstructure in pairs to overcome the anti-phase boundary [43].

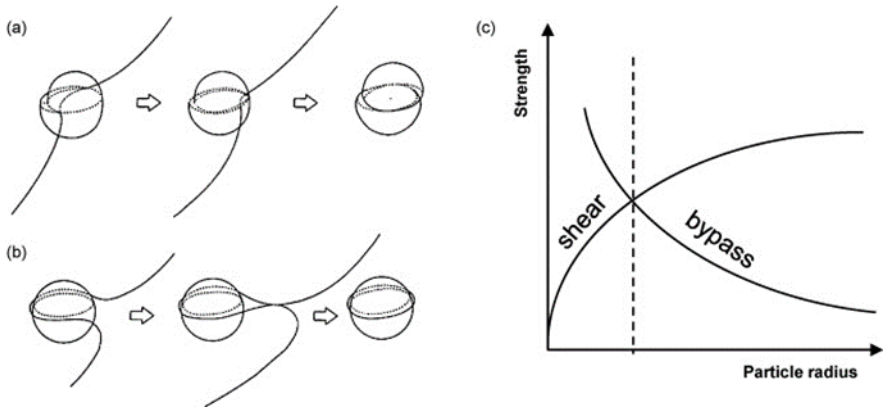

Figure 2.13: a) Dislocation shearing the precipitate b) Dislocation bypassing precipitate (Orowan bowing) c) Shear-bypass relationship with precipitate's radius [44], [45], [46].

Nickel based superalloys have a fairly unique property by exhibiting what is known as anomalous yielding behaviour. This implies that the stress associated with the beginning of the onset of plastic deformation does not decrease as temperature increases, as happens with most materials and alloys. Contrarily, this stress increases with additional temperature up until a point, usually somewhere in the region between 700 – 800 °C, before finally decreasing with subsequent additional temperature. At lower temperatures, segments of γ' superpartial dislocations cross-slip from the {111} slip plane to the cross-slipped {001} plane, forming Kear-Wilsdorf locks when under loading. These cross-slipped segments act as microstructural locks, resisting deformation because they cannot move without trailing anti-phase boundaries. When the temperature increases beyond the peak strength, typically around 800°C, cube slip on the {100} planes becomes dominant, reducing the impact of Kear-Wilsdorf locks. [2], [48].

2.1.4 Manufacturing of Superalloys

Ni-based superalloys are manufactured using one of several manufacturing routes, the cast and wrought route, the powder metallurgy route, by investment casting, or by using the Bridgman technique to create directionally solidified or single crystal alloys. All these steps are discussed in detail in the following sections.

Cast and Wrought Route

The cast and wrought route is one of two methods used for manufacturing superalloys intended for turbine disc applications. In this process, the material is initially cast into ingots and then undergoes sequential thermo-mechanical processing at elevated temperatures, typically through forging. This processing aims to tailor the microstructure to achieve desired

mechanical properties required for critical load and environmental conditions, such as those experienced by turbine discs in gas turbine engines. Consequently, it is crucial to understand the microstructural evolution and precipitation mechanisms during thermo-mechanical processing [25]. This processing includes various heat treatments, such as homogenisation and recrystallisation, as well as forging operations performed below or above the temperature at which precipitates dissolve (sub and super-solvus forging), using both open and closed-die techniques. The entire manufacturing process, from raw material conversion to the final part, is illustrated schematically in Figure 2.14 and will be discussed further in subsequent sections.

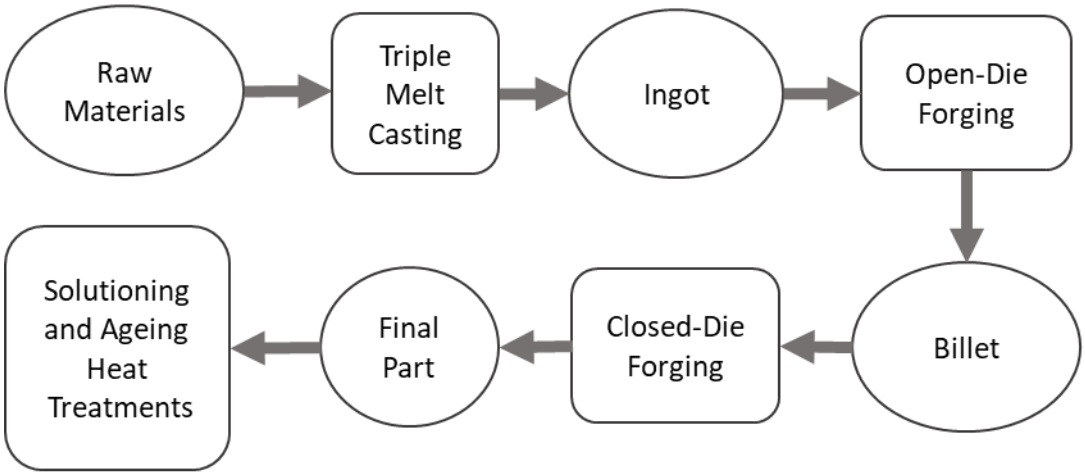

Figure 2.14: Typical Cast and Wrought manufacturing route of superalloys.

Casting

The cast and wrought route firstly involves melting of the raw materials to ensure an alloy of very high quality with high purity and consistency in the distribution of chemical compositions. This is then followed by thermo-mechanical processing. The first step in the triple melting process consists of vacuum induction melting (VIM).

Vacuum Induction Melting (VIM)

As the name suggests, in this process the material is melted under a vacuum using induction heating as shown in Figure 2.15. Conducting the melting process in a vacuum has several advantages. Firstly, it de-gasses the alloy, resulting in the reduction of the quantities of oxygen and nitrogen in the melt. These elements are prone to reacting with other elements present in the alloy, like titanium, aluminium etc. to form oxides, leading to a minimised loss of alloying

elements to oxidation. Secondly, melting in a vacuum also helps to reduce impurities in the mixture both by removal of low melting point elements (e.g., lead, bismuth, copper etc.), and dissolved gases in the melt (e.g., hydrogen). Although the melting takes place at an induction frequency sympathetic to the crucible and materials, often refractory materials such as sulphur, from the crucible and crucible lining mix in with the melt. Desulphurisation often takes place by the addition of lime as, due to the sealed nature of the furnace, it is difficult to modify the melt by compositional changes to the initial starting materials [49].

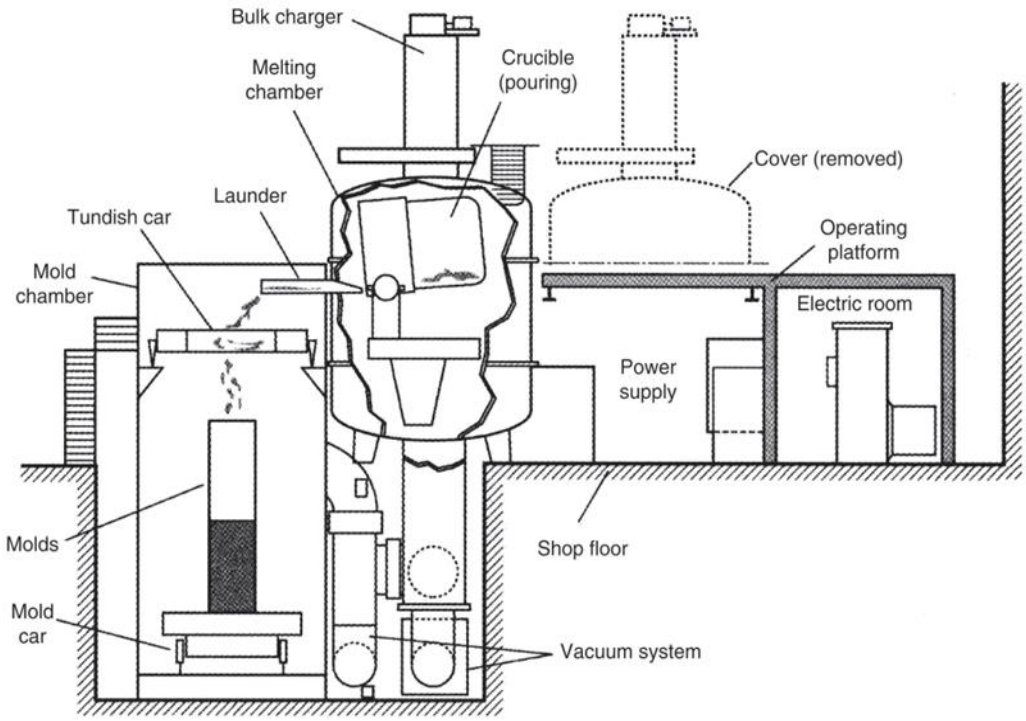

Figure 2.15: Diagram showing the Vacuum Induction Melting (VIM) process in a double chamber vacuum induction furnace [49].

Electro-Slag Remelting (ESR)

The next stage in the triple melting process is the Electro-Slag Re-melting (ESR) step. This process involves the re-melting of the solidified material from the VIM process. The material is used as a consumable electrode as shown in Figure 2.16. An electrical current is passed through the electrode and the conducting slag which is typically made up of alumina, lime, and calcium fluoride. This slag conducts and melts due to its high level of electrical resistivity. Since the electrode is immersed in the molten slag, it is eventually heated up and melted. The molten, dripping metal from the electrode is then refined as it passes through the slag before cooling and solidifying. One of the major disadvantages of ESR is its susceptibility to freckles,

tree-ring patterns and white spots which occur in the microstructure of the resolidified material from the melt. This can negatively affect the mechanical properties and overall quality of the ingot.

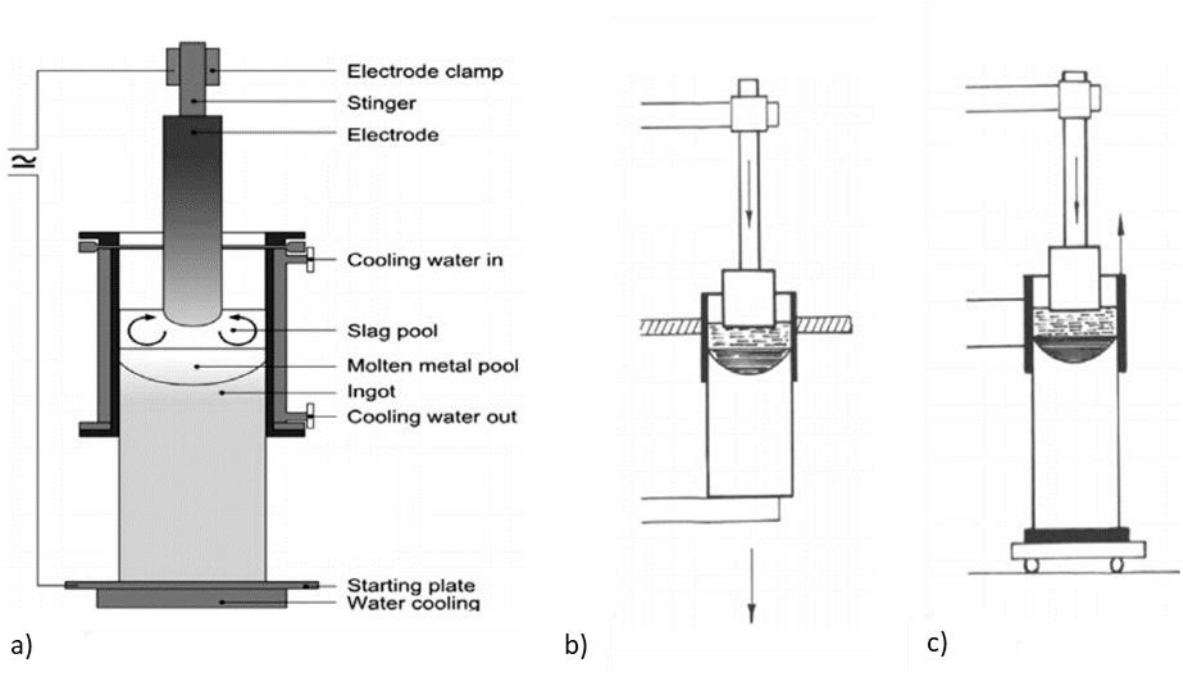

Figure 2.16: Diagram showing the Electro-Slag Remelting (ESR) process; a) overview of process, b) a retracting ingot, and c) a rising mould [50].

Vacuum Arc Remelting (VAR)

The final stage of the triple melting process involves Vacuum Arc Remelting (VAR). In VAR, depicted in Figure 2.17, a small portion of the ingot is melted and placed at the base of a crucible. The remaining material serves as an electrode, which, in a vacuum environment, is brought close to the molten alloy at the bottom of the crucible. An electric current is then passed through the electrode, creating a spark that melts the alloy at the crucible's base. This process is repeated to maintain continuous melting. VAR is aimed at reducing impurities and degassing the material, similar to VIM. However, VAR has limitations—it cannot produce large ingots due to the inability to exchange electrodes in a vacuum environment, and it may cause the evaporation of desired alloying elements [49].

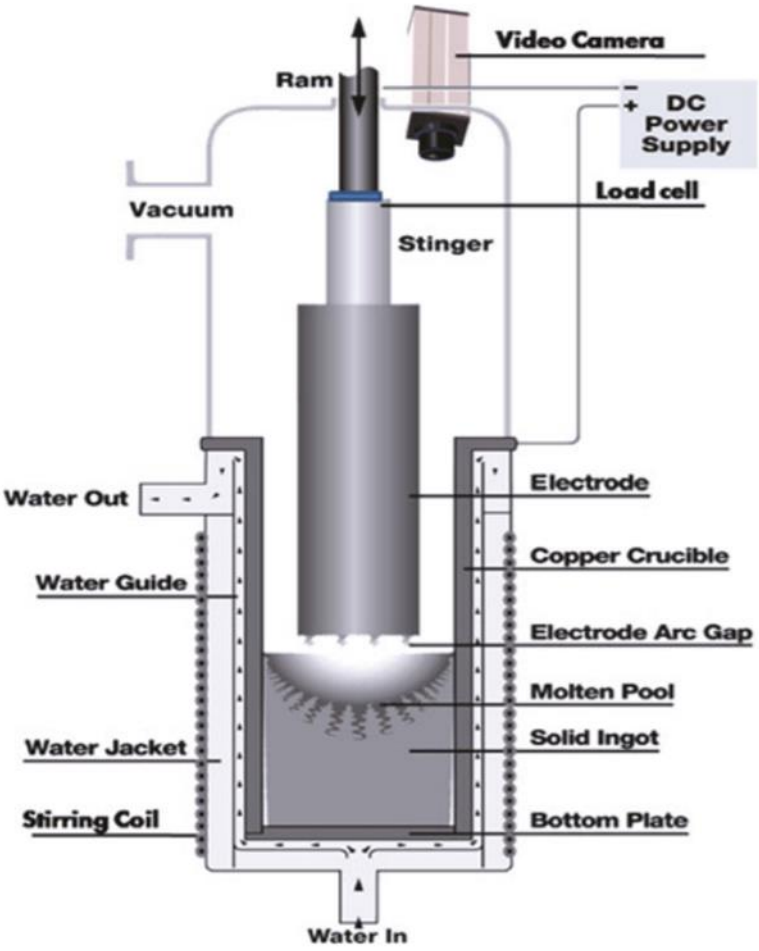

Figure 2.17: Diagram showing the Vacuum Arc Remelting (VAR) Process [51].

Thermo-Mechanical Processing

Following the triple melting process, the as-cast ingot is then subjected to thermo-mechanical processing to design and modify the microstructure for desired mechanical properties. The thermo-mechanical processing usually begins with open-die forging, which involves the upsetting and cogging processes. Upsetting occurs early in the ingot-to-billet conversion process, during which the material is forged axially with an upset ratio typically between 1.2 and 1.4 of its length. The upset ingot also undergoes cogging, where it is struck and deformed radially while being rotated about its axial axis repeatedly. This process leads to an increase in length and a decrease in cross-section, often resulting in the shape of an octagon. For Ni-based superalloys, the upsetting and cogging operations at the very early stages of open-die forging may be repeated several times. During cogging, constant strikes on the ingot occur at temperatures above the γ' solvus, where the material lacks its potential strength. Both the

cogging and upsetting processes are essential for controlling the microstructure, particularly the grain size of the ingot. Before undergoing upsetting and cogging, the grain size of the as-cast ingot is large and inhomogeneous. These processes help homogenise the microstructure, resulting in a finer grain size throughout the ingot cross-section, often through the initiation of dynamic recrystallisation (DRX), and increase the ingot's density [52]. Upsetting is typically needed to deform the ingot at its core, as the deformation caused by cogging does not usually reach the centre, which is necessary to provide enough driving force for a consistent recrystallisation throughout. Following the cogging process, the ingot is then forged in an open-die press, hot working the metal in all directions to form a billet. The billet is then forged by blocking, meaning that the metal is forged often in an open-die press towards a shape representative of the final shape, and finally by a closed-die forge. Figure 2.14 shows the sequence of these processes schematically. This completes the typical ingot to billet conversion process. It is important to note that there will often be several forging passes at all stages and there are often various heat treatments dispersed in between these stages seeking to further control the microstructure. The different forging stages can take place above and below the relevant solvi in Ni-based superalloys [53].

Powder Metallurgy Route

The powder metallurgy route is the second of the two heavily utilised manufacturing routes used for superalloy development for turbine disc applications. Due to the nature of Ni-based superalloys, increasing the volume fraction of γ‘, particularly past the 60% mark, results in increased strength which makes the thermo-mechanical processing of the alloys more challenging. In order to better forge and mechanically work the alloys with high γ‘ volume fraction, heating the alloys above their γ‘ solvus, where the primary strengthening mechanism precipitates would be dissolved and the alloy would be weaker and more workable, was thought of as being the best solution. However, this often leads to problems like incipient melting of the material and problems with tool wear. If the temperature was lowered to below the γ‘ solvus, the γ‘ precipitates strengthens the material, making the forging and hot working very difficult [2], [54]. The solution to this predicament was the development of the powder metallurgy processing route. In this process, firstly the materials which are to make up the alloy are atomised typically via the use of inert gas (often Argon) or by high water pressure. These metals are then in a powder state and can be mixed to form the chemical composition of the alloy. The next step for superalloy development typically involves hot isostatic pressing

(HIP) being applied to the powder composition mix. The powder composition mix is loaded into a mould, and as the HIP name suggests, when at elevated temperature, the material is pressed using an isostatic pressure usually from an inert gas like argon. This helps to reduce the porosity of the material, increase the density, and improve the mechanical properties. Furthermore, using this technique also allows for near net shape castings to be created, giving this method an advantage over the cast and wrought route which requires parts to be thermo-mechanically worked. It also offers another significant advantage over the cast and wrought route as the γ‘ volume fraction can be increased leading to a stronger material. One of the significant disadvantages of this technique however is that it is typically more costly than the cast and wrought processing route, particularly for the atomised metal [2].

Heat Treatments and Ageing

Once the initial cast and wrought or powder metallurgy processing route, laid out above, is complete, the material then undergoes a series of heat treatments to tailor its mechanical properties for its in-service operation. The main methods of industrial heating are convection heating and induction heating. Convection heating, the most popular method, uses heating elements from electric furnaces or heat from gas furnaces to create a convection current that heats the billet. Induction heating, where an induction coil generates heat in a billet through electromagnetic induction, is also sometimes used. Resistivity heating, which involves passing current directly through the billet to generate heat, is less commonly employed. For most superalloys, and particularly those used for turbine disc applications, this typically involves a solution heat treatment, and then an ageing or possibly multiple ageing steps. Initially the material is solution heat treated either slightly above its γ‘ solvus, known as a super-solvus solution heat treatment, or below its γ‘ solvus, known as sub-solvus solution heat treatment.

If the alloy is solution annealed below its γ‘ solvus, it will therefore retain some coarse primary γ‘ precipitates which reside at the grain boundary and help prevent excessive grain growth. Solution annealing at this temperature will not dissolve the primary γ‘, but it will dissolve the secondary and tertiary γ‘ phases. Upon cooling and during the subsequent ageing heat treatments, the γ‘ will then precipitate in both the secondary and tertiary size classification known as the trimodal state, depending on the temperature and time at temperature [41].

In the super-solvus solution heat treatment scenario, the temperature surpasses the γ‘ solvus threshold, causing all γ‘ precipitates to dissolve into the matrix. Subsequently, during cooling

and ageing, γ‘ precipitates form in both the secondary and tertiary categories, resulting in the alloy being in a bimodal state devoid of primary γ‘ [41]. Consequently, the material relies on carbides and borides to hinder excessive grain growth at elevated temperatures.

Upon cooling from the solution annealing heat treatment temperatures, depending on the cooling rate, secondary and tertiary γ‘ will precipitate out of the γ matrix. Secondary γ‘ will precipitate first at the higher temperatures and will then grow as the alloy continues to cool. As cooling continues, tertiary γ‘ will then begin to precipitate. It has been shown that if the cooling rate from the super-solvus temperatures is very fast, it is possible to suppress the precipitation of tertiary γ‘ altogether [33]. The same work also showed that as the cooling rate is increased, the volume fraction of both secondary and tertiary γ‘ is decreased. Furthermore ref [33] have shown that the morphology of precipitates is also directly related to the cooling rate. They showed that for various superalloys, a faster cooling rate leads to fine spheroidal secondary γ‘, whereas a slower cooling rate leads to large dendritic secondary γ‘ with trace amounts of tertiary.

Depending on the type of superalloy, the solution heat treatment can often be much more complicated than that described above. Often temperatures are ramped up over the course of the heat treatment to achieve a balance between the high temperatures, which are necessary to dissolve the elements, and lower temperatures such that the incipient melting point of the alloy is not reached [60]. These types of solution heat treatments are often carried out in a vacuum furnace to prevent contamination by oxides with the parts often being cooled through forced air/gas cooling before being aged. This type of heat treatment is particularly prevalent when dealing with single crystal superalloys [61].

Following the solution heat treatment, the superalloy will then typically be aged. Ageing heat treatments are carried out at temperatures often substantially below that of the solution heat treatment temperatures, and in the region of 700°C but with temperatures varying depending on the alloy [2], [33], [36]. The purpose of the ageing heat treatment is to impart strength into the material through precipitation of secondary and tertiary γ’ and or other types of precipitates such as δ-phase and γ” where possible. The kinetics of γ‘ nucleation, growth and coarsening are complex. Following solution annealing and cooling of the material, the γ‘ phase is dissolved into the γ matrix with some secondary or tertiary γ‘ having already precipitated depending on the cooling rate. Depending on the ageing temperature and time spent at the

temperature, tertiary γ‘ will begin to precipitate or/and secondary γ‘ will begin to coarsen. It has been shown by [2], [41] that peak strength and hardness is reached early on in the ageing cycle when the tertiary γ‘ is at its highest volume fraction level. Once the tertiary γ‘ began to coarsen, the strength and hardness are decreased.

2.1.5 Summary of Nickel Based Superalloys

Ni-based superalloys have been around for the best part of 80 years, often including the alloying of 10 or more elements in the austenitic FCC γ matrix. The $Ni_3(Al,Ti)$ γ' precipitates, which depending on their size can be categorised into primary, secondary, and tertiary, are the primary strengthening mechanism of this class of materials. There is also a lesser contribution from the solid solution strengthening and high temperature strengthening, which arises from high temperature entanglements of screw dislocations known as Kear-Wilsdorf locks.

Carbides and borides form at the grain boundaries for these materials, contributing to the strength of the material. These are particularly important at the higher super-solvus temperatures when the primary γ' has been dissolved and can no longer pin the grain boundaries to prevent unwanted and excessive grain growth. TCP phases are often deleterious to the materials properties, and develop when too much or too little of an alloying constituent is added, negatively impacting performance.

Ni-based superalloys are the choice materials for use as turbine discs due to their excellent mechanical, creep, and fatigue properties at elevated temperatures in the region of 700˚C as well as their excellent resistance to corrosion. As the operating conditions for turbine discs have become increasingly more challenging, with higher temperatures and higher stresses, the volume fraction of γ' has had to increase to meet this challenge. This has meant that manufacturing Ni-based superalloys using the less expensive cast and wrought manufacturing route has become difficult, giving rise to an increase in the number of superalloys being manufactured via the costly powder metallurgy route.

2.2 AD730

While previous sections have provided a general overview of superalloys, focusing primarily on polycrystalline superalloys used in turbine disc applications, this section narrows the scope to one specific alloy under investigation in the PhD thesis: alloy AD730. The following discussion

delves into the background of the alloy, including its composition, microstructure, heat treatments, and mechanical properties.

2.2.1 Background

AD730 was invented by Alexandre Devaux and Philipp Heritier of the Aubert & Duval Company. A patent application was first filed for the alloy with the US patent and trademark office in 2010 [3]. The invention was designed to have constituent alloying elements which were cheaper to obtain than those used in other similar alloys (e.g., Udimet 720), to have better forgeability and similar mechanical properties at elevated temperatures (≈700 °C) to those of alloy IN718 Plus, all whilst being manufactured via the conventional cast and wrought route [3]. The patent filed states that the material is to be used for components in both land and aeronautical turbines with the operating temperature to be in the region of 700°C.

2.2.2 Composition & Microstructure

The chemical composition range stated in the patent is shown in Table 2.2. The alloying elements have a specified range rather than a fixed % wt., allowing for slight alterations to certain chemical compositions within the alloy resulting in distinctly noticeable changes in the materials properties or behaviour. The impact of these elements and the variation of the composition are discussed in the following sections.

Table 2.2: Chemical Composition Ranges for Alloy AD730 (% wt.) from Patent [3].

Element	Al	Co	Cr	Fe	Mo	Nb+ Ta	Ti	W	B	C	Zr	Ni
Range	1.3 - 2.8	Trace - 11	14 - 17	Trace - 12	2 - 5	0.5 - 2.5	2.5 - 4.5	1 - 4	0.003 - 0.03	Trace - 0.1	0.01 - 0.06	Bal.

γ Matrix and Solid Solution Stabilisers

Most of the following information comes from the initial patent [3] for AD730. The molybdenum and tungsten added to the alloy primarily make up the solid solution strengthening mechanism within the γ matrix. Their percentages can be altered within the ranges specified in Table 2.2 to give the optimal strengthening effects to the alloy. However, it was found that if the joint combination of molybdenum and tungsten was too high, they would enable the formation of μ or σ TCP phases. It was also found that an increase in these

elements also lead to decreased forgeability with the temperature window with which the alloy could be successfully forged, sometimes referred to as the 'forgeability domain', being reduced.

Molybdenum and tungsten also have relatively high atomic numbers, offering a higher density penalty when compared to other alloying elements. This is of particular importance in the aerospace sector. AD730 contains substantial amounts of chromium to better resist the effects of corrosion and oxidation, particularly when at temperature. There is the problem that chromium levels surpassing that of 17 % wt. in this alloy, will negatively impact the hot stability and as such have been limited. Due to the high cost of cobalt, it makes up no more than 11 % wt., with this addition improving the creep strength of the alloy.

The rest of the FCC structured γ matrix is typically made up of nickel but for the addition of one last element, iron. Iron is typically substituted in place of nickel and cobalt such that the overall cost of the alloy is reduced. Too much Iron added to the alloy can increase the likelihood of TCP phases developing and thus it has been limited to a maximum of 12 % wt. to obtain a stable microstructure.

γ' Stabilisers

The γ' phase is typically made up of Ni_3Al with the additional γ' stabilisers, such as tantalum, niobium and titanium, acting as what is known as γ' 'genes'. The presence of these alloying elements in sufficient quantities helps to promote the formation of the γ' phase with their combined %wt. giving a γ' volume fraction in a range of 30-44% with a solvus temperature of no higher than 1145 °C. It has been shown however that the γ' solvus is actually closer to 1100 ˚C - 1110 °C [35], [62], [63], [64]. Although the maximum permissible limit of γ' volume fraction is 44%, it is preferable for it to be less than 40% to improve the forgeability of the alloy and to preserve the ability of the alloy to be processed via the cast and wrought route (see Figure 2.21).

In the patent, it was further noted that the ratio of titanium, tantalum, and niobium to aluminium should lie between 0.7 and 1.3, but for *optimal* hardening of the alloy, the ratio should be between 1 and 1.3. The precipitation of needle like η or δ phases occurs, like those shown in Figure 2.18, where if the ratio is greater than 1.3, the hot ductility of the material is decreased. AD730 has more titanium than niobium and tantalum because of the weight of titanium being less than the other two. Because of the more expensive price and heavier

atomic mass of tantalum in comparison to niobium, the latter is found in greater quantities, however not in quantities so much that it detrimentally impacts the hot crack propagation in the material [3].

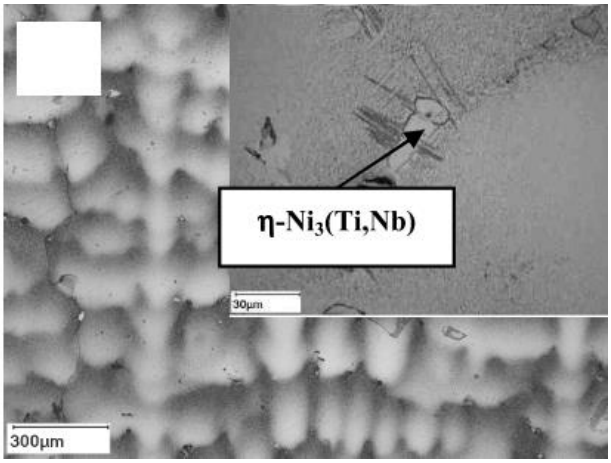

Figure 2.18: η Phases observed in a post-VAR AD730 [65].

Borides and Carbides in AD730

Carbon and boron both segregate at the boundaries and form carbides and borides. Figure 2.19 illustrates an instance of MC and $M_{23}C_6$ forming at the grain boundary of a Ni-based superalloy. The presence of these carbides and borides enhances both the strength and ductility of the material. However, exceeding the upper limits of these elements, as listed in Table 2.2, can adversely affect the forgeability of the material and lower the alloy's melting point.

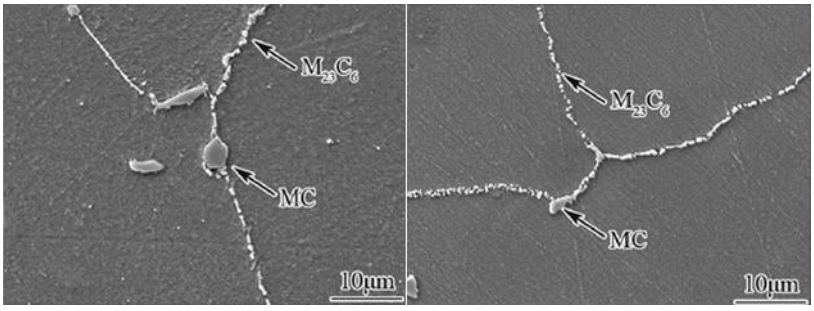

Figure 2.19: Examples of MC and $M_{23}C_6$ carbides shown to have segregated at the grain boundaries in a Ni-based superalloy. Adapted from [66].

TCP Phases in AD730

As previously mentioned, TCP phases have a detrimental impact on certain aspects of the performance of an alloy. AD730 has shown susceptibility to the formation of these phases

which usually precipitate by the addition of too little or too much of an alloying constituent. The formation of μ, σ, η, and δ phases have been seen to impact the ductility and mechanical strength of AD730 [3]. The use of THERMOCALC software in the design of this alloy, helped determine the upper limits in % wt. of some of the alloying elements. In particular, the titanium + niobium to aluminium ratio was found to be key to the formation of η phase as shown in the phase diagram presented in Figure 2.20 [65].

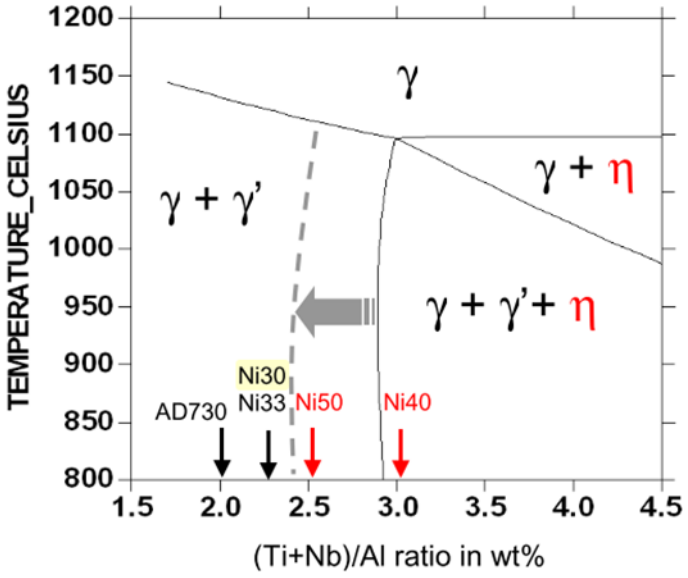

Figure 2.20: Phase diagram calculated in THERMOCALC software showing stability of η phase in AD730 as a function of the titanium + niobium to aluminium ratio, and temperature [65].

2.2.3 Thermo-Mechanical Processing of AD730

Although in some instances it has been shown that AD730 can be produced via a triple melt process [64], it is more common for it to be produced via a double melt process [15], [65]. Firstly, by VIM to de-gas and reduce the impurities in the alloy, and then by VAR to then reduce impurities further. Devaux *et al* [65] showed that after the alloy had been through the VAR stage, it then underwent a homogenisation step before being converted to a billet. The homogenisation step takes place at temperature range of 1160°C to 1220°C to better control the η phase which can develop at the end of the dendrites in the as-cast structure during the VAR process. The same work showed a billet, free of defects or cracks, was produced by open-die forging above and below the γ‘ solvus, before a closed-die forging operation below the γ‘ solvus. Challenges faced in the ingot to billet conversion cause large unrecrystallised grains and inhomogeneous γ’ distribution to remain in the billet after conversion, leading to

inhomogeneous or anisotropic mechanical properties which is undesirable for aerospace applications [67], [68]. It can therefore be seen that there are still significant challenges in finding the optimal thermo-mechanical processing path and the ideal process variables for alloy AD730 using the cast and wrought manufacturing route. The potential of a clear gap for the development and validation of a model used to predict the closed-die forging operation of alloy AD730 during its thermo-mechanical processing is explored more in a later section. The basic thermo-mechanical processing route can be seen in Figure 2.21 with the closed-die forging and heat treatments shown in more detail in Figure 2.22. Closed-die forging is carried out below the solvus at significantly slower strain rates than those of open-die forging, often of the order of 0.01/s to 0.1/s. Following this, the temperature is raised to 1080 °C for solution annealing. AD730 tends to crack during water quenching from temperatures close to the γ' solvus due to rapid cooling rates. Therefore, it is either oil quenched or subjected to forced air cooling, using a fan to blow air across the part, after solution annealing, before undergoing final ageing at 760 °C

Throughout this process, significant residual stress is induced in the part due to mechanical operations such as forging, as well as cooling operations like quenching or forced air cooling following solution annealing. These residual stresses not only hasten fatigue fracture but also cause parts to deviate from dimensional tolerances during machining, affecting the manufacturing process [69]. While destructive testing can reveal the distribution of residual stress profiles in each part, it renders the part unusable thereafter. Although non-destructive methods exist, they have limitations, as discussed in subsequent sections. Therefore, modelling remains the optimal approach to comprehensively understand the evolution of residual stresses during thermo-mechanical processing without sacrificing the part.

Ageing is known to reduce the level of stress present in Ni-based superalloy parts [70], [71], however the evolution of stress during this process has never been investigated for alloy AD730. There has been little work done on understanding the residual stress evolution during thermo-mechanical processing of alloy AD730, and the further investigation of a knowledge gap for the development of a validated model used to predict the stress relaxation behaviour during ageing is investigated more in later sections. Having a validated model to predict the stress relaxation during ageing could help prevent some of the previously mentioned challenges such as premature failure due to residual stresses etc.

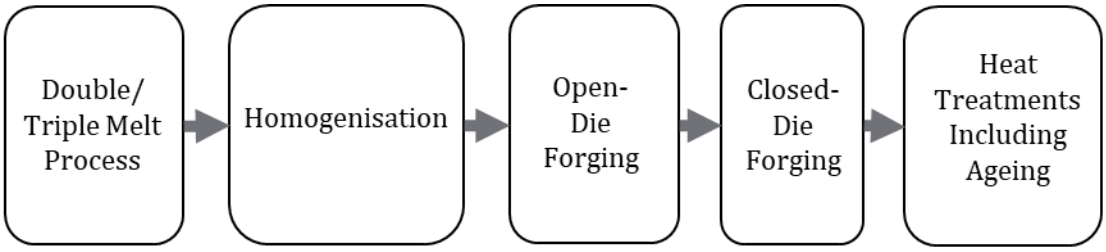

Figure 2.21: Basic Thermo-Mechanical Processing Route of AD730.

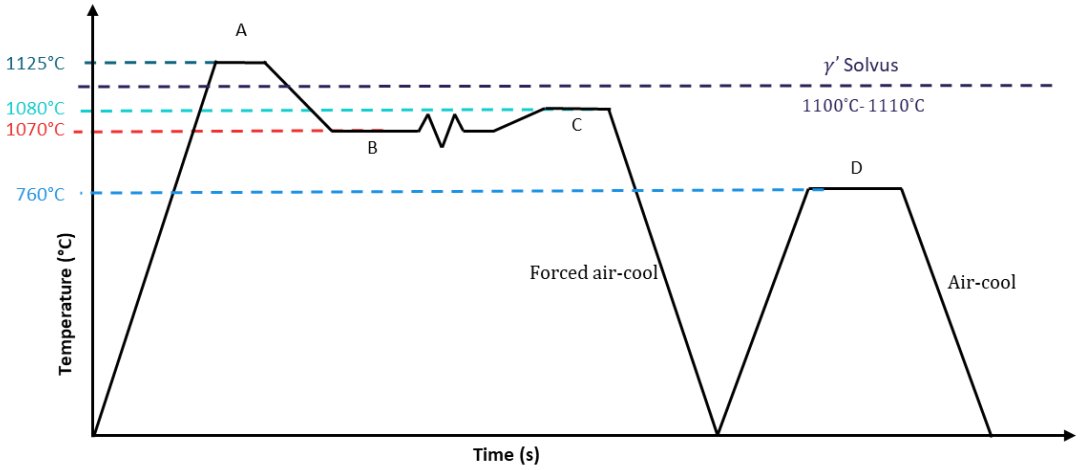

Figure 2.22: Detailed processing route including ageing of AD730 Billet where A is a 1 hour hold, B is a 4 hour hold, C is a 4 hour hold, and D is an 8 hour hold [65].

2.2.4 Summary of AD730

A balance between cost and properties has been a significant driving force in the development of many modern superalloys, particularly the newly developed AD730. This alloy was specifically engineered to offer better forgeability and lower production costs compared to Udimet 720. Designed to be manufactured via the cast and wrought route, AD730 also boasts superior high-temperature properties compared to similar alloys like ATI 718Plus.

Under investigation in this thesis, alloy AD730 is an FCC low γ/γ' mismatch alloy. It can be produced through both double and triple melt routes. The manufacturing process involves a homogenisation heat treatment followed by a combination of super-solvus and sub-solvus forging to convert it into a billet form. Subsequently, closed-die forging and additional heat treatments are conducted. However, challenges persist in the thermo-mechanical processing of the alloy via the cast and wrought route.

One such challenge is the presence of large unrecrystallised grains, which are believed to negatively impact the material's mechanical properties. Additionally, the generation of residual stresses during closed-die forging and their evolution during cooling and ageing pose significant concerns. These stresses have been shown in other Ni-based superalloys to lead to poor fatigue life, dimensional tolerance issues during machining, and premature failure. Consequently, these challenges prompted further investigations into potential knowledge gaps related to alloy AD730.

The first area of focus was residual stresses, including measurement and control methods, which are discussed in section 2.4. Subsequently, a review of existing models in the literature used to predict the closed-die forging behaviour and stress relaxation during ageing of alloy AD730 was conducted, as detailed in Section 2.5.

2.3 Inconel 718

The following section is focused on the other Ni-based superalloy under investigation in this thesis, IN718. A summary of the background of the material, microstructure, and thermo-mechanical processing are discussed to provide context for later work.

2.3.1 Background

IN718 was invented by Herbert L. Eiselstein of the International Nickel Company and patented in 1962 [72]. The invention was designed to be an age-hardenable and malleable nickel-chromium based alloy with high strength and ductility from room temperature to 760°C [72]. Other critical objectives of this invention were for the material to demonstrate improved rupture life at elevated temperatures, and to have the yield strength constitute as much of a percentage of the ultimate tensile strength as possible, whilst still having high levels of elongation. Due to good weldability of the material after being casted, early development was both as a weldable sheet alloy [34] and as a replacement for welded assemblies in jet engines [72].

2.3.2 Composition & Microstructure

The chemical compositional range stated in the patent is shown in Table 2.3. As the patent for IN718 was filed a considerably long time ago, the amounts of each element added by manufacturers has been perfected based on the intended application. A short discussion on the impact of each element on the properties of the alloy is included in the following sections.

Table 2.3: Chemical Compositions Range of alloy Inconel 718 [72].

Element	Ni + Co	Cr	Fe	Al	Mg	Mo	Nb	Ti	Zr	B	C	Si
Range	Bal.	15 - 23	<= 30	0.2 - 2	<= 1	2 - 4	4 - 8	0.2 - 2	<= 0.5	0.005 - 0.015	<= 0.1	<= 0.5

γ Matrix and Solid Solution Stabilisers

Most of the following sections come from the patent for IN718 [72]. Chromium and molybdenum are added to the material for good solid solution strength and for high temperature corrosion resistance. Molybdenum imparts strength to the alloy but can be replaced with tungsten without being detrimental to the properties, except for the hot malleability which is reduced. It is important to note that molybdenum does not contribute to the age hardenability of the material. The addition of iron adds a good cost benefit to the material as iron is relatively cheap and readily available. Adding iron to the material also leads to good machinability and weldability, as well as high strength [73]. The rest of the bulk of the γ matrix is made up of nickel. It was found that the maximum tensile properties lay between 45 %wt to 58 %wt nickel content, and maximum rupture properties at 750 °C occurs between 51 %wt to 56 %wt nickel plus cobalt content.

The Main Precipitates in Inconel 718 (γ', γ'' & δ)

IN718 is strengthened by a combination of body centred tetragonal (DO_{22}) γ'' with Ni_3(Nb, V) stoichiometry, and ordered cubic ($L1_2$) γ' with Ni_3(Al, Ti, Nb). The theoretical maximum volume fraction of γ' and γ'' given by Brooks et al. was 14% and 21% respectively, however other works have shown that after ageing, the limits are closer to 3% and 20% respectively [34], [74]. γ' forms in the material coherently and looks like small spherical particles, whereas γ'' forms semi-coherently as disc like particles. The γ'' solvus is reported to be between 900 °C and 930 °C [34], [74], [75]. Both phases precipitate between 600 – 850 °C [76]. This is shown by the T-T-T diagram presented in Figure 2.23.

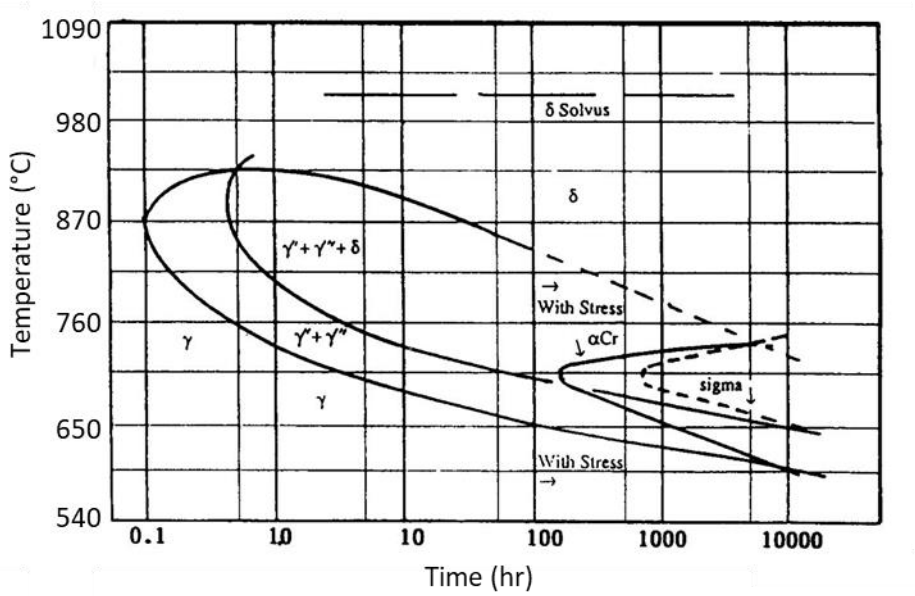

Figure 2.23: T-T-T Diagram of IN718 recreated from [77].

Aluminium and titanium, essential components of the γ' phase, give malleability, age hardenability, and high strength to the alloy when their concentration exceeds 0.2% each. γ'' is the metastable form of Ni_3Nb and precipitates in the alloy when the concentration of aluminium and titanium exceeds 0.2% each. γ'' has been shown to significantly contribute to the age hardening of IN718, enhancing its strength and mechanical properties. The γ'' phase forms coherent precipitates within the γ matrix, thereby strengthening the alloy and improving its resistance to deformation and creep. The volume fraction and distribution of γ'' precipitates play a crucial role in determining the mechanical properties and performance of the alloy under various operating conditions.

δ represents the orthorhombic stable form of Ni_3Nb, which precipitates at temperatures above 650 °C [78]. The δ is incoherent with the γ matrix and does not contribute to the age hardening of IN718. Therefore, when δ precipitates at the expense of γ'' above 650 °C, there is a loss of hardenability [79]. The δ solvus temperature has been reported to be 1000 °C and 1010 °C [34], [75], [79], [80], depending on the Niobium content [79], with the precipitation rate of this phase shown to be highest at 900°C [79] . Possessing the ($D0_a$) crystal structure, δ initially precipitates along the grain boundaries before extending outward into the grains in the form of thin plates. This phase has been demonstrated to inhibit grain growth in small amounts and

can even provide resistance to grain boundary creep fracture [79]. This phase can however lead to decreased stress rupture properties and a decrease in ductility [81].

Borides and Carbides in Inconel 718

Boron contributes to the high strength and ductility of the material at elevated temperatures. It has been shown that increasing the amount of boron beyond 100 ppm can increase the tendency of hot cracking, so the total content must be limited [73]. The addition of zirconium increases the malleability and contributes to the age hardening of the material. However, it has been shown that increasing the amount of zirconium in IN718 beyond 200 ppm changes the morphology and volume fraction of borides, which would be detrimental to the mechanical properties [73]. Therefore, care must be taken when varying the quantities of both boron and zirconium with them interacting with one another. The primary carbide that exclusively forms at the grain boundary, as depicted in Figure 2.24, is the MC carbide. Comprising predominantly of niobium and/or titanium, these carbides are recognised for their ability to impede grain growth in small quantities [76].

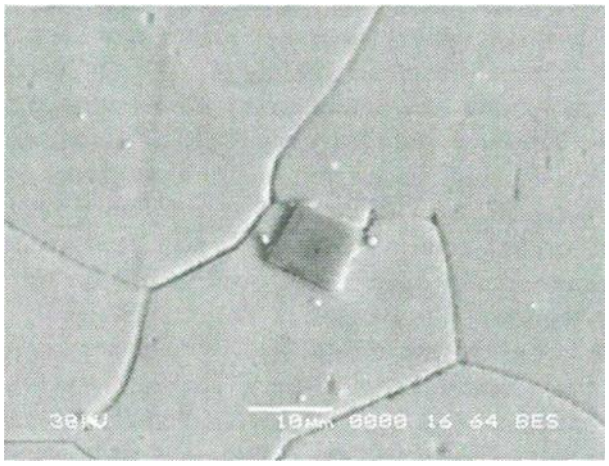

Figure 2.24: SEM micrograph of a MC carbide in an IN718 sample [76].

TCP Phases in Inconel 718

The presence of laves in IN718 has been shown to be detrimental to the ductility, strength, impact, and fracture toughness properties at room temperature, as well as ductility, rupture, Low cycle fatigue (LCF), and fatigue crack growth properties at elevated temperature [82]. Casting of IN718 leads to inter-dentritic regions where high amounts of niobium can form leading to the formation of laves. The laves phase is a hexagonal close packed intermetallic compound with AB2 structure. The formation of this phase leads to the lowering of mechanical

properties and a lowered incipient melting temperature. A homogenisation heat treatment is required to eliminate the formation of the laves phase but often this is not completely successful and can mean some of the laves phases are carried into the billet of the material [76]. Too high a niobium or molybdenum content can also lead to the generation of laves phases. Increasing the nickel content or reducing the iron content can help reduce the amount of laves present in the material, as can adding silicon into the material [83]. Reduction of chromium has also been shown to reduce the formation of the laves phase [84].

2.3.3 Thermo-Mechanical Processing of Inconel 718

The thermo-mechanical processing of IN718 is often complex and involves many sequential stages like forging, ageing, water quenching etc. It is through careful selection and management of these steps, that the microstructure and subsequent behaviour of the material can be controlled. The basic thermo-mechanical processing route for IN718 is the same as that for alloy AD730 and can be seen in Figure 2.21, with the material typically produced using the VIM/VAR double melt process [85] as opposed to the triple melt process, which is more widely used when larger than standard ingots are to be produced [86]. The material then undergoes a homogenisation heat treatment which must be kept below 1160 ˚C so as to avoid the incipient melting temperature which is reported to be between 1167 ˚C and 1180 ˚C. Typically homogenisation is carried out at 1150 ˚C [85], [87].

After upsetting and cogging (i.e., open-die forging) and closed-die forging, the part then undergoes several heat treatments, as shown schematically in Figure 2.25. A crucial step in the thermo-mechanical processing of IN718 includes the solution heat treatment of the material near the solvus for the δ-phase, followed by rapid cooling, usually by quenching in water. The purpose of this treatment is to put all the γ’ and γ’’ stabilisers into solution in preparation of the subsequent ageing heat treatments, and to keep some δ remaining at the grain boundaries to prevent excessive grain growth. The water quenching process causes the part to experience extreme thermal gradients which in turn generate residual stress fields of high magnitudes which the subsequent ageing heat treatments often do not fully remove. These residual stresses are generated because of the different rates which the part contracts at when being cooled, causing localised plastic deformation between the hotter and cooler sections. The rate of cooling is a critical factor influencing the magnitude and distribution of residual stress in a part.

While some studies have explored the effects of water quenching on residual stress in IN718, little research has been conducted on how quenching process parameters affect stress evolution. This includes variations in quenching media, part sizes or shapes, and the configuration during quenching. Furthermore, there has been no attempt to model the impact of these process parameters on the stress evolution. This is a clear knowledge gap which warrants further exploration and has been done so in section 2.4

A double ageing heat treatment is carried out at 720˚C for 8 hours to grow both γ' and γ'' and is then furnace cooled to 620˚C and held for 8 hours to grow just the γ' precipitates [88]. It is this precipitation and the subsequent strength and influence on the materials microstructure that are critical for the high temperature performance of the material. As mentioned previously, it is known that the ageing heat treatment reduces the residual stresses in Ni-based superalloys. For IN718, there has been some work carried out to quantify and model the stress relaxation during ageing [89], however this is not an area which has been very well explored. The exploration into residual stresses and the modelling of their generation during water quenching and evolution during ageing is further investigated in sections 2.4 and 2.5.

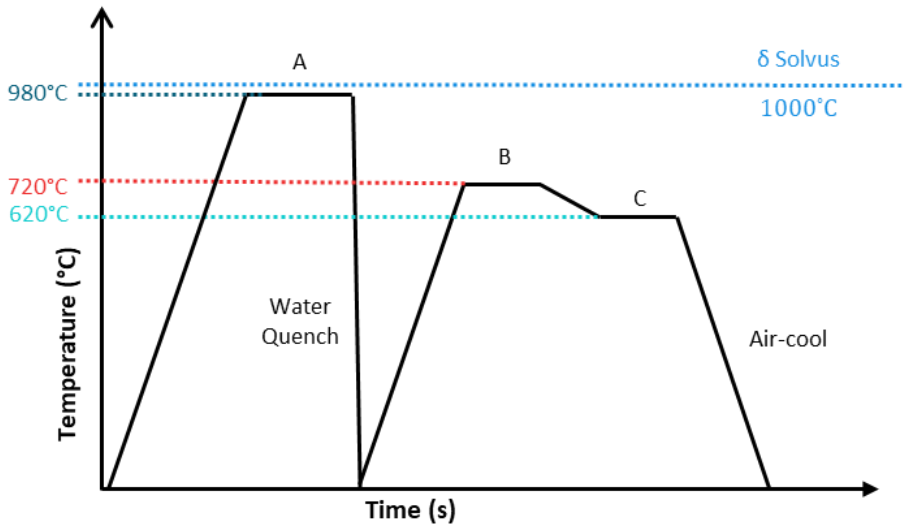

Figure 2.25: Detailed heat treatment route for IN718, typically practiced in industry for forging and the subsequent ageing heat treatments, where A is a dwell time of 1 hour, B is a dwell time of 8 hours, and C is a dwell time of 8 hours [90], [91].

2.3.4 Summary of Inconel 718

IN718 was designed to be a high strength alloy with applications at temperatures up to 760°C for welding and as a replacement for welding assemblies in jet engines. The $\gamma/\gamma'/\gamma''$ microstructure is strengthened primarily by the metastable γ'' precipitates which forms between 600 – 850 °C during age hardening heat treatments. The more thermodynamically stable δ phase precipitates in expense of γ'' above 650°C, and although having some δ phase in the microstructure can be beneficial for inhibiting grain growth, the growth of this phase at the expense of γ'' leads to loss of hardenability. The alloy is usually manufactured using the VIM/VAR double melt route but can be manufactured via the triple melt route too. After a homogenisation heat treatment, the ingot then undergoes open-die forging, closed-die forging, and subsequent heat treatments. A key part of the post-forging heat treatment is the solution annealing treatment and subsequent water quenching and ageing process. The water quenching process induces significant residual stress, which remains even after double ageing heat treatments. These residual stresses directly impact subsequent manufacturing stages, leading to part distortions that exceed tolerances during final machining and can impair part performance in service. To date, too little has been done to look at the impact of the process parameters of quenching on stress evolution, such as different quenching media, different parts sizes or shapes, or the configuration of the part when being quenched. The issue of residual stress generation and evolution during thermo-mechanical processing is one of the manufacturing challenges which was the basis for further investigations. Work was done previously looking at the residual stress behaviour during ageing for IN718 [71], [89] however this was an area which is relatively unexplored, and the potential knowledge gap is explored more in section 2.4. A review of existing models in literature used to predict the residual stress generation during quenching and evolution during ageing was explored and the results can be seen in section 2.5.

2.4 Residual Stresses

2.4.1 Introduction

Residual stresses refer to the internal stresses remaining in a part or sample after undergoing mechanical, thermal, or chemical processes. When combined with in-service stresses, these residual stresses can lead to reduced performance, premature failure, and the shortened life of a part. Traditionally, manufacturers have addressed distortion issues by employing methods

like heavy hammering, clamping, or making sections thicker, but these approaches pose risks of inducing local damages like cracks, particularly in critical components such as turbine discs. Consequently, manufacturers have often managed residual stresses by relying on experienced engineers to make informed decisions based on empirical knowledge and expertise. Additionally, techniques like shot peening and cavitation peening have been utilised to locally induce residual stresses and enhance mechanical properties, such as fatigue life. Hence, while residual stresses can offer benefits, they also pose risks, emphasising the importance of understanding and controlling them to prevent part failure or scrapping.

2.4.2 Categorisation of Residual Stress

Residual stresses can be categorised into 3 different types: type I, type II, and type III as described below [69].

- Type I residual stresses are macro-scale stresses which act over several grains spanning scales comparable to the size of the part. The total summation of the forces and moments must self-equilibrate for a part to be at equilibrium. In reality, this means there is a variable residual stress profile across the part which balances to zero. Any change to this equilibrium, such as material removal through machining, can lead to part distortion due to stress redistribution, known as stress relaxation, resulting in a new equilibrium state.

- Type II residual stresses vary over the grain scale. These are intergranular stresses which arise due to the different thermal and elastic properties of adjacent grains. These neighbouring grains act differently (i.e., due to mechanical anisotropy caused by crystallographic orientation) despite undergoing the same loading. Different phases or phase transformations within a material can lead to the development of these stresses.

- Type III residual stresses are micro-scale stresses which vary over the atomic scale. These types of stresses act over the lattice, meaning localised defects such as coherency at the interface, vacancies, and dislocation stress fields are the main causes, which balance out over a small portion of a grain.

The superposition of type I, II, and III residual stresses are what makes up the residual stress profile in a part. Type I macro stresses are generally thought of as the most impactful when

manufacturing components and as such they are the ones in which most effort has been put towards controlling and the focus of this PhD thesis.

2.4.3 Generation of Residual Stress

Macro residual stresses (Type I) arise from various factors, all following the same principle. These stresses originate from mismatches in different regions of the material, triggered by phenomena like localised plastic deformation, phase transformation, segregation, precipitation, and any discontinuity in thermal, physical, and mechanical properties. Examples of such mismatches are depicted in Figure 2.26. They can stem from differential gradients in localised plastic deformation due to heterogeneous mechanical loading, such as *forging*, or through heterogeneous heat treatments and thermal cycles, like *quenching* [92]. Additionally, they can result from chemical processes, such as the nucleation and growth of precipitates in Ni-based superalloys. Several examples of these mismatches are outlined in the following:

- Chemical inconsistencies, for example non-homogeneous volume alterations caused by solid-state phase transformations such as precipitation or the phase transformation of martensite in steel, can induce residual stresses [92], [93], [94]. This type of transformation involves two fundamental mechanisms, displacive and reconstructive. The former elicits substantial strain by deforming the parent crystal, while the latter necessitates uncoordinated atom diffusion to facilitate the creation of a new structure [95].

- Mechanical loading such as *forging*, forming, machining, shot peening etc. are all methods where residual stresses can be induced in a part. They manifest due to uneven plastic distortions across different sections of a component subjected to the specific loading.

- Heterogeneous thermal conditions are a major source of residual stresses in parts, particularly for Ni-based superalloys, where divergent thermal expansion and contraction concurrently unfold at distinct locations within the component [92]. Welding, annealing heat treatments, ageing heat treatments, and of course *quenching* are all examples of heterogeneous thermal conditions which induce residual stresses.

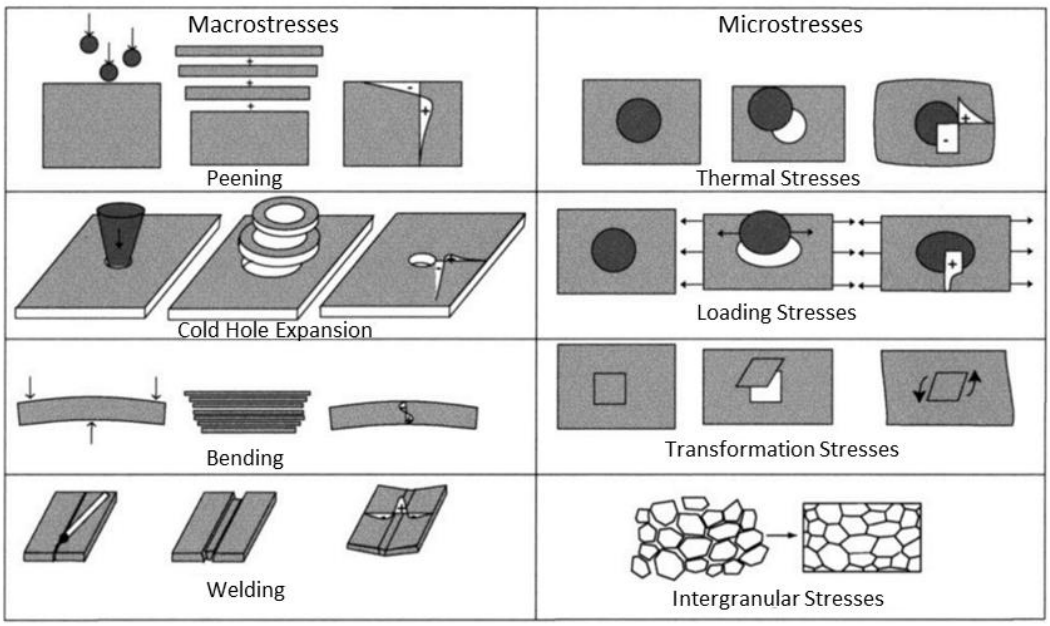

Figure 2.26: Methods of residual stress generation at macro and micro-scales [69].

Quenching is of particular importance to Ni-based superalloys, as it often plays a key role in their thermo-mechanical processing. Quenching is the process in which a material at elevated temperature is rapidly cooled by immersion in a quenching medium, either after being removed from a furnace or from another processing step such as forging. Typically, the surface of the part cools quickly, while the centre cools more slowly. The medium in which parts are quenched (water, air, polymer, oil etc), the state of the medium (non-agitated, agitated, room temperature, elevated temperature etc.), the material itself (will it undergo precipitation or phase transformations), the component geometry (the size of it, does it have any thin webs), and the configuration in which the component is quenched, will all affect the cooling conditions and the resultant residual stress profile [69], [95], [96]. Understanding to what extent some of the key parameters in the quenching process, i.e. the quenching medium and quenching configuration, affect the heterogeneous cooling and subsequent residual stresses generated, is central to this thesis.

The examination of thermo-mechanical processes, notably forging and water quenching, which are both pivotal steps in the manufacturing of Ni-based superalloys, were shown to intricately contribute to residual stress formation. Recognising the significance of stress generation is pivotal for effective material processing. Equally essential though is mastering strategies to regulate these stresses, underscoring their crucial role in ensuring manufacturing success. This

underscores a central focus of this thesis: understanding the stress evolution during thermo-mechanical processing to enhance part integrity, reduce part scrappage, and ultimately lead to better manufacturing outcomes.

2.4.4 Control of Residual Stress

There are many ways of controlling residual stress generation and evolution during different manufacturing processes. Modifying key process parameters during manufacturing, such as those involved in the deposition of additive manufactured parts, can influence residual stress generation. Surface treatment methods, such as shot peening, have demonstrated the ability to reduce or induce compressive residual stresses, as illustrated in Figure 2.26. Additionally, cyclic loading and unloading, where materials undergo repeated straining to induce plastic deformation, with progressively increasing strain amplitudes per cycle, as depicted in Figure 2.27, have been found to reduce residual stresses [97], [98]. Studies indicate that the initiation of plastic flow in one direction leads to a reduction in the yield point in the opposite direction due to the redistribution of residual stresses [98].

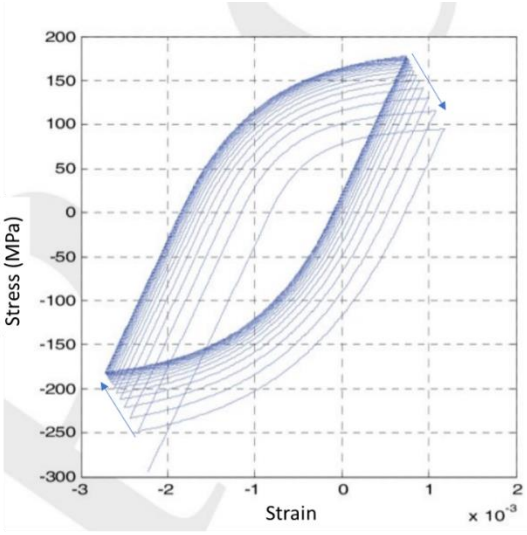

Figure 2.27: Simulated stress-strain response of a material showing stress-relaxation behaviour after being subjected to constant amplitude cyclic loading. Arrows show direction of stress reduction. [97].

Conducting annealing heat treatments at various temperatures, which induce stress relief through microstructural changes like recovery or static recrystallisation, represents another approach to controlling residual stresses. Stress relaxation is a central focus of this thesis, so further expansion on this topic is provided in the subsequent sections.

Stress Relaxation

Stress relaxation is the reduction of stress in a part through conversion of elastic strain to inelastic strain. This can happen through many means, such as dislocation climb, grain boundary sliding, stress-assisted diffusion, and phase transformations. This process happens when a part is strained at a given temperature, usually an elevated temperature, to a total value. Then with the part at constant strain and temperature, the stress decreases over time. A graphic representation of a stress relaxation test is shown in Figure 2.28. Stress relaxation heat treatments are intentionally performed to relieve stress within parts often prior to machining or further operations. There are four different types of inelastic strains involved in stress relaxation according to the ASTM compilation of stress relaxation data . Creep, of which there is three stages (primary, secondary, and tertiary), anelasticity, plasticity, and micro-plasticity [98]. Creep and stress relaxation share similar governing mechanisms.

These phenomena are temperature-dependent, with creep being the dominant mechanism above 40% of the melting temperature ($0.4T_m$), and anelasticity, micro-plasticity, and plasticity dominating below $0.4T_m$. Microstructural changes, such as the nucleation and growth of precipitates in Ni-based superalloys or phase transformations in steels, add complexity to part relaxation. These changes can lead to phenomena like negative creep, where the material's stress increases over time instead of relaxing [71].

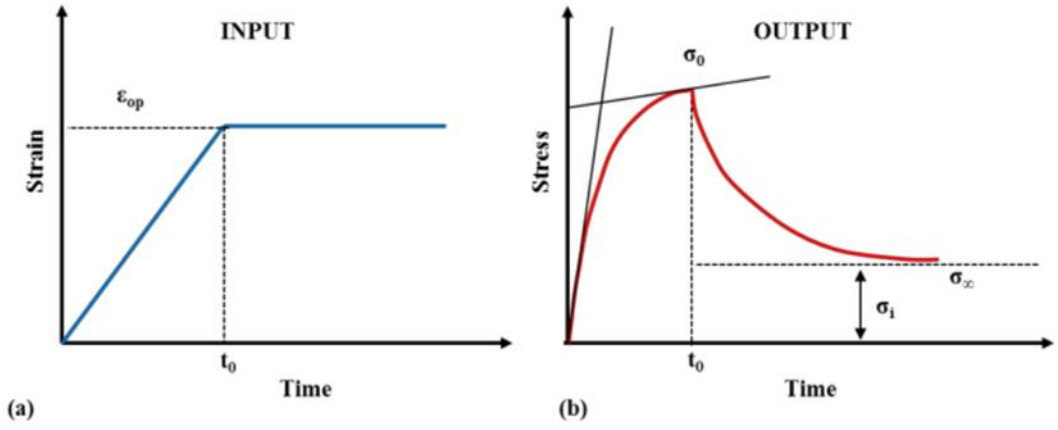

Figure 2.28: A stress relaxation test is schematically represented as follows: a) depicts the strain path, which serves as the input and control for the test, while b) illustrates the output stress relaxation plot [89].

During manufacturing processes like machining, residual stress fields can be altered by material removal, reducing the total residual stresses in the material and allowing the material

to relax. However, this can lead to dimensional tolerance issues as the stresses redistributing to a new equilibrium [99].

For stress relaxation of Ni-based superalloys, the majority of relaxation occurs during the ageing heat treatment. The complex nature of precipitation influences stress relaxation behaviour. If residual stresses aren't adequately reduced during relaxation, it can lead to part distortion. More detailed discussions on stress relaxation mechanisms are provided in subsequent sections.

Creep

Creep is the time-dependant plastic deformation of a material whilst under a fixed load which is lower than its yield point [100]. Creep failure is typically classified into three distinct regions relating to its plasticity as shown in Figure 2.29. Primary creep is where the rate of work hardening is greater than the rate of recovery, leading to a decrease in the strain rate (or creep rate) causing an increase in dislocation density and eventually dislocation entanglements. This restricts dislocation glide and leads to dislocation climb becoming the most dominant mechanism for the transition to secondary creep[101]. Secondary creep, sometimes referred to as steady state creep, is when the rate of work hardening is equal to the rate of recovery meaning the amount of dislocation density is roughly constant. This means the creep rate is constant and is usually the longest of the three stages of creep. Lastly tertiary creep is where the creep rate increases until the part ruptures [100]. There are two distinct mechanisms which are responsible for creep, dislocation creep and diffusion creep.

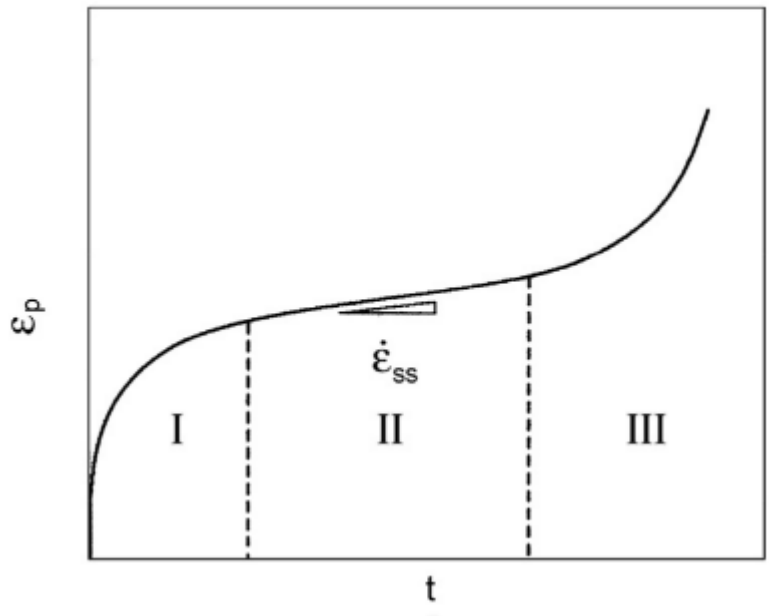

Figure 2.29 - Creep rate behaviour [100].

Diffusion creep is where the atoms of a material move from a position within one metal crystal to another. This usually happens at elevated temperatures and low stresses. There are several different types of diffusion creep, (i) vacancy diffusion where an atom moves from one position to another position of similar size, (ii) interstitial diffusion where smaller atoms move positions between larger atoms, and (iii) grain boundary diffusion where atoms can diffuse along grain boundaries. The atoms flow from vacancies near the grain boundaries parallel to the loading direction, to near the grain boundaries perpendicular to the loading direction due to these boundaries having lower and higher than average vacancies, respectively [102]. When the vacancy flow is through the crystal, then the process is defined by the Nabarro-Herring model and shown in Figure 2.30a, and when the vacancy flow is along the grain boundary, then then process is defined by the Coble model and shown in Figure 2.30b. Temperature is the main contributory factor on whether either of these two models are dominant with the Coble model being more dominant at lower temperatures, and the Nabarro-Herring model more dominant at higher temperatures.

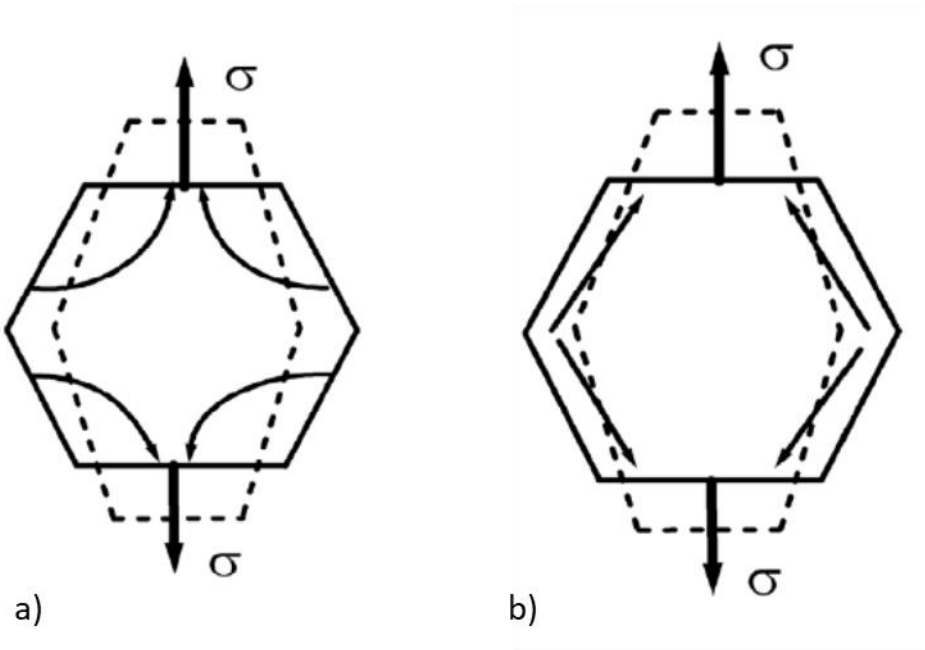

Figure 2.30: Two diffusion-based creep mechanisms demonstrating atom movement during loading within a grain. a) Nabarro-Herring creep mechanism showing atoms flowing through the crystal, and b) Coble creep mechanism depicting the atoms flowing along the grain boundary [103].

In the context of stress relaxation during ageing of Ni-based superalloys, understanding the mechanisms of dislocation creep and dynamic recrystallisation is crucial. Dislocation creep, characterised by the movement of dislocations along slip planes, occurs at higher stresses and can influence the redistribution of residual stresses in the material during ageing. Harper and Dorn's investigation into creep properties, although initially applied to aluminium, provides insights into the behaviour of metallic alloys under creep conditions.

The Harper-Dorn creep model, which describes low-stress creep at high temperatures through dislocation climb, highlights the importance of dislocation dynamics in creep deformation. While this model may have limited relevance to metallic alloys, it underscores the significance of dislocation movement in creep processes. The creep rate is determined not by the glide mechanism of dislocations, but by the rate at which the dislocations can climb over particles such as precipitates. For metallic alloys below 0.5 of the melting temperature (T_m), creep is controlled by glide. For temperatures above this, creep is controlled by dislocation glide plus climb [104]. Moreover, the transition from glide-controlled to climb-controlled dislocation movement, particularly at temperatures above $0.5T_m$, may impact the relaxation behaviour of Ni-based superalloys during ageing. Additionally, dynamic recrystallisation, which becomes

dominant at temperatures exceeding $0.6T_m$, can alter the microstructure and dislocation distribution, potentially affecting the stress relaxation kinetics. Therefore, insights from these creep mechanisms provide valuable perspectives for explaining the stress relaxation mechanisms in Ni-based superalloys during the ageing processes.

Anelasticity

Anelasticity, also known as delayed elasticity, refers to a physical phenomenon that deviates from Hooke's law, which describes linear-elastic behaviour of a material. According to Hooke's law, deformation is directly proportional to the applied force within the elastic regime. Anelasticity arises from internal friction within the material, resulting in a time-dependent response that is non-elastic. This elastic after-effect, or anelastic response, manifests as stress relaxation following the application of strain [105], contributing notably to post-deformation springback, a phenomenon particularly observed in processes such as sheet metal forming. A schematic representation of this phenomenon is illustrated in Figure 2.31.

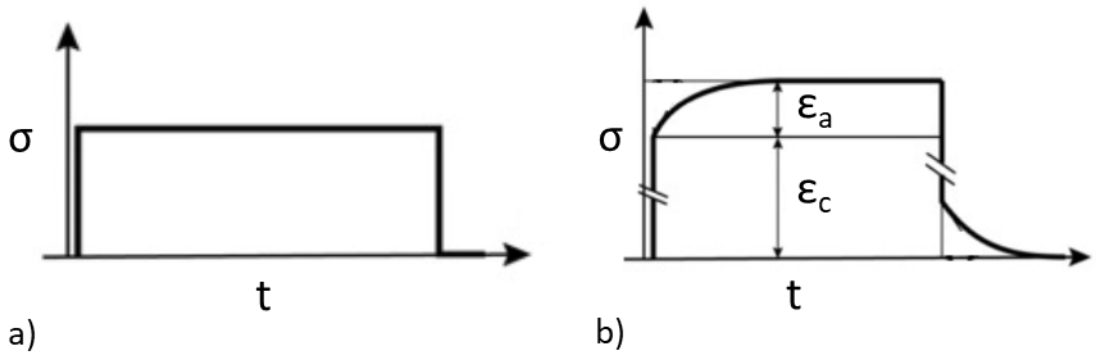

Figure 2.31: Schematic graphs showing a) elastic (ε_c) and b) anelastic (ε_a) components of strain subjected to a sudden stress (σ), altered from [106].

Anelasticity is influenced by various factors including temperature, chemical composition, applied stress, rate of stress application, magnetic properties, and elastic fields. Typically constituting between 2 and 5% of elastic strain, anelastic strain arises from three temperature-dependent motion defects. These mechanisms, briefly outlined here but detailed further in [98], include *point defect relaxation, dislocation movement, and motion of grain boundaries or interfaces*. Point defect relaxation involves the redistribution of defects within the crystal lattice under an applied load, facilitated by diffusion processes such as Gorsky relaxation or reorientation. Reorientation, observed primarily in FCC crystals like those present in Ni-based

superalloys, contributes to anelastic relaxation only in the presence of interstitial atom complexes, not individual interstitial atoms [107].

Dislocation movement is the primary deformation process in metals at low temperatures. Dislocations are 2-dimensional line defects in crystals which cause complicated stress fields, as shown in Figure 2.32. When materials deform plastically or have a high dislocation density, a range of relaxation effects emerge. These arise from diverse causes, including thermal or geometrical kinks facilitating dislocation movement, interactions of dislocations with lattice defects, and the presence of interstitial atoms a shown in Figure 2.33. Elevated temperatures introduce additional factors like dislocation climb[108]. Understanding the interplay between dislocation movement and stress relaxation is essential, especially during the ageing process where the redistribution of stresses can significantly impact material properties over time.

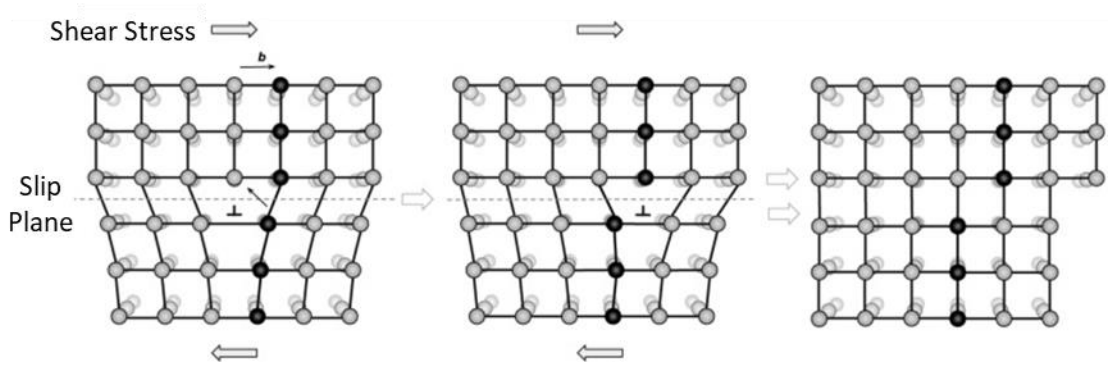

Figure 2.32: Edge dislocation shown to be travelling through crystal structure by glide [109].

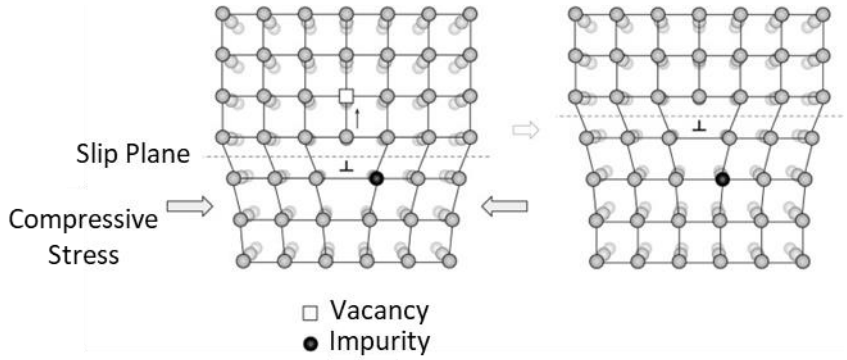

Figure 2.33: The glide of an edge dislocation being impeded by an impurity such as a precipitate, resulting in dislocation climb to avoid the obstacle [109].

The last mechanism contributing to anelasticity is the motion of grain boundaries or interfaces. Grain boundary relaxation occurs mainly through grain boundary sliding, which is predominant

at low temperatures. This relaxation mechanism is particularly prominent in parts with small grain sizes, where the grain boundary constitutes a larger proportion of the part's volume [107]. An illustration of grain boundary sliding can be seen in Figure 2.34. Although the ageing temperatures for both IN718 and AD730 exceed $0.4T_m$ indicating creep as the likely dominant relaxation mechanism, it's crucial to consider the potential contribution of anelasticity to the overall relaxation behaviour of a part.

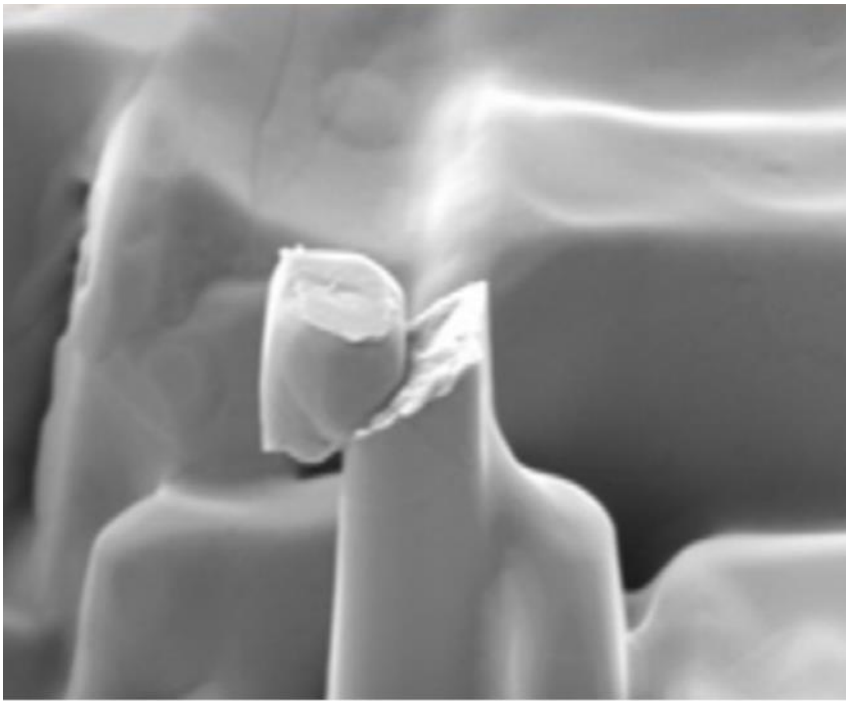

Figure 2.34: SEM micrograph demonstrating grain boundary sliding of a bi-crystal micro-pillar [110].

Plasticity

This is the permanent strain that can be measured in a part after it has been deformed past the elastic limit (i.e., the yield point) and the applied stress is removed. Dislocation movement, twinning, vacancy moment, and phase transformations can all be responsible for plastic deformation [111]. The yield point is a function of the temperature and the strain rate meaning the elastic strain is also influenced by these. An example of this is if the temperature in a part which is under an applied load is increased, the yield point for the higher temperature will be less than for the lower temperature, resulting in elastic strain being converted into plastic strain, which is stress relaxation. Plasticity is therefore shown to redistribute the stresses within a material causing relaxation.

Microplasticity

Microplasticity refers to the localised plastic deformation that occurs within a material when it is subjected to loading within the elastic regime. In such instances, certain regions of the material undergo plastic deformation, causing the part to retain a degree of deformation even after the load is removed. Microplastic strain typically constitutes a small portion of the elastic region, ranging between 5% and 15%, of the overall elastic strain. This, in conjunction with anelastic strain, contributes to the time-dependent nature of strain behaviour below the material's yield point [98]. During thermo-mechanical processing, such as the common practice of water quenching employed with materials like IN718 after solution annealing, microplasticity is known to be significantly introduced. This phenomenon can induce residual stresses within the material, a critical aspect explored in this thesis.

2.4.5 The Contour Method of Residual Stress Measurement

Residual Stress Measurement Techniques Down Selection

Various techniques exist for assessing residual stresses in components and are extensively documented in the literature [69], [112], [113], [114], [115], [116], [117]. Here, a general overview of these methods is provided in the context of measuring residual stresses in Ni-based superalloys during thermo-mechanical processing, and specifically for the purpose of this PhD thesis.

Residual stress measurement techniques can be broadly categorised into two types: diffraction-based methods like X-ray diffraction (XRD) or neutron diffraction (physical), and deformation-based methods such as the contour method or slitting method (mechanical). These techniques are classified based on whether they cause any mechanical damage or deformation to the part. For instance, the incremental hole-drilling technique is considered semi-destructive because it involves creating a small hole on the sample's surface, which can often be eliminated afterwards by machining, unlike the fully destructive contour method. Each technique has limitations regarding the depth range and spatial resolution over which it can detect residual stresses, as depicted in Figure 2.35. Therefore, it's essential to consider these limitations and the depth at which residual stresses are measured when choosing a measurement technique.

Some of the more widely used techniques will be discussed in the following sections [117].

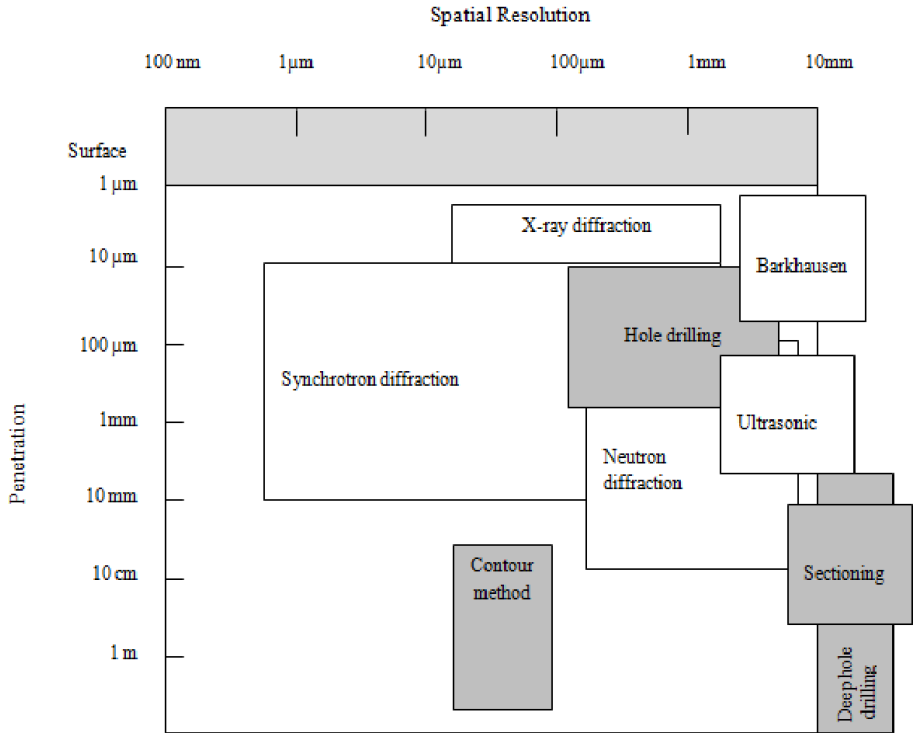

Figure 2.35: Common residual stress measuring techniques as a function of penetration into a part and spatial resolution [117].

Figure 2.35 serves as a guide for selecting the appropriate residual stress measurement technique(s) for this thesis. However, before proceeding, it was essential to define the measurement requirements. As outlined briefly in Section 1, two significant areas of investigation necessitate the measurement of residual stresses.

Firstly, there is a need to understand the influence of quenching configuration and quenching media on the resulting residual stresses in parts made from IN718 subjected to water quenching. Previous chapters have highlighted water quenching as a crucial step in the thermo-mechanical processing of this alloy, inevitably introducing significant residual stresses that subsequent ageing heat treatments may not fully eliminate [89]. It is critical to comprehend the residual stresses generated during this stage to model their evolution during ageing and cooling which are the final stages before machining. Understanding the final residual stress profile before any final machining is essential, as it significantly impacts machining strategies. If not properly addressed, it can result in parts falling outside dimensional tolerances. The measured residual stress profiles will serve as a way of validating the FE model developed to predict the residual stress generation during water quenching of IN718.

Due to the steep temperature gradients through the thickness of quenched parts, the selected residual stress measurement technique must penetrate sufficiently to reach the centre of the sample. The geometry of the parts to be quenched are often larger than 200mm diameter, therefore the maximum depth of penetration needed is beyond 100mm. According to Figure 2.35, both the contour method and deep hole drilling technique appear to be the most suitable options for achieving the required levels of penetration.

Deep hole drilling offers less spatial resolution compared to the contour method but provides stress measurements in two principal directions. In contrast, the contour method, while offering better spatial resolution, only provides out-of-plane residual stresses where the cut is conducted. Considering the increased spatial resolution and the fact that the measured residual stresses are primarily intended for validating the predictive FE model, the contour method was selected as the most suitable option.

Since the contour method is the sole residual stress measurement technique employed in this study, a concise summary highlighting the key points is not given.

Contour Method

The contour method is a fully destructive residual stress measurement technique developed by Prime in 2001 [118]. It is based on Bueckner's superposition principle which was used initially to solve problems related to cracks in materials. The theory of the contour method is that if a sample is cut using a method as close as possible to brittle fracture, and then the out-of-plane displacements on the surface on either side of the cut are measured, then the stresses required to push those displacements back to their pre-cracked position can be calculated, as shown schematically in Figure 2.36 [119].

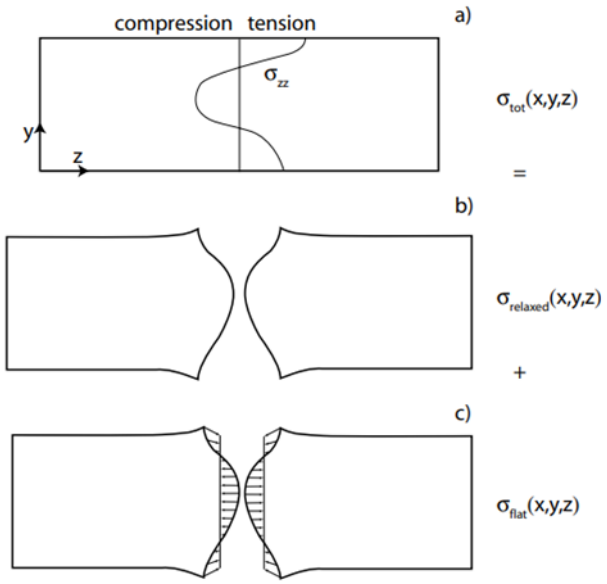

Figure 2.36: Superposition principle used in the calculation of the residual stresses using the contour method [119].

The contour method allows a 2-D map of the residual stresses to be generated for the cut-plane of a part, meaning high spatial resolution when compared to single point analyses like incremental hole drilling. The first step in the method involves cutting of the sample. The cut must induce minimum plastic deformation, must be straight and flat, and the amount of material removed must be minimal. The clamping used on the part is critical, with samples to be clamped on both sides of the cut and as close to the cut as possible. A wire electrical-discharge machine (EDM) is the preferred and suitable option for making the cut because of these requirements. Cutting parameters, such as the flushing rate take on significance due to the cutting method and must be controlled for an optimal cut. Next the cut plane on either side of the cut is measured using a coordinate measuring machine (CMM) with careful attention taken to select an appropriate spacing between measurements. After this, the data is then cleaned and averaged with the opposing mirrored data from the other half of the cut. Finally, a FE analysis is performed to determine the residual stresses using the cleaned and averaged displacement data as boundary conditions [117].

2.4.6 Summary of Residual Stress

Residual stresses are typically classified into three categories: types I, II, and III, based on their length scale. Type I stresses, which encompass macro residual stresses, exert the most significant impact on components during manufacturing. These stresses are responsible for

causing dimensional tolerance deviations in parts, often leading to their scrappage. They operate over a broad scale, ranging from several grains to dimensions comparable to the component's size, and self-equilibrate within this range. The generation of such stresses in parts during manufacturing can arise from various factors, including heterogeneous plastic deformation (e.g., forging, cutting), chemical inconsistencies such as phase transformations (e.g., austenite to martensite in steels), or heterogeneous temperature gradients experienced during processes like water quenching.

There are numerous methods available to manage the formation and evolution of residual stress, ranging from peening techniques and adjustments to key manufacturing process variables to various heat treatments. Stress relaxation, achieved through heat treatments, involves the reduction of stress by converting elastic strain into inelastic strain at elevated temperatures. Below 0.4Tm, stress relaxation primarily occurs through anelasticity, plasticity, and microplasticity, while above this temperature, creep becomes the dominant mode. Creep can be further categorised into primary, secondary, and tertiary stages, with dislocation-based creep and diffusion-based creep being the underlying mechanisms. The dominant mechanism is determined by the applied stress and temperature conditions, with diffusion-based creep favoured at elevated temperatures and low stresses, whereas dislocation-based creep is favoured at higher stresses and elevated temperatures.

Various techniques exist for measuring residual stresses, ranging from non-destructive methods like X-ray diffraction (XRD) and neutron diffraction, to semi-destructive techniques such as incremental hole drilling, to fully destructive approaches like the contour method. Each method comes with its own set of advantages and disadvantages. However, a critical finding from this literature review underscores that only the contour method provides a comprehensive stress distribution map across the entire field, offering the desired spatial resolution for the purpose of this PhD thesis. This feature is particularly advantageous for assessing residual stresses in parts with varying cross-sectional areas and in cases where large heterogeneous stresses are induced in manufacturing processes such as forging or water quenching. Notably, the contour method is well-suited for analysing complex billet shapes used in forging.

2.5 Modelling Residual Stresses

The successful development of a thermo-mechanical numerical model for predicting stress generation and part distortion in Ni-based superalloys requires accounting for the temperature field and phase distribution within the material, as well as the mechanical work. The calculations required for solution convergence in a FE solver can be thought of as being divided into sub-models with each addressing specific physical phenomena. These individual sub-models exhibit intricate and interconnected relationships, underpinned by the material's global properties. The primary sub-models essential for understanding thermo-mechanically induced stress generation and evolution are the mechanical model, the thermal model, and the metallurgical model, as depicted in Figure 2.37 [120]. Each of these models has a strain component attached to them which contribute towards the total mechanical strain using infinitesimal strain theory, and therefore the stress of the material, as shown in Equation 2.4 [121]. Each of these sub-models will be elaborated upon in the following discussion.

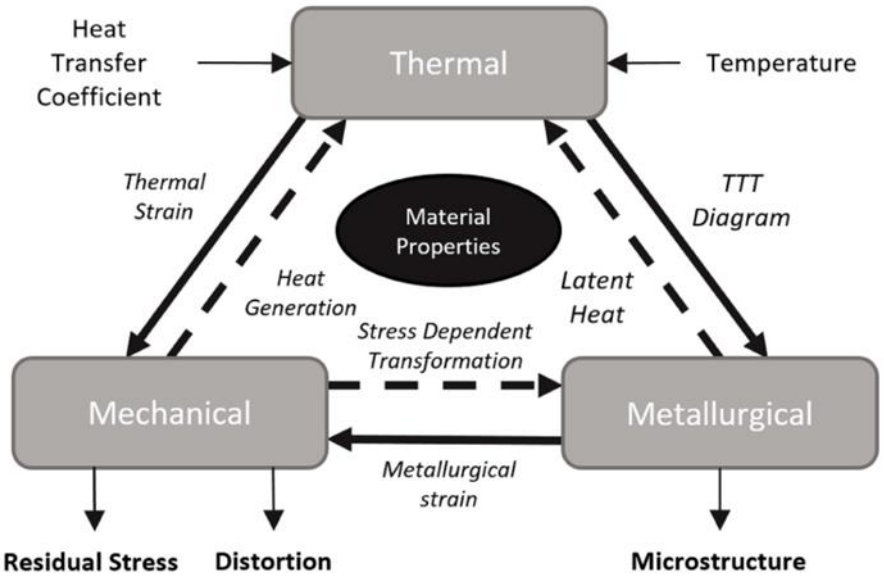

Figure 2.37: Depiction of three sub-models which make up a thermo-metallo-mechanical model and their interaction with one another. Bold black lines are strong interactions, dashed black lines are weak couplings which are often neglected [122].

$$d\varepsilon_{ij}^{total} = d\varepsilon_{ij}^{mech} + d\varepsilon_{ij}^{met} + d\varepsilon_{ij}^{therm}$$

Equation 2.4

2.5.1 The Thermal Model

The thermal model calculates the temperature field of the model. This sub-model is governed by the heat conduction equation (Equation 2.5) where ∇ is the gradient operator, T is the temperature, $\dot{T}$ is the time derivative of temperature, k is thermal conductivity, ρ is density, C_p is specific heat capacity, and $\dot{Q}$ is the heat generated per unit volume per unit of time. In the context of a basic stress-free heat treatment, the thermal calculation assumes heat conduction within the part and heat transfer to the surroundings based on mechanisms such as convection, radiation, conduction, or a combination thereof. Apart from material properties, the two main inputs for this sub-model are the temperature of the part and the heat transfer coefficient (HTC). The HTC quantifies the rate of heat transfer per unit area per unit temperature difference between the part's surface and a surrounding fluid, such as water or air [122].

$$\nabla(k\ x\ \nabla T) = \rho C_p \dot{T} - \dot{Q}$$

Equation 2.5

Obtaining a reliable heat transfer coefficient (HTC) value poses significant challenges due to numerous influencing factors, including the temperature of the part and fluid, material properties, and fluid properties etc. Various strategies can be employed to address this challenge. Firstly, HTC values can be sourced from existing literature. Alternatively, direct measurement of HTC can be conducted using a probe made from the same material and immersed in the same medium [123]. Another approach involves measuring the part's temperature as a function of time and subsequently determining HTC values through an inverse HTC calculation.

Dye et al. utilised the method of embedding thermocouples into parts made from IN718 and quenched them in air, oil, and water to investigate the impact of quenching media on HTC, stress generation, and evolution [96]. Experimental results were as expected, with lower HTC values calculated for quenching in air compared to oil and water.

As illustrated in Figure 2.37, there exists an element of thermally induced strain that serves as a link between the thermal and mechanical models. This strain emerges from temperature fluctuations within the part, stemming from processes like heating and cooling, such as in water quenching. This is discussed more in the mechanical model. The connection between

the thermal model and the metallurgical model is established based on the time-temperature-transformation (TTT) diagram. Consequently, depending on the output of the thermal sub-model, the microstructure of the part will undergo variations which impact the metallurgical sub-model.

2.5.2 The Metallurgical Model

The metallurgical model serves to predict the evolution of a material's microstructure. However, for the thermo-mechanical model under investigation in this study, only the strain induced by metallurgical processes holds significance. Various models exist for predicting different microstructural aspects. The Johnson-Mehl-Avrami-Kolmogorov (JMAK) model, for instance, demonstrates efficacy in predicting the dissolution kinetics of Ni-based superalloys [35]. Another example is the Koistinen-Marburger (KM) equation, which excels in forecasting phase transformation kinetics during cooling [124]. Additionally, the Ostwald Ripening Model has proven adept at predicting precipitate growth [35]. Further details on these models can be found in the literature [35], [124], [125], [126].

2.5.3 The Mechanical Model

The mechanical model is what makes up the mechanical response (meaning the stresses) to the thermal analysis and metallurgical transformations. In this sub-model, the elastic, plastic, creep, thermal, and metallurgical strains all contribute towards the mechanical strain and strain rates as per Equation 2.6.

$$d\varepsilon_{ij}^{mech} = d\varepsilon_{ij}^{el} + d\varepsilon_{ij}^{pl} + d\varepsilon_{ij}^{creep} + d\varepsilon_{ij}^{therm} + d\varepsilon_{ij}^{met}$$

Equation 2.6

Metallurgical Strain

The metallurgical strain component (ε_{ij}^{met}) consists of two elements: the transformation-induced volumetric strain component (ε_{ij}^{tv}) and the transformation-induced plasticity strain component (ε_{ij}^{tp}). Hence Equation 2.6 can be expressed as:

$$d\varepsilon_{ij}^{mech} = d\varepsilon_{ij}^{el} + d\varepsilon_{ij}^{pl} + d\varepsilon_{ij}^{creep} + d\varepsilon_{ij}^{therm} + d\varepsilon_{ij}^{tv} + d\varepsilon_{ij}^{tp}$$

Equation 2.7

Transformation-induced plasticity (TRIP) occurs when materials undergo phase transformations, such as the transition from austenite to martensite during plastic deformation. This phenomenon affects the material's mechanical response by enhancing both strength and ductility. Two mechanisms, the Magee mechanism related to martensitic transformation, and the Greenwood-Johnson mechanism related to diffusion-based transformation, have been proposed to explain this phenomenon [127]. The TRIP component of strain primarily arises from the Greenwood-Johnson mechanism, which is described by:

$$\varepsilon_{ij}^{tp} = k_{ij}^{tp} \Delta f_m s_{ij}$$

Equation 2.8

where k_{ij}^{tp} is a material specific constant, Δf_m is the change in martensitic volume fraction, and s_{ij} is the deviatoric stress component.

Conversely, the transformation-induced volumetric strain component occurs when a material undergoes a transformation, such as precipitate nucleation and growth during ageing. This process can lead to a change in the lattice parameter, as observed in materials like IN718 [71] and AD730 [128], [129]. Consequently, a strain is induced within the part due to these volumetric changes. The transformation-induced volumetric strain can be calculated based on the difference between the unit cell volume, as shown by:

$$\varepsilon_{i\to j}^{tv} = \frac{\Delta V}{V_0}$$

Equation 2.9

This equation can be summed for all phases to give,

$$\varepsilon_{ij}^{tv} = \sum_{i=1}^{n} \varepsilon_{i\to j}^{tv} \Delta f_i$$

Equation 2.10

where ΔV is the change in unit cell volume, V_0 is the original unit cell volume, $\varepsilon_{i\to j}^{tv}$ is the transformation specific volume change strain.

Qin et al. [71] conducted a study on IN718 to analyse its stress relaxation behaviour during ageing. They observed a phenomenon termed "negative creep" at 500 °C and 620 °C, where the material experienced volume shrinkage due to the migration of Niobium atoms to form γ''.

This alteration of the lattice parameter led to volumetric shrinkage. The characterisation of alloy shrinkage strain and creep strain was facilitated through the use of dilatometry and neutron diffraction. Similarly, Durand et al. conducted two separate studies on AD730 [128], [129] and arrived at a similar conclusion as Qin et al. regarding the reduction of lattice parameters of the γ matrix and γ' phase during ageing, resulting in transformation-induced volumetric strain. This finding is anticipated to have implications for the proposed stress relaxation tests in the present study. Durand et al. demonstrated that in certain cases, the transformation-induced volumetric strain could significantly increase the overall stress during stress relaxation tests of AD730 [128], [129]. Consequently, modelling the stress relaxation behaviour may present a considerable challenge, which will be addressed in a later section (see section on Creep Strain).

Thermal Strain

Thermal strain arises from mismatches in expansion and contraction within the crystal lattice during heating and cooling. The thermal strain is mathematically expressed as:

$$d\varepsilon_{ij}^{therm} = \sum_{k=1}^{p} V_k \int_0^T \alpha_k \, dT$$

Equation 2.11

where α_k thermal expansion coefficient of phase k, p is the number of phases, and $V_k$is the volume fraction of phase k [130]. Thus, data regarding the thermal expansion coefficient, the phases of the material, and the thermal field contribute to defining the thermal strain (ε_{ij}^{therm}).

Elastic Strain

The elastic strain tensor is given in Equation 2.12 according to Hooke's law, where E is the Young's modulus, υ is the Poisson's ratio, σ_{ij} is the stress tensor, σ_h is the hydrostatic force, and σ_h is Kronecker's delta.

$$d\varepsilon_{ij}^{el} = \frac{1}{E}[(1-\upsilon)\sigma_{ij} - \delta_{ij}\sigma_h]$$

Equation 2.12

Plastic Strain

In the past, predicting plastic strain often involved linearly interpolating between experimentally obtained flow curves. However, this method can be costly and prone to inaccuracies, especially when the flow behaviour varies significantly across different temperatures and strain rates. To address these challenges, mathematical models in the form of constitutive equations have been developed to describe a material's plastic flow behaviour more accurately. These models enable the prediction of a material's stress response based on inputs such as strain, strain rate, and temperature [131], [132]. FE solvers utilise these constitutive models to simulate the behaviour of materials, incorporating their thermo-physical and thermo-mechanical properties [132].

Constitutive models are typically classified as either empirical-based or physically-based. Empirical-based models, like the Sellars-Tegart's Hyperbolic sine constitutive model [133], [134], or the modified Johnson-Cook model [132], are developed by fitting equations to experimental data, often flow curves, with little regard for the underlying physical mechanisms governing the mechanical behaviour. Obtaining coefficients for these models can be challenging, and their applicability is often limited to the specific range for which they were developed, making them less effective at accurately describing mechanical behaviour beyond this range.

In contrast, physically-based models, such as the combined Estrin-Meckin+Avrami approach [135], [136], aim to comprehend the fundamental mechanisms driving mechanical behaviour, such as work hardening and flow softening, to enhance predictive accuracy. While determining parameters for physically-based models can also be challenging, their broader conceptual foundation allows for more versatile application across different scenarios compared to empirical models.

A substantial body of literature has explored the effectiveness of various constitutive material models in describing mechanical behaviour across different processes like forging [137], [138], [139], [140], [141], with a comprehensive summary provided by Varela-Castro et al. [142]. The following discussion will focus solely on models directly relevant to this thesis, offering an overview within the context of developing constitutive material models for Ni-based superalloys during forging.

A considerable body of literature has showcased the application of the Sellars-Tegart's hyperbolic-sine Arrhenius equation in describing plasticity behaviour [132], [134], [143], [144], [145], [146]. This empirical model is widely adopted and has demonstrated good accuracy in predicting flow behaviour during hot deformation tests. It is relatively easy to integrate into FE solvers, making it computationally efficient. This approach involves determining the activation energy (Q), providing a physical interpretation for one of the parameters used in characterising mechanical behaviour. The main parameters of this model are derived through manipulation of flow curves to ascertain the remaining parameters. Solhjoo provides an excellent overview of this method [133].

Jia-Fu Wu et al. applied the Sellars-Tegart's methodology to effectively model the flow behaviour of Hastelloy C276, as depicted in Figure 2.38 [134]. These findings illustrate the method's capability to predict the hot deformation flow behaviour of a Ni-based superalloy. For the research conducted in this thesis, the Sellars-Tegart's empirical model demonstrates a promising suitability for forecasting flow stress during processes like forging.

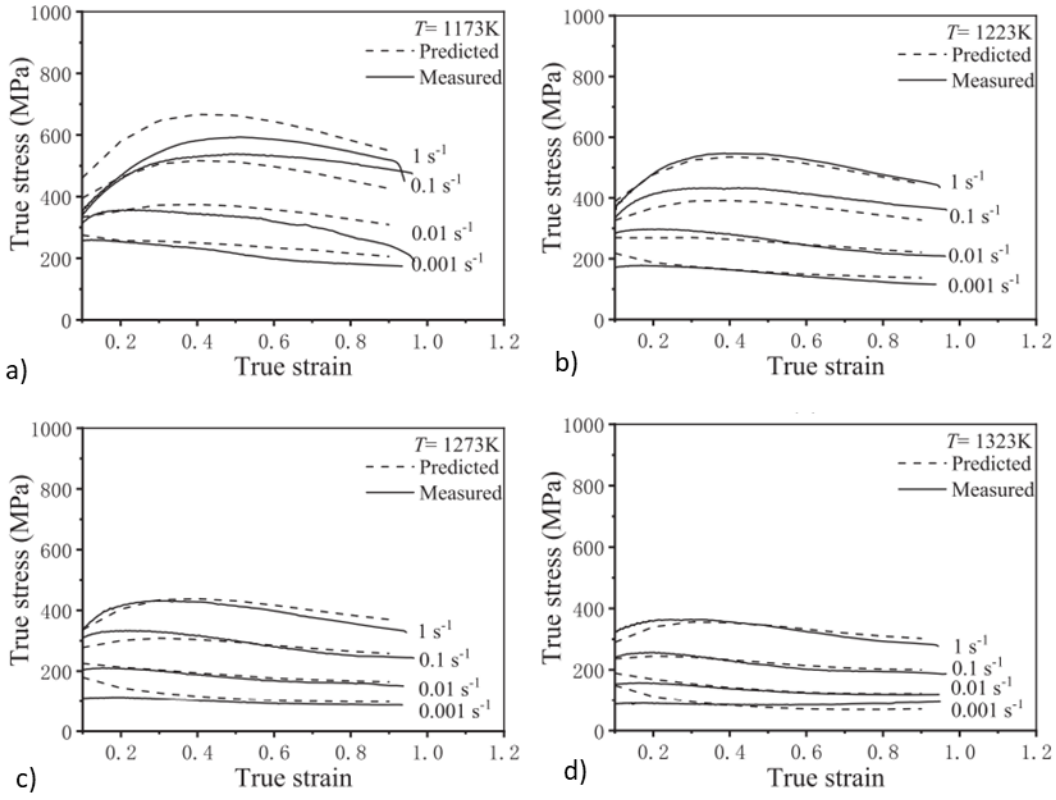

Figure 2.38: Comparison of stress-strain curves at different strain rates for Hastelloy C276, illustrating the difference between predicted and measured stresses at temperatures of a) 900°C, b) 950°C, c) 1000°C, and d) 1050°C [134].

The Estrin-Mecking constitutive model is based on the evolution of dislocation density resulting from a material's work hardening and dynamic recovery behaviours. It establishes a connection between dislocation density and strain hardening rate to forecast the material's deformation response under varying conditions [135], [136], [147]. This model is developed by initially gathering experimental data, often flow stresses. Essential parameters such as initial stress (σ_0) and saturation stress (σ_s), which denotes the stress level at which dislocation generation and annihilation rates reach equilibrium, are determined. The flow stress up to the point of peak stress is plotted, as demonstrated in Figure 2.39 [136]. Tan et al. demonstrated the success of the Estrin-Mecking approach in predicting the work hardening/dynamic recovery behaviour of a novel Ni-based superalloy produced via powder metallurgy [136]. While this method is highly effective in forecasting hot deformation behaviours like those in forging, it cannot anticipate material flow softening. Consequently, it is often paired with another model to accurately predict flow softening [136], [148].

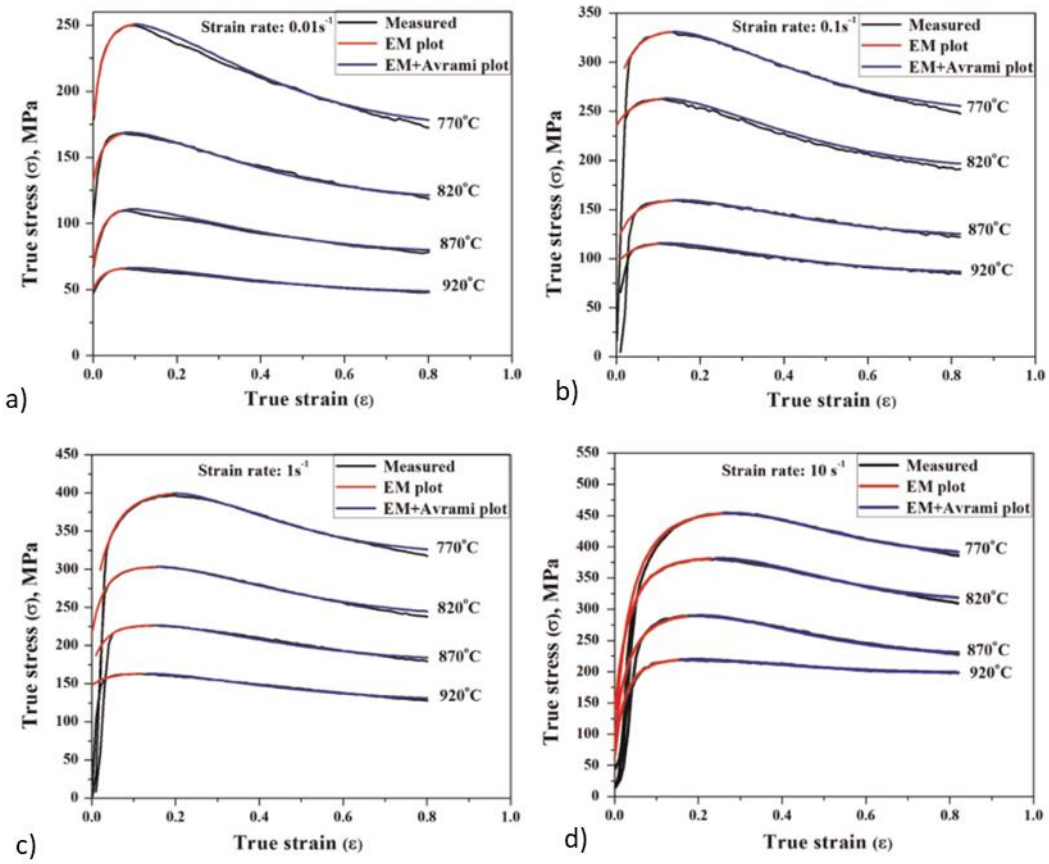

Figure 2.39: Comparison of stress-strain curves at different temperatures for Ti6Al4V, illustrating the difference between predicted and measured stresses at strain rates of a) $0.01s^{-1}$, b) $0.1s^{-1}$, c) $1s^{-1}$, and d) 10^{-1} [136].

The Avrami-based constitutive relationship [149] is a physically-based approach utilised to determine flow softening caused by recrystallisation. Souza et al. demonstrated that when integrated with the Estrin-Mecking model, which predicts work hardening and dynamic recovery behaviours, it becomes a robust tool for forecasting material flow stresses, as illustrated in Figure 2.39. Further investigations by Souza et al. have revealed that the Avrami-based equation can be coupled with the Johnson-Cook model to forecast the flow stress of Inconel 625 during hot deformation across temperatures ranging from 900 °C to 1100 °C, with minimal uncertainties [132] . This research also showcased that the combined Johnson-Cook-Avrami material model could be effectively employed in FE simulations to predict flow stress in a scaled-up geometry, such as a double truncated cone, with high precision, as depicted in Figure 2.40. This modelling approach exhibits significant potential in predicting the hot deformation behaviour of Ni-based superalloys and was easily integrated into a subroutine. Consequently, it stands as a viable option for modelling the hot deformation behaviour of Ni-based superalloys like IN718 and AD730.

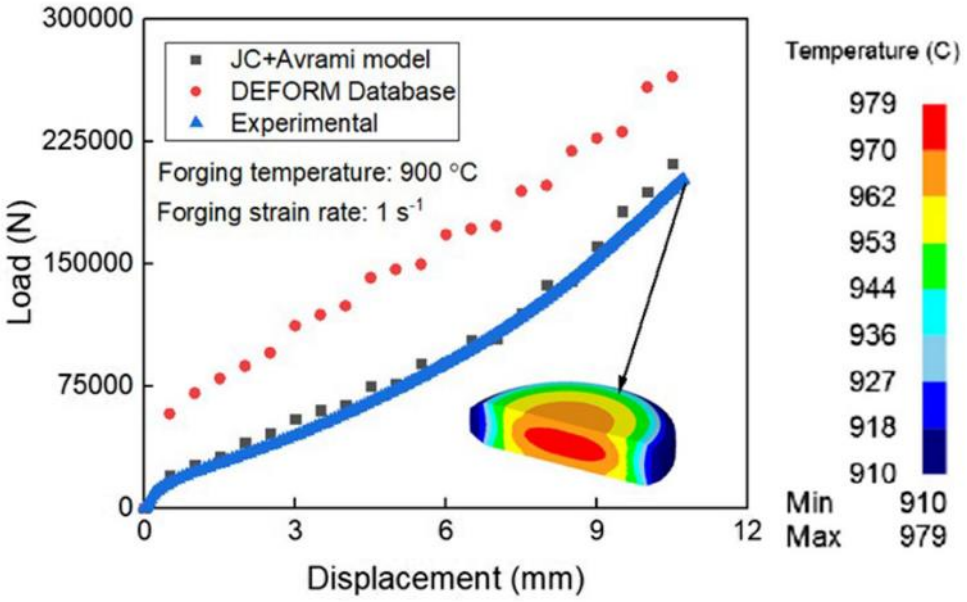

Figure 2.40: Comparison of load-displacement curves for experimentally measured and simulated isothermal compression testing of a Double Truncated Cone using the combined Johnson-Cook and Avrami equations. Note that using the material flow data from the DEFORM's database led to significant over prediction of load [132].

As evident from this literature review section, various types of constitutive material models have been employed to varying degrees of success in predicting flow stresses, especially in Ni-

based superalloys. The accuracy and effectiveness of these models are heavily influenced by factors such as temperature range, strain rate range, flow behaviour, the magnitude of deformation, and the specific model utilised. It's crucial to note that some models may inherently favour certain flow behaviours, impacting their predictive performance. Despite the extensive utilisation of constitutive models for Ni-based superalloy flow stress prediction, to the best of the author's knowledge, there has been no attempt to apply any of these models to AD730.

Prediction of Residual Stress Generation During Quenching

Measuring the residual stresses in parts can be a difficult challenge and one that often requires compromises between the range of measurement depth, the spatial resolution, and whether or not to impart mechanical damage. Therefore, it is not always possible to measure and understand the entire residual stress profile at every stage of the manufacturing process. Numerical simulation, i.e., FE modelling, plays an important role in filling this gap.

Many different models have been used to determine the evolution of stress in a part and some have already been covered in detail in previous sections. Selecting a suitable constitutive model to implement into a FE solver for residual stress determination depends on the process which induces the stress. For instance, the Johnson-Cook model has been shown to be very useful when modelling residual stresses in IN718 generated through shot peening [150], laser shot peening [151], and by turning (i.e., machining) [152]. The Johnson-Cook model is widely used for studying impact and processes with high strain rates [151]. A good summary of the many different material models which have been used for predicting the deformation behaviour and stresses in IN718 and short explanations on how to define the necessary constants can be found in [153]. Hansel-Spittel [154], Sellars-Tegart's Arrhenius based model [155], Zerilli-Armstrong [153], and Khan-Huang-Liang material models [156] have all been developed to model the stress generated in IN718 during different processes, by firstly obtaining experimental data like flow stresses, with good accuracy.

For water quenching, a rate-independent, isotropic linear-hardening model has been shown [91], [96], [157] to be effective in modelling the generation of residual stress. Goldak et al. [157] showed that by assuming a coefficient as shown in Equation 2.13, the yield strength can be plotted as a function of temperature using Equation 2.14.

$$\frac{d\sigma_y}{d\varepsilon_{pl}} = 0.01E$$

Equation 2.13

$$\sigma_y(T) = \frac{\sigma_y(RT) - \sigma_y(HT)}{1 + \exp\left(\frac{T-b}{c}\right)} + \sigma_y(HT)$$

Equation 2.14

Where σ_y is the yield stress, ε_{pl} is the plastic strain, E is the Young's modulus, $\sigma_y(RT)$ is the Young's modulus at room temperature, $\sigma_y(HT)$ is the Young's modulus at high temperature above the γ' and γ'' solvus, T is temperature, b and c are coefficients evaluated from the best fit line shown in Figure 2.41 with data for IN718 from [157]. An important caveat with this method is that it does not consider the kinetics of solute precipitation, which, for phenomenon like γ' coarsening, greatly impact the yield strength [64], [158]. This could potentially be a suitable model used to determine the behaviour of IN718 during water quenching as is proposed in this thesis.

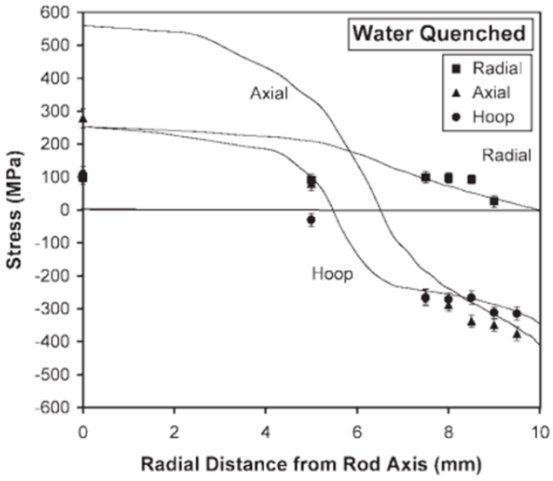

Figure 2.41: Comparison of measured stresses in axial, hoop, and radial direction with predicted stresses for IN718 [96]

Creep Strain

Creep is the gradual increase in the size of a part over time while under load, typically at elevated temperatures. Creep tests provide insights into the long-term deformation behaviour of a material, including time-dependent deformation mechanisms and creep rupture.

Constitutive models, such as the Norton-Bailey model [159] or the Monkman-Grant relationship [160], can be developed from the data obtained in these tests. However, there are some challenges associated with creep tests. Depending on key process parameters such as temperature and load, the duration of a creep test can range from a few hours to a few months [81], [161]. Thus, maintaining consistent process conditions throughout the test period is crucial to ensure test validity. This is particularly true at elevated temperatures, where even small temperature variations caused by factors like drafts or changes in lab conditions can invalidate the test results.

Moreover, creep strain rates are often very small, resulting in minimal deformation. This necessitates the use of high-precision extensometers with high resolution and sensitivity. Consequently, specialised rigs are often required for creep testing purposes.

In contrast, stress relaxation tests, as outlined in section 2.4.4, are typically shorter in duration compared to creep tests and can be conducted using standard uniaxial tensile testing rigs [81], [89]. This gives stress relaxation tests a significant advantage over creep testing. While creep models are well-established and widely used in FE solvers, stress relaxation models are not as easy to implement into a FE solver. Creep and stress relaxation models offer mathematical similarities meaning many creep models can be adapted to describe stress relaxation behaviour.

To derive the creep rate from a stress relaxation test, it is essential to understand the underlying principles [162]. The total strain can be maintained constant during a stress relaxation test by applying the following approach:

$$\varepsilon_{tot} = \varepsilon_{elastic} + \varepsilon_{plastic} + \varepsilon_{creep} = constant$$

Equation 2.15

Thus, the differentiated equation providing the strain rates is:

$$\dot{\varepsilon}_{total} = \dot{\varepsilon}_{elastic} + 0 + \dot{\varepsilon}_{creep} = 0$$

Equation 2.16

The uniaxial elastic strain follows Hooke's law:

$$\varepsilon_{elastic} = \frac{\sigma}{E}$$

Equation 2.17

From which the following relationship can be deduced:

$$\dot{\varepsilon}_{creep} = -\frac{1}{E}\dot{\sigma}_e$$

Equation 2.18

Where $\dot{\varepsilon}_{creep}$ is the creep strain rate, $\dot{\sigma}_e$ is the stress relaxation rate, and E is the Young's modulus. This illustrates the feasibility of deriving the creep strain rate, a task that can be easily integrated into FE solvers, from the stress relaxation rate, which is simpler to measure experimentally than creep strain. As was described in detail in 2.4.4, creep is characterised microstructurally by the migration of dislocations through the grain structure leading to reorganisation of the crystal structure by grain boundary sliding, dislocation climb etc. Stress relaxation is characterised microstructurally by the internal redistribution of stresses though mechanisms such as dislocation rearrangement (i.e. climb, glide), diffusion, or recovery. It can therefore be seen that microstructurally there is some overlap between these time-dependant phenomena.

Therefore, despite sharing common mechanisms at the microstructural level, the simpler equipment required and the shorter duration of stress relaxation tests, along with the ease of converting the stress relaxation rate into a creep strain rate for implementation into an FE solver, meant that stress relaxation tests were preferred over creep tests for this thesis. Consequently, the constitutive models for stress relaxation will be elaborated upon.

Various models are available to characterise the stress relaxation behaviour in materials [163]. One such model, a phenomenological Arrhenius-based equation, has been applied to describe creep rates in polycrystalline alloys [164], as shown in Equation 2.19 [165]:

$$\dot{\varepsilon} = A\sigma^n exp\left(-\frac{Q}{RT}\right)$$

Equation 2.19

In this equation, $\dot{\varepsilon}$ is the creep rate, A is a material constant, σ is the applied stress, Q is the activation energy, n is the stress exponent, T is the absolute temperature, and R is the gas constant. This model has demonstrated reliability in determining creep properties for ferritic Fe-19Cr-4Ni-2Al within the temperature range of 600 °C to 770 °C, suggesting its potential applicability to Ni-based superalloys.

The logarithmic relationship depicted in Equation 2.19 [165] indicates that the strain rate increases with stress, as expected. However, it's worth noting that implementing this model into FE solvers may pose computational challenges due to its dependency on both temperature and stress [165].

An alternative model often preferred and widely used for Ni-based superalloys is the empirical Zener-Wert-Avrami model. This model, described by Equation 2.20 has been applied to investigate stress relaxation behaviour in materials like IN718 subjected to various manufacturing processes such as shot peening [150], laser shot peening [151], and machining [166]. In Equation 2.20, σ^{RS} represents the residual stress after a given time t, σ_0^{RS} the residual stress before ageing, m is a parameter depending on the dominant relaxation mechanism, Q is the activation energy, R is the gas constant, T is the temperature, B is a constant, ΔH is the activation enthalpy for the process, κ is the Boltzmann constant, and T_a is the temperature at given time t. The parameter A is a function of the material and temperature and can be determined using Equation 2.21b [150] , but is more commonly found in literature via Equation 2.21b [151], [165]

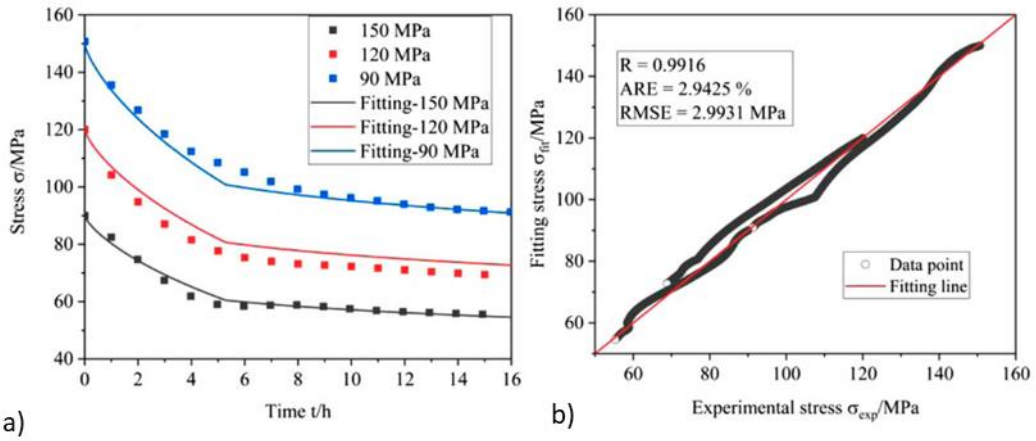

Figure 2.42 a) Comparison of stress-strain curves at different temperatures for 2A14 Al alloy, illustrating the difference between predicted and measured stresses at strain rates, and b) plot of predicted vs experimental stress for all strain rates and temperatures [165].

Although a slightly different method was used by Madariaga et al. [166] whereby a classical stress relaxation test was forgone in favour of carrying out residual stress measurements before and after heat treatment using the incremental hole drilling method, the accuracy of the subsequent modelling using the Zener-Wert-Avrami was still very good demonstrating the

efficacy of this model for predicting stress relaxation behaviour in Ni-based superalloys. As such, this was selected as one of two models used to model the tress relaxation behaviour of IN718 and AD730.

$$\frac{\sigma^{RS}}{\sigma_0^{RS}} = exp[-(At)^m]$$

Equation 2.20

$$A = Bexp\left[-\frac{Q}{RT}\right] \qquad \text{or} \qquad A = Bexp\left[-\frac{\Delta H}{\kappa T_a}\right]$$

Equation 2.21a and b

Rahimi et al. [89] demonstrated the feasibility of modelling the stress relaxation behaviour of solution-annealed IN718 during ageing using a hyperbolic law. Their study revealed a correlation between the initial stress value (σ_0) and the asymptotic stress (σ_∞), which represents the stress level to which the material relaxes over time. While further work is needed to integrate this developed constitutive model into a FE solver and compare it with experimental data, the model exhibited promising accuracy, as evidenced by stress relaxation predictions plotted against a 95% confidence bound (see Figure 2.43). Given its efficacy, particularly for IN718—an alloy of interest in this thesis—the constitutive model was chosen for further development.

Existing research on IN718's stress relaxation behaviour across the full range of ageing temperatures lacks comprehensiveness and has not been incorporated into a model validated with experimental data. Hence, there exists a clear gap for developing and integrating a stress relaxation model for IN718 during ageing into an FE solver.

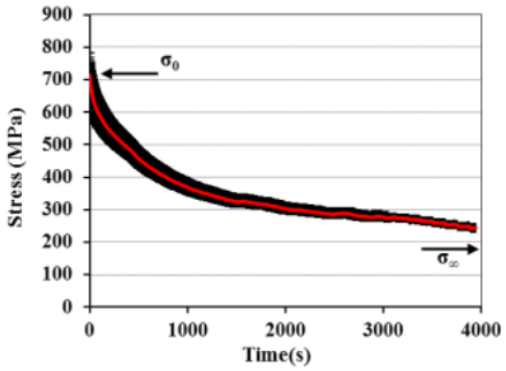

Figure 2.43: A fitted curve with 95% confidence bound (black) to the experimental stress relaxation data (red) for stress relaxation of IN718 at 720 °C [89].

Artificial Neural Networks

Artificial neural networks (ANN's), sometimes referred to as Constitutive Artificial Neural Networks (CANN's) in constitutive modelling, offer a unique approach to predicting the plastic flow behaviour of materials. This approach involves training a model using machine learning techniques, which can sometimes yield more accurate predictions than traditional physical or empirical methods [133].

However, this approach has its drawbacks. Firstly, the model requires training data that may not always be readily available before it can be effectively used for prediction. Secondly, interpreting the results can be challenging due to the lack of transparency and the complexity of the model parameters [167]. Consequently, ANNs are often described as 'black boxes' [168].

Tyagunov et al. utilised a CANN to predict the in-service properties of a Ni-based superalloy solely based on its chemical composition, achieving some level of success [169], which highlights the versatility of this approach. Additionally, other researchers have demonstrated the applicability of CANN's in predicting flow stresses for various materials such as titanium [170], nickel [171], and aluminium alloys [172] using data from hot isothermal compression tests.

Furthermore, CANN's have proven useful in predicting the stress relaxation behaviour of IN718, as shown by Sembiring et al., who successfully predicted residual stress and hardness for a range of Ni-based superalloys as shown in Figure 2.44 [173]. In their study, stress relaxation was induced using Ultrasonic Nanocrystal Surface Modification (UNSM) instead of conventional peening or heat treatments. Although the stress relaxation assessment in

Sembiring et al.'s work [173] did not involve a traditional stress relaxation test outlined in ASTM E328-21 [174] , stress levels were measured using X-ray diffraction (XRD) before and after UNSM treatment.

Although there are some examples of CANN being used to predict the elasto-plastic behaviour or stress relaxation behaviour in metallic alloys, they are still often overlooked in favour of more conventional constitutive equations for predicting the flow stress and stress relaxation behaviour, and in particular there is not a wide application of this method to Ni-based superalloys. With the continued growth of artificial intelligence and machine learning, and the increasing usage of these powerful models, development for the purposes of elasto-plastic prediction in AD730 during hot deformation was to be carried out.

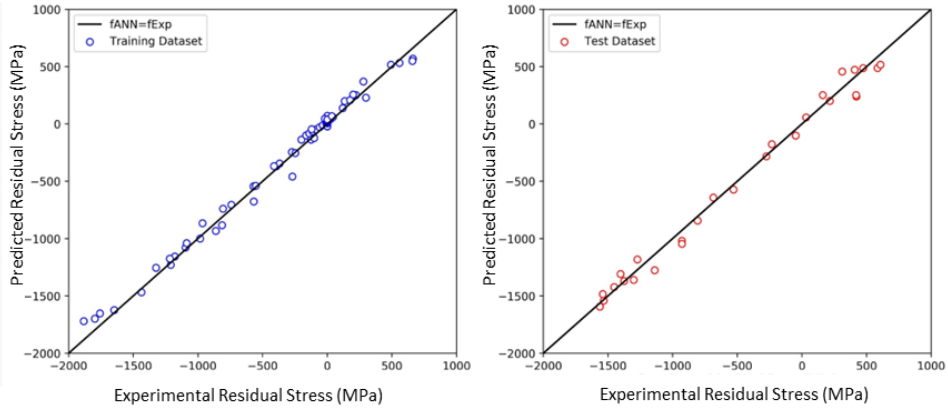

Figure 2.44: Plots comparing predicted and experimental stress for a CANN developed to predict residual stress, illustrating a) the training dataset, and b) the test dataset [173].

2.5.4 Summary of Modelling

To develop an effective thermo-mechanical numerical model for predicting stress generation and part distortion in Ni-based superalloys during forging, several key factors must be considered. These include accounting for the temperature distribution, phase distribution within the material, and mechanical work. In a FE solver, achieving solution convergence involves dividing calculations into sub-models, each addressing specific physical phenomena. The main sub-models crucial for comprehending thermo-mechanically induced stress generation and evolution are the mechanical, thermal, and metallurgical models, as illustrated in Figure 2.37. Each of these models incorporates a strain component, following infinitesimal strain theory, which collectively contributes to the total mechanical strain and consequently influences the material's stress, as outlined in Equation 2.4.

The thermal model computes the temperature distribution within the model, governed by the heat conduction equation. Meanwhile, the metallurgical model predicts the evolution of the material's microstructure. Both models contribute to inducing strain in the material, including thermal strain, transformation-induced volumetric strain, and transformation-induced plasticity strain. These strains are integrated into the mechanical model, which also incorporates elastic, plastic, and creep strain components. This model is responsible for solving these various strain components. This thesis places particular emphasis on reviewing the constitutive models found in literature, especially those used to characterise the plastic behaviour of Ni-based superalloys, with a focus on applications such as hot deformation processes like forging, and those used to model stress relaxation during heat treatments like ageing.

The hot isothermal deformation behaviour of Ni-based superalloys has been effectively modelled using empirical models, physically-based models, and CANNs. However, the accuracy and success of modelling the plastic flow stress depend heavily on various factors including the temperature range, strain rate range, flow behaviour, total deformation, and the chosen model, which may exhibit biases towards certain flow behaviours.

As of now, significant modelling work on alloy AD730 to predict its hot isothermal deformation behaviour has not been conducted. While some efforts have been made to model residual stress generation during water quenching of IN718, utilising a rate-independent, isotropic linear-hardening model, accurate determination of the heat transfer coefficient remains a critical aspect. Factors such as part shape, size, water agitation intensity, quenchant type, and quenching configuration also need further investigation to understand their impact on the heat transfer coefficient and resultant residual stress.

Moreover, there is a lack of research on the stress relaxation behaviour of alloy AD730 during ageing. While it is currently assumed that the ageing heat treatment reduces most residual stresses, this assumption remains untested. Additionally, although some studies have explored the stress relaxation behaviour of IN718, their models lack complete validation against experimental results or implementation into a comprehensive model. Hence, there is an opportunity to develop a fully validated model capable of predicting the stress relaxation behaviour of IN718 during ageing.

3

Methodology

3.1 Methodology Overview for Thesis

In this thesis, Chapters 4 to 8 contain methodology sections outlining the experimental approaches employed to obtain the results presented within each chapter. This section sets out the main challenge addressed and provides an overview of each chapter's research objectives, motivation, and contribution to addressing the overarching challenge. The thermo-mechanical processing routes investigated in this thesis for IN718 and AD730 are shown in Figure 3.1 and Figure 3.2, respectively. These routes were chosen as they are representative of the forging schedules practiced in industry [91], [175], [176].

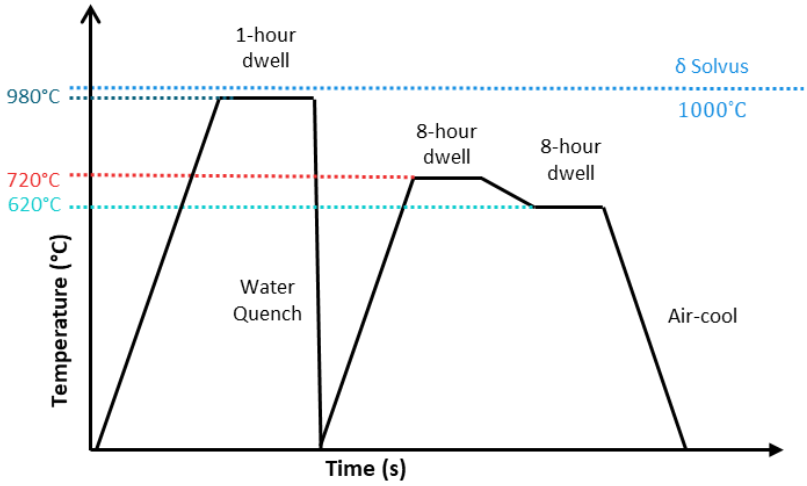

Figure 3.1: Thermo-mechanical processing route of IN718 investigated in this thesis.

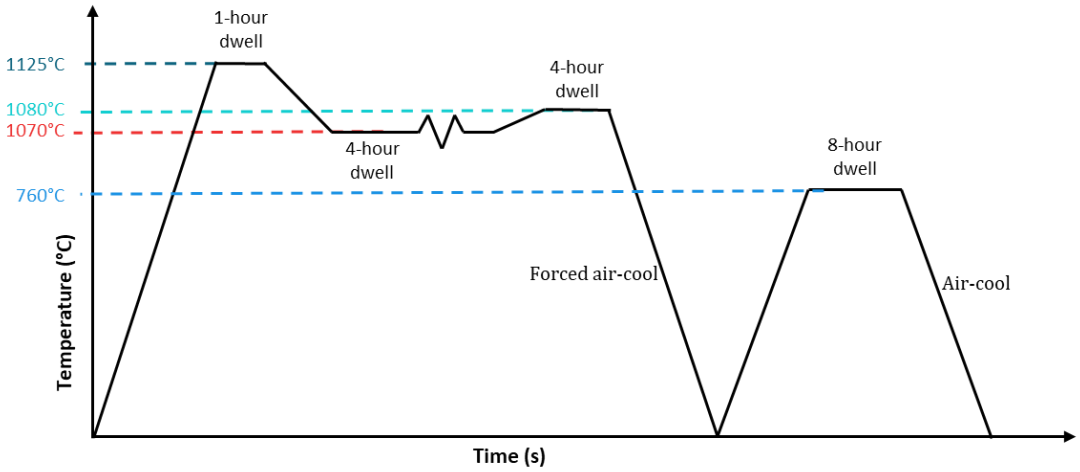

Figure 3.2: Thermo-mechanical processing route of AD730 investigated in this thesis.

The literature review conducted in this thesis underscores the necessity for Ni-based superalloys, which are widely preferred materials for the hot sections of jet engines. Additionally, it highlights the challenges associated with the thermo-mechanical processing of these alloys. Initially, the focus of this work is on IN718, aiming to develop methods for predicting the generation and evolution of residual stress during processing stages like water quenching, ageing, and air cooling. This alloy's well-established nature provides ample literature data for benchmarking and comparison. Subsequently, with confidence in the developed methodology on IN718, attention shifts to investigating AD730, a newer and less-explored alloy. Here, some of the validated methods used for IN718 are applied to AD730, including the development of a constitutive model for predicting stress relaxation during

ageing. Then, a constitutive material model, which was not developed for IN718, is developed to predict the hot deformation behaviour of AD730 during forging. Due to the scarcity of literature data for AD730 in comparison to IN718, predictive FE models for residual stress generation and evolution during forging, cooling, and ageing of AD730 had to be validated against experimental trials.

Chapter 4 investigates the generation of thermally induced residual stress in IN718, resulting from water quenching after the solution annealing stage, which is a representative of the post-forging water quenching in industry. The literature review in this thesis underscores the critical importance of managing the microstructure and understanding stress generation and evolution in Ni-based superalloys throughout their processing route. Water quenching introduces substantial residual stress due to heterogeneous cooling, which impacts subsequent processing stages (e.g., machining), necessitating a thorough understanding of this process. By measuring cooling rates of scaled discs quenched in various configurations and media (i.e., water and air), a FE model assesses residual stress generation. Cooling rates from water quenching and air cooling are utilised to determine residual stress during quenching/air-cooling after solution annealing and ageing, respectively. This involves using measured cooling curves for inverse HTC analyses to obtain suitable HTC values, crucial for residual stress determination in the FE model. The primary contribution of this chapter lies in devising a methodology for determining HTC values for parts undergoing various cooling methods, including water quenching and forced air-cooling.

After water quenching from the solution annealing temperature of 980°C, IN718 undergoes a double ageing heat treatment at 720 °C and then 620 °C. As indicated in the literature review of this thesis, stress relaxation is believed to occur at these temperatures, but the extent of stress relaxation remains not very well understood. Stress relaxation tests are commonly employed to assess the stress relaxation behaviour of materials. Chapter 5 focuses on the creation of a novel miniaturised testing geometry designed for testing precipitation hardenable materials, which is subsequently utilised for stress relaxation testing in Chapter 6.

Accurately determining thermo-mechanical properties in precipitation hardenable materials using an ETMT system poses a significant challenge. The non-uniform temperature distribution resulting from resistivity heating leads to heterogeneous deformation along the gauge length due to the temperature-dependent mechanical properties, complicating direct measurements.

Chapter 5 primarily focused on addressing this challenge by developing a new test methodology and sample geometry for elevated temperature tensile testing of IN718 samples using the ETMT. Once the results were validated against literature data in Chapter 5, the developed methodology and geometry were applied to stress relaxation tests conducted in Chapter 6.

In Chapter 6, stress relaxation test results were used to establish two constitutive stress relaxation models for IN718. A comparison was made to determine the most appropriate model for this material across a range of initial stresses and ageing temperatures. The results were validated against literature findings for accuracy. This marks the completion of the IN718 investigation in this thesis, with developed methodologies for analysing residual stress generation and evolution during water quenching, ageing, and air-cooling stages (as depicted in Figure 3.1). Additionally, stress relaxation tests and model development for AD730 were conducted in Chapter 6, following methodologies similar to those applied to IN718. This chapter initiates the research on AD730 and the beginning of the development of a comprehensive, multi-step, multi-process FE model for the entire thermo-mechanical processing route, as shown in Figure 3.2.

Chapter 7 extends the investigation on AD730 by developing two constitutive material models to characterise its hot deformation behaviour, as depicted in Figure 3.2. Given that forging typically occurs at temperatures around 1070 °C, hot isothermal compression tests were conducted between 1000 °C and 1125°C, covering a range of strain rates from 0.001 s^{-1} to 5 s^{-1} to replicate forging conditions. The results served as inputs for developing the constitutive material models, with the most accurate model selected to represent the material's hot deformation behaviour. An experimental trial involving forging a double truncated cone was conducted, followed by analysis of the out-of-plane residual stress using contour measurement analysis after forced air-cooling. Subsequently, simulation of the forging trial was performed using a FE solver with a subroutine developed and incorporated from the optimal constitutive material model, and the model's accuracy was evaluated against the contour measurement results.

Chapter 8 marks the culmination of the efforts undertaken in chapters 4 through 7. The FE model developed in chapter 7 was built upon, by incorporating multiple subsequent steps to emulate the thermo-mechanical processing route depicted in Figure 3.2. Stress relaxation

during ageing was simulated utilising the outcomes from chapter 6, while HTC values from chapter 4 were applied for air-cooling after ageing. An experimental trial involving a second double truncated cone (DTC), following the thermomechanical processing route in Figure 3.2, was conducted, and measurements of the out-of-plane residual stress were taken post air-cooling. Comparison of the results from the FE model for AD730 and the residual stress measurements using the contour method were used to determine the FE model's accuracy. Chapter 9 serves to summarise the conclusions drawn from this work, and Chapter 10 outlines potential next steps to further advance this research and capitalise on key findings.

4

Impact of Quenching Configuration on Residual Stress Generation and Distribution in an IN718 Scaled-Disc

4.1 Introduction

As discussed in the literature review of this thesis in sections 2.3 and 2.4, the water quenching process causes the part to experience extreme thermal gradients which in turn generate residual stress fields of a high magnitude which the ageing heat treatments often do not fully remove. This step, as highlighted in Figure 4.1, is pivotal in the thermo-mechanical processing of this alloy. The residual stress is generated because of the difference rates which the part contracts at when being cooled, causing localised plastic deformation between the hotter and cooler sections. The rate of cooling is shown to be a key determinant in the magnitude and distribution of residual stress generation in a part.

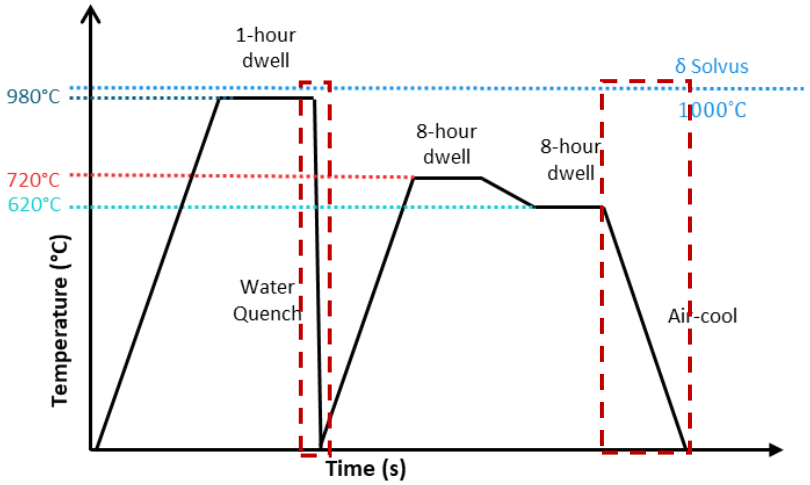

Figure 4.1: Thermo-mechanical processing route of IN718 highlighting the water quenching and air-cooling stages investigated in this chapter.

Understanding the heat transfer between a part and a quenching medium, requires an accurate determination of the HTC. HTC is a parameter which is used to quantify the amount of convective heat transfer between the part, and the quenching medium (in this case water). This parameter is dependent on several factors, including the temperature of the part and quenchant, the state of the quenching medium (i.e., is it in an agitated or still state), and the physical properties of the quenchant. HTC can be determined through empirical methods like that of an inverse heat transfer analysis, where cooling curves measured during quenching are applied as boundary conditions and HTC values are determined using an iterative process.

This approach is often hampered by slow computational time and many data points which are required to give suitably accurate results for localised HTC values. These HTC values can now form a key input into a FE model which can be used to determine the residual stresses formed during the water quenching of IN718 from elevated temperatures (e.g., 980 °C). It is this approach which is employed in this chapter. The results of the FE model can then be compared to results obtained through measurements of water quenched samples measured for residual stresses using the contour measurement method.

The effect of quenching configuration was investigated on a scaled disc, a shape which would be of more relevance to industrial applications. The disc was quenched in two different quenching configurations, and in also two different quenching media, water, and air. The FE model was validated using experimental tests. These are explained in this chapter.

4.2 Methodology

4.2.1 Material and geometry

Five scaled disc components were machined from a single billet of IN718 Ni-based superalloy which was in the as-aged condition, supplied by Aubert & Duval (A&D). The nominal chemical composition for this material, supplied by the manufacturer, is provided in Table 4.1. The sample geometry is a simplified sub-scale disc with a 200mm diameter, a 30mm-by-30mm thick outer rim, and a 2.5mm thin central web, which can be seen in Figure 4.2. The chosen geometry aimed to replicate the thermally induced residual stress generation and distribution found in the webs and drive-arms of industrial turbine discs. By selecting a geometry with varying thicknesses, the goal was to observe different reactions during water quenching, while still maintaining a shape that accurately represents the actual components. As shown in Figure 4.2, the central thin web of the disc was offset by 2.5mm, this was to better understand if the web would deflect by the same magnitude and in the same direction for each water-quench.

Samples for material characterisation using a scanning electron microscope (SEM) and electron back scatter diffraction (EBSD) were extracted from the same billet as the scaled discs. One sample was investigated in the as-received condition, and the other was investigated after a 1 hour heat treatment at 980°C, the purpose of which was to solution anneal the sample. Both samples were mounted, ground, and polished to a mirror finish condition using standard metallographic techniques and then vibratory polished for 4 hours in 0.02 µm colloidal silica suspension. Samples were then characterised using a FEI Quanta 250 SEM interfaced with an HKL-EBSD system by applying an accelerating voltage of 20 kV and using a 100 µm diameter aperture. A typical scan area of 600µm × 500µm was mapped for each sample with 0.5mm step size, where a minimum of 90% of the scanned area was indexed.

Table 4.1: Nominal chemical composition of the IN718 material used in this study, provided by the manufacturer Aubert & Duval

Element	Ni	C	Fe	Cr	Nb	Mo	Ti	Al
Wt.%	Bal.	0.04	18.50	18.00	5.20	3.00	0.90	0.50

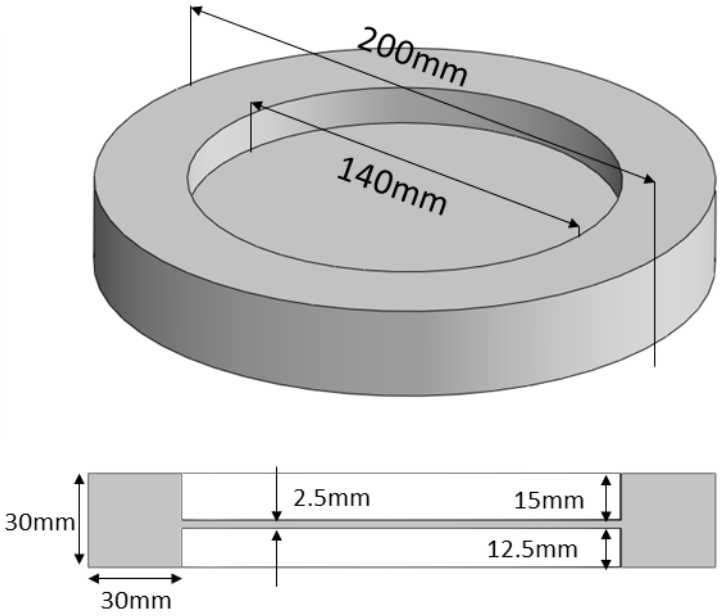

Figure 4.2: Geometry and dimensions of the IN718 scaled-discs used for these investigations.

4.2.2 Quenching conditions and measurement of cooling curves

Discs

Of the five discs that were machined, three were used for fully destructive residual stress measurements using the contour method, and two were used to obtain cooling curves from thermocouples imbedded into the sample at different locations during a heat treatment and water quench. The purpose of obtaining the cooling curves was to perform inverse HTC analysis and as such these tests are hereby referred to as the inverse HTC tests.

Water Quenches for the Inverse HTC Tests

For the inverse HTC tests, holes of 1.1mm were drilled into the discs using a wire EDM drill at the locations shown in Figure 4.3, so that 1mm diameter N-type thermocouples could be installed. All thermocouple tips were positioned on the same plane upon full embedding. Thermocouples near the disc's corners were installed between 1 and 2mm from both edges as shown in Figure 4.3d. Thermocouples located near the rim-to-thin-web transition were installed 2mm from the inside edge and 15mm from the edge running perpendicular to the inside edge as shown in Figure 4.3c. Finally, thermocouples positioned at the centre of the rim section were installed equidistantly, 15mm away from all edges of the 30x30mm rim section,

also illustrated in Figure 4.3c. The axial direction of the disc was parallel to the quenching direction for the horizontal quenching configuration and perpendicular to the quenching direction for the vertical quenching configuration as shown in Figure 4.4. Three tests were carried out on two discs labelled disc A and disc B. Disc A was heated to 980°C, dwelled for 1 hour from the point that the last thermocouple reached 980 °C, and was then water quenched in the horizontal configuration (hereby referred to as the horizontal disc). Disc B went through the same process but was quenched in the vertical condition (hereby referred to as the vertical disc). The vertical disc, once cooled, had all thermocouples removed, the depth of each hole made for thermocouple installation was checked to make sure it wasn't clogged with debris, and then new thermocouples were installed. The vertical disc then underwent the same process except this time it was air-cooled as opposed to water quenched. The results from this are hereby referred to as the air-cooled disc.

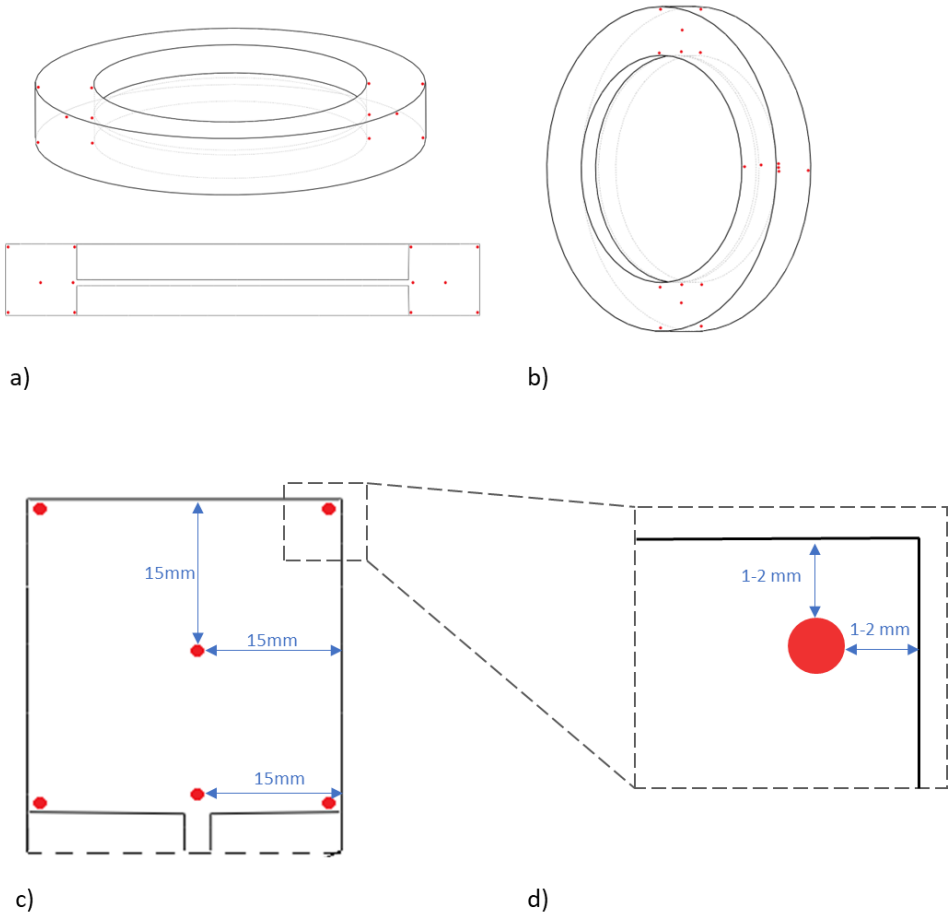

Figure 4.3: a) Thermocouple locations for horizontal quenching configuration, b) thermocouple locations for vertical quenching configuration, c) thermocouple locations showing distances from surface for central located thermocouples, and d) thermocouple locations showing distances from surface for corner located thermocouples.

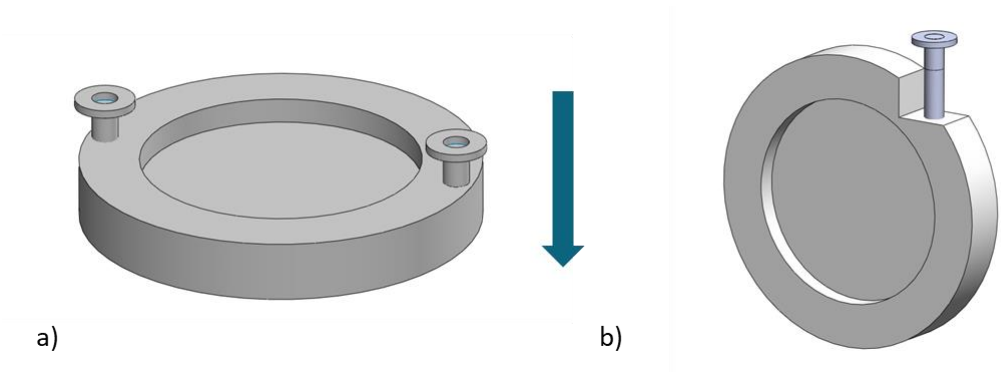

Figure 4.4: Quenching direction for both configurations indicated by arrow. a) horizontal quenching configuration showing fixture locations at 180° spacing, and b) vertical quenching configuration showing notch and fixture location.

Nichrome wire was used to secure the thermocouples onto the disc. The thermocouples were then connected into a National Instruments data acquisition unit and temperatures recorded using National instruments LabVIEW software via the SignalExpress module. Temperature readings were captured at a rate of five readings per second in light of the expected fast cooling rates for the water-quenched tests, and one reading per second for the slower-to-cool air-cooled test. 5 readings per second was as quick as the hardware and software could collect data without the crashing and proved to be sufficient as several readings were captured at the fastest cooling rates as shown in Figure 4.10a. The transfer time from the furnace to the water-quench tank was around 15 seconds and was facilitated using a forklift with a specially designed holder, and fixtures attached to the discs. This was as quick as the forklift could remove and quench the sample, and as shown in Figure 4.10a, the transfer time does not result in any significant temperature loss. The fixtures were secured to the disc using a M16 bolt screwed into a notch for the vertical quench configuration as shown in Figure 4.4b, and two M16 bolts spaced at 180° intervals as shown in Figure 4.4a for the horizontal configuration.

Water Quenching for Residual Stress Measurements

The three discs for residual stress measurement using the contour method were firstly measured using a GOM-ATOS system in the as-received condition to construct their 3D profile. None of the discs had holes wire EDM drilled into them, and thermocouples installed, as this

would have affected the generation of residual stresses. Besides that, the three discs were treated under the same conditions as those for the HTC tests and after being individually heated to 980°C, i) one disc was water-quenched in the horizontal direction, ii) one disc was water-quenched in the vertical direction, and iii) one disc was air-cooled for comparison purposes. Following this process, the profile of each disc was measured using the GOM-ATOS optical measurement system to determine the post-quench deformation when compared to the profiles obtained in the as-received condition. Finally, the samples were then measured for residual stresses using the contour method.

4.2.3 Measurement of Residual Stress

A summary of the processes for measuring residual stresses using the contour method can be seen in Figure 4.5, outlining the four main steps.

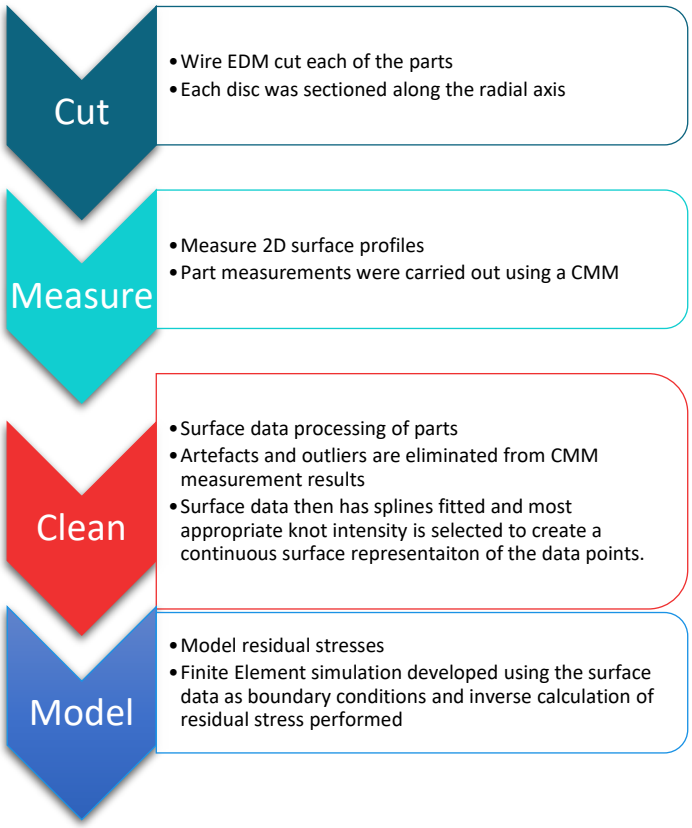

Figure 4.5: Step-by-step procedure for measuring residual stresses using the contour method.

Wire EDM cut

Sectioning of the three discs designated for residual stress measurements was carried out in the radial direction and through the midpoint to create two equal sized halves. A GF Agie Charmilles cut 400 SP wire EDM was used with special care being taken with regards to the cut settings. A "skim cut", whereby the cutting speed was reduced, and the flushing of the cut was increased compared to normal cut settings, was selected so that the surface of the cut was an optimal for measurement using a coordinate measuring machine (CMM). The discs were clamped as close as possible to the cut line and on both sides of the cut to prevent any movement during cutting. Each disc was then cut directly from one end to the other without interruption of the EDM wire.

Surface profile measurement

After the cuts were complete, both halves of each part had their outline and surface profiles measured using a Mitutoyo Crysta Apex C CMM with a 1 mm ruby interfaced to a Renishaw PH10T touch probe. The pitch size for all disc measurements was 300µm.

Data cleaning and surface fitting

The raw surface profile data from the CMM was then analysed and manual removal of any outlying points, which would cause errors or artefacts when modelling the residual stresses, was carried out. Surface profile data from both halves of the same part were then aligned on the same co-ordinate system. The data from one half of a part, hereby known as the floating half, is then mirrored, and placed on top of the data from the other corresponding half part, hereby known as the reference half. A linear interpolation is then carried out and an average of the two data sets was performed. A post-processed surface profile can be seen for a disc in Figure 4.6.

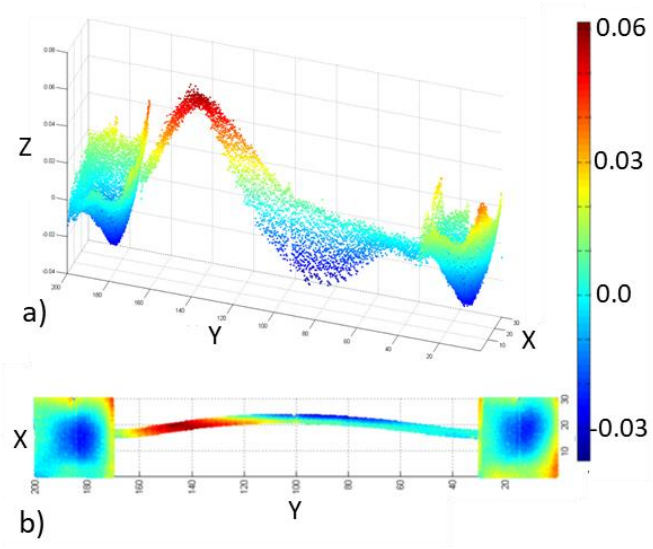

Figure 4.6: Surface displacement data obtained from a CMM for a vertically quenched disc a) 3D view, and b) 2D view.

Bivariate cubic splines were then fitted to the averaged datasets for different knot intensities. Determining a suitable knot spacing requires some degree of iteration. A plot demonstrating five different spline fits for five different knot intensities on a vertically quenched disc can be seen in Figure 4.7. A knot intensity of 3.75mm was selected as the most suitable as it provided an appropriate level of detail without oversimplifying the fit and losing detail as has happened in the case of the 30mm knot spacing. This was the same for the horizontally quenched disc and for the air-cooled disc.

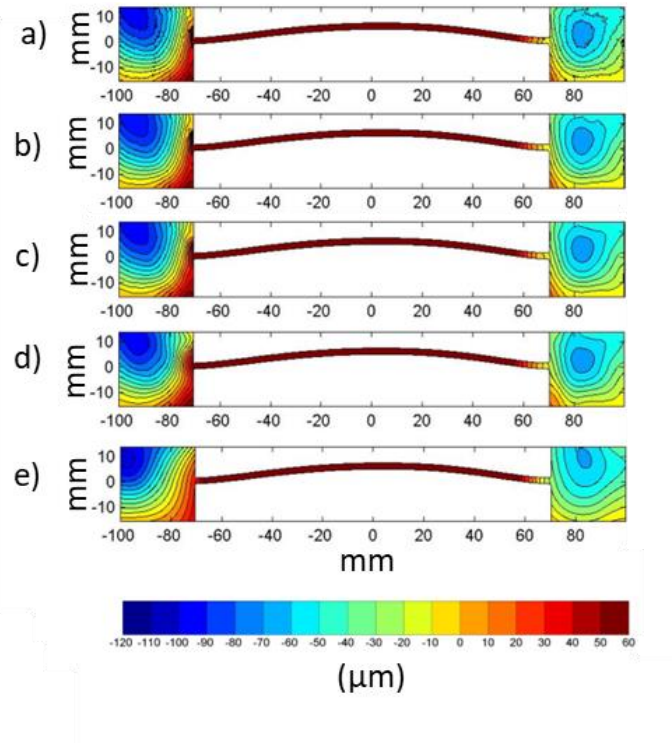

Figure 4.7: Surface fitting of the vertically quenched disc using five different spline sizes with a knot spacing of a) 0.496mm, b) 1.875mm, c) 3.75mm, d) 7.5mm, and e) 30mm.

FE simulation of residual stress

The final step involves the calculation of residual stresses by means of a 3D model which uses the processed surface profile data as a boundary condition in Abaqus CAE. The outline geometry of the reference half was extruded to 500mm in length. Mesh density is defined by the nodes on the outline which are used as mesh seeds. Since the top face is of central interest, a biased meshing regime is used with the mesh density being higher in this area than at the bottom surface as shown in Figure 4.8 for the disc, which was 0.7mm and 10mm, respectively. All parts were meshed using 20-node quadratic hexahedral ($C_3D_{20}R$) elements with reduced integration. The advantage of using the cuboid hexahedral elements is that they match the shape of the discs which were extruded reducing the requirement for a fine mesh for highly detailed sections. An elastic modulus of 197 GPa and a Poission's ratio of 0.294 were assigned to the material, and the residual stresses were determined by deforming the surface to match the average surface profile data reversed in the out-of-plane direction.

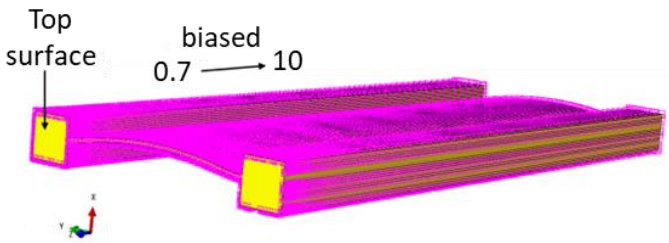

Figure 4.8: An extruded disc sample showing uniform seeding around the cut surface with a bias of 0.7 to 10mm from top surface to the opposite surface.

4.3 Results

4.3.1 Microstructural characterisations

The solution annealed material was heated to 980°C for 1 hour before being water quenched. δ phase (seen in Figure 4.9c and d as white features) precipitates in expense of γ'' at temperatures above 650°C [78] with the δ solvus being reported as ≈1000°C [75], [79], [80] depending on the Niobium content [79]. Therefore, the solutioning temperature of 980°C was not expected to impact the grain size as the δ phase, which inhibits grain growth, was still expected to be present at this temperature albeit with a lesser volume fraction and a different morphology. The IPF orientation image maps, with respect to the out of plane direction, obtained using EBSD for the as-received and the solution annealed material can be seen in Figure 4.9a and b, respectively. The as-received material has an average grain size of 3.0 ± 0.2 µm, and the solution annealed sample had an average grain size of 3.9 ± 0.3 µm showing little change in grain size, as expected. Both microstructures show equiaxed grains with no preferential texture.

Figure 4.9d show a mixture of two different δ phase morphologies which are both distinct from γ'' which as a disc shaped morphology. One morphology is spheroidal and one plate-like. It has been reported that at temperatures over 930 °C, the morphology of δ phase becomes spheroidal, at temperatures below 930°C the morphology becomes plate-like, and at temperatures between 950 °C and 985°C, a mixture of these morphologies is present [175], [176]. This is in line with the observations made in this study. The δ phase also shows a 3-5% drop in the volume fraction from the as-received to the solution annealed sample showing the minor impact of the solution treatment on this phase. The fast cooling associated with water quenching influences the volume fraction, size, and distribution of γ'' precipitates, but has little effect on the grain size and δ phase of the material. The γ'' solvus is reported to be between

900 °C and 920°C [75] meaning it should be completely dissolved during the 1 hour dwell at 980 °C.

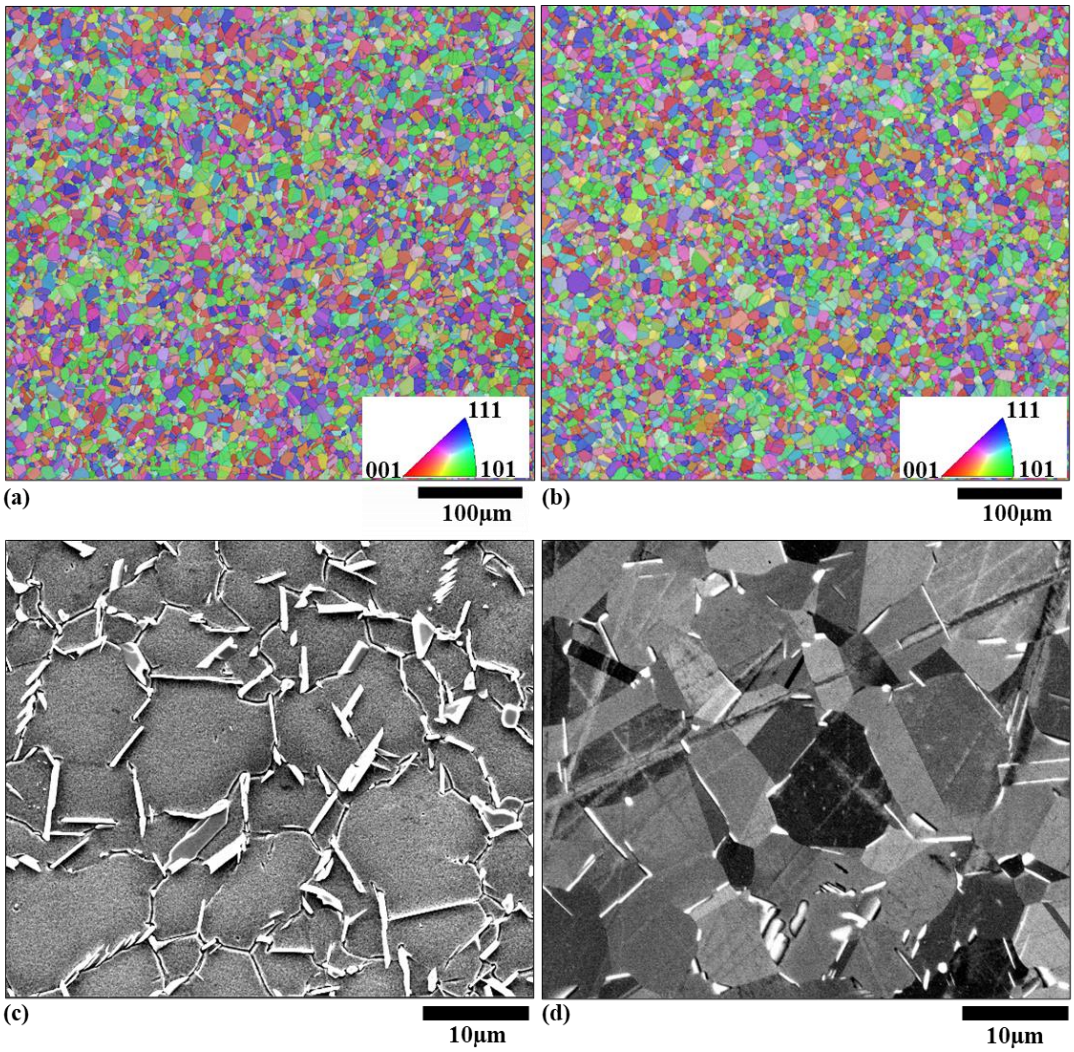

Figure 4.9: EBSD Inverse pole Figures colour orientation maps with respect to the out-of-plane direction for a) the as-received, and b) the solution annealed (1 hour at 980°C) and then water quenched material. Corresponding SEM micrographs can be seen in c) for the as-received material, and d) for the solution annealed material.

4.3.2 Cooling curve measurements

The cooling curves for the vertically and horizontally quenched discs can be seen in Figure 4.10 and Figure 4.11, respectively. Marks 1, 2, and 3 in Figure 4.10a and Figure 4.11a denote the moments when the furnace door was opened, when the part was taken out of the furnace, and when the part was immersed in water, respectively. The transfer time from the furnace to contact with the water was consistently around 15 seconds. When looking at Figure 4.10c, it

can be seen that the thermocouples on the bottom of the sample precedes the corresponding thermocouples at the top of the sample for cooling as is expected for the vertical cooling configuration, indicating good integrity in the experimental method. This difference in cooling demonstrates how stresses may generate with different sections of the disc undergoing different cooling regimes. This will be considered more in the discussion section. Conversely Figure 4.11a shows the corresponding thermocouples on the right and left side of the horizontally quenched sample have very similar cooling profiles, indicating that the axial direction of the disc was perpendicular to the water when it was quenched. Again this indicates good integrity in the experimental method. Three distinct cooling mechanisms can be detected from the point which the discs were submerged in water. The first stage is the vapour stage. At this point the discs are surrounded by a blanket of water vapour known as a vapour blanket. Almost all heat transfer being done at this stage is through the vapour blanket [177]. This is an inefficient stage of the water quenching process and often agitation is used in quench tanks to remove this vapour blanket and to progress the cooling to the second stage. The second stage is the nucleate boiling stage. At this point in the quench, the vapour blanket begins to collapse, and the water comes into contact with the metal. Because of the high temperature of the discs, the water boils upon contact. This is where the highest cooling rates are seen. The third and final stage occurs when the temperature of the discs' surface falls below the boiling temperature of the water. Heat at this stage is removed by convection and this is the slowest cooling stage [178].

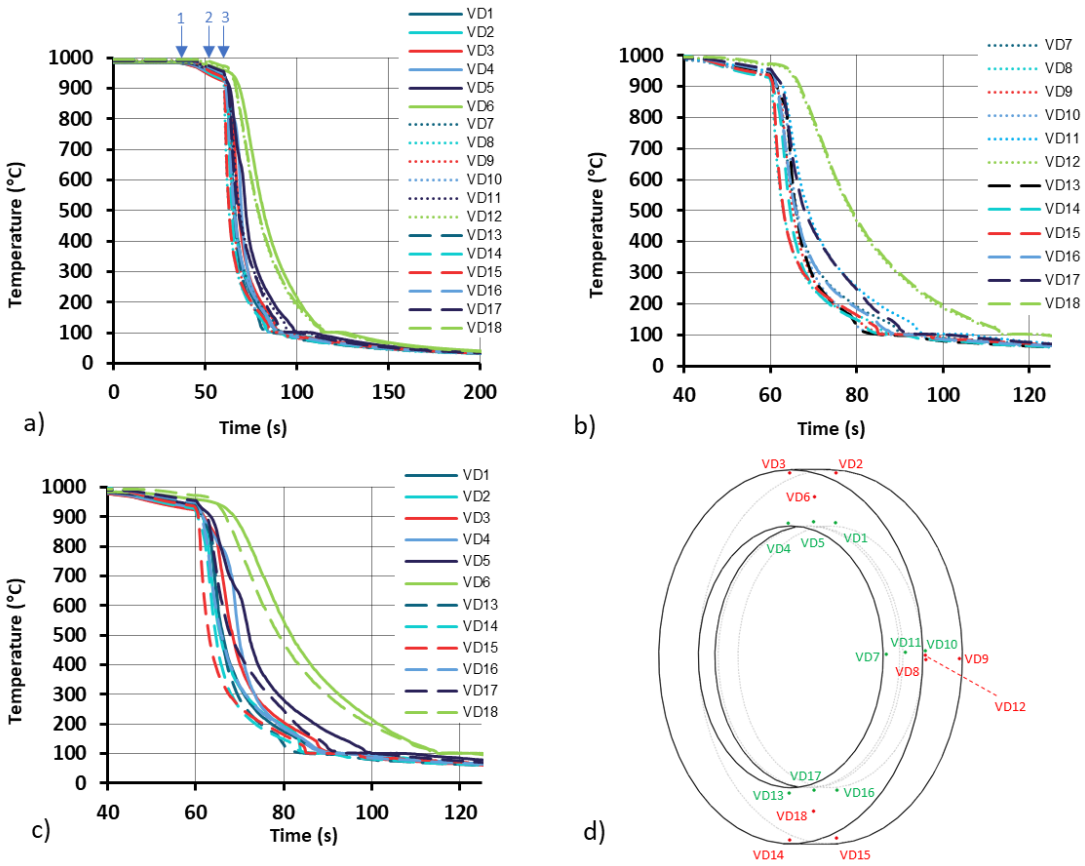

Figure 4.10: Cooling curves for the vertical disc quenching configuration. a) cooling curves from points at every location on the disc, b) cooling curves from the middle and bottom sections of the disc shown in d), c) cooling curves from the top and bottom sections of the disc shown in d), and d) schematic of thermocouple identifiers and locations for vertical quenching configuration.

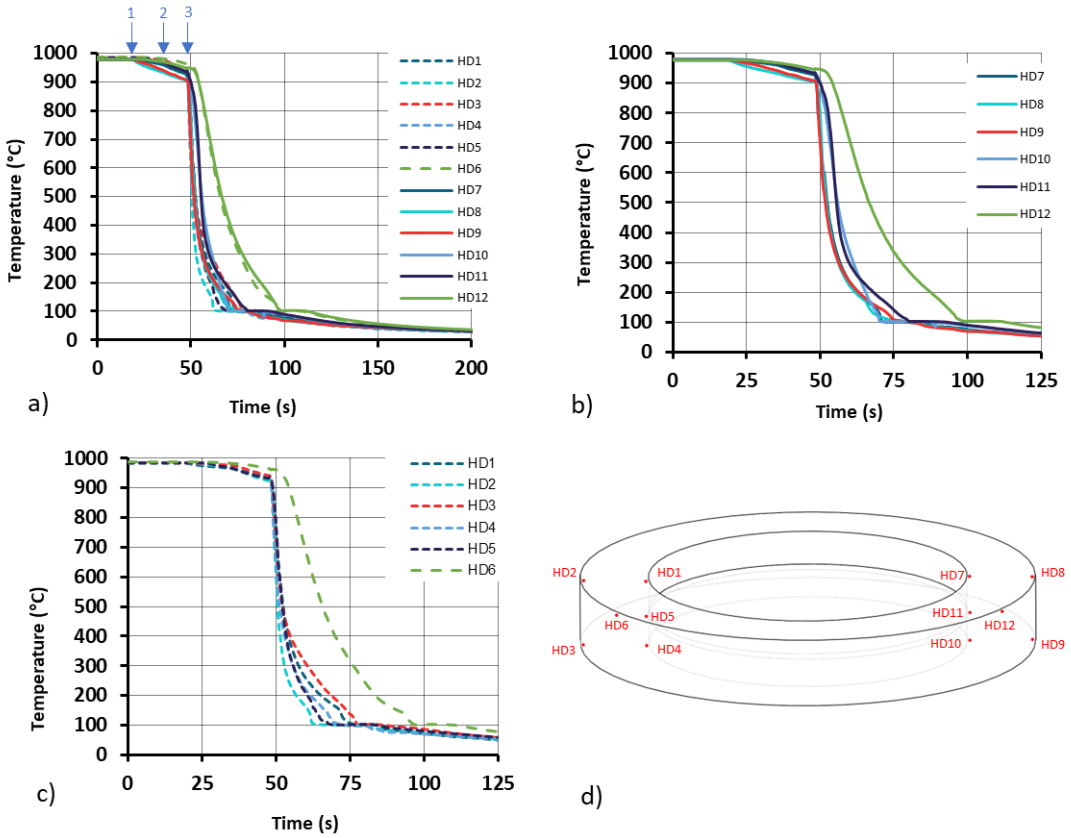

Figure 4.11: Cooling curves for the horizontal disc quenching configuration. a) cooling curves from points at every location on the disc, b) cooling curves from the right side of the disc shown in d), c) cooling curves from the left side of the disc shown in d), and d) schematic of thermocouple identifiers and locations for horizontal quenching configuration.

Figure 4.12 shows the cooling curves obtained from an air-cool of the disc. The transfer time from the disc leaving the furnace to being held stationary in air was the same as for the previous tests at 15 seconds. The cooling curves are more consistent with one another, showing little divergence due to the slow, homogenous nature of the cooling.

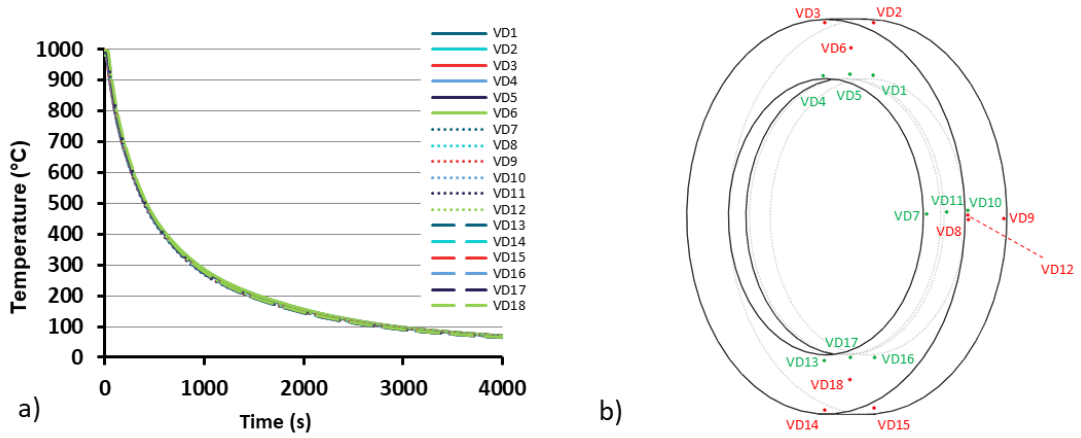

Figure 4.12: Cooling curves for the vertical disc air-cool configuration. a) cooling curves from points at every location on the disc, b) schematic of thermocouple identifiers and locations for vertical quenching configuration.

4.3.3 Distortion Measurements

The design of the discs used in this chapter had two criteria which were of significance. Firstly, they were to be a scaled representation of a disc which was similar to those seen in industry for use as in a turbine. Secondly, they were designed with a thin web to increase the likelihood of high levels of distortion. 3-D GOM-ATOS scans were superimposed onto one another in the as-received and post-quench conditions for each of the vertically water quenched, horizontally water quenched, and air-cooled discs, to give a heat map demonstrating where the most significant amount of deflection took place. There were significant distortions measured in the thin web of the discs, as shown in Figure 4.13. The distortion in the web deflected in all cases towards the side of the disc with the 12.5mm height to the rim, and not the side with the 15mm height to the rim. The peak distortions for the water quenched discs were significantly higher, measuring 6mm and 7.5mm respectively for the vertically and horizontally quenched discs, than the air-cooled disc which measured a peak deflection at 2.5mm. This demonstrates the impact which different quenchants (i.e., air and water) have on the distortion induced on the discs. Furthermore, the difference in deflection between the vertically and horizontally water quenched discs demonstrates the impact that quenching configuration has on the distortion of parts. This will be considered more in the discussion.

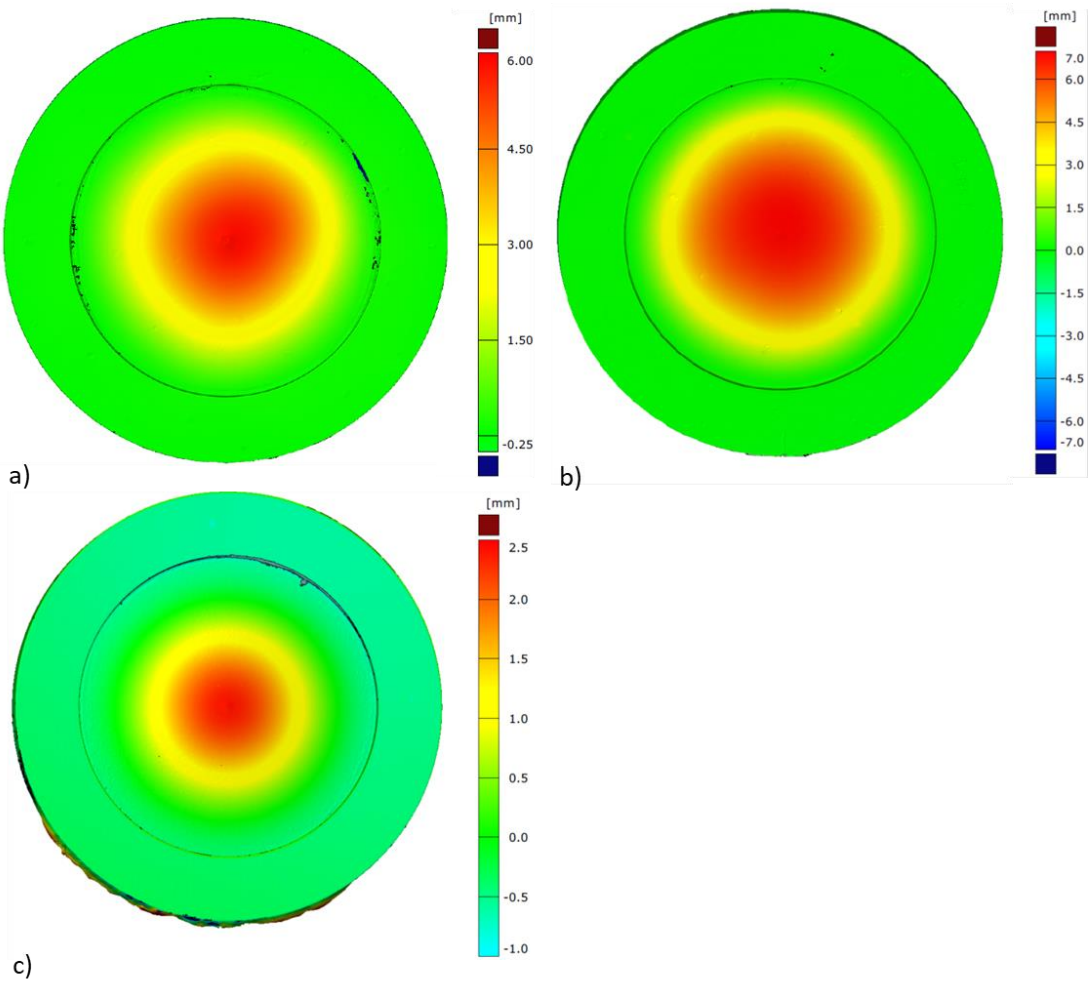

Figure 4.13: Superimpositions of GOM-ATOS 3-D scans for the as-received and post-quenching conditions in a) vertically water quenched disc, b) horizontally water quenched disc, and c) air-cooled disc. Note the different scale bars for each disc.

4.3.4 Residual Stress Measurements

Figure 4.14 and Figure 4.15 show the contour maps of the surface height and the stress maps for the out-of-plane residual stress profiles of the vertically and horizontally water quenched discs, respectively. The quality of the data is very good with very few outlying points. Figure 4.14a, Figure 4.15a, and Figure 4.16a show the corresponding contour maps of the surface height averaged for both halves of the discs. The different quenching configurations for the water quenched discs show slightly different surface height profiles however the air-cooled disc has a completely different profile and much lower values.

For the vertically quenched disc a stress distribution, characteristic of water quenching (i.e., tensile at the core of the rim section and compressive stresses surrounding that core), can be seen. The measured tensile stress ranges from 600MPa to 800MPa, and the compressive stress at the edge of the rim section are between -600MPa and -1000MPa. The bottom section of the vertically quenched disc would be submerged in water before the top section of the disc (i.e., by approximately 2 or 3 seconds) which is believed to be the cause for the noticeably different residual stress magnitudes in the two rim sections shown in Figure 4.14b. The top section of the disc shows peak tensile residual stress of around 800MPa whereas the bottom section of the disc shows a peak stress of around 700MPa. The compressive stress in the top section is higher, near 1000MPa, whereas the bottom section has maximum compressive stress nearer 800MPa. This again shows the impact of quenching configuration. The point of maximum deflection at the centre of the dome has tensile forces on the top-most side, and compressive forces on the bottom-most side.

For the horizontally quenched disc, a strong tensile stress between 400MPa and 550MPa can be seen near the centre of the rim at the right-hand side of the disc, and 600MPa to 800MPa tensile stress can be seen on the left-hand side of the disc near the centre of the rim. The tensile stress is surrounded by compressive stress which increases in magnitude towards the edges to magnitudes between -100MPa to -900MPa. Near the area where the rim meets the web (referred to as the transition zone), there is tensile stress (≈200MPa) on the side closest to the rim, which evolves into compressive stress (-200MPa to -400MPa) on the web side. This description applies to the right-hand side of the disc as depicted in Figure 4.14. In the same figure and on the left-hand side of the disc, there is compressive stress at the transition zone, increasing in magnitude before transitioning to tensile stress at the middle of the thin web on the top side. It is important to note that the thin web stress may not be an accurate representation of the residual stress in the sample prior to cutting. This is because significant plastic deformation at the thin web introduces some uncertainty into this measurement which is examined more in the discussion.

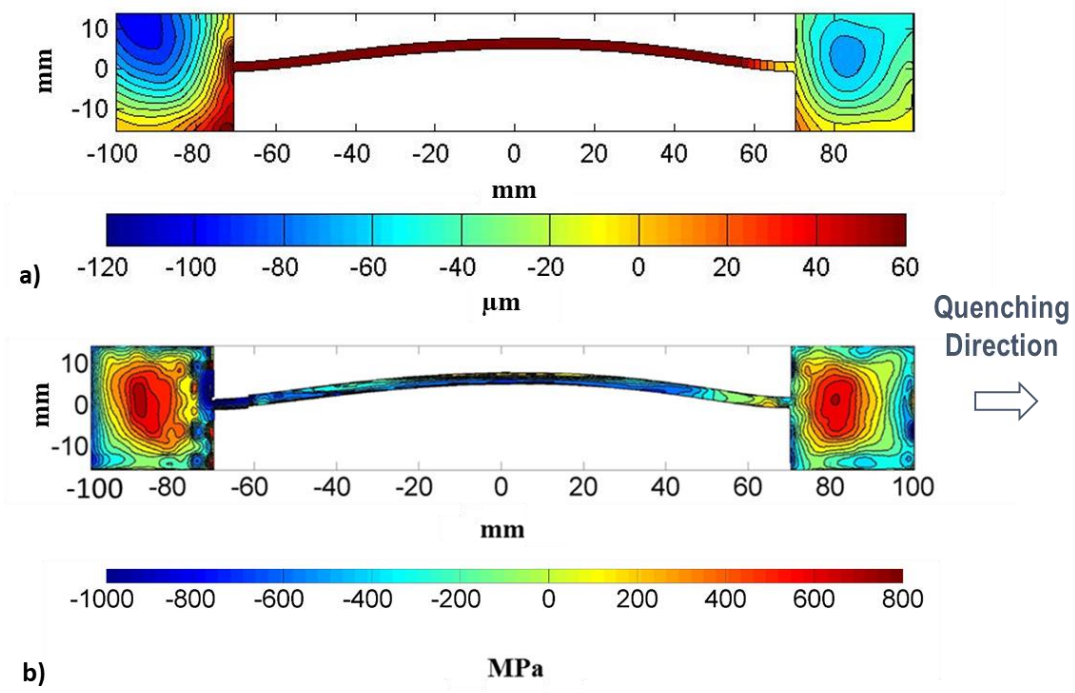

Figure 4.14: a) 2-D contour map of surface height, and b) 2-D stress map of the out-of-plane residual stress for the vertically quenched disc. Note the left hand side is the top of the disc, and the right hand side is the bottom of the disc.

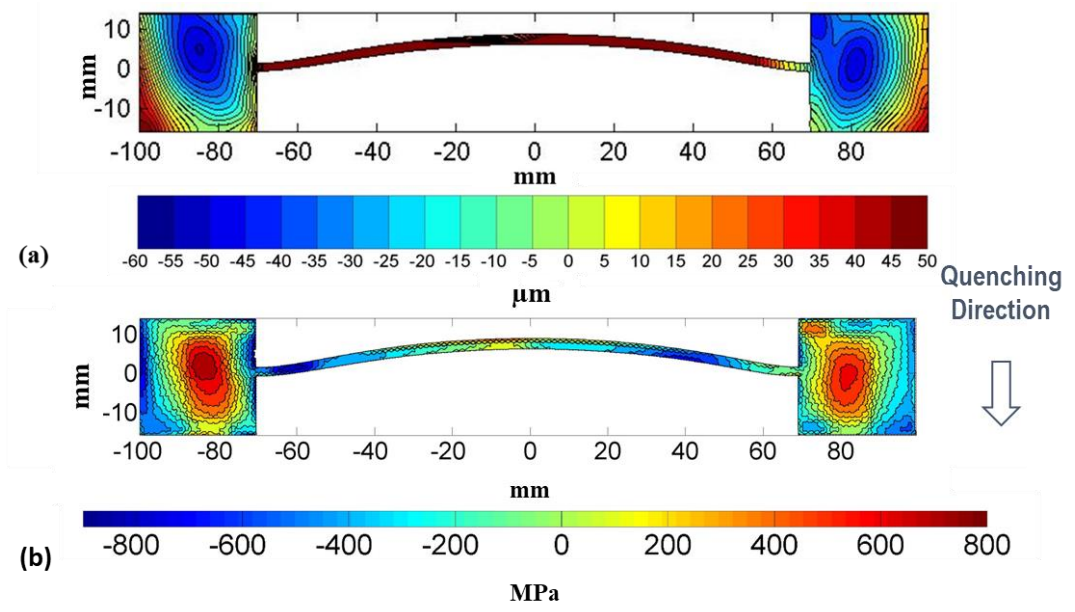

Figure 4.15: a) 2-D contour map of surface height, and b) 2-D stress map of the out-of-plane residual stress for the horizontally quenched disc.

The contour maps of the surface height and the out-of-plane residual stress of the air-cooled sample can be seen in Figure 4.16. Figure 4.16a shows a depression at the outermost corner

on the side where the dome is (12.5mm side). The surface profile changes from this depression at this corner, to a peak on the opposite corner. A rise in the surface contour can be seen across the thin web of ≈30µm. This leads to a stress profile on average of 50MPa of tensile stress near the centre of the rim section on both sides with some heavily localised peaks at ≈300MPa. A wire breakage on the EDM means there is an artefact from the cutting which is indicated by the blue arrow in in Figure 4.16b. Cleaning of the data was not able to fully remove this artefact, which has led to a sudden increase in tensile stresses. These stresses are likely to be artificially high and should be treated with caution when further analysing, but otherwise the data is good. Overall, the magnitude of the stresses, both tensile and compressive are significantly lower for the air-cooled disc than those for the water quenched discs due to the lesser thermal gradients associated with aircooling. The water quenched discs display significant peak tensile stress near the centre of their rims (400MPa-800MPa), surrounded by heavy compressive stress near the edges (-100MPa to -1000MPa). The air-cooled disc has much lower tensile stress near the middle (100MPa) but with no clear and prominent peak, surrounded by slightly compressive stress at the edge (-100MPa).

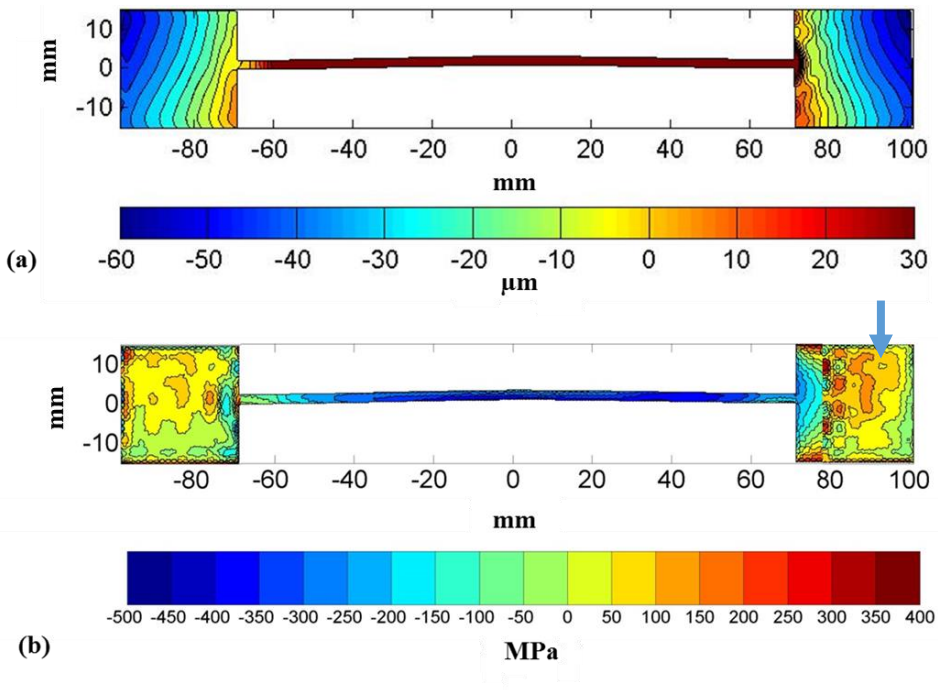

Figure 4.16: a) 2-D contour map of surface height, and b) 2-D stress map of the out-of-plane residual stress for the air-cooled disc.

4.3.5 Inverse Heat Transfer Coefficient Analysis

Heat conduction is the mechanism which drives heat treatments such as air-cooling and water quenching. The model which was used to determine the HTC's of the discs, which were water quenched and air-cooled, are provided in Equation 4.1.

$$\rho C_p \frac{\partial T}{\partial t} = \frac{\partial}{\partial x}\left(\lambda \frac{\partial T}{\partial x}\right) + \frac{\partial}{\partial y}\left(\lambda \frac{\partial T}{\partial y}\right) + \frac{\partial}{\partial z}\left(\lambda \frac{\partial T}{\partial z}\right) + \dot{q}$$

Equation 4.1

Where ρ is density, C_p is the specific heat capacity, T is temperature, λ is the thermal conductivity coefficient, and $\dot{q}$ is the internal thermal energy. The heat flux (q) was calculated through the iterative process of reducing the error between the measured experimental temperature through installed thermocouples in a part, and the simulated values. The HTC can then be given by Equation 4.2.

$$H = \frac{q}{(T_p - T_w)}$$

Equation 4.2

Where q is the heat flux, T_p is the temperature of the surface of the disc at specified locations, T_w is the temperature of the water used for quenching and H the HTC. The inverse heat conduction problem was solved using DEFORM (version 13.1) which has a dedicated module for performing inverse heat transfer problems. For the discs, the problem was set up in 2 dimensions and the parts were modelled axisymmetrically. The environment temperature for the simulation was set to 20°C and material properties was taken from Dye et al. [96] for IN718 over the temperature range necessary for these tests. The temperature dependant properties used for these tests are provided in Table 4.2.

Table 4.2: Mechanical and thermo-physical properties for IN718 taken from Dye et al. [96].

Temp (°C)	Thermal conductivity (Wm^{-1} K^{-1})	Density (kg m^{-3})	Specific Heat Capacity (JKg m^{-3})	Mean Thermal Expansion Coefficient (x10^{-6})	Young's Modulus (GPa)	Yield Stress (MPa)
0	11.02	8226	424	12.8	197	300
100	12.75	8190	434	13.1	197	300
200	14.36	8160	448	13.4	197	300
300	15.96	8130	463	13.8	197	300
400	17.6	8090	480	14.2	197	300
500	19.18	8050	500	14.0	196	294
600	20.77	8010	525	15.1	194	290
700	22.36	7960	560	15.7	187	285
800	23.95	7910	605	16.4	165	251
850	24.53	7890	625	16.8	145	230
900	25.1	7860	636	17.1	130	180
1000	26.83	7810	645	17.5	105	97

Simple linear 2D quadrilateral elements were used for meshing the discs. As can be seen in Figure 4.17, a coarser mesh (average element size of 0.25mm^2) was used for the bulk of the discs, with a 3 layers of finer elements of 0.1mm, 0.15mm, and 0.2mm in width were used near the surface of the discs. The reason for the finer elements is due to the nature of the inverse heat transfer problem, wherein the finer mesh layers are better at simulating the faster heat transfer experienced by the surface during cooling, and the coarser elements are adequate to simulate the heat conduction throughout the part whilst saving on computational time.

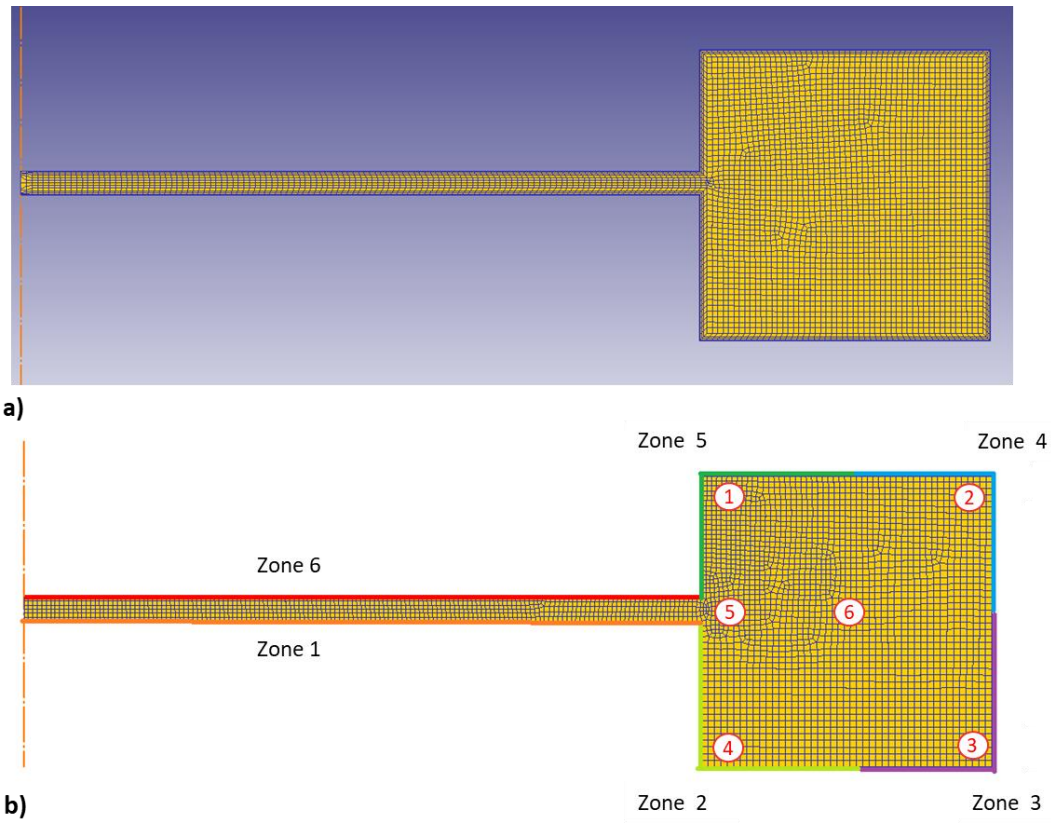

Figure 4.17: a) Illustrates the element density distribution in the disc model used for the FE simulation setup in DEFORM software. Coarse elements are observed throughout the bulk, transitioning to finer elements near the surface. b) Depicts the designated HTC zones for both water-quenched and air-cooled discs, with each zone corresponding to a thermocouple location. Thermocouple locations are denoted by red numbers.

Six zones were used for HTC determination as shown in Figure 4.17b. Each HTC was located next to a thermocouple, in an effort to increase the accuracy of the HTC on that surface section. Obtaining reasonable HTC values which eventually gave a similar stress profile to that measured using the contour method meant that three approaches were trialled in order to calculate the HTC's.

HTC as a Function of Time

The initial approach to address the problem involved calculating the HTC as a function of time. However, the software convergence was impeded by an excessive number of data points, covering either a wide time frame or temperature range. To overcome this, the cooling curves for water-quenched discs were divided into four sections: i) 30 seconds before opening the furnace door, marking the end of a one-hour soak at 980°C, until the door was opened; ii) from door opening to first contact with the quenching water; iii) from first contact with the water to

the end of nucleate boiling and the onset of convection cooling; iv) from the start of nucleate boiling until the temperature dropped below 60°C. Conversely, the air-cooled disc simulation proceeded continuously, benefiting from a slower and more uniform cooling rate that facilitated rapid and accurate software convergence. In this case, HTC values were unrestricted, allowing the software to select the most suitable value to meet boundary conditions. By solving in the time domain, more control points were available, leading to a more precise determination of HTC and faster convergence.

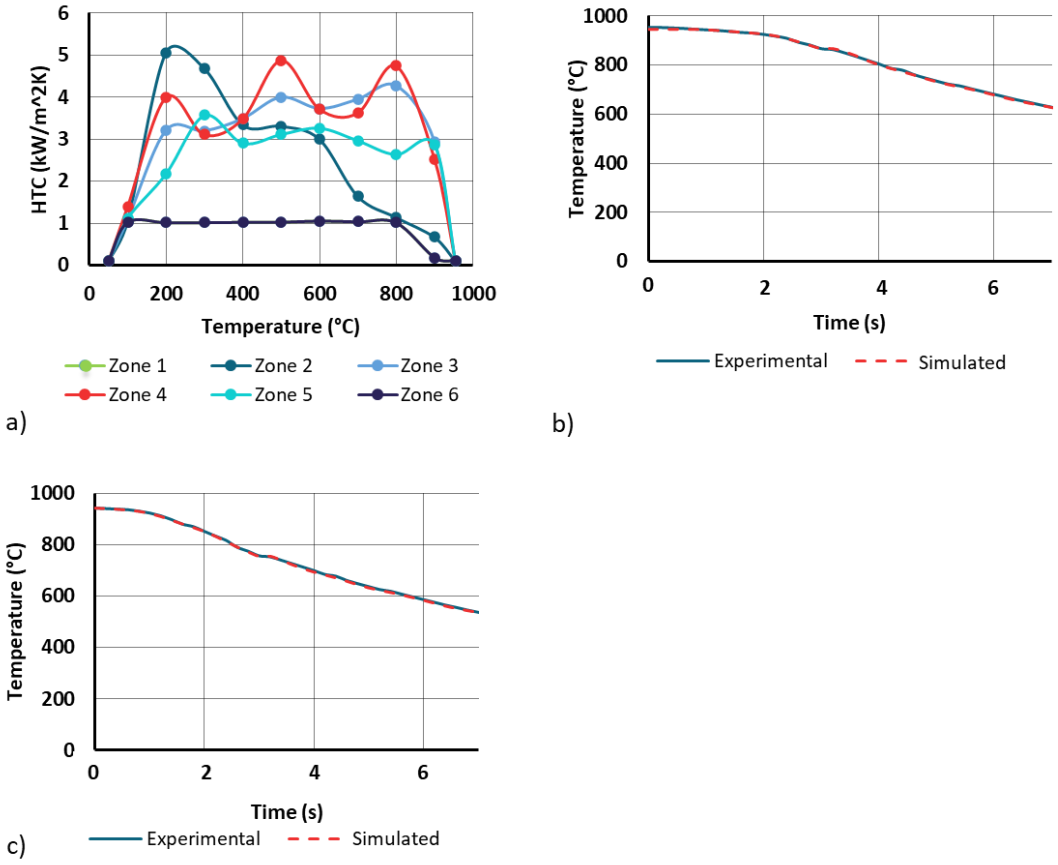

Figure 4.18: Evaluation of HTC for the horizontally water quenched disc, a) HTC values calculated as a function of time at the six zones shown in Figure 4.17b but plotted as a function of temperature, b) and c) thermocouple convergence at location 1 and location 4, respectively.

Figure 4.18 shows the results from the first method of solving for inverse HTC values. The model showed excellent convergence between the experimental and predicted temperature values as can be seen in Figure 4.18b and Figure 4.18c, which show convergence at selected thermocouple locations. While the HTC was computed as a function of time, it is represented

as a function of temperature in Figure 4.18a to facilitate later comparisons with other HTC determination methods.

HTC as a Function of Temperature and Unconstrained

The second approach to determine HTC's involved solving them as a function of temperature. This approach utilised fewer control points, and instead of dividing the cooling curves into sections, the entire curve was solved as a single solution. Like the first method, HTC values were unrestricted, allowing the software to choose the most suitable value to meet the boundary conditions of the cooling curve.

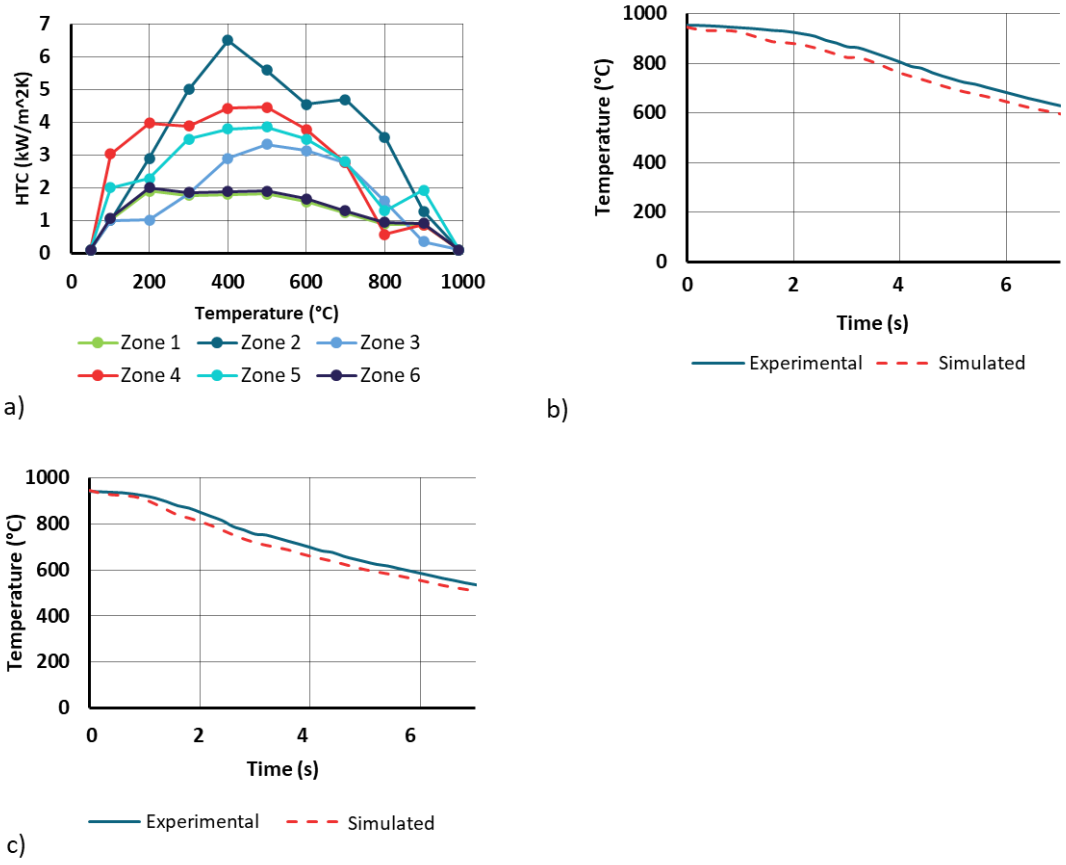

Figure 4.19: Evaluation of HTC for the horizontally water quenched disc, a) HTC values calculated as a function of temperature with no constraints at the six zones shown in Figure 4.17b , b) and c) thermocouple convergence at location 1 and location 4, respectively.

The second methodology of solving for HTC's inversely gave the results shown in Figure 4.19. HTC curves as a function of temperature were produced and showed different values to the results of the first methodology which was solved as a function of time. The convergence of the simulated and predicted cooling curves for thermocouples at locations 1 and 4, shown in

Figure 4.19b and Figure 4.19.c, respectively were not as good as for the first method. Comparison of the determined HTC values from the three different methods can be seen in Figure 4.21 in the following section.

HTC as a Function of Temperature and Constrained

The third method closely resembled the second method, with one notable difference: the software calculated HTC values while imposing lower bound constraints, as depicted in Figure 4.20. These constraints aimed to integrate some understanding of the typical shape of HTC curves into the simulation, ensuring that the final mathematical solution remained physically meaningful. Initial HTC values were obtained from [123], which provides data for water quenching of Inconel 600, as shown in Figure 4.21d. Due to the limited literature available on water quenching of Ni-based superalloys, particularly IN718, a compromise was reached by selecting values for Inconel 600 and allowing them to vary within reasonable lower bounds also derived from [123]. Figure 4.21 illustrates the difference between the determined HTC values from the three methods for the horizontally quenched disc.

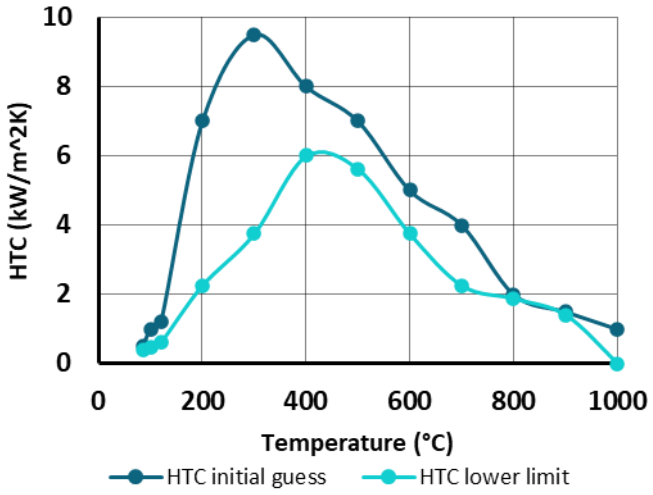

Figure 4.20: Initial guess and lower constraints for HTC determination using inverse HTC analysis.

The third method was implemented, and the results of the predicted inverse HTC analysis shown in Figure 4.22 for all quenching configurations, and the corresponding convergence curves are given in Figure 4.23 - Figure 4.26. The HTC curves determined for the horizontally quenched disc shows higher values than those of the vertically water quenched disc, suggesting that it experiences faster cooling. This could be because a larger surface area of the

disc comes into contact initially with the water than with the vertically water quenched disc. The convergence of the simulated cooling curves towards the experimentally determined curves for this quenching configuration, shown in Figure 4.23, demonstrate reasonable correlations. The correlation between the simulated and experimental cooling curve results is not as good as method 1, however, the shape of the HTC curve is more comparable to those seen in literature [123], so a compromise was sought with this method.

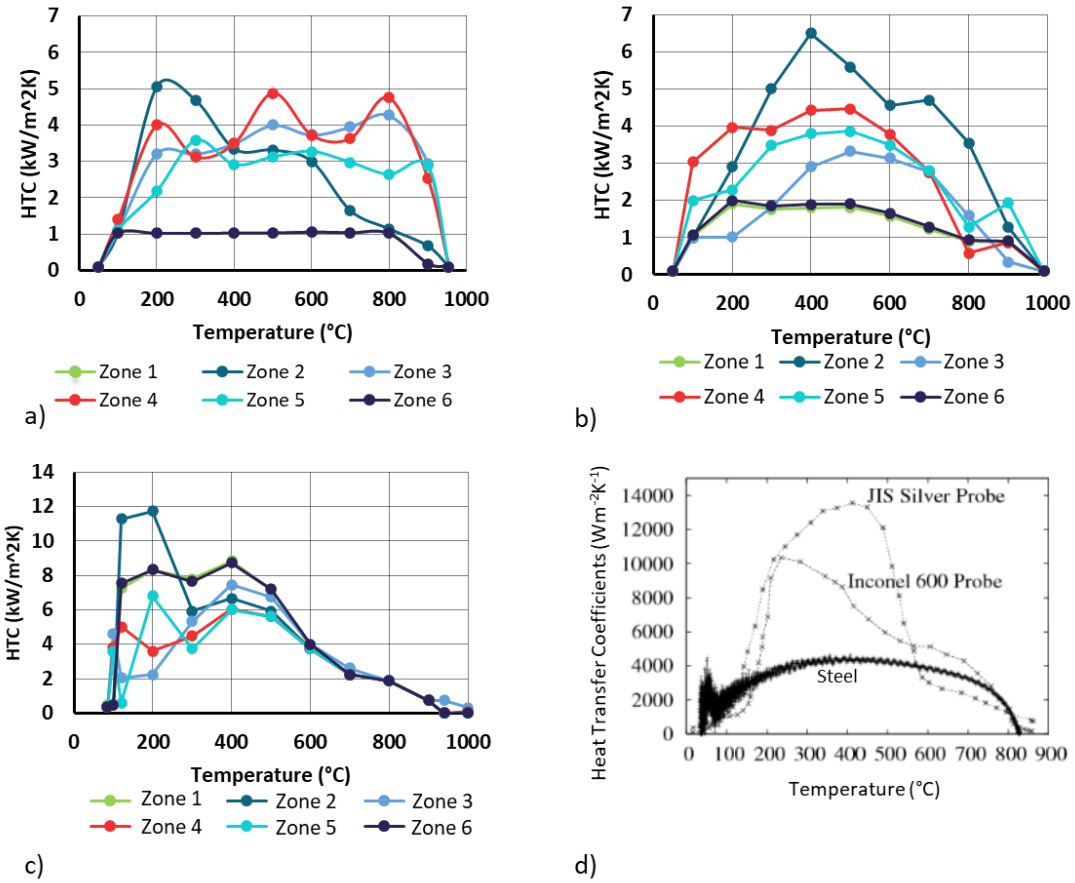

Figure 4.21: Evaluation of HTC for the horizontally water quenched disc at the six zones shown in Figure 4.17b. a) HTC values calculated as a function of time with no constraints, b) HTC values calculated as a function of temperature with no constraints, c) HTC values calculated as a function of temperature with constraints, and d) Initial guess for HTC determination using the third method, sourced from data for Steel, Inconel 600, and JIS Silver [123]. Note the different scale for HTC in c).

The vertically water quenched disc shows similar HTC values at the top and bottom section of the disc because the software has iteratively converged on HTC values which are equal to the lower bound constraint values set for the HTC determination. This can be seen in Figure 4.22b and c. The HTC values below 200 ˚C differ, but the values from 980 ˚C-200 ˚C are the same.

This has happened initially in the case of the horizontally water quenched disc too as seen in Figure 4.22a from 980°C to 600°C. The convergence of the simulated cooling curves towards the experimentally measured data for the vertically water quenching configuration, shown in Figure 4.24 and Figure 4.25, also show a reasonable correlation.

The HTC values of the air-cooled disc are comparatively small; however the shape of the HTC curve is similar to those shown in literature [123] so gives confidence in the results. The HTC values for the air-cooled disc had no constraints due to the low values. Overall the convergence of the experimentally measured and simulated cooling curves is reasonably good for method 3, and the shape of the HTC curves as well as the HTC values themselves seem comparable to literature [123], so this methodology was further explored for each of the water quenching configurations by performing a quenching simulation using a FE solver, the results of which are shown in section 4.3.6.

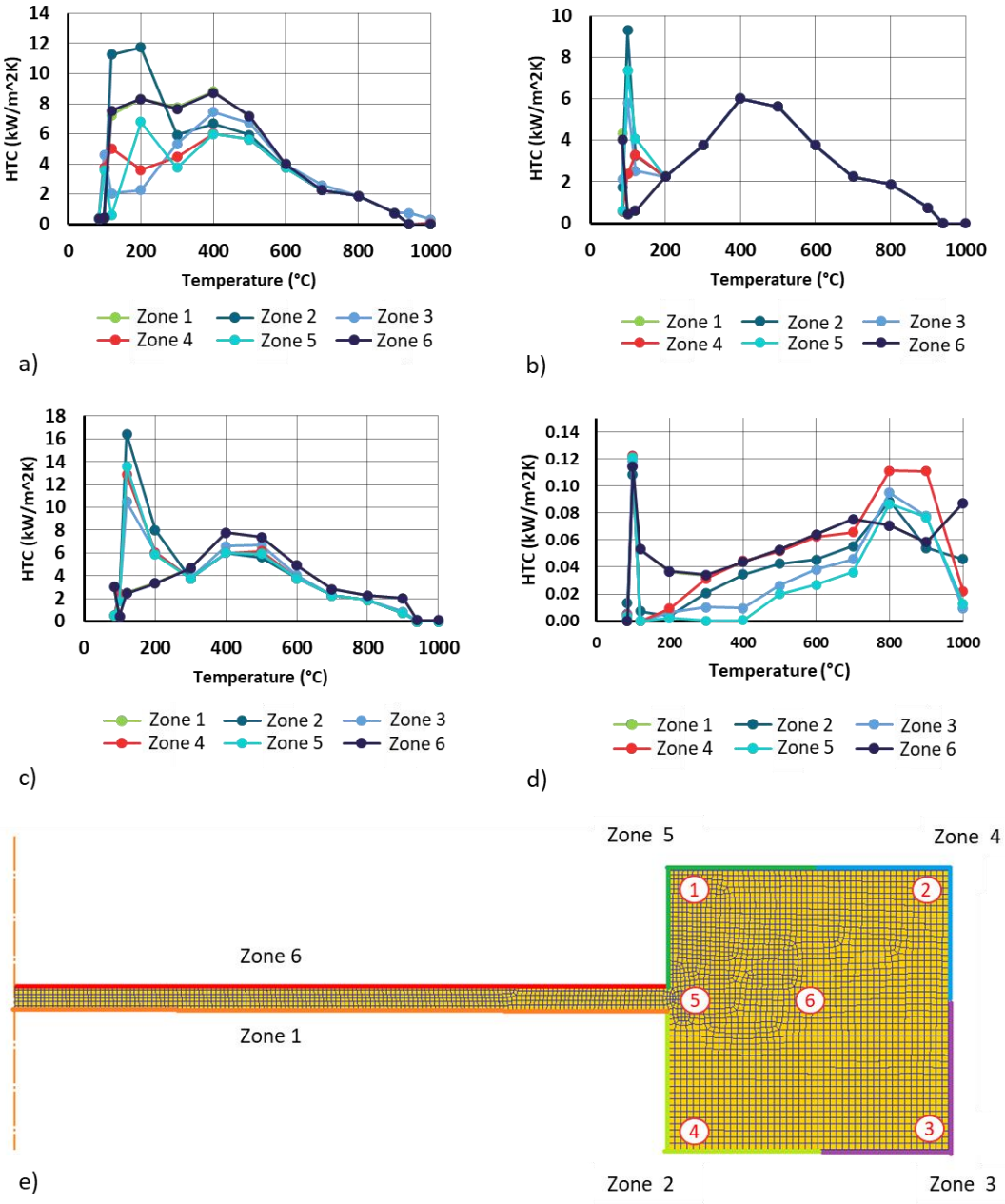

Figure 4.22: HTC values for a) horizontally water quenched disc, b) vertically water quenched disc at the top section, c) vertically water quenched disc at the bottom section, d) air-cooled disc, and e) HTC zones highlighted with different colours and assigned numbers for all quenching configurations. Note the different scale bars, especially for the air-cooled disc shown in d).

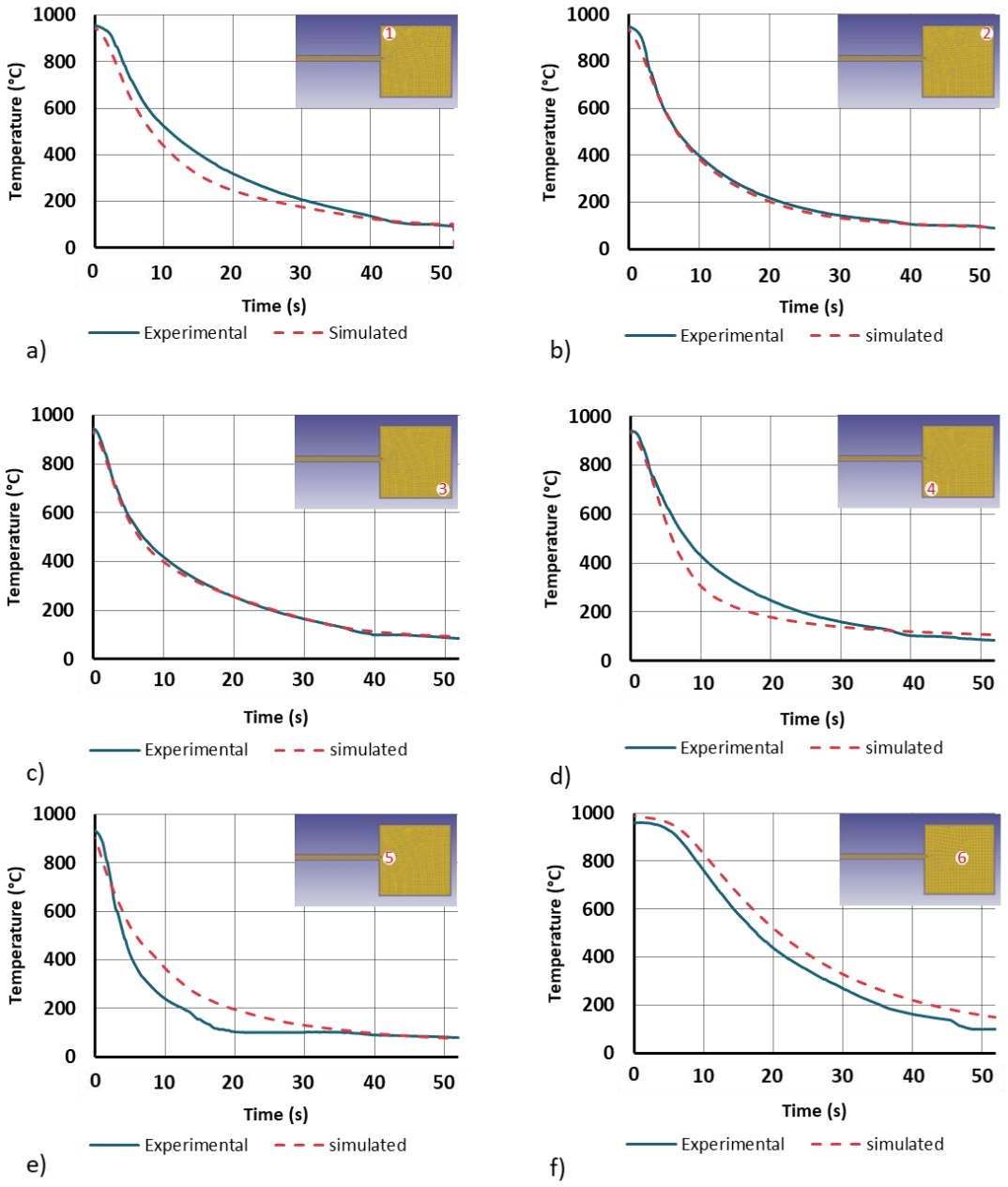

Figure 4.23: Comparison between the experimentally measured cooling curves and the simulated data for the horizontally water quenched disc showing the convergence of the predicted curve towards the measured curve at, a) location 1, b) location 2, c) location 3, d) location 4, e) location 5, and f) location 6.

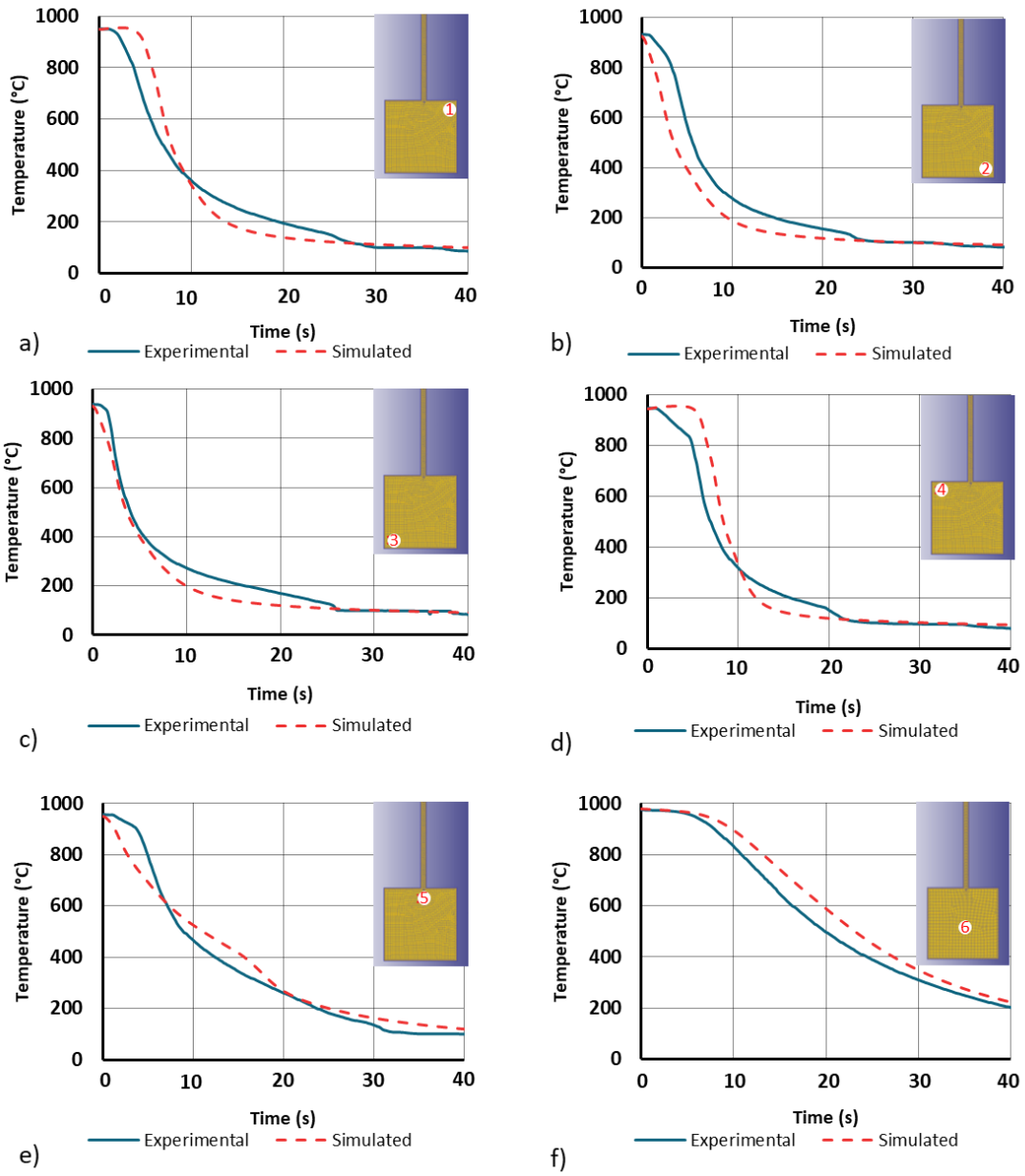

Figure 4.24: Comparison between the experimentally measured cooling curves and the simulated data for the vertically water quenched disc at the bottom section showing the convergence of the predicted curve towards the measured curve at, a) location 1, b) location 2, c) location 3, d) location 4, e) location 5, and f) location 6.

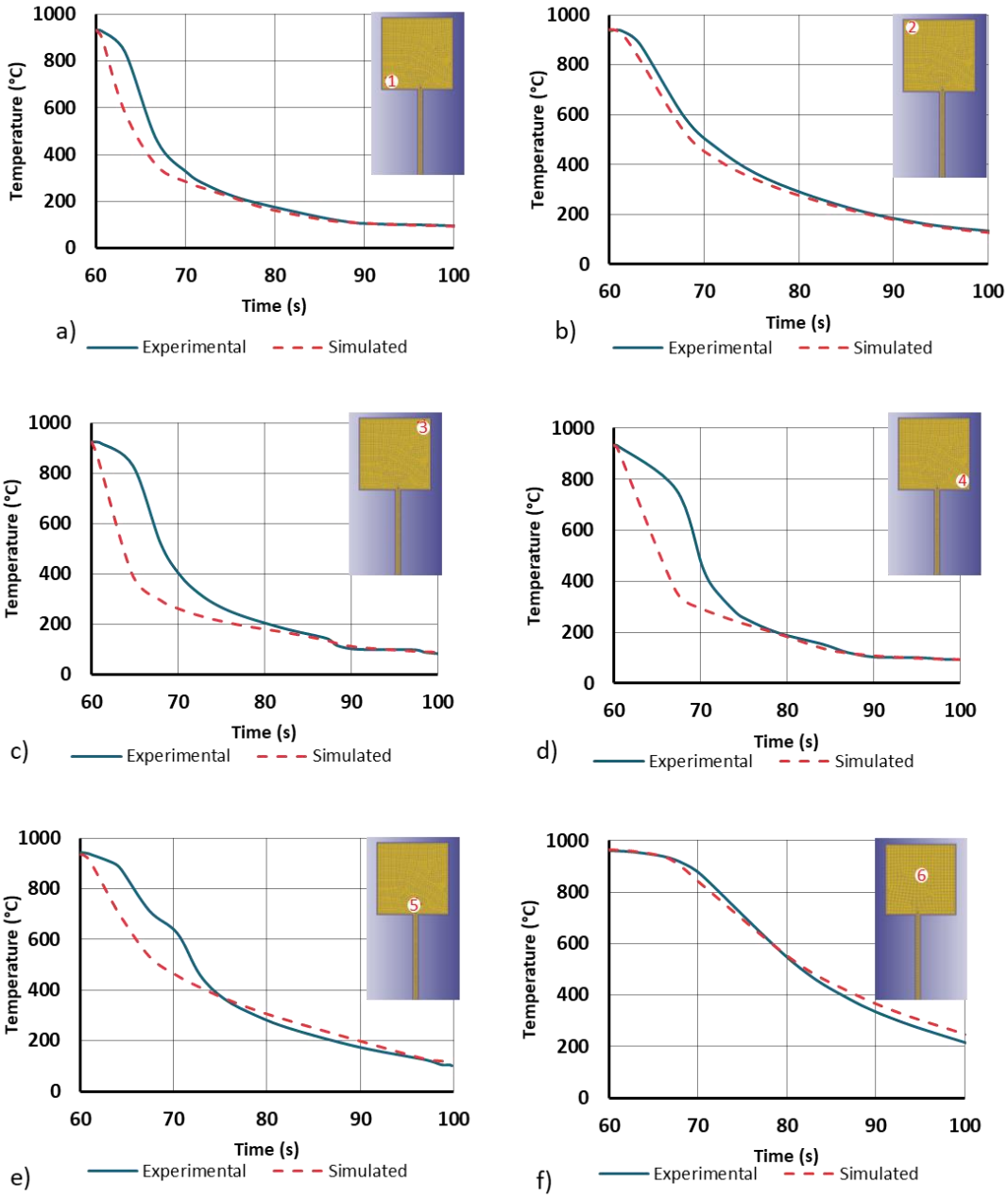

Figure 4.25: Comparison between the experimentally measured cooling curves and the simulated data for the vertically water quenched disc at the top section showing the convergence of the predicted curve towards the measured curve at, a) location 1, b) location 2, c) location 3, d) location 4, e) location 5, and f) location 6.

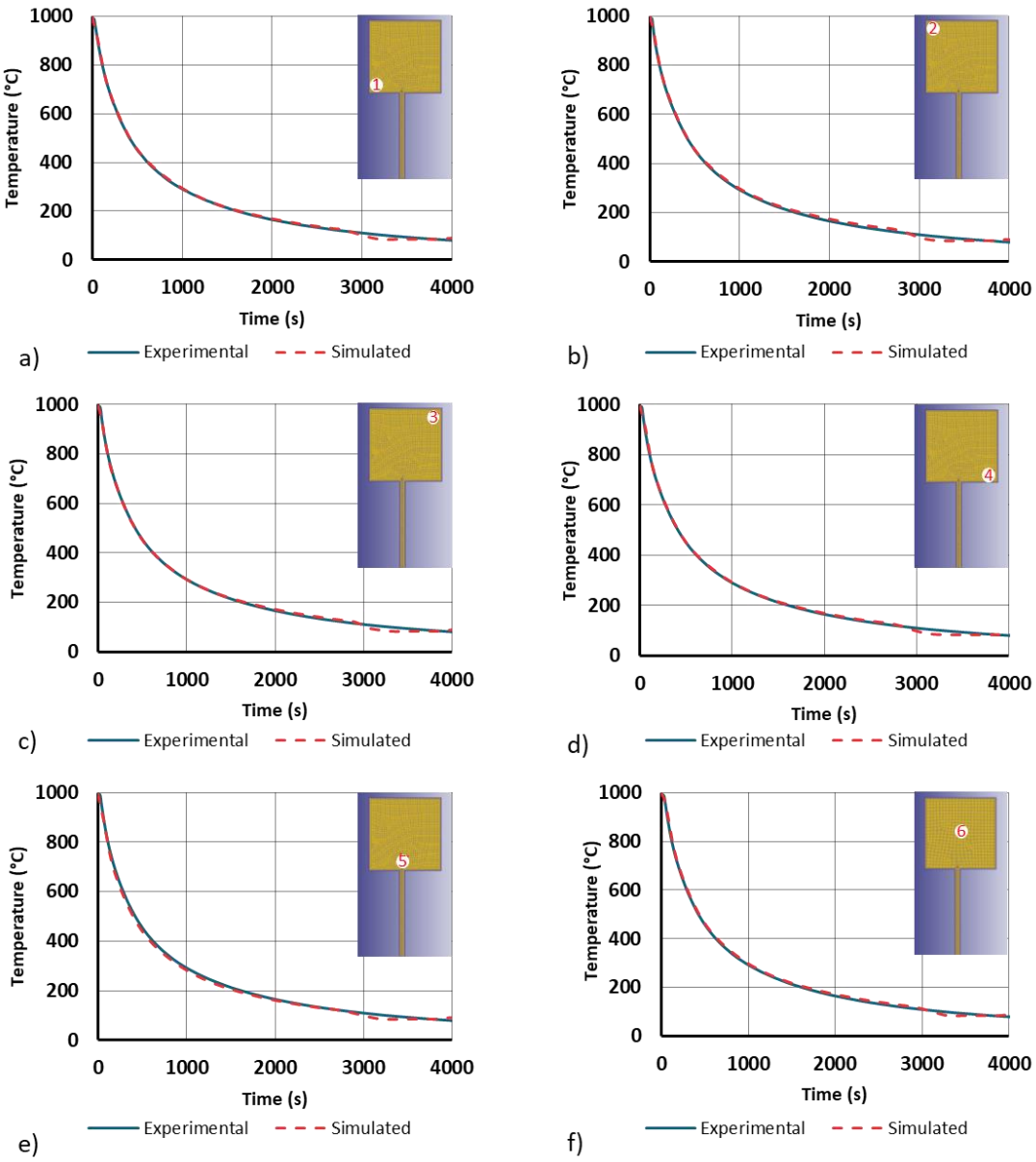

Figure 4.26: Comparison between the experimentally measured cooling curves and the simulated data for the air-cooled disc showing the convergence of the predicted curve towards the measured curve at, a) location 1, b) location 2, c) location 3, d) location 4, e) location 5, and f) location 6.

4.3.6 Residual Stress modelling and prediction

DEFORM software was used to carry out 2-D modelling of the horizontally and vertically water quenched discs as well as the air-cooled disc. Simple linear 2D quadrilateral elements were used in the simulations of the discs. The average size of the elements was 0.25 mm^2 as can be seen in Figure 4.27. The MUMPS solver was used alongside the Newton-Raphson iteration

method. The initial temperature of the discs was set to 980˚C to replicate the solution annealing temperature of the experiments. Corresponding HTC's calculated from the inverse HTC analysis were applied to the matching surfaces as boundary conditions to simulate the heat flux with the water. The heat flux and surface temperature are related by the assigned HTC's which determine the magnitude of the heat exchange with the environment [179], [180]. The same thermo-physical properties listed in Table 4.2, which were used for the inverse HTC analyses, were used for the residual stress prediction modelling.

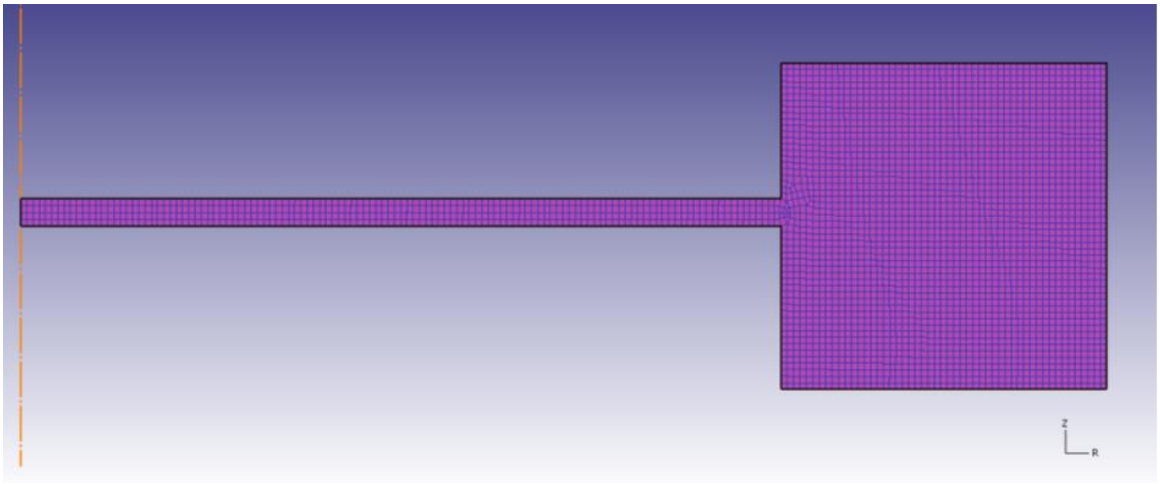

Figure 4.27: a) Illustration of the mesh density of the FE simulation set up for the scale-disc component for residual stress prediction.

Figure 4.28 compares experimentally measured residual stress using the contour method for the horizontally water-quenched disc with residual stress profiles determined from FE simulations using HTC values determined from methods 1, 2, and 3 outlined in section 4.3.5. Figure 4.28c and d display the out-of-plane residual stress distribution on two different scales: the first matches those of the experimental results for easy comparison, while the second provides a reduced scale to identify peak tensile and compressive stresses. This approach was applied to all three FE simulations. Figure 4.28c and d show an average match to the measured residual stress values in Figure 4.28a and b. The stress profile closely resembles that in Figure 4.28a, with two peak tensile stresses - one centred at the core of the rim section and another near the top-left corner of the rim, although the simulation exhibits slightly lower peak tensile values.

The results of the FE simulation using HTC values determined from method 2 are depicted in Figure 4.28e and f, revealing a weak correlation with the values obtained from the contour measurement method. There is no clear peak defined, and the tensile values are significantly lower than the experimental ones. Conversely, the FE simulation results obtained using HTC values from method 3, shown in Figure 4.28g and h, exhibit a strong correlation with the contour method results. Although the peak stress values are slightly lower by approximately 150MPa compared to the experimental measurements, the distribution closely matches the measured data shown in Figure 4.28b. The results presented in Figure 4.28 indicate that the third method for HTC determination yielded the most accurate prediction of residual stress. Consequently, this method was selected for predicting HTC values to be employed as input in the FE model for assessing the residual stress generated in both the vertically water-quenched discs.

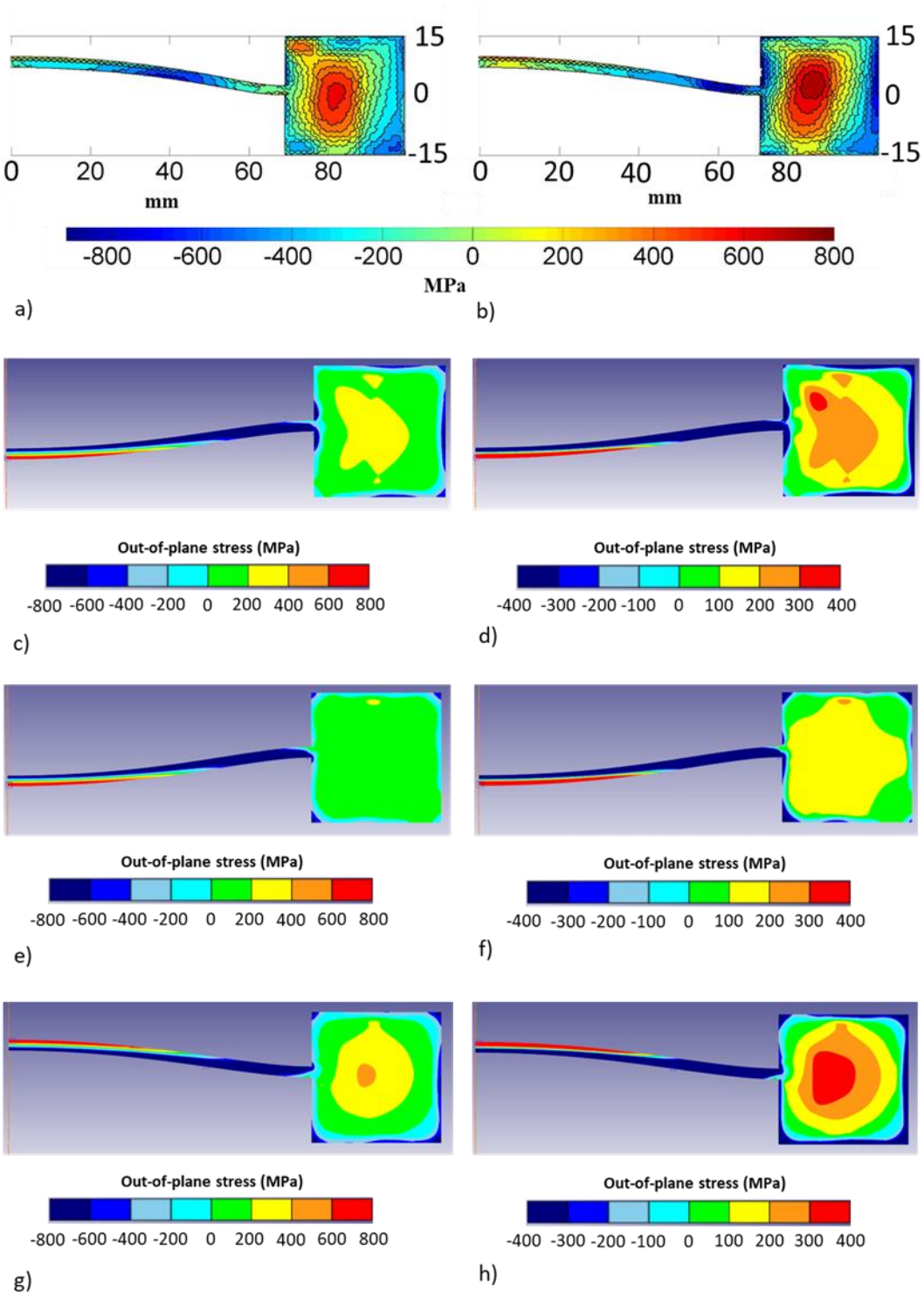

Figure 4.28: Results for the horizontally water-quenched disc. a) and b) Experimentally determined 2-D stress maps of the out-of-plane residual stress for either side of the disc shown in Figure 4.15, c) and d) out-of-plane residual stress profile calculated using HTC determination method 1, e) and f) out-of-plane residual stress profile calculated

using HTC determination method 2, and g) and h) out-of-plane residual stress profile calculated using HTC determination method 3.

Figure 4.29 shows the results of the simulation used to predict the residual stresses for the horizontal water quenching configuration. Figure 4.29e shows the maximum displacement of the part which is 5.88mm at the tip of the dome. When comparing this with the horizontally water quenched disc measured using the GOM-ATOS and shown in Figure 4.13b, the predicted 5.88mm displacement is an underestimation of the 7.0mm measured displacement, showing reasonable accuracy in the modelled displacement. Figure 4.29c and d both show the out-of-plane stress but with different scale bars. Figure 4.29c shows the range of stresses from -800 to 800 MPa. Large tensile stress is obtained near the middle of the rim section, which become increasingly more compressive nearer the edge of the rim. Because the full-range of stresses are being shown in Figure 4.29c, some key details, such as the location of the peak tensile stress in the rim, are missing. Reducing the range of stress displayed gives higher fidelity in the tensile region and as such the location of peak tensile stress can be better determined and the stress profile more thoroughly understood, as seen in Figure 4.29d. The transition zone from the rim to the web can be seen to have compressive stress which then become tensile stresses towards the upper-side of the dome. The overall stress profile is very similar to that measured using the contour method for the horizontally water quenched disc shown in Figure 4.29a . The magnitude of the stresses are also very similar however the absolute value of the peak tensile stress in the centre of the rim is lower in the simulation than in the measured values. The peak of the tensile stress near the centre of the rim section were modelled to be between 400 and 450MPa compared to the measured case of 400 to 550 MPa. Peak tensile stress was modelled near the mid-point of the dome section of the thin web to be 903MPa as opposed to the measured stress at ≈800MPa. The maximum modelled compressive stress is -1060MPa compared to the measured stress of -900MPa. Overall, there is reasonably good agreement between the modelled and measured stresses, as well as the modelled and measured dome deflection for the horizontally water quenched disc.

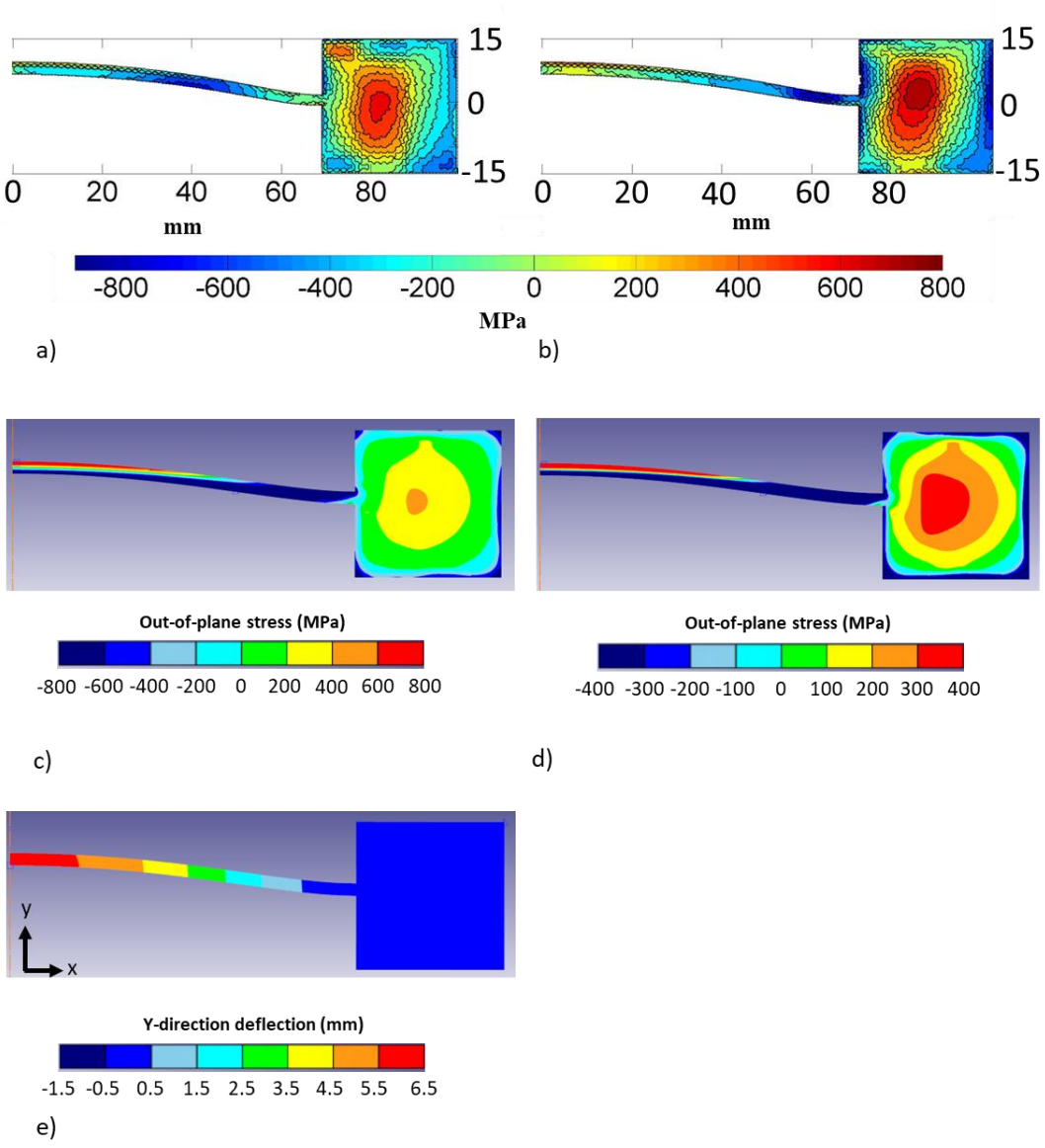

Figure 4.29: Results for the horizontally water-quenched disc. a) and b) Experimentally determined 2-D stress maps of the out-of-plane residual stress for both sides of the disc illustrated in Figure 4.15, c) Out-of-plane stress distribution across the entire stress range computed using the FE simulation, d) Out-of-plane stress distribution within the range of -400MPa – 400MPa computed using the FE simulation, and e) Displacement in the y-direction computed using the FE simulation.

For the vertically water quenched disc, one interesting observation is that in the case of the top section, the peak deflection is 5.79mm, whereas in the bottom section, the deflection is 6.69mm. The experimentally measured value was 6mm as shown in Figure 4.13a, meaning it lies between the two predicted values. The different cooling rates at the top and bottom sections of the disc could be responsible for the different deflection values. The top and

bottom sections were modelled individually as a 2-D axisymmetric model, meaning any interaction of stresses from the bottom section with the top section has not been considered. Perhaps this interaction would be enough to equalise the different deflection values to a value close to the measured 6mm. A way to test this theory would of course be to model this water quench in 3-D. Attempts were made at this, but due to long computation times and the complexity of the model set-up, a compromise of modelling in 2-D was made.

The predicted out-of-plane stress profiles of both the top and bottom sections of the vertically water quenched discs shown in Figure 4.30c and d and Figure 4.31c and d match up reasonably well with those measured via the contour method shown in Figure 4.30a and Figure 4.31a, respectively. There is however some large compressive stress in the transition area between the rim of the disc to the web section for the top part of the disc shown in Figure 4.30d which was not accurately predicted. The predicted peak tensile stress values near the centre of the rim are lower than those measured experimentally as was the case previously when comparing the predicted and experimental peak stress values for the horizontally water quenched disc at the same location. This appears to be a key attribute to the overarching methodology used for predicting these residual stresses. The peak tensile and compressive stresses near the mid-point of the domes (-1090MPa to 925MPa in case of the top section and -1200MPa to 939MPa in case of the bottom section) match up well with the experimental values (-1000MPa to 800MPa). A key observation is that the predicted peak tensile stress value is greater on the bottom section of the disc than the top section of the disc as seen in Figure 4.31d and Figure 4.30d, respectively, however for the experimental values, this is reversed as can be seen in Figure 4.30a and Figure 4.31a. This could be another artefact of not modelling the residual stress for the water quenched disc in 3-D.

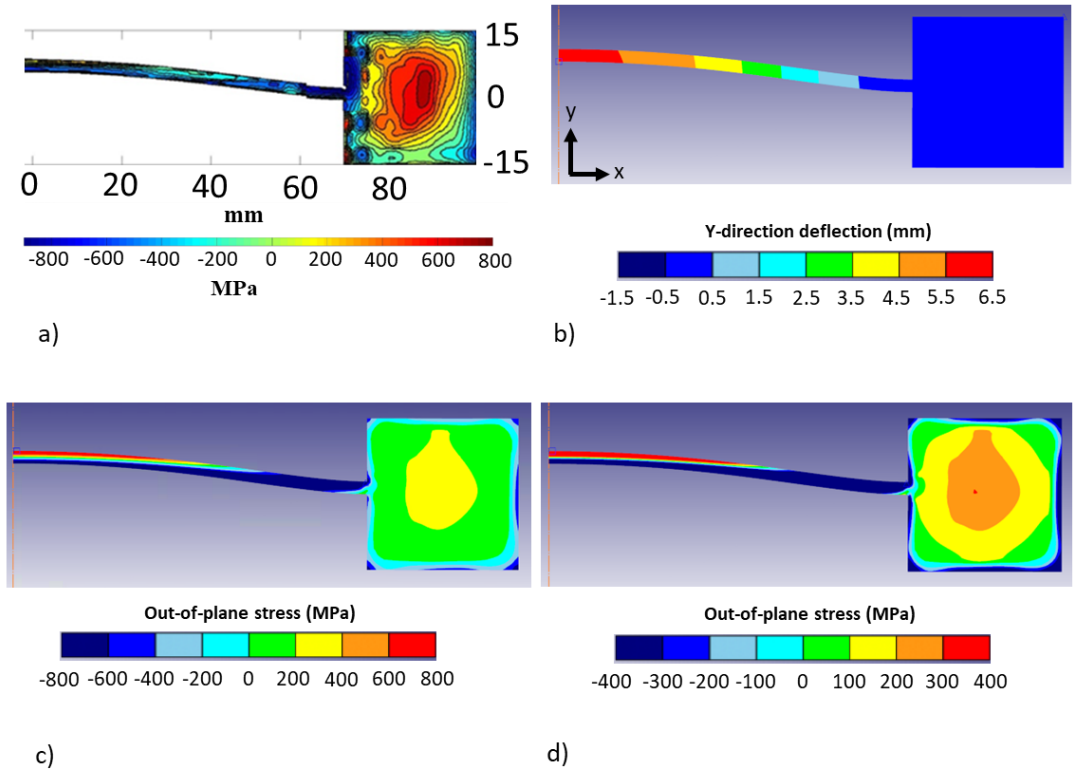

Figure 4.30: Results for the top section of the vertically water-quenched disc. a) Experimentally determined 2-D stress map of the out-of-plane residual stress, b) Displacement in the y-direction computed using the FE simulation, c) Out-of-plane stress distribution across the entire stress range computed using the FE simulation, and d) Out-of-plane stress distribution within the range of -400MPa – 400MPa computed using the FE simulation.

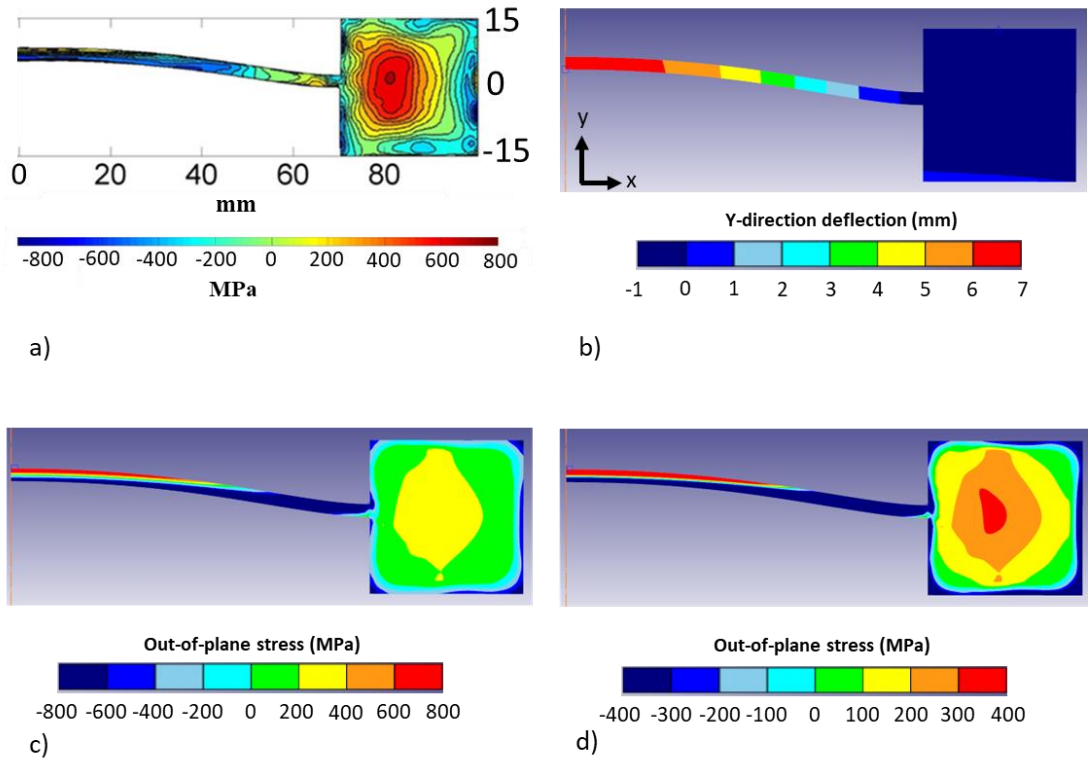

Figure 4.31: Results for the bottom section of the vertically water-quenched disc. a) Experimentally determined 2-D stress map of the out-of-plane residual stress, b) Displacement in the y-direction computed using the FE simulation, c) Out-of-plane stress distribution across the entire stress range computed using the FE simulation, and d) Out-of-plane stress distribution within the range of -400MPa – 400MPa computed using the FE simulation.

The predicted out-of-plane stress for the air-cooled disc is presented in Figure 4.32c and d. The stress profile in this instance matches up relatively well with the values measured via the contour method and shown in Figure 4.32a and b. The measured stress profile shows tensile stress at the outer edge of the rim, progressing towards compressive stress near the transition from the core to the web and continuing through the web. The predicted stresses are predominantly tensile and comparable to the values measured via the contour method. Lastly the amount of deflection predicted at the peak of the dome (0.91mm) and shown in Figure 4.32e was significantly lower than the measured value of 2.5mm. A possible explanation for the poor correlation between the simulated and experimentally determined stress profiles could be that during the inverse HTC analysis, the software may have converged on a mathematical solution which has poor physical significance.

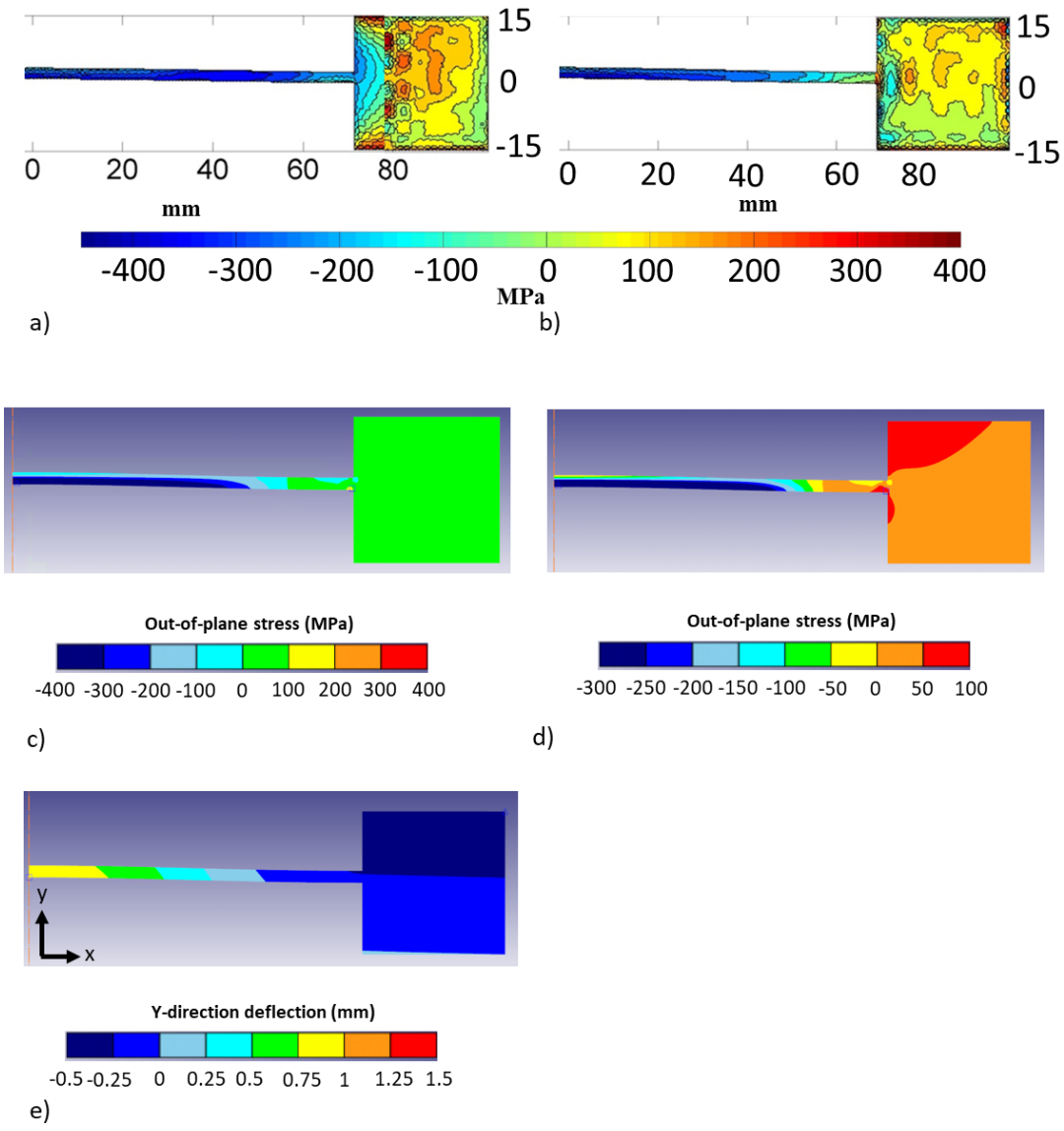

Figure 4.32: Results for the air-cooled disc. a) and b) Experimentally determined 2-D stress maps of the out-of-plane residual stress for both sides of the disc illustrated in Figure 4.16, c) Out-of-plane stress distribution across the entire stress range computed using the FE simulation, d) Out-of-plane stress distribution within the range of -600MPa – 100MPa computed using the FE simulation, and e) Displacement in the y-direction computed using the FE simulation.

4.4 Discussion

The solution annealing heat treatment at 980˚C for 1 hour had very little impact on the size and shape of the γ matrix, as desired. The purpose of this heat treatment was to simulate the close-die forging temperature which is often carried out at temperatures just below the δ phase solvus (1000 ˚C). The temperature of 980˚C was chosen so as to have minimal impact on

the microstructural features, such as grain size, which is also often chosen as the forging temperature. A slight increase in the average grain size was shown (≈0.9 µm increase) and a slight reduction in the volume fraction of δ phase present was also noted (3-5% decrease), but overall the microstructure was relatively unchanged. One important caveat to this is of course the γ'' precipitates which weren't shown in any if the images in Figure 4.9. Fast cooling like that associated with water quenching from above the γ'' solvus leads to precipitation of small γ'' which cannot be seen with an SEM nor detected using EBSD meaning there is a small unknown as to the size and volume fraction of these precipitates. These precipitates are known to cause the material to harden making further machining operations more difficult. Therefore, reducing the time spent within the temperature range for these precipitates is best for reducing the materials hardness. Fast cooling like that associated with water quenching will reduce the amount of precipitation hardening the material will undergo, however, it can have other undesired effects like residual stress being generated in the part which are just as equally if not more troublesome for further machining operations as this can lead to distortion in the part. Therefore, a compromise is often sought between cooling rate, annealing time and temperature, and ageing [181], [182] .

Cooling from the solution annealing temperature, with thermocouples installed, for the discs demonstrated that different areas of a part cool quicker than others, as shown clearly in Figure 4.23 to Figure 4.26. Not only this, but a comparison was made for the same thermocouple locations during different quenching configurations as can be seen in Figure 4.33. This showed that the quenching configuration plays an important role on the cooling of a part which will subsequently influence the residual stress profiles and stress magnitudes in the part. The cooling curves shown in Figure 4.23 to Figure 4.26 show that the outer edges of the disc cool quickest when water quenched. This means the outer shell cools first whilst the core of the rim remains hot. The core of the rim cools more slowly meaning a tensile stress is developed over time in that area. The web of the disc contracts very quickly and begins to deflect due to the nature of the quick cooling and high stresses developing. The results of the web must be interpreted carefully as the parts have stressed significantly beyond the yield point and an elastic model is used to calculate the residual stress. To prevent high cooling rates, increasing the temperature of the quenching media, in this case water, would decrease the temperature differential and therefore decrease the cooling rate as would changing to a different quenching medium such as oil or polymer. This can be advantageous for reducing the quench-

induced residual stress, but would influence the distribution of γ'', so a trade-off would have to be made.

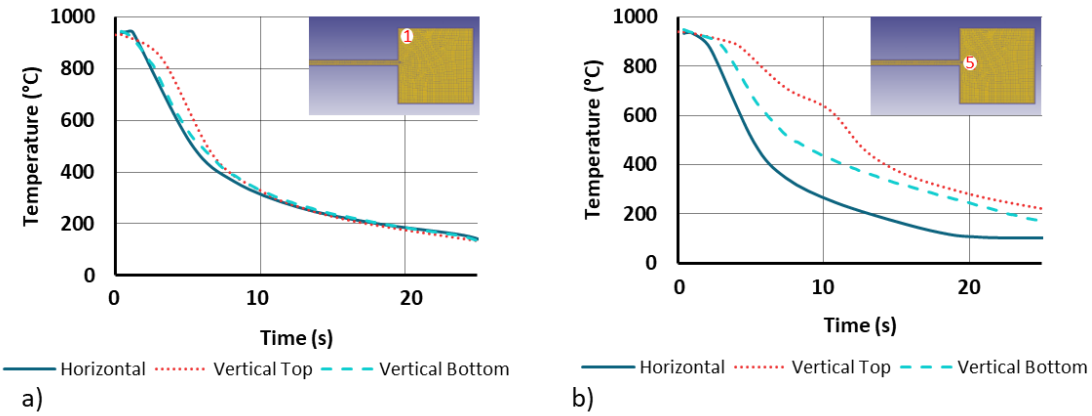

Figure 4.33: Comparison between cooling curves obtained for horizontal and vertically water quenched disc at a) thermocouple location 1 and, b) at thermocouple location 5. See Figure 4.17b for the thermocouple locations.

The distribution of the residual stresses measured for the horizontally and vertically water quenched discs are relatively similar. Tensile stresses develop in the centre of the core, gradually transitioning to compressive stresses near the edge. These stresses arise due to the thermal gradients within the core during water quenching. As quenching begins, the edge cools and contracts rapidly, while the centre remains warm, generating tensile forces in the core's interior. This explains the stress distribution shown in Figure 4.14b and Figure 4.15b. Comparison between Figure 4.14b and Figure 4.15b shows compressive stresses at the transition area between the rim and web of the part for the vertically water quenched disc, particularly at the top section of the disc, and significantly tensile stresses at the same area for the horizontally water quenched disc. It is difficult to understand the potential impact of these stresses in the out-of-plane direction on the distortion of the part, particularly in the thin web area, however they are noteworthy.

The increased deflection of the thin web in the horizontally water quenched disc when compared to the vertically water quenched disc, and the broadening of the deflection peak as shown in Figure 4.13b, indicates that the thin web of the disc experiences substantially different cooling rates which impact the residual stress generation and deflection of the part based on quenching configuration. This is not to say however that the horizontally water quenched disc necessarily experiences higher cooling in the thin web than the vertically water

quenched disc, just that the cooling rate of the rim, the transition zone between the rim and the web, and the coupling of the stress evolution at these areas all impact on the deflection of the thin web caused by the quenching configuration. The vertically water quenched disc shows a higher magnitude of tensile residual stresses at the core of the rim than the horizontally water quenched disc. The regions of tensile residual stress at the core of the rim are balanced with regions of compressive stress near the edge of the rim such that the stresses are in equilibrium.

It has been shown that the cooling rate from above the γ’ and γ’’ solvus can affect the size and morphology of the precipitates, with quicker cooling rates resulting in smaller tertiary precipitates, and slower cooling rates resulting in larger secondary precipitates. Furthermore, it has been shown that if the cooling rate is sufficiently high enough, it is possible to completely suppress the precipitation of these phases [183]. At the cooling rates shown in Figure 4.34, tertiary γ’ and γ’’ precipitates will have nucleated and grown meaning there will be an increase in hardness.

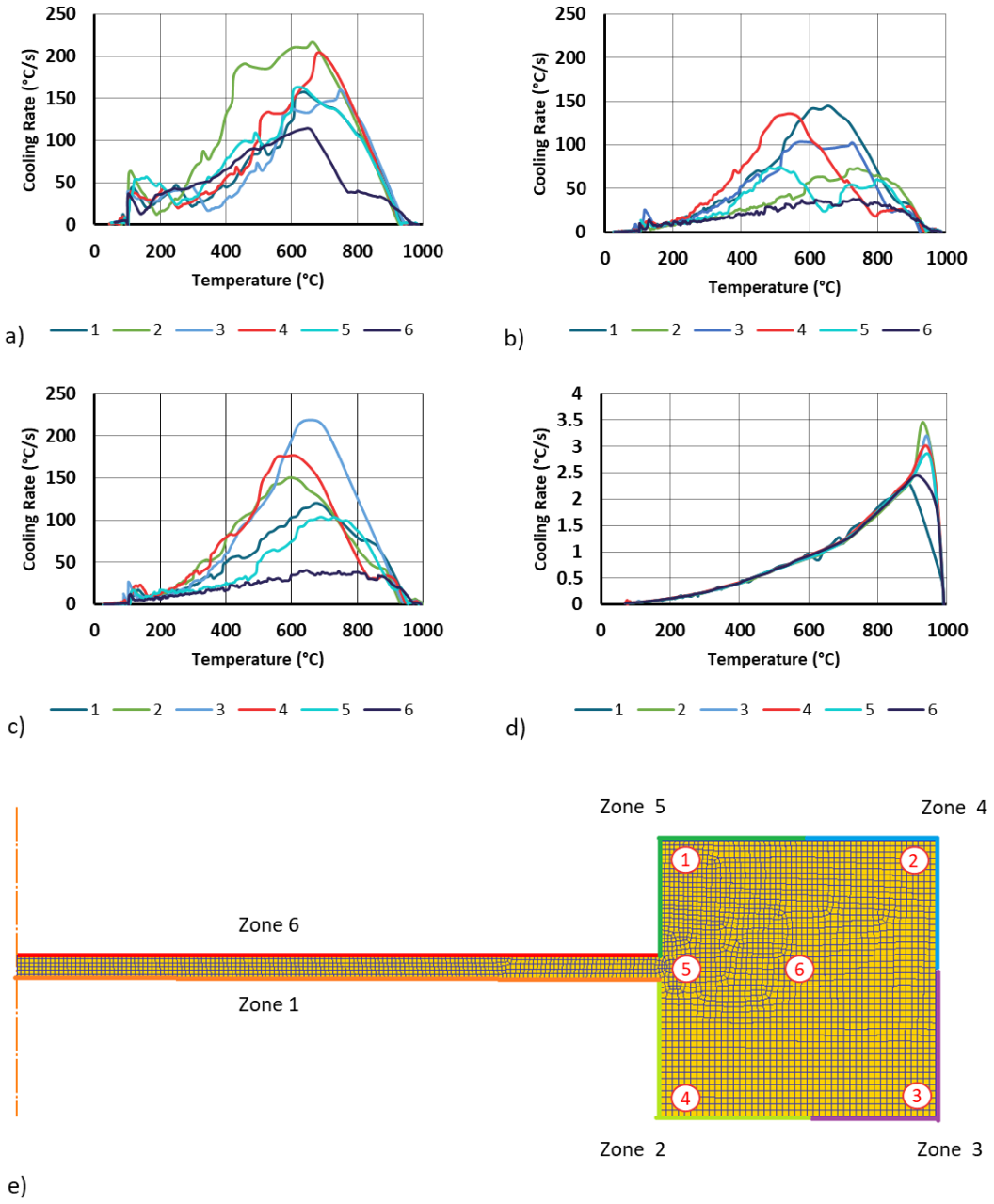

Figure 4.34: Cooling rates at thermocouple locations 1 to 6 of a) horizontally water quenched disc, b) vertically water quenched disc at the top section, c) vertically water quenched disc at the bottom section, d) air-cooled disc, and e) thermocouple locations.

The inverse HTC model went through several iterations before a suitable methodology was found. The first attempt involved solving the inverse analysis for HTC values as a function of time. This approach offered the advantages of maximising the number of control points and in turn gave the best convergence against the experimental cooling curves as shown in Figure

4.18b and c. A consistent issue appeared at this stage of the inverse HTC analysis. Thermocouple 5 was consistently not cooling quick enough, but the neighbouring thermocouples 1 and 4 were cooling too quick. The inverse HTC analysis was trying to balance these competing thermocouples and this was the case for all water quenched discs. This can be seen in Figure 4.23 to Figure 4.25. The reason this is thought to take place, is because the HTC values of the thin web are not being predicted correctly. Unfortunately, the only way to accurately determine those HTC values is to imbed a thermocouple in the web, which is impossible because of it being very thin. The residual stress was modelled by implementing the HTCs obtained via method 1 (see section 4.3.5), and it was seen that the model failed to predict the correct direction of deflection for the thin web which impacted the residual stress generation throughout the part, creating the underestimation of the predicted stress distribution, so this method was ruled out. The second method (see section 4.3.5) calculated the HTC's as a function of temperature and underwent several iterations. The results obtained from method 2 are shown in Figure 4.19. Similar to method 1, there is reasonable correlation between the measured and predicted cooling curves, the HTC values look plausible, but the thin web deflects in the wrong direction and negatively impacts the residual stress profile so was ruled out as a valid methodology. The process for determining the HTC values for a given set of cooling curves was itself iterative and was found to heavily rely on the initial seed value as a first guess. Initial values of 1 were entered for method 1 as laid out previously. A seed value of 3 and 5 was tested to see the impact on the results. Different seed values gave slightly different HTC values but the same incorrect deflecting direction and importantly the incorrect stress distribution were predicted. This showed that there were multiple mathematical solutions to the inverse HTC problem for the given set of cooling curves, but none of them where physically correct.

A third methodology was attempted which calculated the HTC using the inverse method as a function of temperature but instead of having a single constant seed value of 1, a range of seed values where input as a function of temperature for each HTC zone as shown in Figure 4.20. The initial values selected were from literature for a different alloy, however the shape of the curve is common for metallic alloys being water quenched. The main stages of quenching are shown graphically in Figure 4.35. It is important to note that the nucleate boiling stage happens after the point at which maximum cooling occurs. The point at which the maximum HTC value occurs is near the middle of the nucleate boiling point as shown in Figure 4.36.

Therefore, for the cooling curves obtained from water quenching of the discs, peak HTC values should be reached at ≈400˚C or thereafter as was generally the case. From Figure 4.22 it can be seen that there is sometimes a spike near 150°C which is when the disc is cooling by convection as per Figure 4.35 and Figure 4.36. This is thought to be because the HTC curves are constrained at the minimum permissible values up to ≈400˚C and as such the simulation is not able to match the exact rate of cooling from 980°C to 400°C. Below 400°C the HTC values must be increased beyond the minimum values and because the simulation up to the point of 400°C has not matched the cooling rate, over-compensates with HTC values which are higher than they should be at this stage. The Leidenfrost point and transition boiling are shown in Figure 4.35. The Leidenfrost point is where the vapour blanket becomes stable and transition boiling is the regime where the vapour blanket begins to break down and the quenchant media periodically comes into contact with the surface of the part.

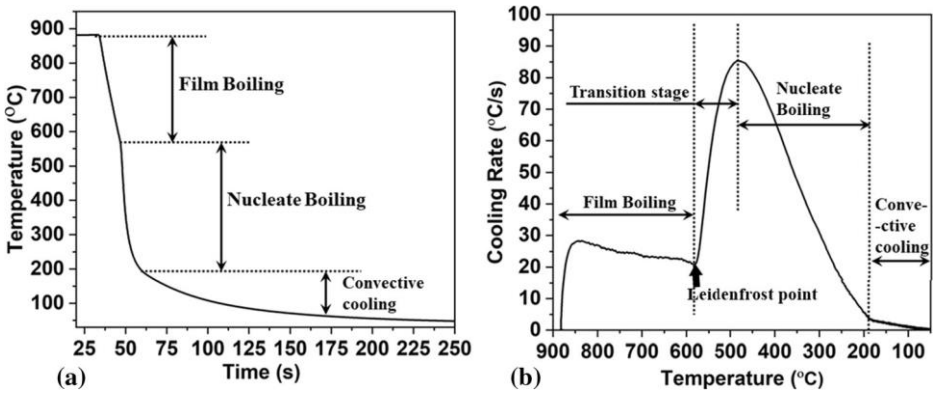

Figure 4.35: a) Example cooling curve showing the three stages of water quenching, and b) cooling rate as a function of temperature also showing the three main stages of quenching as well as the transition stage [184].

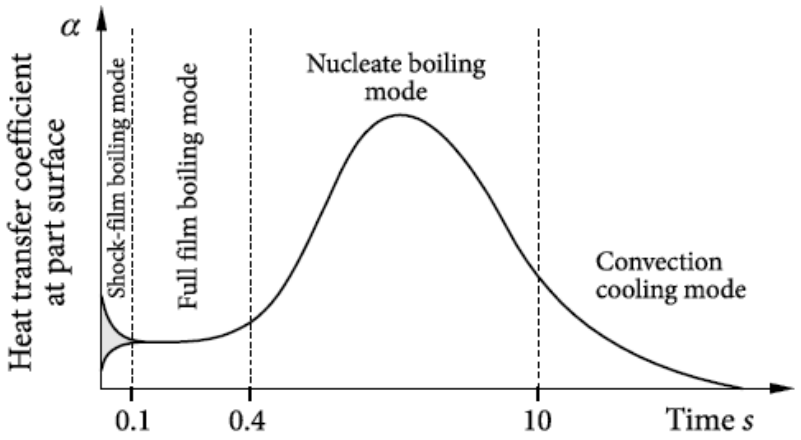

Figure 4.36: Example of HTC curve as a function of time detailing where the peak of a HTC curve from water quenching occurs in relation to the three stages of water quenching [178].

For the third methodology (see section 4.3.5), lower bound constraints were calculated at each temperature as 75% of the initial seed values. The thought behind no upper bound constraints being used was to allow the model freedom to compensate as much as necessary for the lower bound constraint. The idea of using the initial values from literature and setting some constraints, was to try and find a physically meaningful and mathematical solution to the inverse HTC problem for the experimentally obtained cooling curves. The HTC curves shown in Figure 4.22 show that the lower bound constraints have been reached and selected as the optimum solution. This means the software would most likely have chosen lower values if the lower bound constraint values were lower still, however in that instance, may have meant a mathematical solution was obtained, and not a physically meaningful solution as was the case for methodologies 1 and 2. This approach meant that the convergence of the experimentally calculated cooling curves with the predicted values obtained from the software were not as good as the first methodology, but were viewed as a necessary trade-off. The thermocouple locations used to obtain the cooling curves were placed at the corners, near the thin web, and at the centre of the rim. Thermocouples were placed at the corners to try and understand the complex coupled nature of cooling from two different faces in a bid to increase accuracy. Instead, it meant that the HTC zones which were initially designed to relate to one face, were adapted to include two faces for the rim area of the disc. As previously mentioned this was to allow one thermocouple to relate to one HTC zone and in a bid to increase accuracy, but instead likely decreased the accuracy. The coupling of the different cooling rates on each face was captured by the thermocouple, but the subsequent calculated HTC is likely not

representative of the HTC at either end of the zone. In future, it is recommended installing thermocouples on the face of an edge and not at a corner.

The residual stress predictions using the calculated HTC's showed reasonable accuracy in a number of areas. Firstly, the direction of deflection for the thin web was predicted correctly in all instances. Secondly, the magnitude of deflection was predicted reasonably well in the case of the water quenched discs, but less so in case of the air-cooled disc. A percentage prediction error of 16% was calculated for the case of the horizontal disc, a 3.5% and 11.15% percentage prediction error were calculated for the vertically water quenched disc at the top and bottom sections, respectively, and a 63.76% percentage prediction error was determined for the case of the air-cooled disc. It is important to bear in mind that the total deflection of the air-cooled disc was substantially less than the water-cooled disc. A summary of the measured and simulated deflections of the thin web are given in Table 4.3. Note the percentage prediction error was calculated as shown in Equation 4.3.

$$Percentage\ prediction\ error = \frac{(measured\ value - predicted\ value)}{measured\ value} x100$$

Equation 4.3

Table 4.3: Summary table of measured and simulated deflection with percentage prediction error for each disc.

	Measured deflection (mm)	**Simulated deflection (mm)**	**Percentage prediction error (%)**
Horizontally water quenched disc	7	5.88	16
Vertically water quenched disc (top section)	6	5.79	3.5
Vertically water quenched disc (bottom section)	6	6.669	11.15
Vertically air-cooled disc	2.5	0.906	63.76

As was shown in Figure 4.29 to Figure 4.31, the residual stress profile of each of the water quenched discs matched up nicely with the contour measurement results shown in Figure 4.14b and Figure 4.15b. As mentioned previously in Section 4.3.6, from the contour

measurement results, the top section of the vertically water quenched disc demonstrates higher tensile and compressive stresses than the bottom section indicating it was cooled quicker. This is thought to be because the vapour blanket was possibly removed by the bubbles generated from the nucleate boiling which occurred in the bottom half of the disc due to agitation caused during submergence. The residual stress prediction model however predicts that the bottom section of the water quenched disc actually has higher levels of compressive and tensile stresses present at the rim section. In all cases, the magnitude of the predicted peak tensile stresses at the centre of the rim were between 90MPa and 200MPa less than those measured by the contour method, and the compressive stresses surrounding this and at the thin web, were about 200MPa more at peak areas than what was measured. This begins to show the limitations of the residual stress predictions, with the model possibly having a tendency towards the compressive stresses and less able to accurately determine the tensile stresses. Another possible reason for this is of course that the HTC values calculated weren't as accurate as was necessary to correctly determine the residual stress magnitudes. Again, this could be argued to be a limitation of the software though and the experimental method used for obtaining cooling curves and the subsequent HTC values. In general, the residual stress profiles are similar and the magnitudes whilst in some areas are slight over/under-estimations, are generally acceptable.

4.5 Conclusions

Temperature induced residual stresses in five scaled discs which were either water quenched or air-cooled from 980˚C were investigated with the goal of determining the influence of quenching configuration and quenchant media on the generated residual stress profile. Calculating the HTC values, using inverse analysis, from the cooling curves obtained from two of the five discs, then using these HTC values to model the residual stresses and comparing them with measured residual stresses determined using the contour method on the remaining three discs, lead to the following conclusions.

- Quenching configuration has been shown to play a significant role in the stress generation in water quenched discs. Firstly, a horizontally water quenched disc has more deflection in thin web areas than the same part quenched vertically. The reason for this is due to the different residual stress profile generated through heterogenous cooling at different locations in the part when being water quenched.

- The vertically water quenched disc shows higher tensile stress in the core of the rim sections, suggesting these sections cool quicker for the vertically water quenched disc than for the horizontally water quenched disc.
- The magnitude of the out-of-plane residual stresses are higher in the vertically water quenched disc, particularly at the top section of the disc compared to the bottom, potentially because of the vapour blanket being disrupted by the bubbles from the nucleate boiling of the bottom section of the disc.
- The impact of quenching media is significant on the residual stress profile and magnitude of stresses. Air-cooling produces a more homogenous stress profile throughout the part and significantly less deflection in thin web areas compared to parts quenched in water.
- The inverse HTC calculation was discovered to be sensitive to initial (seed) values. Seed values for HTC were input as a function of temperature with lower bound constraints to get best results.
- A combined approach of finding a mathematically correct and physically viable solution was taken which successfully converged and proved to be the best method.
- The locations of the thermocouples near the corner proved not to be optimal, and instead it is recommended placing a thermocouple along an edge in future.
- In future developing a method of measuring the cooling rate of thin webs being water quenched would substantially increase the accuracy of results.
- Modelling the vertically water quenched disc in 3D would undoubtedly increase the accuracy of the model.
- The residual stress profiles where well predicted, and the magnitude of the stresses were also reasonably predicted for the water quenched and air-cooled discs.
- The deflection predicted at the thin web was reasonably well predicted in case of the water quenched discs, but less so in the case of the air-cooled disc.

The methodology developed in this chapter for determining HTC values, although applied to IN718, will later be utilised in Chapter 8 for the development of a multi-step, multi-process

model simulating the forging behaviour of AD730. The HTC values determined during air-cooling will be employed for this purpose. Further discussion on this will be provided in Chapter 8.

5

Optimisation of Sample Geometry for Thermo-Mechanical Testing of Ni-based Superalloys Using ETMT

5.1 Introduction

The next step to be investigated in the thermo-mechanical processing of IN718, is the ageing step as illustrated in Figure 5.1.

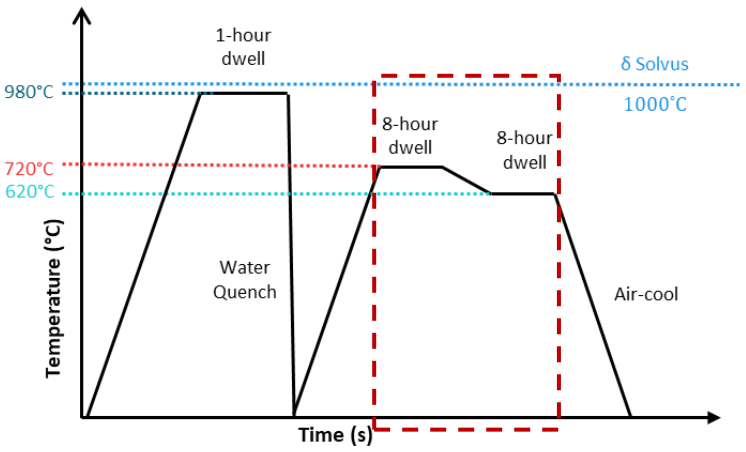

Figure 5.1: Thermo-mechanical processing route of IN718, emphasising the ageing stage which is further explored in this chapter.

It has been shown in the literature review of this thesis that the mechanical properties of materials vary with temperature and as such, mechanical testing at elevated temperatures is often required to gain a clearer understanding of materials behaviour. Conventional testing rigs typically equipped with convection and/or induction furnaces for heating the test piece to the target temperature, are often used as the means for testing materials thermo-mechanical behaviours. The time taken for these furnaces to reach and stabilise at the test temperature vary depending on the target temperature, the size of the specimen, as well as the type of furnace used. This is usually no quicker than 20 minutes for testing medium scale samples [89]. Within this period, before the commencement of the mechanical test and whilst the sample is reaching the target temperature and stabilising, there are often microstructural changes taking place which affect the mechanical properties and are not captured in the test results. This is because the sample is in such a dynamic state whilst heating for a prolonged period of time. The inability of the conventional test rigs in capturing these microstructural changes which take place during heat-up, and the long heat-up time itself, are of course disadvantages. However, these are not the only challenges, for instance adhering to ASTM standards E8/E8M-21 [185] and E21-20 [186], which require fairly large sized samples used for tensile testing, can be disadvantageous for manufacturing samples from costly materials such as aerospace grades nickel-based superalloys and titanium alloys. Furthermore, if the sample is to be manufactured from a part, as is often the case, and the part is small or complicated, it can be impossible to cut out a full-sized specimen. Undoubtedly, such challenges lead to prolonged experimental approaches using alternative methods to optimise forging conditions and to certify materials for service conditions.

To combat some of these challenges, the National Physical Laboratory (NPL), in conjunction with Instron, developed the Electrical-Thermal Mechanical Testing (ETMT) system capable of performing tests to assess both the thermo-mechanical and the thermo-physical properties of materials [187]. One of the major advantages of the ETMT system is its swift heating that is based on a material's electrical resistivity. It maintains temperature control through the use of water-cooled grips at the top and bottom of a sample. Despite its advantages in heating up samples to the target temperature at very fast rates, as well as the capability of very fast cooling rates, the very physical nature of the assembly (i.e., cooling grips) leads to a parabolic distribution of temperature along the length of the sample with the hottest part being in the middle of the gauge length [188], [189]. This leads to two distinct challenges. Firstly, this non-

uniform distribution of temperature leads to a heterogeneous deformation (i.e., strain) along the gauge length due to the dependency of materials mechanical properties on temperature and the development of an effective gauge length, which makes the direct measurement of these properties complicated. The effective gauge length is a shorter region within the gauge length of a sample where the peak of the parabolic temperature distribution normally causes all of the strain to localise [187]. This can be seen in Figure 5.2a. Linear engineering strain (ε) is defined as,

$$\varepsilon = \frac{\Delta L}{L_0}$$

Equation 5.1

where ΔL is the change in length of a sample and L_0 is the initial gauge length, in this case meaning the effective gauge length. Figure 5.2b shows three example stress-strain curves which all derive from the same data (meaning the crosshead displacement [ΔL] is the same in all tests) but with different effective gauge lengths selected. Selecting a smaller effective gauge length (L_0) than appropriate will have the effect of increasing the engineering strain which will subsequently make the material appear to have a lower stiffness and a greater elongation. Equally selecting an unduly large effective gauge length will have the opposite effect and critically can lead to the appearance of premature failure in the material. If the strain value is calculated over a gauge length of 6mm, but the effective gauge length is actually 2mm, then the localised strain magnitude at the effective gauge length is far higher than the calculated value meaning it will appear to fail sooner. It can therefore be seen that an accurate determination of the effective gauge length is crucial for determining the materials mechanical properties. The NPL good practice guide recommends determining this effective gauge length using FE methods or by experimentation. Both of these methods have significant challenges. A FE approach requires a material model which may not be available, and performing several exploratory tests to determine the effective gauge length experimentally can be time consuming and costly, especially if the material being investigated itself is expensive, as is

often the case for tests carried out with the ETMT.

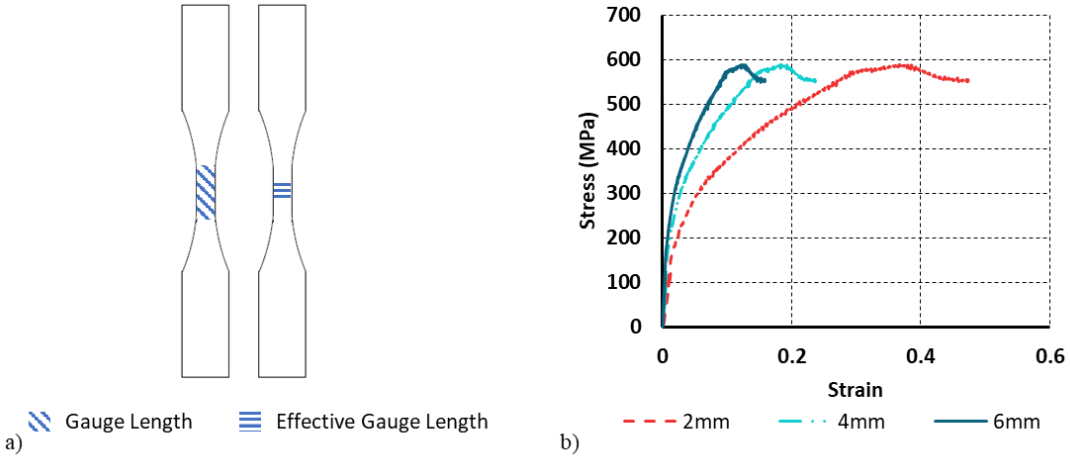

Figure 5.2: a) Dog-bone sample showing the difference between the gauge length and the effective gauge length, and b) example stress-strain curves showing the impact of 3 different effective gauge lengths of 2mm, 4mm, and 6mm.

The second distinct challenge created by the parabolic temperature distribution, relates to the class of material being tested. For most materials, the hottest region typically becomes the weakest and undergoes deformation under comparatively lower loads. This is however not the case for precipitation hardenable materials such as different grades of nickel-based superalloys for aerospace applications (e.g., turbine discs), where the hottest part of the specimen can become the strongest depending on temperature [89]. This can lead to a drift in plastic deformation away from the hot mid-gauge section of the sample, where the temperature is known, out towards the end of the gauge length where the temperature is significantly lower and unknown. It is possible to estimate the temperature at the outer gauge length by using numerical approaches, but this often leads to erroneous results [190]. In this instance, if the crosshead displacement is used as the basis for the evaluation of strain, then the determination of the material's mechanical properties, and the level of plastic deformation becomes compromised as the displacement is coming from regions at the edge of the gauge length where the temperature is unknown, and not in the middle of the gauge length where the temperature is recorded. This very phenomenon is mentioned in the NPL good practice guide [187], especially for precipitation hardened nickel-based superalloys over a temperature range (i.e., ageing temperatures) where different strengthening particles are stable [34], [89], [191].

A recent study [192] has attempted to address this issue by using DIC to measure the displacement map, in-situ, from which the strain has then been evaluated. However, this study has only used a scaled-down sample geometry on a single crystal that may not be applicable to all nickel-based superalloys. In the present study, the existing sample geometry recommended by NPL's good practice guide [187], and also a number of other geometries, including both modified and adopted from previous reports[187], [192], [193], have been tested with an ETMT, in-situ, using DIC to track the spread of deformations, to find a geometry most suitable to satisfy three critical conditions. Firstly, the deformation (and hence strain) must be centred at the middle of the gauge length with no measurable drift. This will give confidence that the plastic strain and mechanical properties are for the recorded temperature and not an unknown, cooler temperature closer to the grips. Secondly, the size of the effective gauge length must be known, preferably prior to test commencement. This means there would be homogenous deformation across the effective gauge length allowing for a far easier determination of the materials plastic strain and mechanical properties. Thirdly and finally, the temperature distribution across the effective gauge length must be within 1% of the recorded temperature at the centre of the sample. ASTM E21-20 states that the temperature must not exceed ±3˚C for test temperatures of 1000˚C and ±6˚C for test temperatures above 1000˚C when heated with a convection furnace. The parabolic temperature distribution present in the case of the ETMT makes these limits very challenging, so a more achievable target of 1% of the recorded temperature at the centre of the sample was selected. Only when all three of these criteria are satisfied will a geometry be classed as suitable. These tests are conducted on IN718, a Ni-based superalloy, over a range of temperatures that are used in industry for forging process and subsequent ageing heat treatments. A thermal imaging camera was used on the sample which satisfied the above criteria best, as well as on the rectangular geometry recommended in the NPL's good practice guide [5], to investigate the temperature distributions. Finally, a set of interrupted mechanical tests were carried out using the best performing sample geometry for the determination of mechanical properties to compare with existing data on IN718 in literature.

5.2 Methodology

5.2.1 Material and Samples

All test samples were manufactured from a 2000 mm × 250 mm diameter billet of IN718 nickel-based superalloy in the as-aged condition, supplied by Aubert & Duval (A&D). The nominal chemical composition for this material, supplied by the manufacturer, is provided in Table 5.1. Specimens were cut out using an electrical discharge machine (EDM) and tested in the as-received condition. All samples were cut in the same direction to avoid any potential impact of mechanical anisotropy on the test results.

Table 5.1: Nominal chemical composition of the IN718 material used in this study, provided by the manufacturer.

Element	Ni	C	Fe	Cr	Nb	Mo	Ti	Al
Wt.%	Bal.	0.04	18.50	18.00	5.20	3.00	0.90	0.50

Four different sample geometries were tested, including (i) rectangular sample, recommended by the NPL good practice guide for testing with the ETMT system [187]; (ii) standard tensile sample (hereby referred to as the dog-bone sample), which is a scaled-down classic dog-bone shape slightly modified from the NPL good practice for testing with the ETMT system for nickel-based superalloys [187]; (iii) winged sample, adopted from a methodology developed for thermo-mechanical testing with increased uniform temperature distribution using a Gleeble thermal-mechanical physical simulation system which is similar to the ETMT system in principal [193]; and (iv) modified dog-bone sample, developed during the course of this study and hereby referred to as the short gauge length sample. The optimisation criteria for development of the short gauge length sample was to force the deformation to the hottest area of the sample (i.e. centre of the gauge length). This was (i) to equate the gauge length and the effective gauge length to the same size, i.e., homogenous deformation across the gauge length for far easier determination of the materials plastic strain and mechanical properties, and (ii) to have a temperature distribution across the effective gauge length of no more than ±1% of the recorded temperature at the centre of the sample. There were three key design variables which were taken into consideration to meet the optimisation criteria. The gauge length of the sample was reduced from the 6mm of the winged sample and 5mm of the dog-bone sample, to 2mm to make the gauge length and effective gauge length the same size. Having sharper fillets of 1.5mm radius as opposed to 20mm radius in an attempt to prevent

strain migration from the centre and the deformation encroaching on the cross-sectional area at the fillets which is unknown and larger than the cross-sectional area at the gauge length, hence it would impact the stress values and was undesirable. Finally, the maximum width of the sample could be no more than 6mm to fit between the screws in the grips. A value of 5mm was selected to allow 1mm for clearance. Figure 5.3 shows schematic sketches for these geometries with all the relevant dimensions provided.

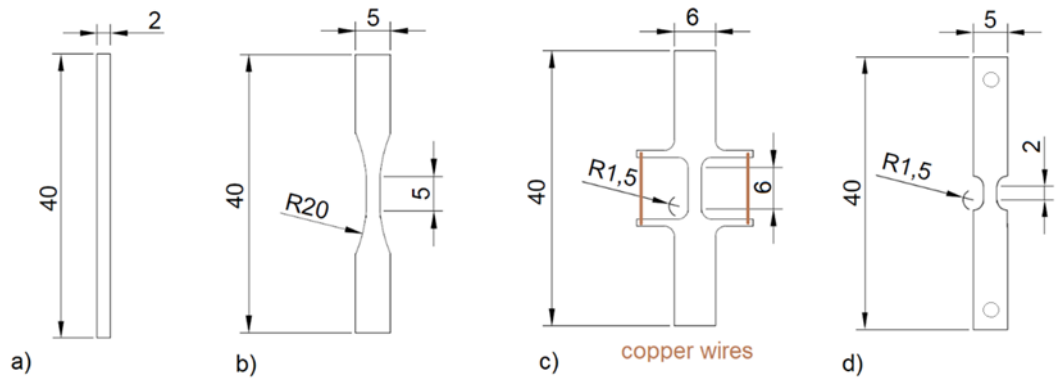

Figure 5.3: Four sample geometries investigated in this study for testing with the ETMT system, (a) rectangular, (b) dog-bone, (c) winged, and (d) short gauge length. All dimensions are in mm. Note: in (c) the coloured lines connecting the wings are schematic representation of the copper wires used to create an electric short-cut.

5.3 Thermo-Mechanical Testing

5.3.1 Equipment and Methodology

The experiments were carried out using an Instron© ETMT 8800 system, equipped with a mechanical assembly capable of testing in tension and compression up to a maximum load of 5 kN. A customised gripping system was designed in-house, to accommodate samples of different geometries with a high accuracy and repeatable alignment. The grips were sand-blasted to increase the friction coefficient and reduce the potential for slip in the samples without pinholes. The sample gripping assembly was water cooled during operation for temperature control. The samples were heated with the aid of a 400 A DC power supply based on electrical resistivity (i.e., the Joule effect). For each test, the temperature was measured and controlled through an R-type thermocouple, composed of 0.1 mm diameter wires consisting of platinum and platinum-13% rhodium, spot-welded to the sample at the centre of the gauge length under a condition where a bead was formed as a result of melting both wires.

Figure 5.4 shows the basic ETMT assembly and Figure 5.5 shows an image of a typical bead formed during spot-welding.

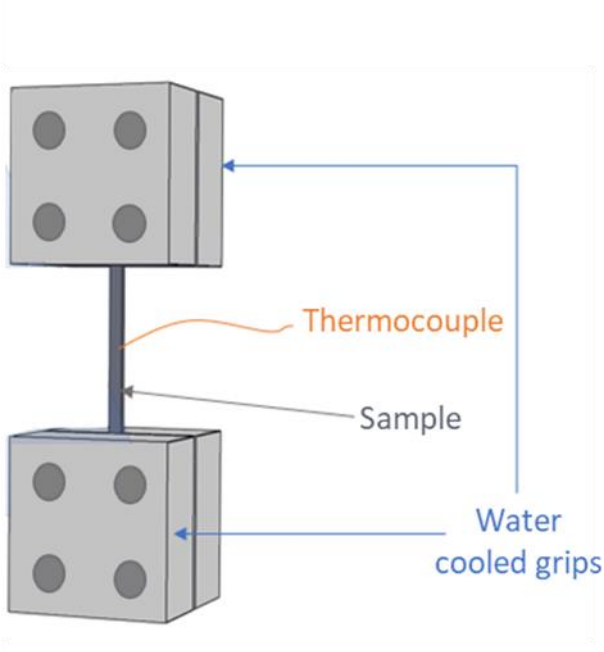

Figure 5.4: Sketch of the experimental set-up demonstrating the basic ETMT grips and the area explored by DIC.

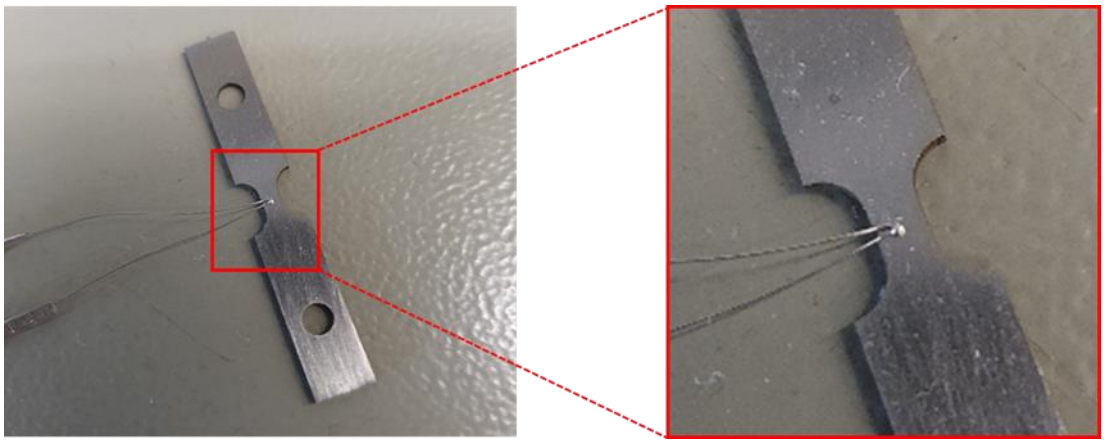

Figure 5.5: Photograph of a short gauge length sample with a thermocouple bead spot-welded onto the middle of the gauge length.

During each mechanical test, displacement of the top moving grip was measured with a built-in Linear Variable Differential Transformer (LVDT). Concurrently, the surface strain along and across the gauge length for each sample was measured during the test using a 3D Digital Image Correlation (DIC) system, which was capable of mapping in-plane and out of plane displacements. Ten images were captured at one second intervals, and the displacements in

the x and y directions (denoted u and v, respectively) were measured. Consequently, the strain in the x, y, and xy directions (denoted ε_{xx}, ε_{yy}, and ε_{xy}, respectively) were calculated using the same settings as for the actual tests whilst at temperature. Both the spatial and temporal standard deviations (STD's) were computed to understand the level of uncertainty associated with the DIC measurements as can be seen in Table 5.2 and Table 5.3. The values for displacement and strain are an order of magnitude higher than what has been reported in literature for noise values calculated at room temperature, but are in line with noise values calculated at elevated temperatures as was the case in these tests[194], [195].

Table 5.2: Noise floor given by spatial and temporal standard deviations for displacements.

	U (pixel)		**V (pixel)**	
Sample Geometry	**Spatial STD**	**Temporal STD**	**Spatial STD**	**Temporal STD**
Rectangular	0.119	0.258	0.093	0.175
Winged	0.039	0.087	0.047	0.070
Dog-bone	0.048	0.139	0.042	0.084
Short-Gauge length	0.074	0.134	0.039	0.088

Table 5.3: Noise floor given by spatial and temporal standard deviations for strain.

	ε_{xx} (%)		**ε_{yy} (%)**		**ε_{xy} (%)**	
Sample Geometry	**Spatial STD**	**Temporal STD**	**Spatial STD**	**Temporal STD**	**Spatial STD**	**Temporal STD**
Rectangular	0.079	0.053	0.047	0.047	0.038	0.031
Winged	0.024	0.023	0.025	0.026	0.014	0.017
Dog-bone	0.018	0.030	0.022	0.031	0.013	0.020
Short-Gauge length	0.036	0.047	0.039	0.042	0.027	0.032

For the measurement of surface displacement with DIC, a fine speckle pattern was produced on the surface in the area of interest, using a white high temperature paint as a background with an overspray of a black paint of the same type. This method has been shown to produce a consistent pattern with high contrast between features at elevated temperatures which makes it ideal for this application [192], [196]. The size of the black speckles varied from ~0.01mm to ~0.2mm in diameter. The resulting pattern with random distributions of fine objects with light, dark, and grey contrast offered an appropriate number of features for tracking. It is important

to note that the speckle pattern deteriorated when held at temperature, though the contrast was good enough for tracking displacements by DIC. An example of a surface with speckle patterns at room and elevated temperatures are provided in Figure 5.6. As the spatial and temporal standard deviations were calculated at elevated temperatures when the speckle pattern had deteriorated, the impact of texture evolution of the paint has been mitigated as much as possible.

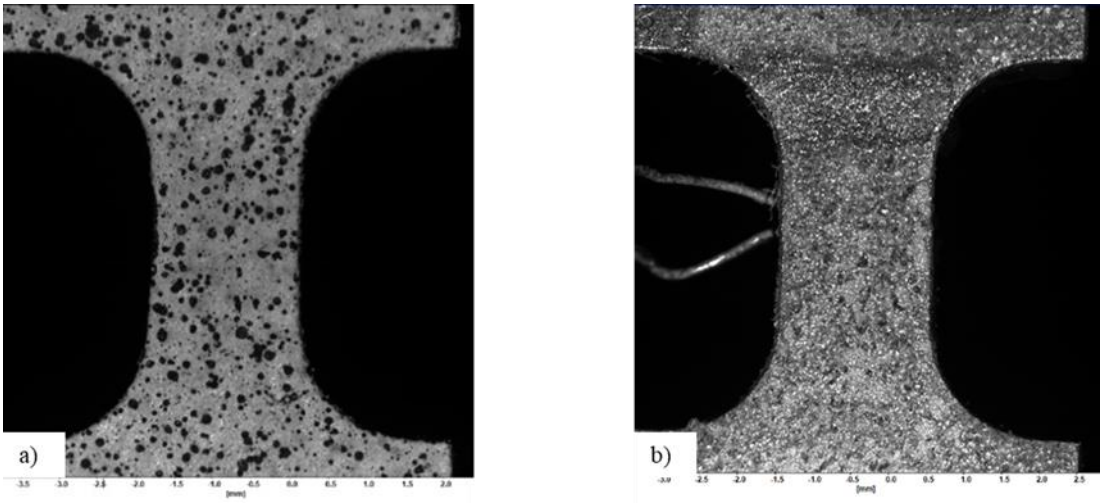

Figure 5.6: Examples of surfaces with speckle patterns (a) at room temperature, and (b) at 770˚C, prepared for displacement mapping during thermo-mechanical testing with the ETMT system.

Consecutive images of the sample surface were recorded using LaVision's MX4M digital cameras installed on a Zeiss Discovery V12 3D stereo microscope. To eliminate any possible black body radiation emitting from the sample whilst at temperature, blue LED lights and a filter were used during image acquisition. For each test, images were recorded from the beginning of the test to the end at a frequency of 10 Hz using an incremental correlation mode, meaning each image is correlated to the previous image and each incremental deformation is summed. This increases the amount of error in the correlation compared to a correlation with a single reference image, however for large displacements where the DIC pattern is likely to change substantially, this is the preferred method. Analogue signals for load, LVDT, and temperature transmitted from the ETMT, were connected to the DIC system through a signal interface unit. This enabled the relevant data to be collected and recorded in real-time and used for synchronising the mechanical test data measured by the ETMT with those of the DIC. The images obtained during the tests were analysed by the LAVision DaVis image correlation software (version 8.3.0) to evaluate the strain maps. The International

Digital Image Correlation Society's good practice guide recommends a practical subset size of 21 × 21 pixel^2 for correlation [197], however as these tests had features which were larger and more sparse, the strain maps were obtained using a 41 × 41 pixel^2 subset size. The same good practice guide recommends that the step size is between one-third to one-half of the subset size [197], so a step size of 20 was selected. A second order polynomial smoothing filter with 3 × 3 pixel^2 was used to smooth the results and reduce noise. Comparison with unfiltered results showed no significant bias. In these tests one pixel was equivalent to 5.2 µm, except for the case of the short gauge length sample, where field of view was less of a priority so the magnification was increased slightly so that one pixel was 3.65µm. The Fast-Fourier transform algorithm was used to correlate the images.

5.3.2 Effect of Sample Geometry on Deformation

For the evaluation of a suitable sample geometry, the thermo-mechanical test procedure started with heating the sample to 980°C at a 10 °C/s heating rate, dwelled at this temperature for ten minutes to annihilate any pre-existing residual stress and to dissolve the γ'' precipitates present (note the γ'' solvus temperature is reported to be between 900 °C and 930°C [34], [74], [75]. This heat treatment resembles the final closed-die forging operation which is typically done at 980 °C for IN718, and normalises the microstructure of all samples relative to one another in the gauge length. The sample was then cooled at a rate of 50 °C/s (i.e., to resemble the quenching condition) to the target test temperature at 720°C and soaked for 2 minutes to allow the temperature to homogenise throughout the gauge length. The ageing temperature of 720°C is an optimised temperature for effective precipitation of γ'' and hence was selected for these analyses. The rationale was to understand the effect of the onset of precipitation at ageing temperatures on the evolution of residual stress generated following the fast cooling from the forging temperature. The mechanical loading was then commenced and continued until either the sample failed or was deemed to have slipped. These measurements were controlled by the LDVT to ensure that the level of localised deformation to be measured by the DIC was in excess of 2% as a minimum.

All tests were carried out at a constant crosshead speed of 4 ×10^{-3} mm/s and a starting engineering strain rate of 2 × 10^{-3}/s. The effective gauge length was assumed to be 2mm for all geometries. The size of the effective gauge lengths is central to this study and before the tests

were performed it was acknowledged that they may differ to this original assumption of 2mm in size. An accurate determination would be made by use of the in-situ DIC results obtained later. Therefore the decision was taken to keep the crosshead speed constant for all tests, acknowledging that if the effective gauge lengths were greater or smaller than the assumed 2mm, this would mean differing engineering strain rates for each sample.

A typical displacement and temperature versus time plot is shown in Figure 5.7 outlining the test procedure.

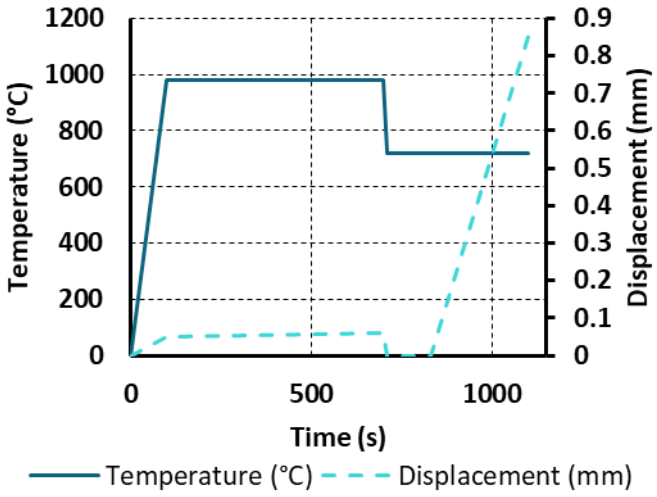

Figure 5.7: Typical plot of nominal temperature and displacement profiles against time, applied during a test.

5.3.3 Analysis of Temperature Distribution by Thermal Imaging

For the short gauge length and rectangular geometries (Figure 5.3), in addition to the temperature measurement using R-type thermocouples, an arc-thermal imaging camera manufactured by Ametek Land Instruments was also used to measure the temperature distribution over the gauge lengths. The camera had a spectral response of 8 to 14 µm and a field of view of 22°. It had a focus range of 0.3 m to infinity, a maximum recording frequency rate of 30 Hz, and a thermal image resolution of 384 × 288 pixel^2. The camera has an accuracy of ± 2 % or ± 2 °C (whichever was greater) of reading for a blackbody target (i.e., emissivity value of 1).

5.3.4 Determination of Mechanical Properties at Different Temperatures Using the Optimised Sample Geometry

Following the selection of an optimised sample geometry, additional tests were carried out on the short gauge length sample at various ageing temperatures to further ascertain this geometry's suitability in the testing of nickel-based superalloy's by the ETMT system. Similarly, to the test procedure implemented for samples of different geometries, for these tests the samples were initially heated to 980°C at 10 °C/s heating rate and maintained at this temperature for 10 minutes for the annihilation of residual stress and dissolution of existing γ' and γ'' precipitates. The samples were then cooled down to the target ageing temperature at a rate of 50° C/s (see Figure 5.7). Four tensile tests were carried out at different final ageing temperatures including 620˚C, 670˚C, 720˚C and 770˚C. The Young's modulus was calculated for each test via the strain output from the DIC system and the stress calculated from the ETMT system's load cell. The equipment and set-up used were the same as those used for the geometry evaluation tests. Meanwhile, for the evaluation of the surface displacement with DIC system, the strain maps were obtained using 41 × 41 pixel^2 subset size with a step size of 20. In these tests one pixel was equivalent to 3.65 µm and the image capture rate remained at 10 Hz. Information was only gathered up until the 0.2% yield point as the purpose of these tests was to determine the Young's modulus at the precipitation hardening temperatures, and compare them to the existing data, particularly those measured by conventional tensile test rigs where considerable time (~ 20-30 min) is needed for the sample to reach and stabilise at the target temperature [89].

5.4 Results

5.4.1 Effect of Sample Geometry

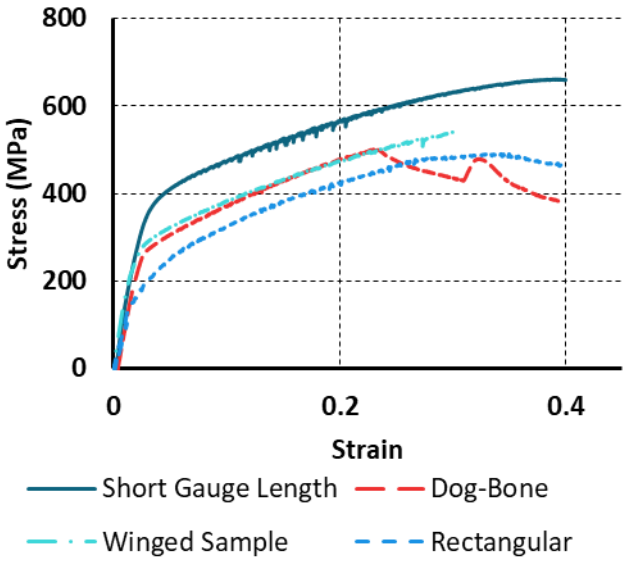

Figure 5.8: Plots of stress-strain curves measured by the LVDT interfaced to the ETMT for all sample geometries.

Figure 5.8 shows the stress-strain curves plotted using the data recorded by the LVDT and load cell of the ETMT. Firstly, it is important to note that both the dog-bone sample and the rectangular sample showed signs of slip as the tests progressed at 23% and 36% of strain respectively, but the data is still suitable for the majority of the test for comparison with other samples. Secondly, there is a high degree of variation in the stress-strain curves. A reasonable conclusion would be that the only variable in these tests was the sample geometry thus demonstrating the significant impact that this has on the resultant curves. Without the use of DIC, that would have been the conclusion drawn. The reason for this variation was further investigated by use of DIC to plot strain maps to better understand the strain distribution in the ε_{yy} direction.

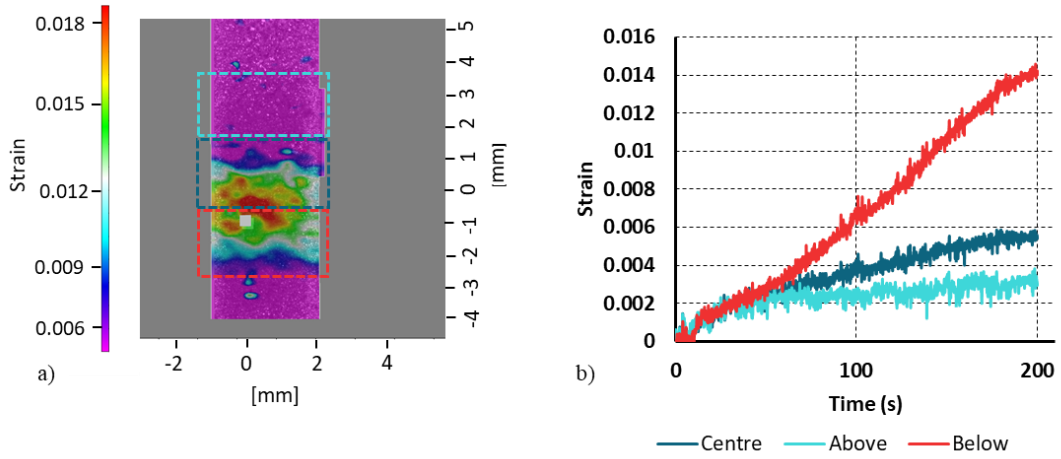

Figure 5.9 a) Strain map obtained in the ε_{yy} direction by DIC for the rectangular geometry at 40% strain read-out on the ETMT (i.e., measured by the LVDT) after 200 seconds, and b) plots of strain evolution measured in the ε_{yy} direction by DIC as a function of time for the rectangular geometry over three different areas with a 2mm gauge length each at the middle, above the middle and below the middle section of the sample. Note that the maximum temperature was reached in the centre of the sample.

Figure 5.9, Figure 5.10, Figure 5.11, and Figure 5.12 show the strain distribution maps for each of the 4 different sample geometries. In each case, a target of 40% strain of the original 2 mm effective gauge length (i.e., 0.8mm grip-to-grip separation) was applied via the ETMT system. Only the data up to 155 seconds is presented for the winged geometry, after which, significant amounts of slip began to take place which impacted the results. Critically, these strain localisations did not take place in the centre of the sample for most geometries, where the temperature was maximum, as demonstrated in the strain maps. For a clearer demonstration, the mid-section of each sample was divided into three areas with 2 mm gauge length each with no overlap, and the strain evolution as a function of time was evaluated from the DIC data to explore the magnitude of strain localisation. This was to show that the majority of the deformation occurred out with the region where the temperature was the highest.

The strain distribution measured for the rectangular geometry (Figure 5.9a) shows the strain localisation 1 mm below the centre point. Figure 5.9b shows that despite a small majority of the strain still coming from the centre of the sample, a significant portion of the deformation takes place away from the midsection of the sample, in particular in the 2 mm section immediately below the middle 2 mm mid-section of the sample.

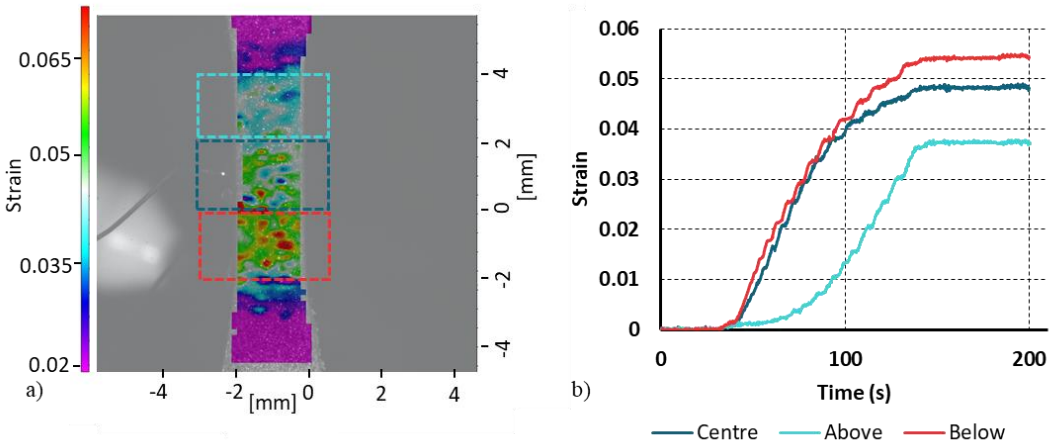

Figure 5.10: a) Strain map obtained in the ε_{yy} direction by DIC for the dog-bone geometry at 40% strain read-out on the ETMT (i.e., measured by the LVDT) after 200 seconds, and b) plots of strain evolution measured in the ε_{yy} direction by DIC as a function of time for the dog-bone geometry over three different areas with a 2mm gauge length each at the middle, above the middle and below the middle section of the sample. Note that the maximum temperature was reached in the centre of the sample.

The strain distribution map for the dog-bone geometry shown in Figure 5.10a reveals that a significant strain localisation had taken place within the 5 mm gauge length. However, closer inspection shows that the strain concentration was 2.5 mm below the centre of the gauge length. Figure 5.10b confirms that the majority of the measured deformation did not occur at the middle of the sample, but rather at the area with 2 mm gauge immediately below the mid-section. Figure 9b also shows serration in the strain vs time plots which is believed to be quantisation from the virtual strain gauge, this could be due to the size of the virtual strain gauge.

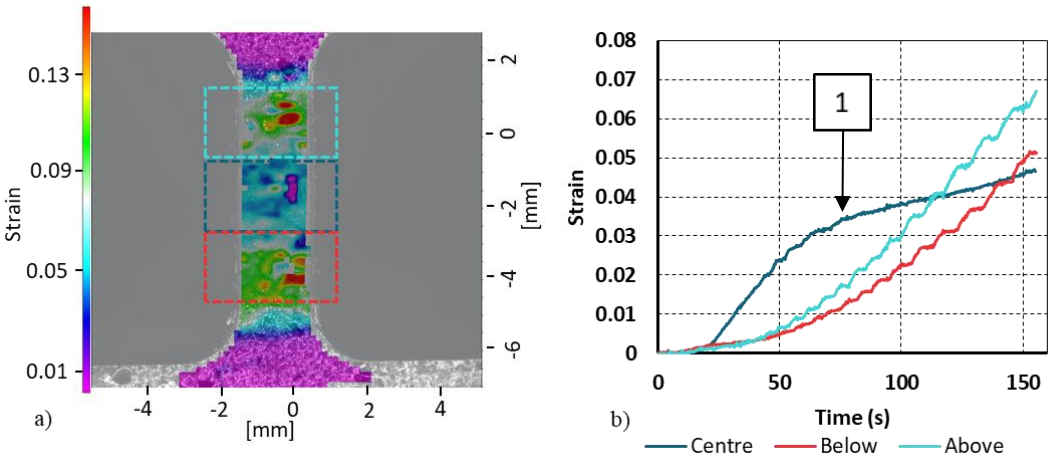

Figure 5.11: a) Strain map obtained in the ε_{yy} direction by DIC for the winged geometry at 30% strain read-out on the ETMT (i.e., measured by the LVDT) after 155 seconds, and b) plots of strain evolution measured in the ε_{yy} direction by DIC as a function of time for the winged geometry over three different areas with a 2mm gauge length each at the middle, above the middle and below the middle section of the sample. Note that the maximum temperature was reached in the centre of the sample.

As for the winged geometry, the strain localisation has drifted away from the mid-gauge area to regions between 2 - 2.5 mm above and below the centre, as can be seen in Figure 5.11a. After 60 seconds the rate of strain in the mid-section can be seen to drop as the sample hardens in that area (marker 1), and then continues to deform at a lower rate compared to the 2 mm areas immediately above and below. Figure 10b shows serration in the strain vs time plots suggesting that this sample is showing quantisation because of the use of a virtual strain gauge.

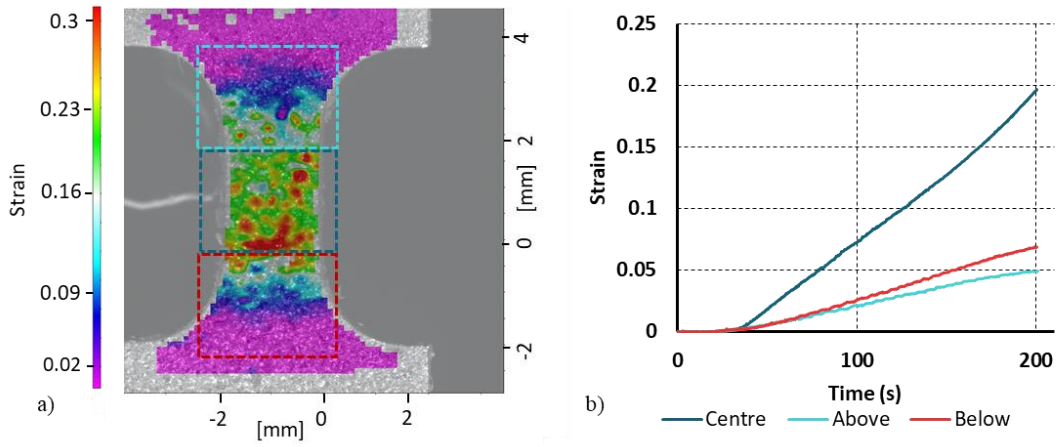

Figure 5.12: a) Strain map obtained in the ε_{yy} direction by DIC for the short gauge length geometry at 40% strain read-out on the ETMT (i.e., measured by the LVDT) after 200 seconds, and b) plots of strain evolution measured in the ε_{yy} direction by DIC as a function of time for the short gauge length geometry over three different areas with a 2mm gauge length each at the middle, above the middle and below the middle section of the sample. Note that the maximum temperature was reached in the centre of the sample.

Meanwhile, for the short gauge length geometry, the strain concentration occurred nicely in the central 2 mm gauge length area of the sample satisfying the first condition of no strain drift. For this sample, it appeared (Figure 5.12a) that the strain concentration encroaches out-with the 2mm gauge length where the cross sectional area increases due to the fillets, and as Figure 5.12b shows, the strain out-with the central 2mm section of the sample is not negligible. This means the second condition of having the gauge length and effective gauge

length as the same value is not entirely satisfied, however, this geometry does show a clear majority of strain at the centre. The impact that the strain encroaching into the fillet section has on the strain calculated from the LVDT sensor is analysed more in the discussion section). These measurements and observations suggest that the only sample geometry which satisfies the necessary criteria for appropriate deformation (i.e., localised at the centre-point of the sample), where the target temperature is reached, is the optimised geometry with short gauge length developed in this study. The short gauge length sample partially meets the second criteria of having the gauge length and the effective gauge length as the same size.

5.4.2 Temperature Distribution

Figure 5.13 and Figure 5.14 show the temperature distributions measured by a thermal camera for the rectangular and short gauge length samples. The temperature at a position 1 mm above the centre line and 1 mm below the centre line was measured for both samples and gives an indication of the temperature stability across the 2 mm total gauge length. In the case of the rectangular sample, the largest temperature drop was 1.89˚C over the 2 mm gauge length, and for the short gauge length sample, the largest temperature drop was 1.97˚C. This represents a 0.263% and 0.274% difference from the edge of the 2 mm gauge length to the centre for the rectangular and short gauge length samples, respectively.

The NPL's Good practice guide indicates that for a rectangular geometry, the temperature difference across a 2 - 4 mm gauge length is ± 3 ˚C at a temperature of 1250 ˚C, and less than ± 3 ˚C at lower temperatures [187]. The results of these tests carried out using a thermal camera are in good agreement with those from the NPL's Good practice guide. It can therefore reasonably be said that the short gauge length sample likely satisfies the necessary criteria of the temperature remaining as consistent across a 2 mm gauge length with a difference of < 0.28 % at 720˚C.

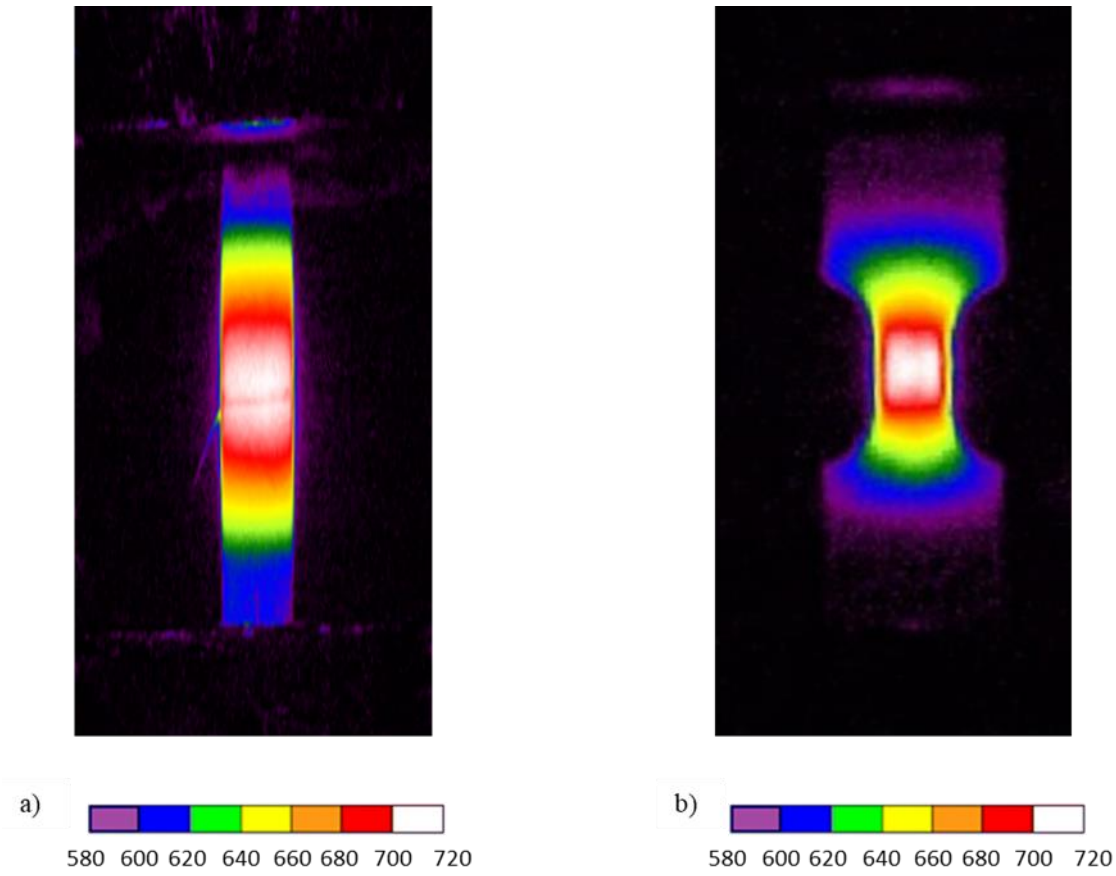

Figure 5.13: Temperature distribution maps measured by a thermal camera at 720 °C after a 2-minute dwell across the sample length for (a) a rectangular sample, and (b) a short gauge length sample.

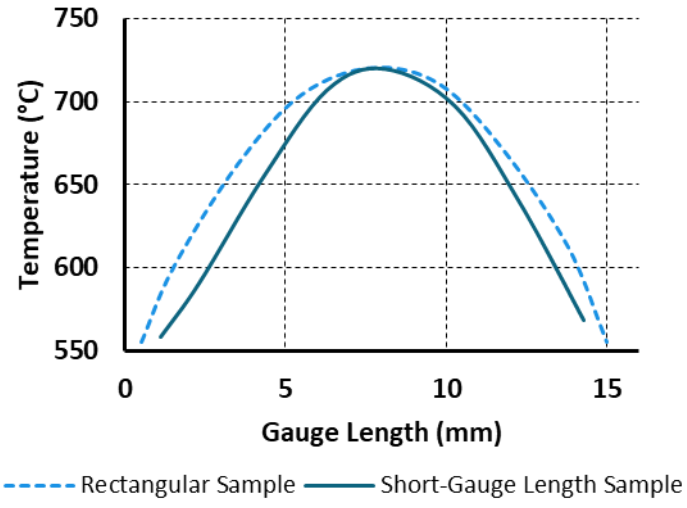

Figure 5.14: Temperature distribution plot measured by a thermal camera at 720 °C after a 2-minute dwell across the gauge length of the rectangular sample and the short gauge length sample.

5.4.3 Temperature Dependant Mechanical Properties

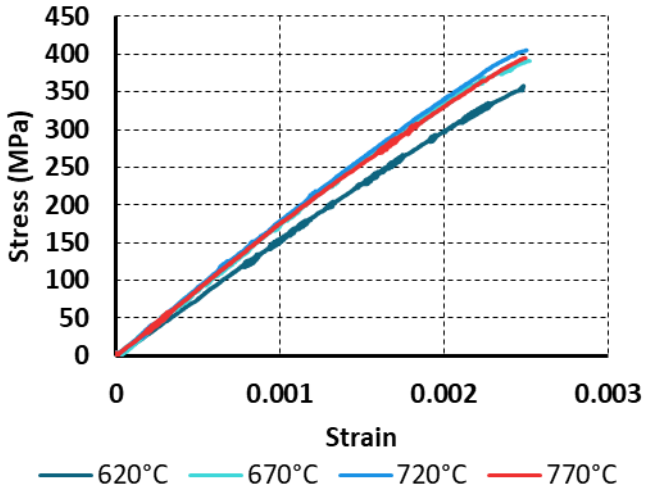

Figure 5.15: Plot of stress-strain curves evaluated from the data measured by LVDT on the short gauge length sample for the temperature dependant mechanical properties tests carried out at different temperatures. All tests were done within the elastic limit.

It can be seen in Figure 5.15 that the results produced from the LVDT sensor of the ETMT are fairly consistent with one another for temperatures between 670°C-770°C. The curve produced for the test carried out at 620°C, shows a less severe slope in the elastic portion of the test meaning that the Young's modulus is noticeably less than for the other tests (see Table 5.4). It has been shown for this material and at these temperatures that as the ageing temperature decreases, the Young's modulus increases [39], [89]. The Young's modulus values calculated from the LVDT sensor of the ETMT do not exhibit this trend as Table 5.4 shows. The results of the tests carried out at 620˚C and 770˚C give values which are much smaller and much larger respectively when compared with similar tests in literature and shown in Table 5.4.

Table 5.4 also shows the measured Young's modulus values at 5 different temperatures on the optimised short gauge length sample geometry calculated by DIC. At all temperatures, the determined Young's modulus values calculated using the DIC are smaller than those from the two other comparable reports. The difference between the Young's modulus at room temperature is relatively small and could be due to differences in the thermal or mechanical processing histories of the materials, or in the chemical compositions. Meanwhile for the tests carried out at the ageing temperature range there is a general trend of decreasing Young's

modulus as temperature increases for the data calculated using DIC, matching the other two studies. However, at lower ageing temperatures the data measured by the DIC were significantly lower than those reported in literature. This is due to the fact that the data reported in literature, including a previous study by the authors [10], were all obtained using conventional testing rigs equipped with furnaces whereby a significant time (~ 20 – 30 min) was required to reach the target temperature, which is long enough for the precipitation of considerable amount of γ'' [34], leading to a material with higher stiffness. Whereas for the tests conducted with the ETMT, the sample was heated to the target temperature almost instantly (i.e., within a few seconds) with little time for γ" precipitation to occur, resulting in a material with lower stiffness. Meanwhile, by increasing the temperature towards the ideal temperature for γ" precipitation (i.e., 720 °C) the difference in the measured Young's modulus by ETMT with those reported in literature reduces. This can be due to the higher kinetics of γ" precipitation at higher temperatures, meaning that sufficient volume of strengthening precipitate could become present in the material, despite being heated quickly by the ETMT. Note that the material used for these analyses were all solution annealed prior to the test.

Overall, there is good agreement in the values emphasising that the short gauge length sample satisfies both the thermal and mechanical criteria needed for successful mechanical properties (e.g., Young's modulus) determination at elevated temperatures where heavy γ" precipitation is likely to occur for IN718.

Table 5.4: Summary of the mechanical properties, including Young's Modulus and yield strength, measured by the ETMT for IN718 nickel-based superalloy in comparison to the data in literature.

Temperature (˚C)	Young's Modulus calculated from the ETMT LVDT (GPa)	Young's Modulus calculated from the ETMT and DIC tests (GPa)	Young's Modulus calculated from Rahimi et al. [89] (GPa)	ASM Specialty Handbook values [39] (GPa)
20	176	183	193	200
620	149	158	184	169
670	166	150	175	164
720	171	155	167	160
770	166	142	143	155

5.5 Discussion

The material investigated in this study, IN718, is a precipitation hardenable nickel-iron based superalloy containing considerable fractions of Nb and Mo, and small fractions of Ti and Al (see Table 5.1). This grade of superalloy achieves its superior mechanical strength for high temperature applications from precipitation phases, predominantly made of Ni_3Nb, with varying fractions of Ti and Al substituting for Nb in form of $Ni_3(Al, Ti)$ [28], [34], [198]. δ-phase, is the most stable form of Ni_3Nb precipitates (≈700℃ - 1000℃) that usually nucleates intergranularly (i.e., at grain boundaries), with a possibility of intragranular nucleation (i.e., within grains) in a presence of γ″ precipitate. γ″ is the main strengthening phase in IN718 with thermodynamic stability over the 620℃-900℃ temperature range, which has the same chemical stoichiometry (i.e., Ni_3Nb) as that of the δ-phase. Additionally, the existence of a small fraction of γ′ in the microstructure with $Ni_3(Al, Ti)$ form and stability comparable with that of γ″, provides extra strength to the alloy [18], [28], [34], [75], [81], [89], [198], [199].

The test plan implemented in this study, included a 10 min annealing at 980℃, followed by cooling to the ageing temperature at 50 ℃/s rate, and then mechanical testing at this temperature after a 2 min dwell time. The initial annealing temperature leads to the dissolution of all γ′ and γ″ precipitates, and also a minor dissolution of the δ-phase (i.e. less than 10% dissolved), over the majority of the gauge length, since 980℃ is approaching the upper limit stability of δ-phase [34], [89]. Due to the parabolic distribution of temperature in the middle section of the sample, the dissolution rate of δ-phase over the gauge length may differ. However, considering the < 2℃ difference in the temperature between the extreme ends of the gauge length and the centre of the sample (see Figure 5.13 and Figure 5.14), the local temperatures are still well beyond γ′ and γ″ stability, and hence these precipitates are all dissolved throughout. When the sample is cooled to the ageing temperature range, which is an ideal temperature for γ″ precipitation [34], an onset of precipitation starts to occur at the centre of the gauge length, with reduced precipitation kinetics towards either ends due to the < 2℃ difference, caused by parabolic distribution of temperature. This heterogeneity in the precipitation kinetic results in γ″ with different size and distribution throughout the gauge length, which has implications on the mechanical properties.

This is manifested clearly in the flat rectangular geometry proposed by NPL's good practice guide [187] for testing with ETMT, after mechanical testing at 720 ℃ (see Figure 5.9). As can be seen from the strain map in Figure 5.9a, localised deformation occurs in a zone which is slightly below the central part of the specimen where the temperature is highest for the rectangular

geometry. Figure 5.9b shows that the information recorded during the test is only just dominated by the deformation behaviour of the central region, and that the regions out with the area of interest with a known temperature (i.e., where the thermocouple was installed) show significant levels of strain.

In an attempt to address this problem, a dog-bone geometry (see Figure 5.3b) recommended by NPL's good practice guide, which was also used in a previous study [192], was slightly modified and selected as an alternative geometry. As can be seen in Figure 5.10a, strain localisation was still observed to consistently occur in a region below the central zone of the sample. Similarly, this indicates that the hardening effect caused by γ" precipitation was strong enough to shift the strain localisation away from the middle of the sample where the temperature was the highest and the cross-sectional area was least.

To resolve this problem, the winged geometry was adapted from literature [193]. This geometry was originally designed for testing on a Gleeble 3800, an apparatus that works based on similar principals as those of the ETMT, i.e., both systems use electrical resistivity to heat the samples to the target temperature. However, unlike the ETMT, the sample used for testing with the Gleeble was not miniaturised. Nevertheless, the problem arising from the parabolic temperature distribution across the gauge length was shared by both systems. It was shown in reference [193] that by manufacturing samples with wings extending out from both sides of the sample, above and below the gauge length area (Figure 5.3c), and then connecting each side from top to bottom with copper wires, it is possible to make the temperature distribution at the gauge length more homogeneous. This is to create a parallel circuit which would heat the sample and extend the hot zone out from the gauge length. It was thought that a similar design might be deployed for testing with the ETMT using a smaller sample. The geometry manufactured (Figure 5.3c) was a refinement of the flat specimen recommended by NPL's good practice guide, with additional wings.

Based on the results of a previous study [193], the winged sample was expected to have a uniform temperature distribution across the gauge length which would in turn lead to a uniform distribution of precipitation and hence deformation. However, Figure 5.11a shows that the strain was not evenly distributed throughout the gauge length where a clear shift in strain was observed away from the centre towards the top and the bottom. Therefore, the winged sample, despite its success in testing using the Gleeble 3800 [193], was observed to be

unsuitable for testing IN718 at 720°C, using the ETMT. The combination of a miniaturised sample and having a lower current output from the ETMT, which means a sharper parabolic temperature distribution across the gauge length, was likely the cause of this problem.

In all the rectangular, dog-bone and winged sample geometries, deformation occurred out-with the area of interest (i.e., centre of the gauge length) where the temperature was measured to be highest. It was thought that this was predominantly because of the gauge length of these geometries being too long, i.e., 16 mm, 5 mm and 6 mm for the rectangular, dog-bone and winged samples, respectively. Therefore, it was decided to reduce the gauge length to 2 mm in the short gauge length geometry to force the deformation into the centre of the sample. As such, the radii of the fillets for the standard dog-bone sample was 20 mm to avoid any stress localisation that leads to fracture in this area. This was possible when the fillets are too sharp and likely to happen when the material is brittle. However, a radius of 1.5 mm was considered for the optimised geometry. As can be seen in Figure 5.12a, the strain map obtained for the short-gauge length sample with sharp fillets shows deformation centred in the middle of the sample, indicating that it successfully satisfied the first criteria. The third criteria, having a temperature distribution across the gauge length of less than 1% can be seen to have been satisfied as shown in Figure 5.13 and Figure 5.14. The second criteria of having the effective gauge length equal to that of the actual gauge length is only partially satisfied. The majority of deformation does indeed come from the middle of the sample, far more so than in the case of any other geometry tested, however, there is still a small but significant proportion which does not and comes from areas just outside the central 2mm region. This still means that the sharper fillets combined with the reduced gauge length enabled successful tests of IN718 nickel-based superalloy at the ageing temperature range (i.e., 620 °C - 720 °C) to take place, however care must be taken when interpreting strain results from the LVDT sensor.

The Young's modulus is a difficult quantity to measure using DIC due to the small level of displacements to be measured, which can often be smaller than the noise of the DIC [200]. It is however an excellent quantity to measure for the sake of comparison with other reports in literature [39], [89], [201]. As such this was selected as the final qualifying criteria in a bid to find a sample geometry suitable for the determination of thermo-mechanical properties in superalloys. The work carried out by Rahimi et al. [89] was used for comparative purposes, as was the results published in ASM Specialty Handbook [39]. To extract data for the temperatures examined in this study, a linear interpolation was applied to the results from the

ASM Specialty Handbook as the exact temperatures did not match up with the test temperatures carried out in these tests.

Finally, an approach has been suggested to equate the strain measured using the DIC system over the 2 mm gauge length of the short gauge length sample, with the strain measured by the LVDT. This was done by correcting the strain measured by the LVDT to the strain measured using the DIC using a generalised reduced gradient solver built into Microsoft excel. The average absolute relative error (AARE) seen in Equation 5.2 where E_i is the experimental stress values, P_i is the predicted stress values, and N is the number of data points, was used as an objective function and the strain measured using the LVDT was corrected to two different equations and then compared. The first equation was the standard equation of a straight line ($y=mx+c$) and the second equation was the power law ($y=mx^b$). The only constraint applied was for the value of c in the equation of a straight line to equal zero as would have to be the case.

$$AARE\ (\%) = \frac{1}{N}\sum_{i=1}^{N}\left|\frac{E_i - P_i}{E_i}\right| x100$$

Equation 5.2

Figure 5.16a and b shows the plots of strain versus time measured by both the DIC system and the LVDT for both equations. The values for m and b in the power law were 0.740 and 1.289 respectively. The value of m for the equation of a straight line was 0.460. The AARE for the power law equation was 15.15% and the AARE for the equation of a straight line was 28.43% meaning the power law is a better fit at correcting the strain measured from the LVDT sensor of the ETMT to the data from the DIC. This can be seen in Figure 5.16a and b where the power law shows a much closer fit than the straight line. Polynomial equations were not selected for comparison as the power law showed good accuracy and was simpler than a polynomial equation for prediction. The reason for the divergence of the uncorrected LVDT strain from the DIC strain, especially at the beginning of a test, is because the LVDT sensor is attached to the grips of the ETMT machine and therefore not sensitive enough to detect the impact of machine compliance and/or that of sample straightening during testing in cases where they haven't been aligned perfectly. The LVDT sensor reads displacement along the sample, even if the sample is yet to fully settle into the grips and align with the direction of tension. DIC is more astute at detecting this phenomenon which is thought to be the reason behind the early

divergence in the curves. Thereafter, the difference in strain continues to grow between the uncorrected LVDT strain value and the DIC measured strain. Figure 5.12 shows that the majority of the strain comes from the 2mm gauge length in the middle of the sample, but there was still some strain measured out with this gauge length. The strain out with this gauge length is thought to be the reason behind the difference in the uncorrected strain measured from the LVDT and the strain measured using the DIC. Therefore it can be seen that the correction applied is predominantly to address the strain out-with the 2mm gauge length in the centre of the sample. Constitutive models have been used to predict the flow stress at elevated temperatures [132], [134], [135], [136], [143], however, it is well known that a constitutive model is heavily dependent on the material characteristics (i.e., microstructure), the strain rate and the temperature which the tests were carried out at. Therefore it is assumed that further work would need to be carried out to determine the robustness of Equation 5.3, and to see if it is representative of all precipitation hardened materials, and for what temperature and strain rate regimes.

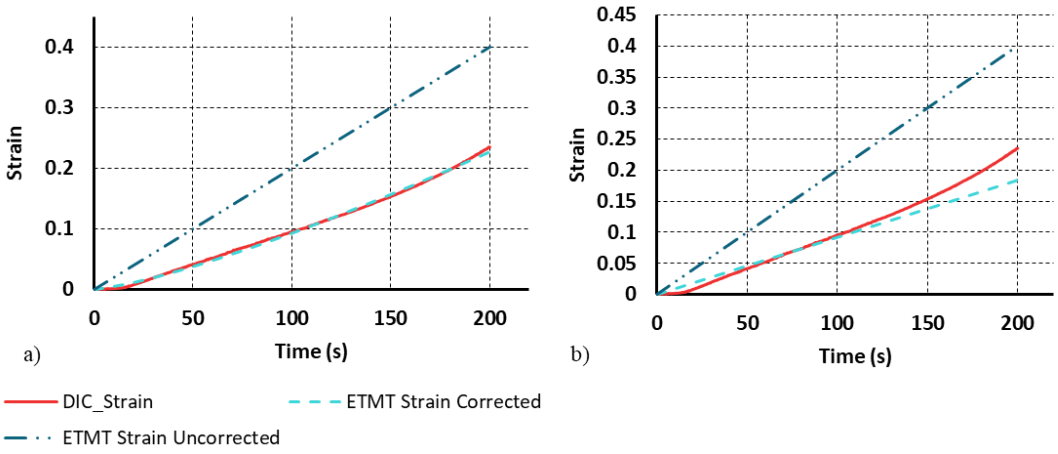

Figure 5.16 a) Plots of strain vs time at 720˚C for the uncorrected LVDT strain, the strain measured by DIC and a) strain data collected from the LVDT sensor of the ETMT and corrected using a power law equation and b) strain data collected from the LVDT sensor of the ETMT and corrected using the equation of a straight line.

$$\varepsilon_{ETMTcorrected} = 0.74 * \varepsilon_{ETMTuncorrected}1.289$$

Equation 5.3

Where $\varepsilon_{ETMTcorrected}$ is the strain measured from the LVDT sensor of the ETMT after correction to the strain measured by the DIC system and $\varepsilon_{ETMTuncorrected}$ is the strain measured directly from the LVDT sensor on the ETMT. This approach enables one to confidently rely on the strain measured by the LVDT without a need for a DIC system. The

authors recommend further work to understand the impact which temperature and strain rate have on this equation, as well as its applicability with other precipitation hardened materials. Furthermore, the development of this empirical equation though rooted in practicality, could potentially be better strengthened if it were to be rooted in a physical-based model. This would require additional data at different temperatures and strain rates which were beyond the scope of this work. Although, additional data is needed to verify this approach for other materials as the coefficients can vary, the proposed methodology works for the IN718 nickel-based superalloy at a temperature of 720˚C, for a starting engineering strain rate of 2 ×10-3/s. Nevertheless, the sample geometry is essential in obtaining the correct data for this class of materials (i.e., precipitation hardenable) by the aid of ETMT, and this study has demonstrated the appropriate sample geometry.

5.6 Conclusions

Four different sample geometries were examined to determine their suitability for thermo-mechanical testing of a precipitation hardenable material, IN718 nickel-based superalloy, using an ETMT system. The following conclusions can be drawn:

- The results of surface displacement and strain mapping by the aid of digital image correlation showed that in all geometries strain localisation occurred away from the centre of the gauge lengths of the samples, where the deformation is expected to be, with the exception of a modified geometry with a short gauge length. This sample showed strain localisation perfectly at the centre of the sample.
- The short gauge length sample showed 0.274% difference in temperature between the centre of the gauge length and its 2 mm outer edge at a temperature of 720°C. In comparison, this value was 0.263% for the standard rectangular sample over a matching 2 mm gauge length and at the same temperature.
- The short gauge length sample is suitable for determining arguably the most difficult of mechanical properties, the Young's modulus, for the precipitation hardenable material IN718 at room temperature, as well as at ageing temperatures in the region of 620˚C to

770˚C where significant γ' and γ'' precipitation takes place making the material stronger, by making use of digital image correlation.

- These results suggest that the modified geometry designed, tested and verified in this study is in fact suitable for mechanical testing of precipitation hardenable materials, such as nickel-based superalloys, at elevated temperatures.
- A methodology is proposed to facilitate the use of the short gauge length sample in accurately determining the strain from the ETMT's LVDT sensor for IN718 nickel-based superalloy.

The sample geometry designed in this chapter will be used in Chapter 6 for stress relaxation tests conducted on the ETMT. These tests will aid in developing constitutive stress relaxation models for both IN718 and AD730.

6

Constitutive Modelling of Stress Relaxation Behaviour in IN718 and AD730

6.1 Introduction

In this chapter, the stress relaxation behaviours of two Ni-based superalloys, IN718 and AD730, during their respective post-forging ageing heat treatments are examined, as highlighted on the thermo-mechanical processing routes for both materials illustrated in Figure 6.1 and Figure 6.2. After optimising the sample geometry for ETMT testing, as discussed in Chapter 5, stress relaxation tests were conducted on the materials examined in this thesis. IN718 was the initial focus due to its well-established properties, with results compared to existing stress relaxation data. Once the methodology was established for IN718, the same approach was applied to AD730. For IN718, the temperature range investigated was 620 °C to 770 °C, while for AD730, it was 730 °C to 790 °C, covering typical ageing heat treatment temperatures for these materials.

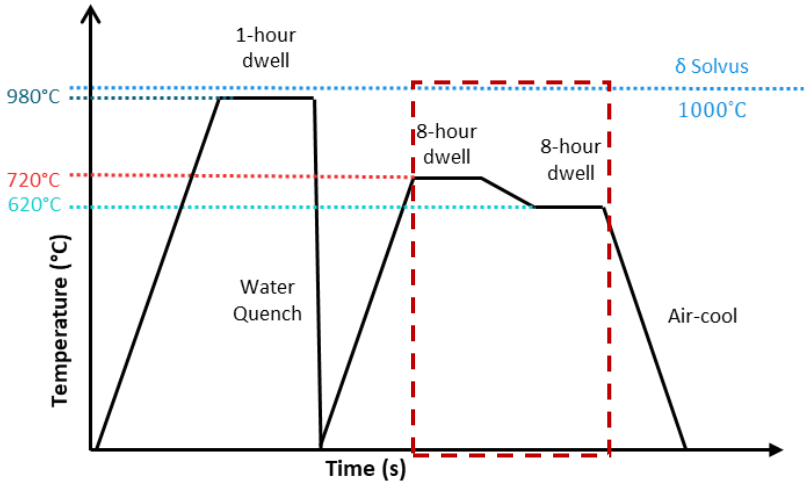

Figure 6.1: Thermo-mechanical processing route of IN718, emphasising the ageing stage which is further explored in this chapter.

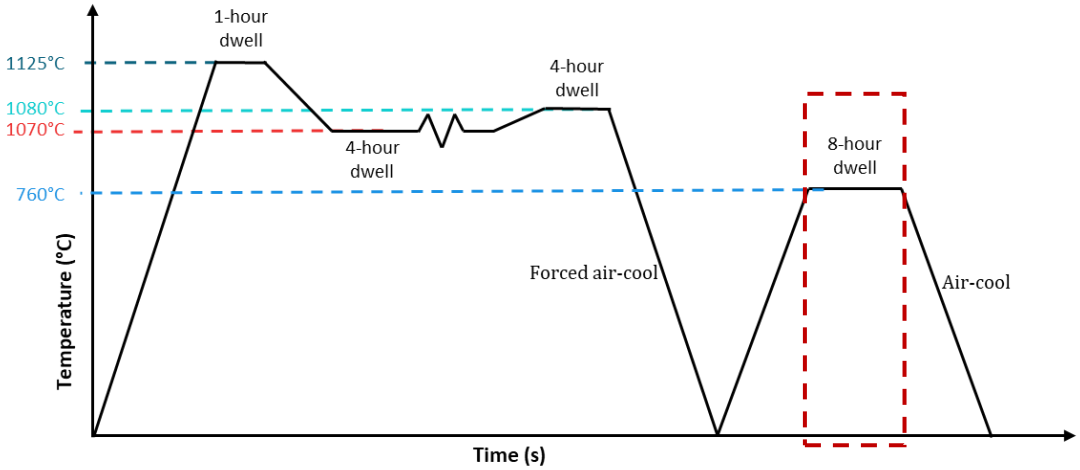

Figure 6.2: Thermo-mechanical processing route of AD730, emphasising the ageing stage which is explored in this chapter.

Two stress relaxation models were developed for each material for comparison. The first model, known as the Zener-Wert-Avrami (ZWA) model, is empirical and was chosen for its documented accuracy and robustness in determining stress relaxation behaviours across various materials, as highlighted in Section 2.5.3 of the literature review of this thesis [150], [151], [166].

The second model, based on the hyperbolic law, was selected for several reasons. Firstly, it has been successfully applied to IN718 within the same temperature range in a previous study [89], suggesting its potential applicability to AD730. Secondly, its relatively simple constitutive

equation made it an interesting candidate for comparison with the more complex ZWA model. Lastly, this model has received less attention in the literature compared to the ZWA model, presenting an opportunity for its development and application to these materials. After developing the models, the discrepancy between the predicted and the experimental values was assessed.

6.2 Methodology

6.2.1 Material

The IN718 material was sourced from the same billet, possessing identical chemical composition and initial microstructure, as the discs discussed in Chapter 4. The AD730 used in this study was provided by Aubert & Duval. The as-received material had undergone a double melt cast and wrought manufacturing process and was supplied in the form of a billet. The chemical composition of the material is provided in Table 6.1.

Table 6.1: Chemical Composition of AD730.

	Ni	Cr	Mo	W	Co	Fe	Nb	Ti	Al	Other
Wt. %	Bal.	15.7	3.1	2.7	8.5	4	1.1	3.4	2.25	Zr, B,C

6.2.2 Material Characterisation

A small section of the as-received material was sectioned using wire EDM and following standard metallographic techniques, was ground and polished to a mirror finished condition. It then underwent eight hours vibratory polishing, using 0.02 µm colloidal silica as a suspension. The sample was then characterised using a FEI Quanta 650 field-emission gun (FEG) scanning electron microscope (SEM) equipped with a back scatter electron detector (BSE). Electron backscatter diffraction (EBSD) was then carried out using an Oxford Instruments EBSD camera. Micrographs and EBSD maps were taken. An aperture of 100 µm diameter and an accelerating voltage of 25kV was used. The EBSD results were captured and post-processed according to E2627-13 [202]. This meant that each map had a minimum of 50 grains per scan and grains which had less than 100 indexed points were excluded. A misorientation tolerance of ±5° was used to determine whether points belonged to the same grain or not. Lastly, boundaries at 60° orientation and often referred to as twin boundaries are excluded with a tolerance of ±5°. For determining the fraction of recrystalised grains, the mean grain orientation spread (GOS) was

used with a threshold of <2°. The mean GOS is the average of the misorientation angles to the grain mean orientation. A step size of 0.52 µm was selected, the scan area was 555 x 337 μm^2, and the resulting average indexing rate was greater than 99.16 %.

6.2.3 Tensile and Stress Relaxation Tests

Tensile tests were conducted for both materials across their respective temperature ranges until reaching failure. These tests were conducted in accordance with ASTM E8M-22 [185] standards using the ETMT for mechanical loading, while strain measurements were captured by the Digital Image Correlation (DIC) system. Detailed descriptions of these machines are provided in Chapter 5. Tests on IN718 were performed following an hour heat treatment at 980 °C followed by a water quenching, as described in Chapter 4 for the scaled discs, while tests on AD730 were conducted in the as-received condition. For IN718, tests were conducted at 620 °C, 670 °C, 720 °C, and 770 °C, and for AD730, tests were conducted at 730 °C, 760 °C, and 790 °C. These temperatures corresponded to those also used for stress relaxation tests.

The samples underwent preparation using grade 2000 SiC paper to eliminate the re-cast layer resulting from wire EDM cutting, before being cleaned with acetone. K-type thermocouples were fabricated using the method described in Section 5.3.1 of Chapter 5 and spot-welded onto the samples. K-type thermocouples were chosen due to their cost-effectiveness compared to R-type thermocouples and because the temperature range fell within the operating limits of this type.

For the tensile tests of IN718, specimens were preheated to 980 °C for 10 minutes to alleviate residual stress from the water quenching process. Subsequently, they were cooled at 50 °C/s to the target temperature, held for 15 minutes to ensure temperature stability, and then subjected to mechanical testing. A strain rate of 0.05 s^{-1} was applied on the ETMT, monitored by the LVDT sensor, translating to a cross-head speed of 0.001 mm/s. This strain rate corresponds to 0.00025 s^{-1} as measured by the DIC system, aligning with ASTM E8M-22 recommendations for determining yield stress during tensile tests. This experimental schedule is shown schematically in Figure 6.3a. All specimens were strained until failure. For AD730, the as-received material had not been water quenched, so samples were heated directly to the target test temperature, dwelled for 15 minutes, and then strained until failure. This has been shown schematically in Figure 6.3b. An example of a stress-strain curve is shown in Figure 6.4a for AD730 at 790°C.

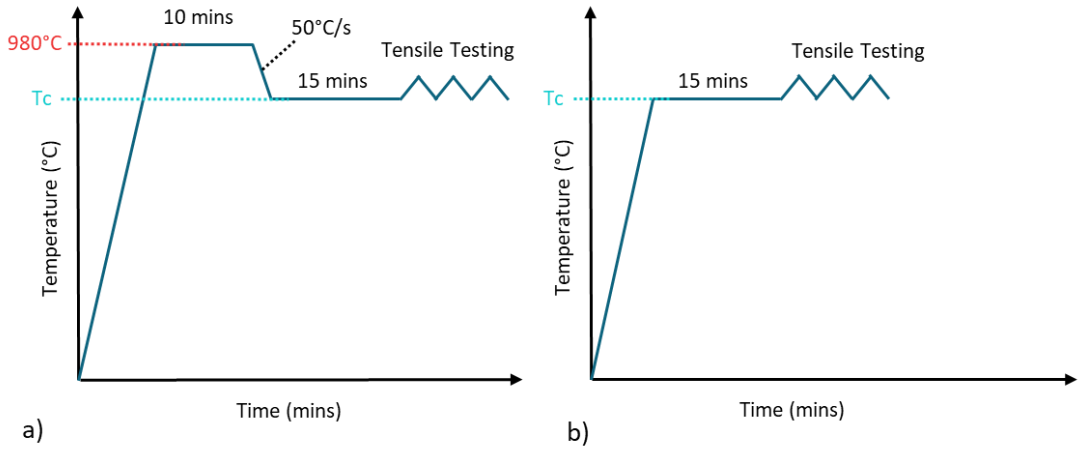

Figure 6.3: Schematic diagram of hot tensile testing routine carried out on the ETMT for a) IN718, and b) AD730.

The aim of the tensile tests was to establish the elastic properties, such as Young's modulus, and the yield point of the material, crucial for subsequent stress-relaxation tests. Within the elastic region, three deformation levels were identified, emphasising the selection of a point close to the upper limit of this range where initial signs of yielding were observed. This choice aimed to maximise the level of elastic stress (or residual stress) in the material. Figure 6.4b illustrates the method employed to determine suitable deformation values for the stress relaxation tests, with horizontal lines representing the selected initial nominal stress values.

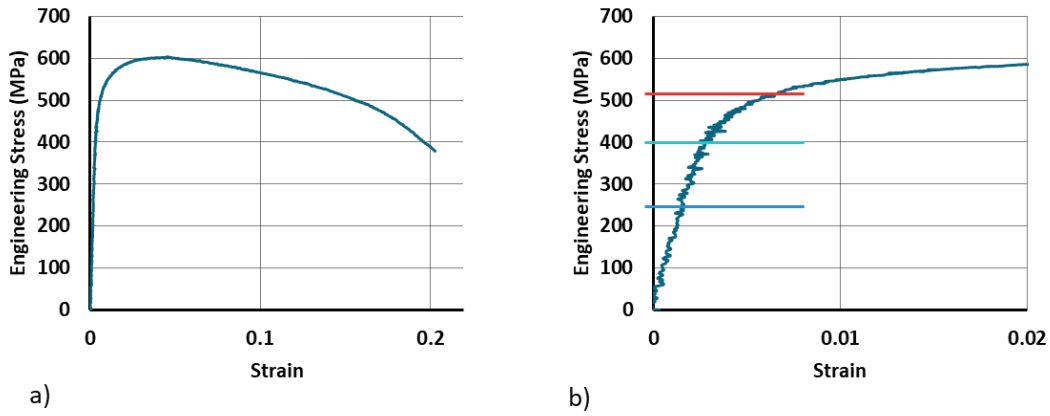

Figure 6.4: Tensile test at 790 °C for AD730 showing a) full stress-strain curve, and b) the same stress-strain curve but magnified in the elastic region showing the method for selecting the stress levels to carry out subsequent stress-relaxation tests.

The stress relaxation tests were then carried out in accordance with ASTM E328-21 [174]. The methodology used for both materials was the same as the tensile test methodology up until

the point in which the samples where mechanically loaded, at which point rather than the samples being loaded until failure, they were strained until a target stress value was reached, and then the LVDT sensor was used to hold the sample at a constant strain value whilst the stress relaxed. The stress relaxation behaviour was monitored for one hour at which point the stress had tended towards a horizontal asymptotic stress denoted as σ_{∞}. A schematic of this can be seen in Figure 6.5, and the stress values for each material and each temperature are provided in Table 6.2. Note that Figure 6.5 is a continuation of the schematics shown in Figure 6.3 for the full tensile tests, but in this case the tensile test was replaced with the stress relaxation tests.

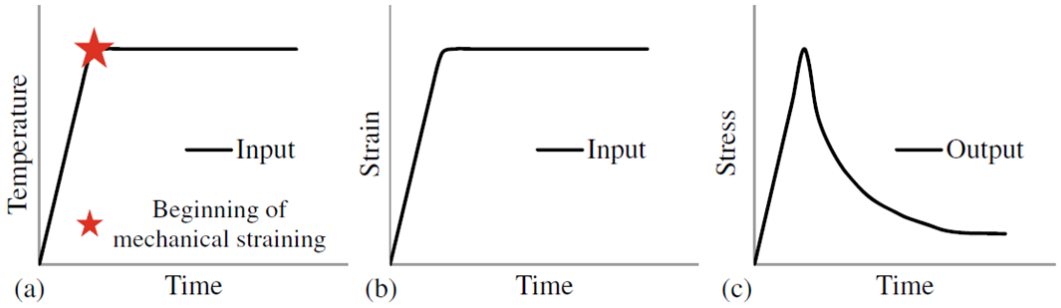

Figure 6.5: Schematic representations of the stress relaxation test including a) temperature profile, b) strain controlled by the LVDT sensor, and c) stress evolution during a typical test [129].

Table 6.2: Target stress values for stress relaxation tests carried out on IN718 and AD730.

Material	Temperature (°C)	Target Stress Value (MPa)	Material	Temperature (°C)	Target Stress Value (Mpa)
IN718	620	225	**AD730**	730	350
IN718	620	350	**AD730**	730	550
IN718	620	420	**AD730**	730	780
IN718	670	300	**AD730**	760	300
IN718	670	450	**AD730**	760	500
IN718	670	550	**AD730**	760	650
IN718	720	350	**AD730**	790	250
IN718	720	550	**AD730**	790	400
IN718	720	670	**AD730**	790	520
IN718	770	200			
IN718	770	300			
IN718	770	365			

For displacement and strain measurements with the DIC, a noise floor was calculated using the same method as laid out in Section 5.3.1. Ten images were taken at one-second intervals at the target temperature to capture displacements. Subsequently, displacements in the *x* and *y* directions were determined using the same parameters as those applied in the actual tests conducted at temperature. Spatial and temporal standard deviations (STDs) were computed to assess the uncertainty associated with the DIC measurements. The spatial standard deviation in the *x* and *y* direction where between 0.0002 and 0.0006mm and for the temporal standard deviations, were between 0.0002 and 0.002mm, respectively. To measure surface displacement using DIC, a fine speckle pattern was applied to the area of interest using a white high-temperature paint as a base, followed by over-spraying with black paint of the same type. It's worth noting that the degradation of the speckle pattern when heated to elevated temperatures was smaller than those presented in Chapter 5 by randomising the direction of the SiC paper used to remove the EDM recast layer and using more acetone to de-grease the

sample. It can be seen in Figure 6.6 that the contrast remained sufficiently clear for surface displacement tracking by DIC.

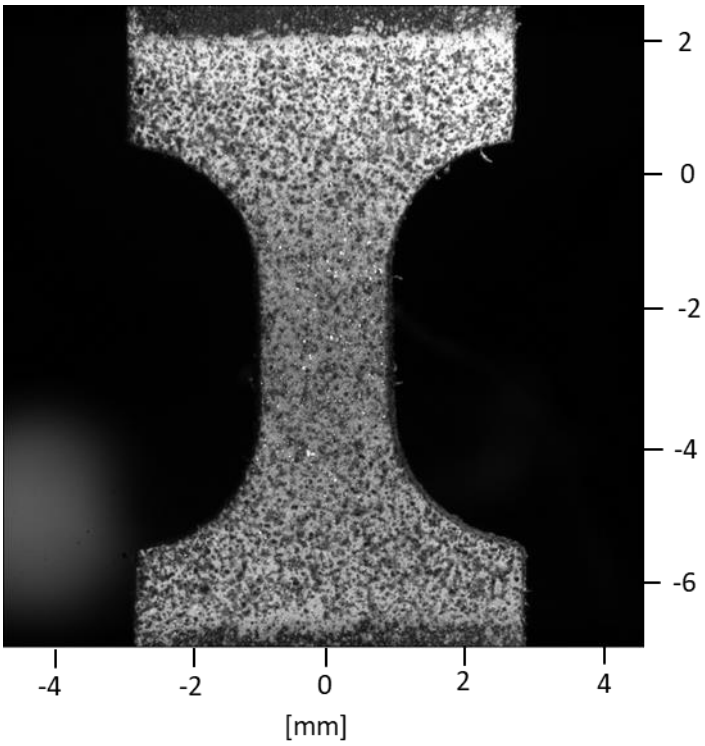

Figure 6.6: An example of a speckle pattern on a sample tested at 620°C prior to the commencement of tensile testing.

During the tests, the surface of the sample was continuously imaged using LaVision's MX4M digital camera mounted on a Zeiss Discovery V12 3D stereo microscope. The images were captured by using a single camera. To minimise any potential interference from black body radiation emitted by the sample at elevated temperatures, blue LED lights and a filter were employed during image capture. Throughout each test, images were captured at a frequency of 10 Hz from the test's initiation to its conclusion using an incremental correlation mode.

The analogue signals for load, LVDT, and temperature from the ETMT were linked to the DIC enabling synchronisation between mechanical test data from the ETMT and DIC measurements. The images acquired using the DIC system were analysed using LAVision DaVis image correlation software (version 8.3.0) to generate strain maps. While the International Digital Image Correlation Society's good practice guide suggests a practical subset size of 21 × 21 pixels² for correlation [197], the features in these tests were larger and more dispersed. Hence, strain maps were obtained using a 35 × 35 pixels² subset size. Following the guide's

recommendation that the step size should be between one-third to one-half of the subset size, a step size of 15 pixels was chosen for all tests.

To refine the results and minimise noise, a second-order polynomial smoothing filter with a 3 × 3 pixels² kernel was applied. Comparison with unfiltered results revealed no significant bias. The Fast Fourier Transform algorithm was utilised for image correlation. Each pixel in these tests represented 4.55 µm.

6.3 Results

6.3.1 Microstructural Characteristics

The as-received microstructure is shown in Figure 6.7. Figure 6.7a and b show primary γ' at the grain boundaries, and smaller intragranular secondary γ' throughout the grains. They also show a reasonable amount of spread in the grain size, which is confirmed in Figure 6.7f. The recrystallisation fraction determined by grains having a GOS of less than 2° is 83%, which seems to be predominantly the smaller grains, with the larger grains remaining unrecrystallised, shown in Figure 6.7d and e. This is a well-known characteristic of this material which stems from its thermo-mechanical processing [191], [203]. The inverse polefigure in Figure 6.7c shows no preferential texture and the average grain size determined by the equivalent circle diameter method is 10.11 ± 6.9 µm

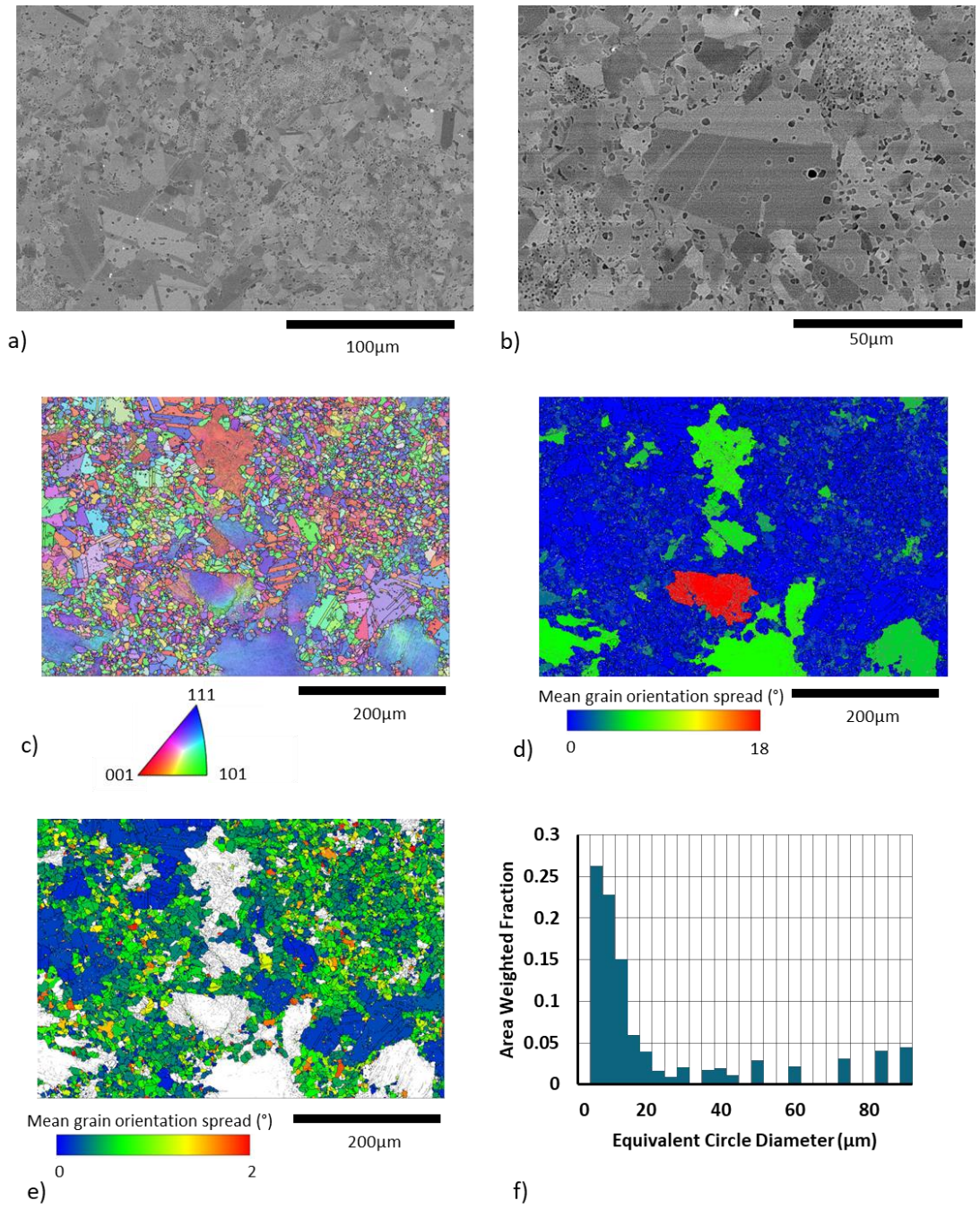

Figure 6.7: Microstructural characteristics of the as-received material; a) and b) SEM BSE micrographs c) EBSD inverse polefigure map with respect to the out-of-plane direction, d) and e) mean GOS map showing 83% recrystallisation for two different thresholds, and f) grain size distribution histogram.

6.3.2 Tensile Tests

The results of the tensile tests for AD730 and IN718, obtained by ETMT, are plotted in Figure 6.8, and the key mechanical properties summarised in Table 6.3. For IN718, from Figure 6.8a

and b, as well as Table 6.3, it can be seen that the mechanical properties of the material severely deteriorate at temperatures above 720 °C. This is because the precipitation rate of γ'' at 770 °C is lower than those at the lower investigated temperatures so the microstructure does not have as much γ'' present to impart strength. It's crucial to emphasize that γ'' is only in a metastable state at this temperature. Additionally, the δ-phase precipitates over 650°C at the expense of γ'', potentially diminishing both the volume fraction of γ'' and the material's strength. Although the precipitation rate of the δ-phase is most significant around 900 °C [76], the exact rate of precipitation at this temperature remains unknown. From Figure 6.8a, it can also be seen that with increasing temperature comes shorter percentage elongation, until the temperature goes higher than 720 °C, at which point, the elongation increases significantly. The reason for this reduction in ductility could be due to the heat treatment and water quenching before testing. The 10 minutes dwell at 980 °C eliminates γ'' throughout the microstructure as it is above the γ'' solvus [34], [74], [75]. Importantly this heat treatment eliminates γ'' from the grain interiors and reduces δ-phase at grain boundaries, and upon quenching the former starts to nucleate again during cooling, meanwhile, the δ-phase does not have time to grow sufficiently. When the samples were then taken to their target temperature, the grain interiors were significantly stronger (i.e., due to nano-size γ'' precipitates), and with the weaker grain boundaries the tensile tests led to brittle failure at the grain boundary [34], [89].

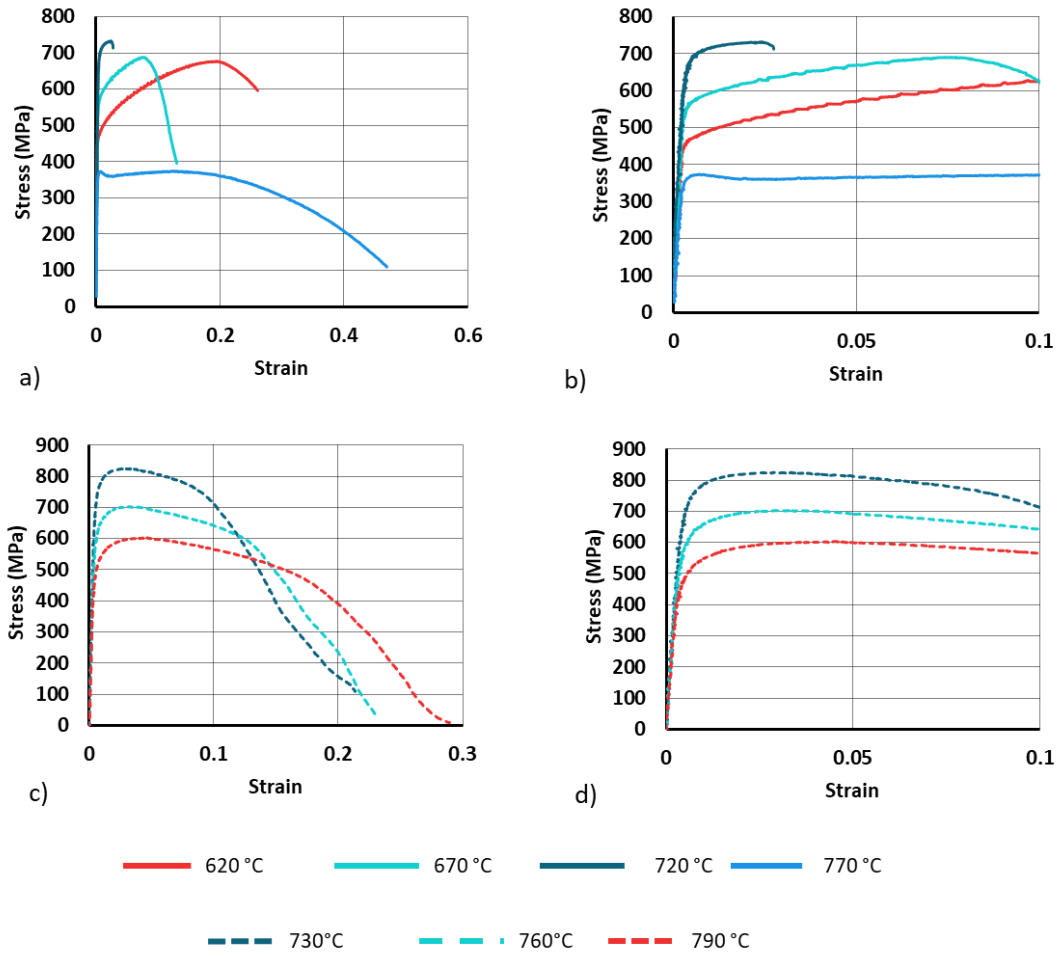

Figure 6.8: Engineering stress-strain curves obtained from tensile tests conducted at various temperatures; a) full stress-strain curve for IN718, b) magnified view of the elastic region and onset of plastic deformation for IN718, c) full stress-strain curves for AD730, and d) magnified view of the elastic region and onset of plastic deformation for AD730.

Table 6.3: Summary of mechanical properties measured during tensile testing of IN718 and AD730.

Material	Temperature (°C)	Young's Modulus (GPa)	0.2% offset (MPa)	UTS (MPa)	Elongation (%)
IN718	620	163	474	677	26.1
IN718	670	179	568	689	13.0
IN718	720	170	690	733	2.7
IN718	770	129	370	374	46.8
AD730	730	165	746	828	21.3
AD730	760	151	613	704	23.0
AD730	790	142	500	604	28.9

For the tensile tests conducted on AD730, as depicted in Figure 6.8c and d and summarised in Table 6.3, it's observed that increasing temperature results in decreased strength and increased ductility. This trend aligns with expectations for most non-precipitation-hardenable materials, influenced by factors such as grain growth, dynamic recovery, recrystallisation, and increased dislocation movement at higher temperatures. However, in the case of a γ'-strengthened nickel alloy like AD730 within this temperature range, this behaviour might seem unexpected. This can be partially explained by examining previous studies [150], which indicated that for tensile tests conducted at 700 °C on AD730 samples subjected to various ageing sequences, the peak in strengthening occurred around 730 °C, despite a higher rate of γ' precipitation being observed at 760 °C. Consequently, the decrease in strength with increasing temperature could be attributed, at least in part, to the ageing temperatures chosen, with temperatures beyond 730 °C (e.g., 760°C and 790°C) having shown to lead to a reduction in material strength.

6.3.3 Stress Relaxation Tests

An example of the stress relaxation curves for IN718 at 620 °C are illustrated in Figure 6.9 with different initial stress magnitudes. Due to the extensive time frame covered by the data, it may be challenging to discern that instead of stress values decreasing over time as is typical and shown in Figure 6.5, they are, in fact, increasing, as emphasised by the magnified view of the stress relaxation curve for an initial stress level of 420 MPa depicted in Figure 6.9b. This phenomenon, known as negative creep, has been documented previously for IN718 [71] and is attributed to volumetric shrinkage in the lattice parameters of the matrix due to the precipitation of γ' and γ''.

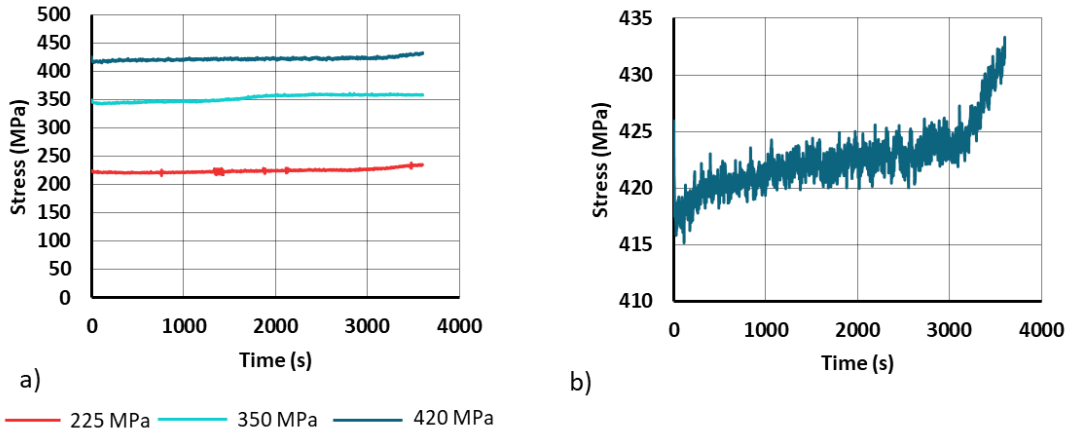

Figure 6.9: For IN718 at 620°C a) Stress relaxation curves at three different initial stress levels, and b) isolated stress relaxation curve for the initial stress level of 420 MPa.

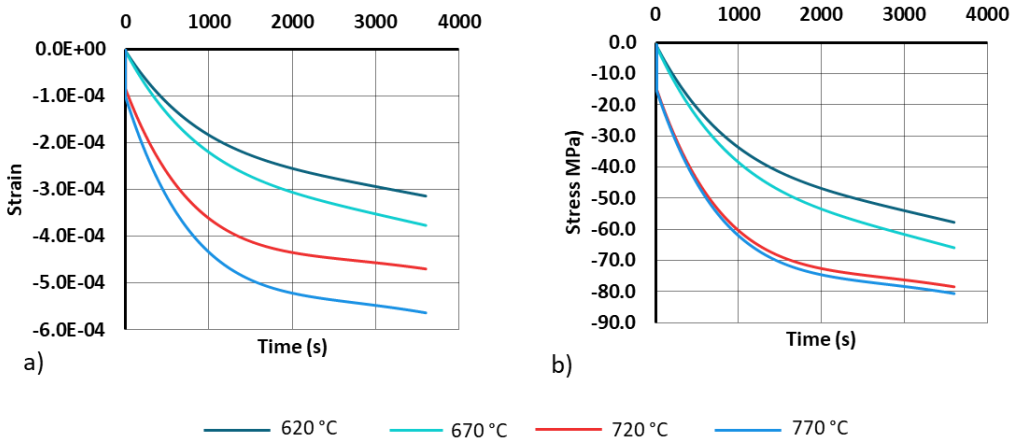

Figure 6.10: a) Dilatometry curves at various isothermal temperatures reconstructed from [71] for IN718, including interpolated curves at 670 °C and 770 °C representing the stress-free condition and demonstrating sample contraction, b) their corresponding stress values calculated using Hooke's law of elasticity.

Dilatometry tests under stress-free conditions at isothermal temperatures were conducted by Qin et al. [71] at 500 °C, 620 °C, and 720 °C to isolate the effect of volumetric shrinkage. Linear interpolation of this data was performed to generate plots for temperatures of 670 °C and 770 °C. Figure 6.10a presents a reconstruction of the plot from Qin et al. [71]incorporating the interpolated data. Since these strains were elastic, the equivalent stress evolution was derived by converting to stress using Young's modulus, as demonstrated in Figure 6.10b. Consequently, the impact of volumetric shrinkage at a given temperature and over time is now quantified in terms of the additional stress it imparts to stress relaxation tests and can be subtracted. Figure

6.11a displays the stress relaxation curve for IN718 at 620 °C for an initial stress state of 420 MPa as measured by the ETMT, while Figure 6.11b depicts the same data with the stress induced by volumetric sample contraction removed. This adjustment renders the shape of the stress relaxation curves more typical and facilitates the application of constitutive models such as the ZWA and hyperbolic (see Section 2.5.3 for more info).

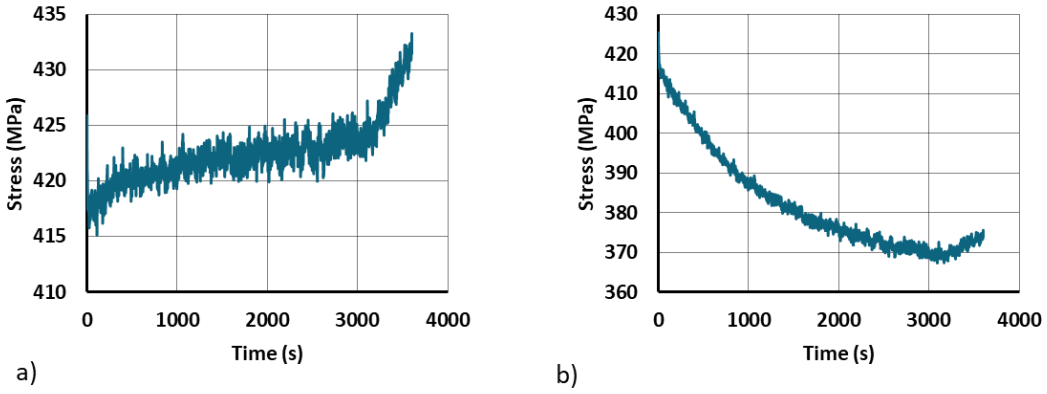

Figure 6.11: Stress relaxation curve for IN718 at 620 °C with an initial stress of 420 MPa, presented as a) as-measured data from the ETMT, uncorrected for sample contraction, and b) the same data after correction for sample contraction.

The stress relaxation plots for IN718 after having the correction for volumetric contraction are shown in Figure 6.12b-e. Stress relaxation can be seen to increase with higher temperatures, and also generally is more pronounced with greater initial stress levels. Figure 6.12a shows the initial loading of the samples at 620 °C before the commencement of stress relaxation, demonstrating good repeatability in the experiments due to overlap of the curves.

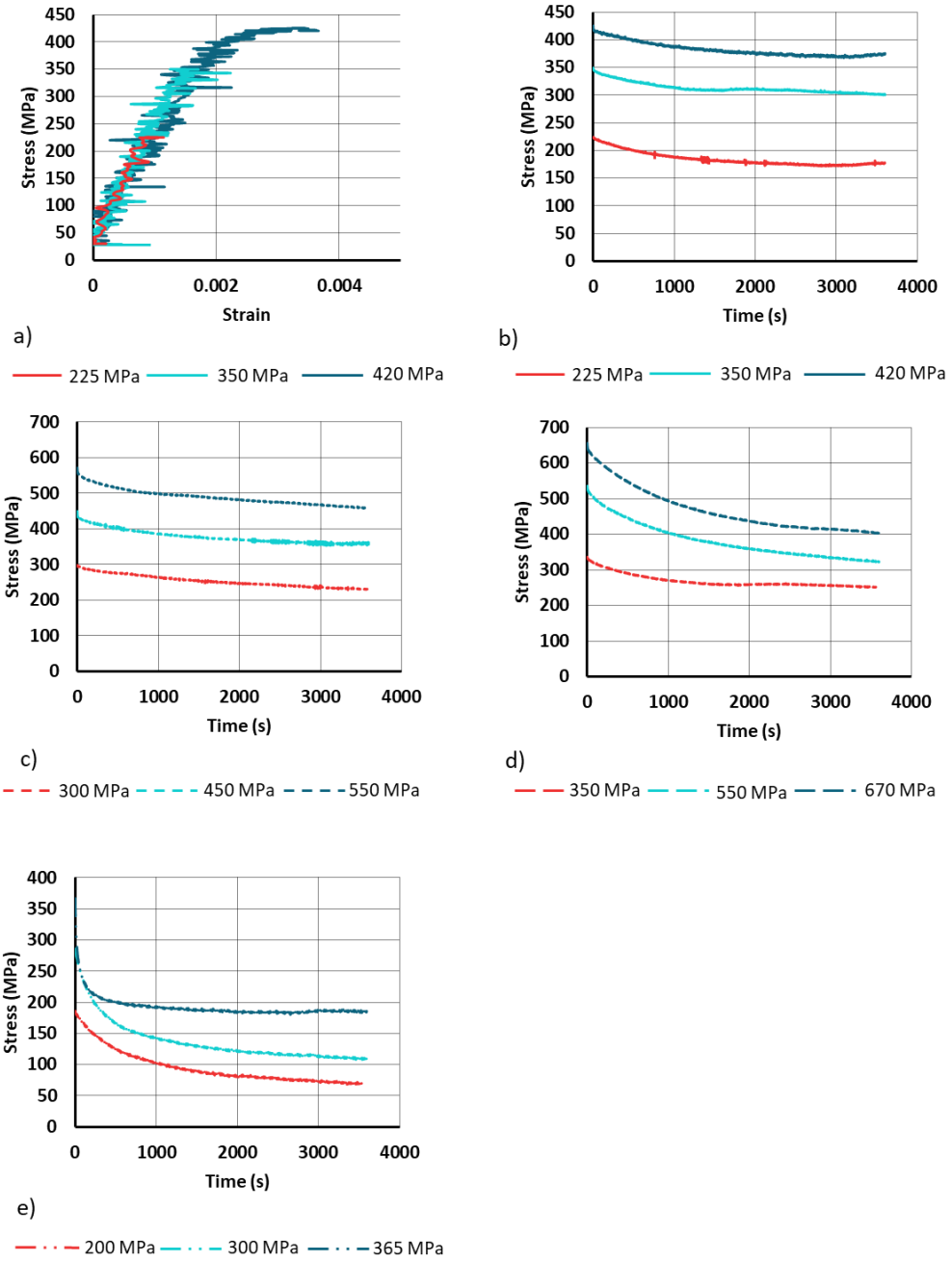

Figure 6.12: Results of stress relaxation tests conducted on IN718 at different temperatures, depicting: a) Engineering stress-strain curves measured by the DIC system at 620 °C, and Stress relaxation plots at b) 620 °C, c) 670 °C, d) 720 °C, and, d) 770 °C.

The approach employed for IN718, which involved using dilatometry data from literature and subsequently converting creep strains to stress to assess the impact of volumetric shrinkage on stress relaxation curves, was replicated for AD730. The dilatometry data utilised is presented in Figure 6.13a, while the resulting stress evolution is depicted in Figure 6.13b. The influence of

this evolution on the stress relaxation curve for AD730, conducted at 730 °C with an initial stress value of 350 MPa, is illustrated in Figure 6.13c and d.

Upon comparing the stress relaxation curves before and after removing the effects of volumetric shrinkage (Figure 6.13c and d), it's evident that the curve still exhibits a sustained increase in stress over a period of nearly 1000 seconds. Additionally, a sustained plateau in stress levels was observed near the beginning of the tests conducted at 730 °C with an initial stress level of 550 MPa, as well as at 760 °C with an initial stress level of 300 MPa. This indicates that the dilatometry data extracted from literature does not align sufficiently with the microstructure and chemical composition of this material to completely mitigate the effects of volumetric shrinkage. Nonetheless, the dilatometry data was utilised to prove the method.

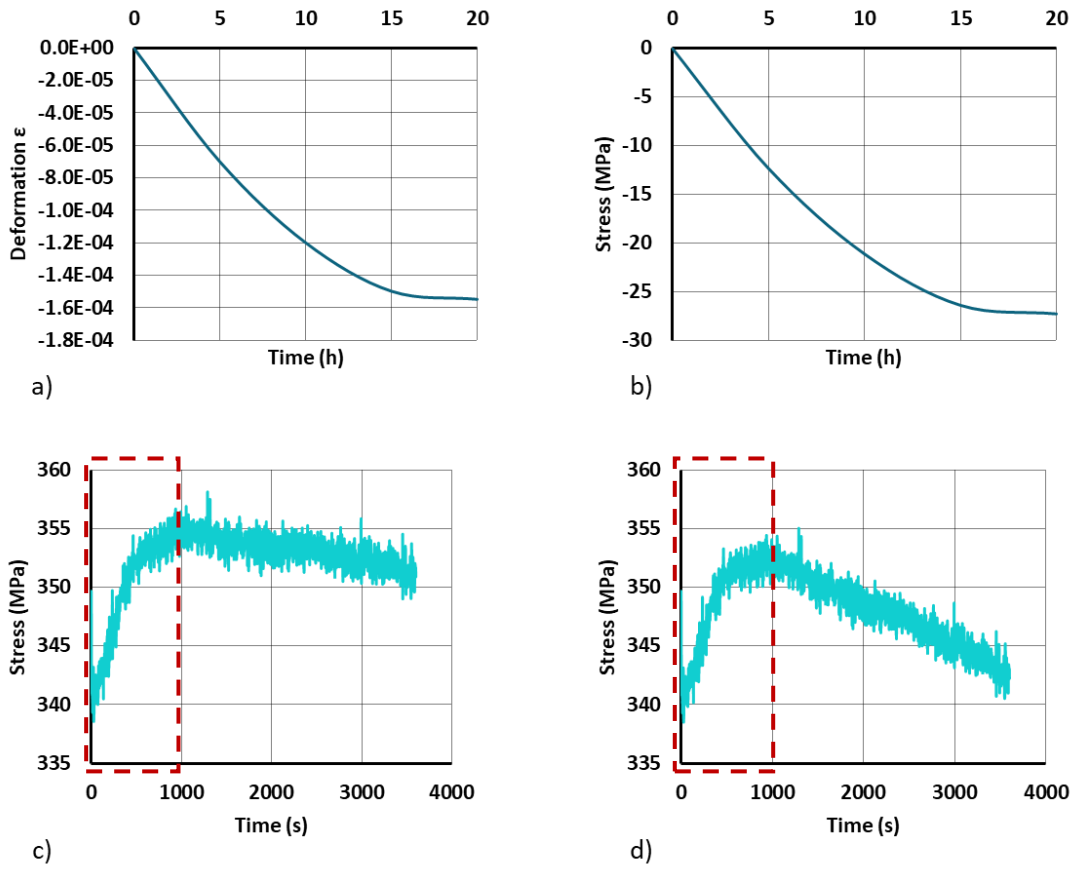

Figure 6.13: a) Isothermal dilatometry curve measured at 760 °C for AD730 showing sample contraction in the stress-free condition, reconstructed from [129], b) its corresponding stress value calculated via Hooke's law for elasticity, c) the as-measured and uncorrected stress relaxation curve for AD730 at 730 °C with an initial stress of 350 MPa, and d) the corrected stress relaxation curve for the data in (c).

The stress relaxation data for AD730 corrected for volumetric shrinkage can be seen in Figure 6.14. As was the case with IN718, an increase in the temperature or an increase in the initial stress value at a given temperature, leads to an increase in the magnitude of stress relaxation within the material.

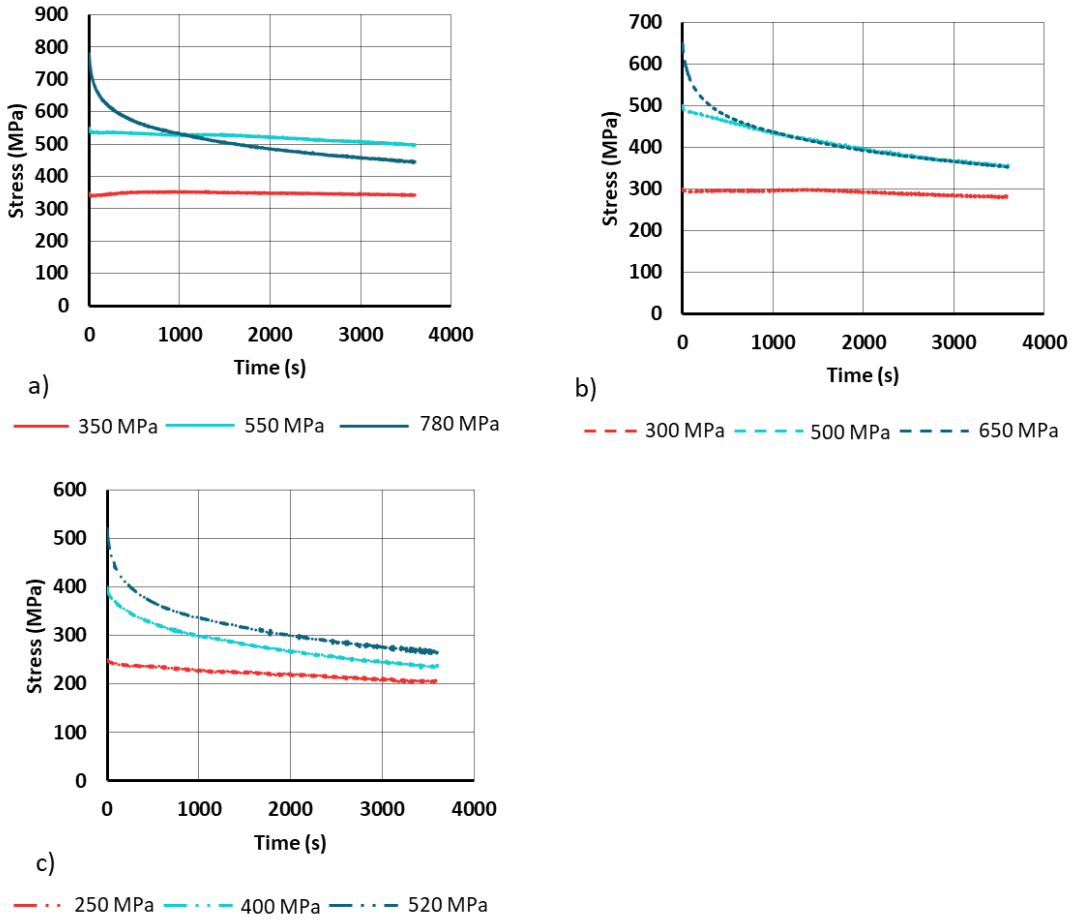

Figure 6.14: Results of stress relaxation tests conducted on AD730 at different temperatures, depicting relaxation plots at a) 730 °C, b) 760 °C, and d) 790 °C.

6.3.4 ZWA Stress Relaxation Model

Based on the experimental results of the stress relaxation tests, the material constants for the ZWA stress relaxation model can be developed. The ZWA equation, represented by Equation 6.1, describes the stress after relaxation (σ_R), where σ_0 is the initial residual stress, t is the annealing time, m is a material constant associated with the mechanism of stress relaxation. Equation 6.2 defines A, where B is a material constant, k is Boltzmann's constant which is 8.617343×10^{-5} eV/K, T is the annealing temperature, and ΔH represents the activation enthalpy during stress relaxation.

$$\frac{\sigma_R}{\sigma_0} = \exp\left(-(At)^m\right)$$

Equation 6.1

$$A = Bexp(-\frac{\Delta H}{kT})$$

Equation 6.2

By taking the natural logarithm of Equation 6.1 and applying a logarithmic transformation, Equation 6.1 can be rewritten as Equation 6.3. By plotting log(-ln($\frac{\sigma_R}{\sigma_0}$)) vs. log(t) for each temperature and initial stress value, this allows for assessing whether the ZWA equation holds true for the stress relaxation curves. In Figure 6.15, most instances exhibit a straight line with a good fit, indicating satisfaction of the ZWA equation. The slope of these lines represents the material constant, m. However, different slope values pose challenges in achieving a global fit, likely due to the complex interaction between γ', γ'', and δ precipitations with stress relaxation [150]. Further linear regression analysis enables determination of the average ΔH, and the parameters A and B. Due to the challenge in determining a global set of parameters which accurately model the stress relaxation behaviour of the two investigated materials, an approach for local fitting tailored to each curve's temperature and initial stress, was applied.

$$\mathrm{Log}\left(-\ln\left(\frac{\sigma_R}{\sigma_0}\right)\right) = mlogA + mlog(t)$$

Equation 6.3

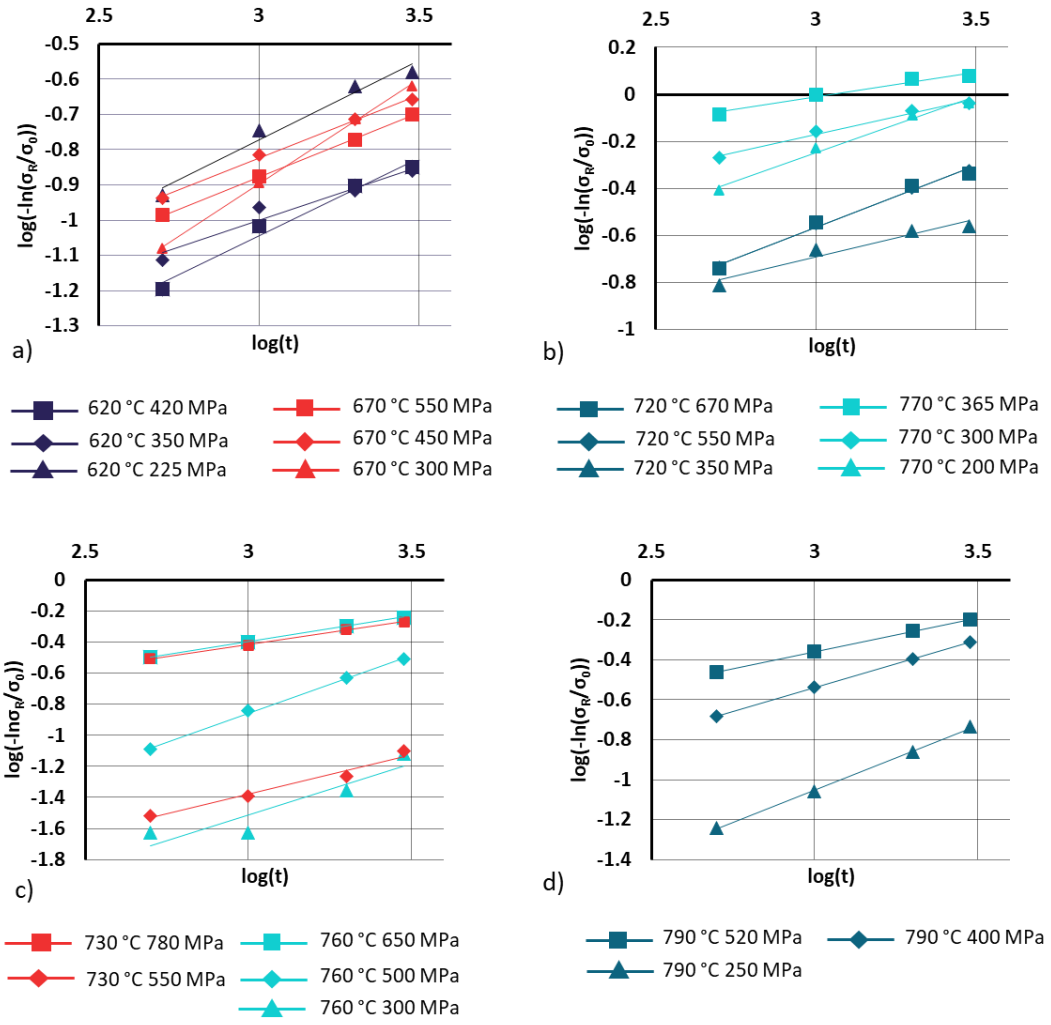

Figure 6.15: Plots of log(-ln($\frac{\sigma_R}{\sigma_0}$)) vs. log(t) used to determine m value for a) IN718 at temperatures of 620 °C and 670 °C, b) IN718 at temperatures of 720 °C and 770 °C, c) AD730 at temperatures of 730 °C and 760 °C, and d) AD730 at 790 °C.

The local fit parameters for IN718 and AD730 are provided in Table 6.4 and Table 6.5, respectively. Model accuracy was assessed by calculating the root mean square error (RMSE), the average absolute relative error (AARE), and the coefficient of determination (R^2) which are expressed in Equation 6.4, Equation 6.5, and Equation 6.6 respectively, where E_i is the experimental stress values, P_i is the predicted stress values, N is the number of data points, and $\overline{E_t}$ is the average value of E_i. The accuracy of both fits can be seen from the plots in Figure 6.16. For IN718, the AARE, RMSE, and R^2 are 1.66%, 5.25, and 0.99, respectively, while for AD730, the corresponding values are 0.86%, 3.95, and 0.99. In both cases this represents an excellent fit and shows that the ZWA model was a suitable choice and is functioning correctly.

$$RME\ (MPa) = \sqrt{\frac{1}{N}\sum_{i=1}^{N}(E_i - P_i)^2}$$

Equation 6.4

$$AARE\ (\%) = \frac{1}{N}\sum_{i=1}^{N}\left|\frac{E_i - P_i}{E_i}\right| x100$$

Equation 6.5

$$R^2 = 1 - \frac{\sum(E_i - P_i)^2}{\sum(E_i - \bar{E}_i)^2}$$

Equation 6.6

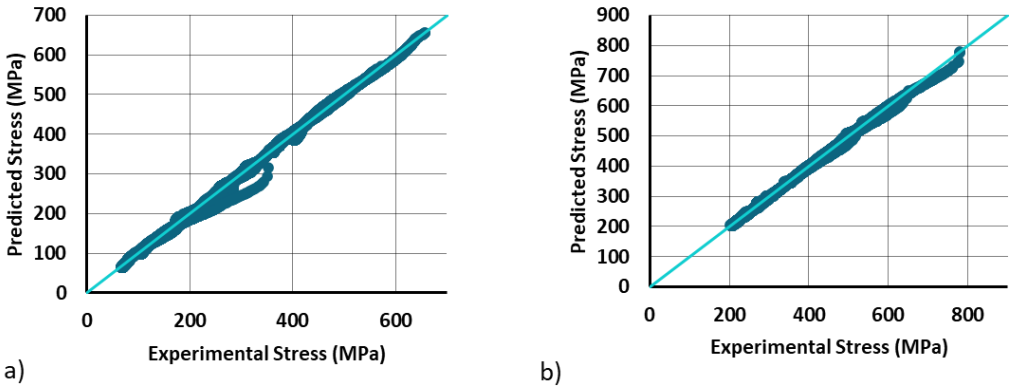

Figure 6.16: Correlation of experimental stress with predicted stress by the ZWA model using locally fitted parameters for a) IN718 and b) AD730.

Table 6.4: Local fit parameters for ZWA model of IN718.

Temperature (°C)	Initial Stress Value (MPa)	m value	Average ΔH (eV)	A value (s^{-1})	B Value
620	225	0.451	0.513	1.95×10^{-5}	1.52×10^{-2}
620	350	0.306	0.513	5.47×10^{-7}	4.27×10^{-4}
620	420	0.443	0.513	4.39×10^{-6}	3.43×10^{-3}
670	300	0.593	0.513	3.08×10^{-5}	1.69×10^{-2}
670	450	0.359	0.513	5.12×10^{-6}	2.81×10^{-3}
670	550	0.363	0.513	3.87×10^{-6}	2.12×10^{-3}
720	350	0.326	0.513	7.51×10^{-6}	3.0×10^{-3}
720	550	0.529	0.513	8.50×10^{-5}	3.41×10^{-2}
720	670	0.525	0.513	8.34×10^{-5}	3.33×10^{-2}
770	200	0.485	0.513	3.08×10^{-4}	9.24×10^{-2}
770	300	0.302	0.513	2.74×10^{-4}	8.23×10^{-2}
770	365	0.213	0.513	8.84×10^{-4}	2.65×10^{-1}

Table 6.5: Local fit parameters for ZWA model of AD730.

Temperature (°C)	Initial Stress Value (MPa)	m value	Average ΔH (eV)	A value (s^{-1})	B Value
730	350	0.350	0.21	4.9×10^{-9}	5.49×10^{-8}
730	550	0.509	0.21	1.96×10^{-6}	2.17×10^{-5}
730	780	0.306	0.21	4.38×10^{-5}	4.85×10^{-4}
760	300	0.658	0.21	5.08×10^{-6}	5.62×10^{-5}
760	500	0.745	0.21	7.09×10^{-5}	7.85×10^{-4}
760	650	0.332	0.21	6.33×10^{-5}	7.0×10^{-4}
790	250	0.664	0.21	2.34×10^{-5}	2.6×10^{-4}
790	400	0.476	0.21	7.43×10^{-5}	8.22×10^{-4}
790	520	0.333	0.21	8.60×10^{-5}	9.52×10^{-4}

For IN718, achieving a satisfactory fit with global parameters proved challenging. Consequently, the dataset was divided into one set of parameters applied to temperatures of 670 °C and below, and another set to temperatures of 720 °C and above. Table 6.6 displays the corresponding values, with AARE, RMSE, and R^2 calculated for each temperature range. Notably, for temperatures of 620 °C to 670 °C, the AARE, RMSE, and R^2 are 2.67%, 9.01, and 0.99, respectively, reflecting a good fit. Conversely, for temperatures of 720 °C to 770 °C, the AARE, RMSE, and R^2 values are 36.2%, 62.1, and 0.745, indicating a less favourable fit.

Figure 6.17 highlights this difference in fit quality, which can be attributed to the different response from tests carried out at 770 °C. This distinct behaviour is observed in the tensile test results carried out at 770 °C and shown in Figure 6.8a. Thus, model parameters for temperatures of 720 °C only were developed, and the fit evaluated only against the data collected at 720 °C. This resulted in an improved AARE, RMSE, and R^2 values of 5.55%, 20.916, and 0.96, respectively (Figure 6.17c). This adjustment effectively captures the stress relaxation behaviour within this temperature range.

The precise temperature in-between 670 °C and 720 °C at which the first set of key parameter values used for temperatures of 670 °C and below become less suited to predict stress relaxation behaviour, and the second set of parameter values used for temperatures of 720 °C become more suited is yet unknown. An arbitrary cut-off of 695 °C was therefore selected. The data collected at 770 °C shows different behaviour compared to the other temperatures such that a third fit would have to take place to model the stress relaxation behaviour at that temperature. The author chose not to do that as the temperatures covered are thought to sufficiently cover the most common ageing temperatures associated with this material.

Table 6.6: ZWA parameters developed for IN718 for two different temperature ranges.

Temperature (°C)	Average m value	Average ΔH (eV)	A value (s^{-1})	B Value
620-670	0.420	0.513	7.08×10^{-6}	4.61×10^{-3}
720-770	0.460	0.513	4.77×10^{-5}	1.9×10^{-2}

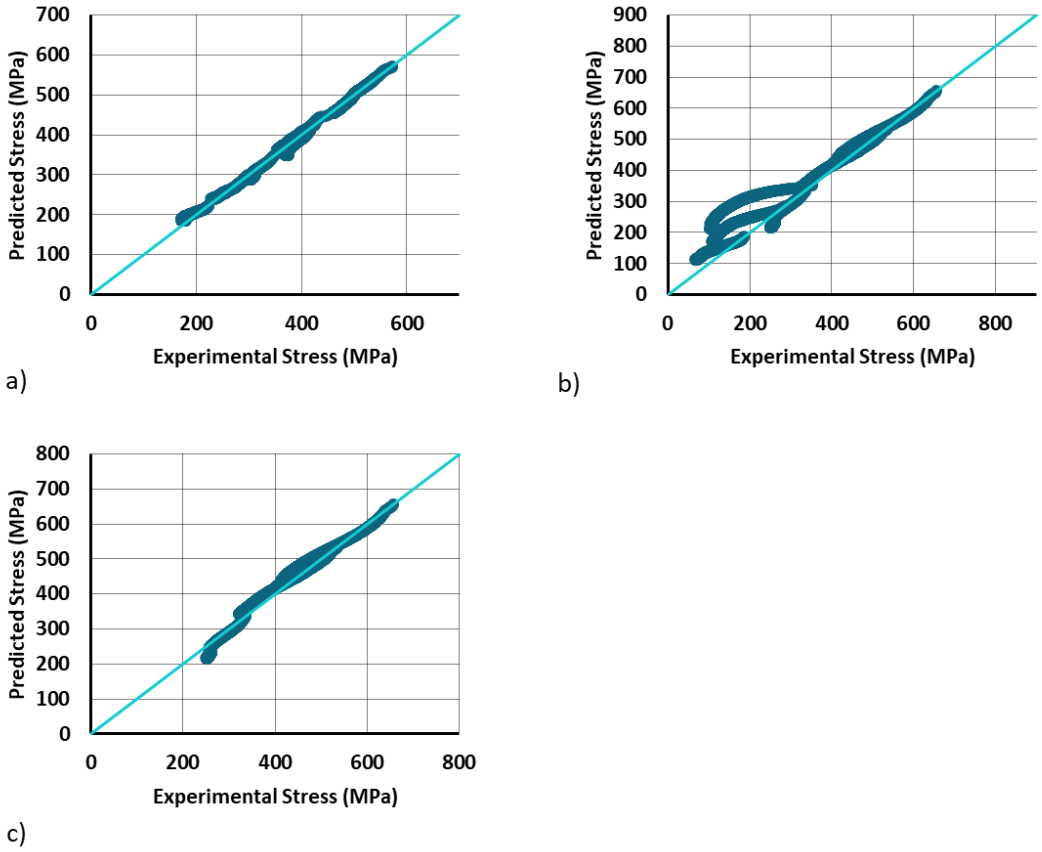

Figure 6.17: Correlation of experimental and predicted stress from ZWA model for IN718 for a) temperatures of 620 °C to 670 °C, b) temperatures of 720 °C to 770 °C, and c) a temperature of 720°C.

Obtaining a global fit, or even a semi-global fit as was the case for IN718, also proved challenging for AD730. The stress relaxation behaviour did not seem to differ based on the different temperatures as much as it did based on the different initial stress values. The relaxation behaviour above an initial stress value of 400 MPa showed sufficiently different behaviour that it warranted a different set of values for the key ZWA parameters. The different values based on the range of initial stresses can be seen in Table 6.7. The AARE, RMSE, and R^2 values for the initial stress of 400 MPa and below is 4.51%, 15.02 and 0.86, and the values for initial stresses above 400 MPa are 12.01%, 78.374 and 0.36. The accuracy of the fit can be seen in Figure 6.18 and demonstrates a good fit for tests at lower initial stresses, but a less than average fit for tests at the higher initial stresses. This represented the best compromise for this dataset.

Table 6.7: ZWA parameters developed for AD730 for two different ranges of initial stresses.

Initial Stress Value (MPa)	Average m value	Average ΔH (eV)	A value (s^{-1})	B Value
<400	0.604	0.21	1.15×10^{-5}	7.93×10^{-5}
≥400	0.451	0.21	1.05×10^{-4}	1.16×10^{-3}

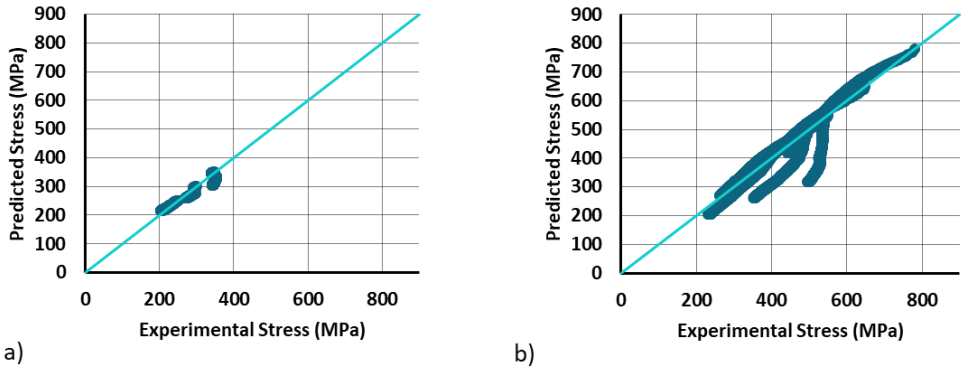

Figure 6.18: Correlation of experimental and predicted stress from ZWA model for AD730 for a) initial stress values of < 400 MPa, and b) initial stress values of ≥ 400 MPa.

6.3.5 Hyperbolic Stress Relaxation Model

The hyperbolic law for stress relaxation is expressed by Equation 6.7 [89], where σ(t) represents the stress value at a specific time, σ_∞ is the horizontal asymptotic stress, and a, b, and m are material parameters. Rearranging Equation 6.7 and taking the natural logarithm gives Equation 6.8.

Plots of σ_∞ / σ_0 for each material (Figure 6.19) were generated to analyse the relationship between the ratio of initial stress and asymptotic stress. These plots aid in understanding the consistency of stress relaxation behaviour at a given temperature, and across different temperatures.

Figure 6.19 illustrates that for IN718, the ratios of σ_∞ / σ_0 remain relatively consistent at each temperature but decrease with increasing temperature, particularly evident in tests conducted at 770 °C. This divergence indicates that the stress relaxation behaviour at 770 °C deviates from that observed at lower temperatures. These findings align with the results of the ZWA model fitting discussed in the previous section, where tests performed at 770 °C exhibited distinct behaviours necessitating different fit parameter values.

$$\sigma(t) = \sigma_{\infty} + b(t+a)^{-m}$$

Equation 6.7

$$\ln[\sigma(t) - \sigma_{\infty}] = lnb - mln(t+a)$$

Equation 6.8

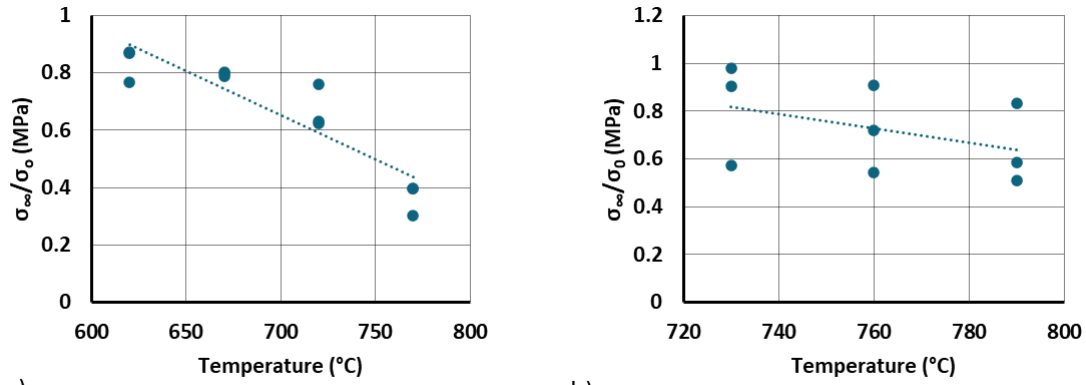

Figure 6.19: Ratios of σ_{∞}/σ_0 at different temperatures used to determine the consistency in stress relaxation behaviour, for a) IN718, and b) AD730.

Using linear regression methods, the value of *m* can be determined from the slope of the $\ln[\sigma(t) - \sigma_{\infty}]$ vs. $ln(t+a)$ plots for each test. To ensure a straight line in the plot, an appropriate value of *a* must be selected, as depicted in Figure 6.20. Subsequently, the y-intercept and the value of *b* can be determined.

To select suitable values of *a*, *b*, and *m*, a reduced gradient solver built into Microsoft Excel was utilised. This tool helped in determining *a, b,* and *m* values that minimised the AARE between the experimental and predicted stress values for each temperature and initial stress. The permissible ranges for *a, b,* and *m* were set between 1 and 1,000, 1 and 10,000MPa, and 0 and 1, respectively. This approach provided a local fit for each curve, and the resulting values for IN718 and AD730 are presented in Table 6.8 and Table 6.9, respectively, with the fit illustrated in Figure 6.21.

For IN718, the AARE, RMSE, and R^2 values are 3.81%, 12.04, and 0.99, respectively. Similarly, for AD730, these values are 2.34%, 10.58, and 0.989. This indicates an excellent fit, as expected from this type of local fit.

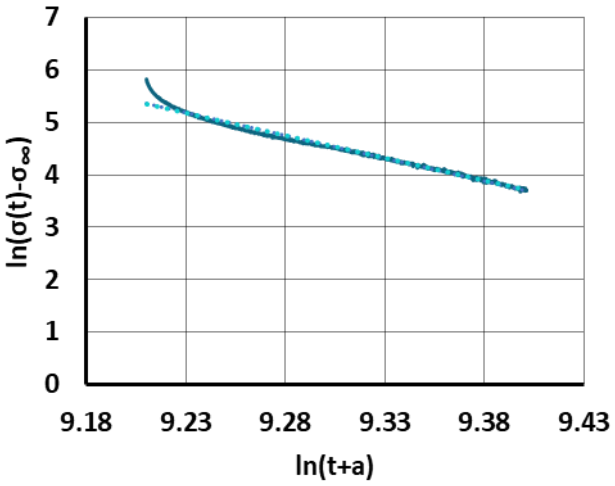

Figure 6.20: $ln[\sigma(t) - \sigma_\infty]$ vs. $ln(t + a)$ plot for AD730 at 730°C with an initial stress of 780MPa demonstrating the method used to determine the slope value m, by altering the value of a.

Table 6.8: Local fit parameters for Hyperbolic model of IN718.

Temperature (°C)	Initial Stress (MPa)	a value	m value	b value (MPa)
620	225	194	0.97	1 X 10^4
620	350	342.4	0.9	1 x 10^4
620	420	219.6	0.95	1 X 10^4
670	300	317	0.86	1 X 10^4
670	450	227	0.87	1 X 10^4
670	550	336	0.77	1 X 10^4
720	350	149.6	0.92	1 X 10^4
720	550	156.9	0.73	1 X 10^4
720	670	132.6	0.71	1 X 10^4
770	200	149.5	0.85	1 X 10^4
770	300	97.4	0.85	1 X 10^4
770	365	74.6	0.88	1 X 10^4

Table 6.9: Local fit parameters for Hyperbolic model of AD730.

Temperature (°C)	Initial Stress (MPa)	a value	m value	b value (MPa)
730	350	1000	0.32	78.67
730	550	1000	0.55	2998
730	780	138.3	0.69	$1 X 10^4$
760	300	1000	0.74	5251
760	500	338	0.7	$1 X 10^4$
760	650	140.9	0.71	$1 X 10^4$
790	250	592.5	0.84	$1 X 10^4$
790	400	243	0.73	$1 X 10^4$
790	520	141	0.74	$1 X 10^4$

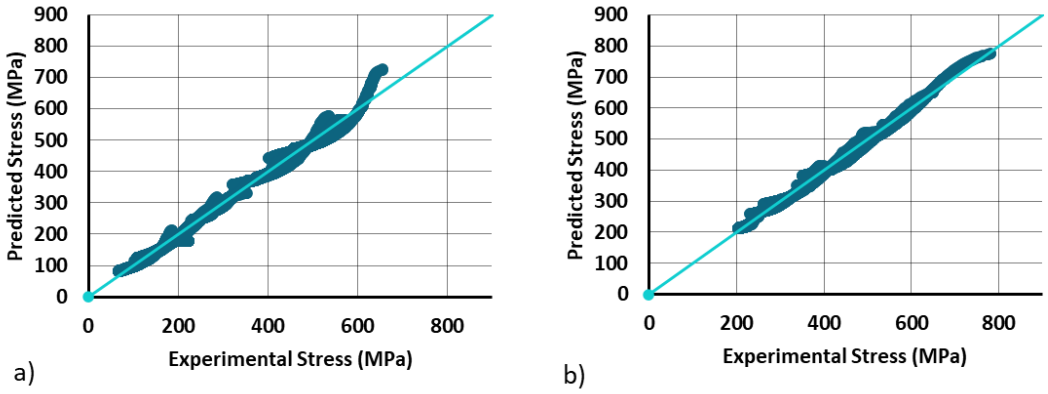

Figure 6.21: Correlation of experimental and predicted stress from hyperbolic model using locally fitted parameters for a) IN718, and b) AD730.

Similarly to the approach used for the ZWA model, a semi-global fit was attempted for IN718 by dividing the data into two temperature ranges. The same temperature ranges were selected, and the results are illustrated in Figure 6.21.

For temperatures of 670 °C and below, the AARE, RMSE, and R^2 values are 2.41%, 11.72, and 0.98, respectively. For temperatures of 720°C and above, these values are 6.37%, 28.29, and 0.95, respectively. The corresponding parameters are provided in Table 6.10. Overall, this approach demonstrates a reasonable fit to the experimental data.

Table 6.10: Hyperbolic parameters developed for IN718 for two different temperature ranges.

Temperature (°C)	Average a value	Average m value	Average b value (MPa)
620-670	223.4	0.92	$1 X 10^4$
720-770	66.04	0.89	$1 X 10^4$

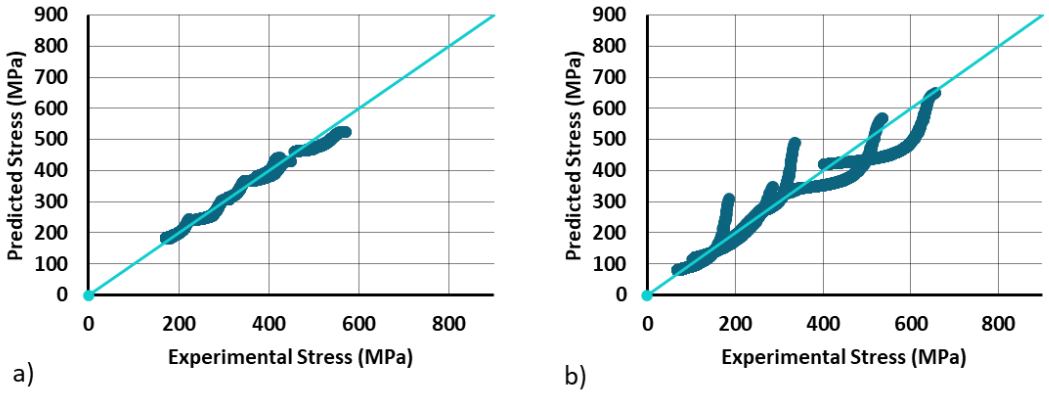

Figure 6.22: Correlation of experimental and predicted stress from hyperbolic model for IN718 a) at temperatures of 620°C to 670°C, and b) temperatures of 720°C to 770°C.

A semi-global fit was applied to AD730 using the hyperbolic model, following a similar approach to the separation used for the ZWA model. Data with initial stress values below 400MPa were grouped together, and a set of parameters was determined for this subset. Conversely, tests with initial stress values equal to or greater than 400MPa were treated separately, with a distinct set of parameter values determined for the hyperbolic model. The corresponding parameter sets are listed in Table 6.11.

For initial stresses below 400MPa, the AARE, RMSE, and R^2 values are 2.21%, 8.44, and 0.98, respectively. For initial stresses equal to or above 400MPa, these values are 3.92%, 22.76, and 0.94, respectively. This is illustrated in Figure 6.23.

Table 6.11: Hyperbolic parameters developed for AD730 for two different ranges of initial stresses.

Initial Stress Value (MPa)	Average a value	Average m value	Average b value (MPa)
<400	433.85	0.9	$1 X 10^4$
≥400	170.58	0.73	$1 X 10^4$

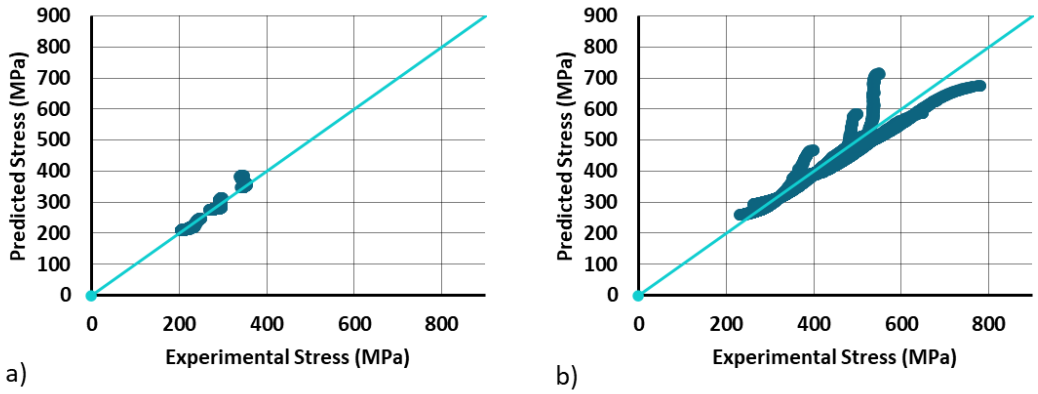

Figure 6.23: Correlation of experimental and predicted stress from hyperbolic model for AD730 a) initial stress values of < 400 MPa, and b) initial stress values of ≥ 400 MPa.

6.4 Discussion

The stress relaxation behaviour observed in both IN718 and AD730 (Figure 6.9) deviates from the typical relaxation behaviour by exhibiting an increase in stress over time rather than a decrease. This unusual relaxation phenomenon has been previously reported in literature for both alloys. Qin et al. [71] conducted neutron diffraction studies on IN718, revealing a contraction in lattice strain during ageing due to the migration of niobium atoms and the formation of γ'' precipitates. This led to an overall contraction in the sample's volume, termed as "negative creep". Despite the significant contraction observed, macroscopic relaxation was still evident at certain temperatures and initial stresses. It was shown that the sample contraction was greatest at a temperature of 720 °C, which is often the first temperature in the two-stage ageing of IN718 and shown to grow γ''. Despite this, the sample still showed macroscopic relaxation at that temperature, demonstrating the competing phenomenon of stress relaxation and volume contraction. The concept of volume contraction being temperature-dependent underscores the necessity of incorporating this phenomenon into constitutive models.

In this chapter, efforts were made to separate the influence of volume shrinkage from stress relaxation behaviour and to model stress relaxation using established constitutive models. As demonstrated by Qin et al. [71] , the contraction of the sample is dependent on the ageing temperature, emphasising the need to consider this factor. For IN718, stress-free isothermal dilatometry data from literature was extrapolated to relevant temperatures, while for AD730, data at 760 °C was utilised for all test temperatures. This provided strain vs. time data, which

was converted to stress using the linear-elastic stress-strain relationship. Subtracting the stress reduction due to volumetric contraction yielded relaxation plots minus the influence of volumetric contraction. New plots where then formed and thought of as pure stress relaxation plots. Although this approach resulted in typical relaxation plots for IN718, some atypical behaviour persisted in AD730 plots.

The precipitation of γ' and γ'' precipitates in Ni-based superalloys is influenced by various factors, including alloy composition, thermal history, and cooling rate from above the solvus temperature. Obtaining dilatometry data specific to these microstructures could have provided a more accurate assessment of sample contraction. However, due to time and budget constraints in the project, collecting such data was not feasible, leading to reliance on literature data with potentially different microstructures.

The stress relaxation behaviour of AD730 and IN718 curves exhibit varying relaxation rates based on initial stress and temperature. This phenomenon, previously attributed to dominant relaxation mechanisms at specific conditions [129], can be better understood through Norton diagrams and Norton's law. Norton's law, expressed as Equation 6.9, provides insights into creep behaviour, with σ representing stress, $\dot{\varepsilon}_p$ denoting creep strain, A as the material constant, and n as the Norton coefficient.

$$\dot{\varepsilon}_p = A\sigma^n$$

Equation 6.9

The Norton coefficient value indicates the underlying deformation mechanism:

- n=1: Diffusion is the primary mechanism.
- 1<n ≤ 7: Deformation mechanisms involve diffusion, dislocation-based phenomena, or a combination.
- N>7: Dislocation-based mechanisms govern relaxation.

Norton diagrams for IN718 and AD730 are depicted in Figure 6.24 and Figure 6.25, respectively. For IN718, n values initially exceed 7 at 620 °C and 670 °C, suggesting dislocation-based mechanisms, then transitions to values between 1 and 7, indicating a mixture of diffusion and dislocation-based mechanisms. AD730 exhibits predominantly n values greater than 7 for higher stresses, and values between 1 and 7 for lower stresses, indicating

dislocation-based mechanisms for higher stress, and a combination of dislocation and diffusion-based mechanisms at lower stresses. There were occasional negative n values due to noisy stress data which were omitted for both materials, but especially so for A730. Attempts were made using an exponential smoothing filter built into Microsoft Excel to reduce the noise, however this proved unsuccessful, and a suitable *n* value was not able to be determined.

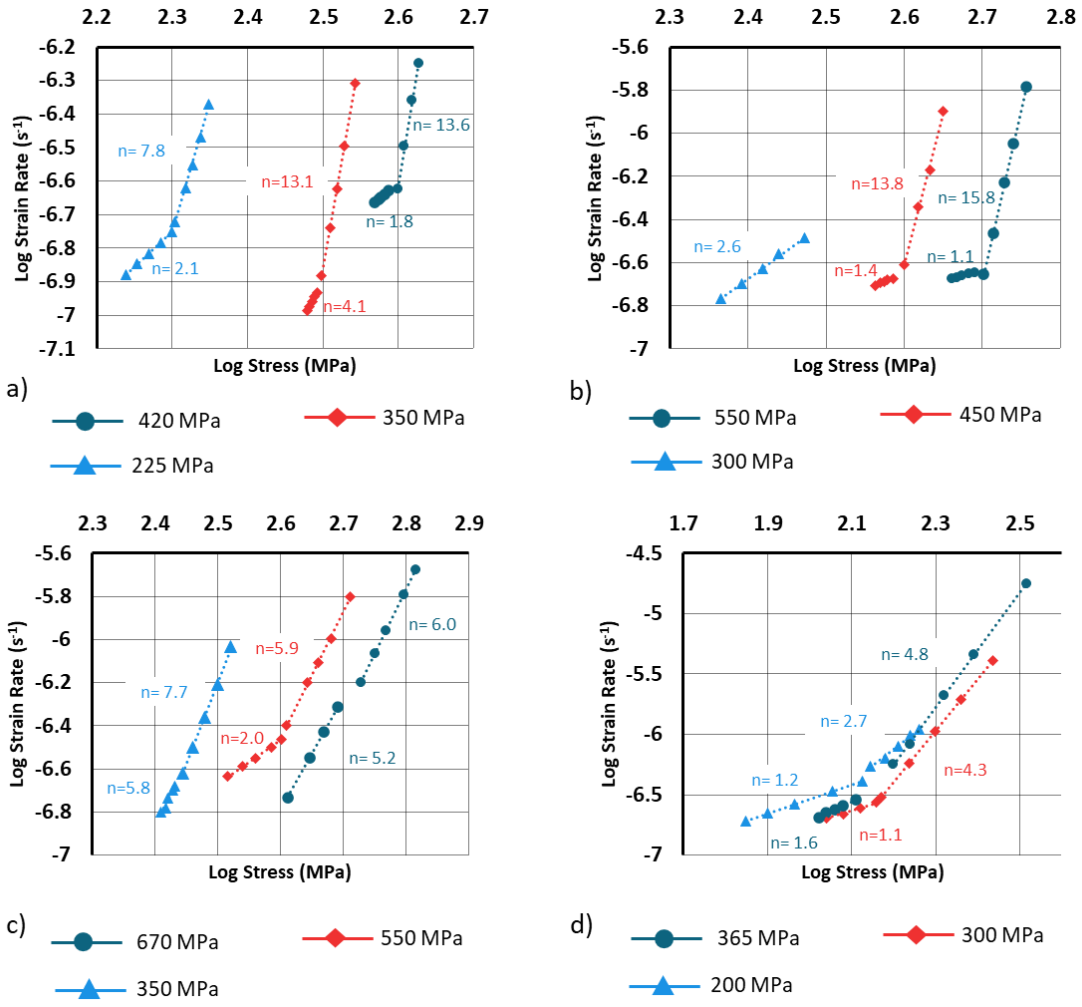

Figure 6.24: Norton diagram for IN718 at different temperatures a) 620 °C, b) 670 °C, c) 720 °C, and c) 770 °C.

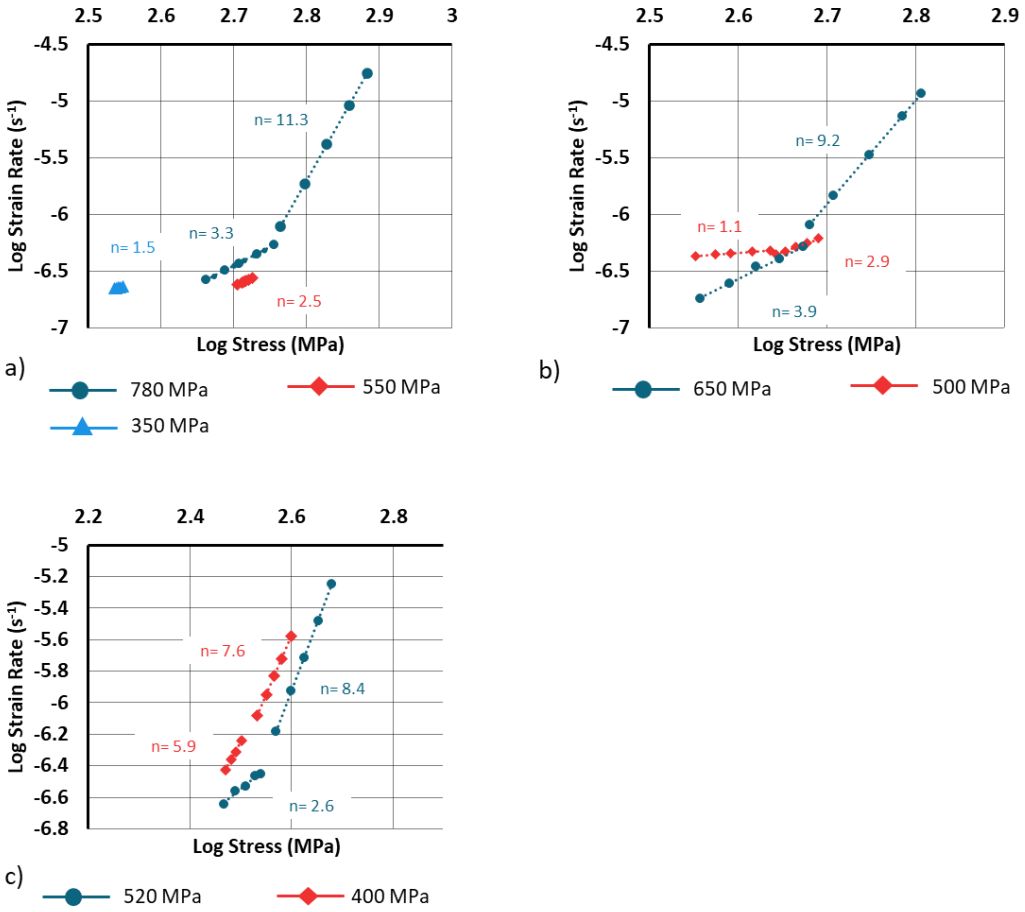

Figure 6.25: Norton diagram for AD730 at temperatures a) 730 °C, b) 760 °C, and c) 790 °C.

Both the ZWA and hyperbolic laws were unable to accurately characterise the relaxation behaviour of the investigated materials through a global fit. The Norton diagrams presented in Figure 6.24 and Figure 6.25 shed light on this challenge. For IN718, a semi-global approach was adopted by grouping data at 620 °C and 670 °C together, using one set of fitting parameters, and grouping data at 720 °C and 770 °C together with a different set of parameters. As depicted in Figure 6.24, the *n* values for 620 °C and 670 °C exhibit similarities, especially in the initial stages of relaxation, where all *n*-values exceed 7, indicating dislocation-based mechanisms driving the behaviour. Conversely, at 720 °C and 770 °C, the *n* values are lower, suggesting a mixture of dislocation- and diffusion-based mechanisms. This implies that different relaxation mechanisms necessitate distinct sets of parameters for the constitutive stress relaxation model. Similar trends were observed for AD730, as shown in Figure 6.25, where higher initial stresses correspond to *n* values exceeding 7, indicative of dislocation-

driven relaxation, while lower initial stresses result in *n* values close to 1, suggesting a predominantly diffusion-based deformation mechanism. However, the wide range of *n* values does not neatly align with specific temperatures or initial stress values, posing challenges for semi-local fitting based on these parameters alone. Future efforts may benefit from characterising *n* values independently and utilising them as crucial criteria for defining semi-local fitting strategies for specific datasets. Of course, further thought would have to be given into how such an approach of discriminating on the grounds of the *n* value could be implemented into a FE model.

When developing a constitutive model to describe stress relaxation in materials like IN718 and AD730 during ageing, understanding the volume contraction behaviour as a function of temperature is crucial. This knowledge helps in modelling a range of ageing temperatures, especially if the part undergoes non-isothermal heat treatment or if the ageing temperature varies. The next step of this work would be to develop a more complex constitutive model that couples volumetric contraction as a function of temperature and stress relaxation behaviours.

6.5 Conclusions

In this chapter, we investigated the stress relaxation behaviour of IN718 and AD730 during ageing heat treatments. Stress relaxation tests, following the ASTM E328-21 standard, were conducted for both materials across various ageing temperatures. Subsequently, two constitutive models, the ZWA and the hyperbolic models, were developed and their accuracy were evaluated. The following conclusions were drawn:

- Stress relaxation tests were carried out for both materials and at times showed atypical relaxation behaviour with the stress appearing to increase over time. This had been previously reported in literature for both materials and was due to precipitation of the γ’ and γ’’ causing depletion of the γ’ and γ’’ formers in the γ matrix, shortening the lattice parameter causing volumetric shrinkage in the material. This was deemed to be the cause of the atypical stress relaxation curves obtained in this study.
- Some curves, despite the volumetric shrinkage, still showed typical stress relaxation behaviour. This was due to the competing phenomenon of vacancy diffusion and dislocation gliding (i.e., relaxation mechanism) with volume contraction. It can be said that in the case of typical relaxation plots, the relaxation mechanisms where more dominant than the effect of the volumetric shrinkage.

- De-coupling of the stress relaxation behaviour and volumetric contraction was attempted by making use of stress-free isothermal dilatometry data from literature. For a more accurate de-coupling of these phenomenon and determination of the volumetric shrinkage, it is recommended that dilatometry test is carried out for the materials and microstructures investigated in this study, and not to rely on data from literature.
- Norton diagrams were plotted to better understand the deformation mechanisms driving the stress relaxation behaviour for both materials. Higher stress and lower temperatures tended to be driven by dislocation-based mechanisms, whereas higher temperature and lower initial stresses tended to be driven by a mixture of dislocation and diffusion-based deformation mechanisms.
- The hyperbolic law demonstrated better suitability in modelling the stress relaxation behaviour of both materials, utilising a semi-local fit with lower AARE across all cases compared to the semi-local fit of the ZWA model.

The stress relaxation data obtained in this chapter is utilised in Chapter 8 to develop a multi-step, multi-process model for AD730. The ageing sequence of this model is informed by the findings of this chapter.

7

Constitutive Modelling of Hot Deformation Behaviour in AD730

7.1 Introduction

The study in this chapter looks to understand the hot deformation behaviour of alloy AD730 during hot isothermal compression tests in the temperature range of 900 ˚C – 1125˚C for strain rates of 0.001 – 5 s^{-1}., as illustrated in Figure 7.1. The stress-strain curve of a Ni-based superalloy can be broken down into three stages as shown in Figure 7.2. This includes work hardening in stage I, flow softening in stage II, and stead-state deformation in stage III. In the early stages of high temperature deformation tests, work hardening emerges as the dominant mechanism, causing an increase in stress during deformation, as depicted in Figure 7.2. Dynamic recovery during this stage is not strong enough to counteract the effects of an increase in stress caused by the dislocation density. During stage II whilst dislocations continue to accumulate, dynamic recrystallisation begins once the critical strain (ε_C) is surpassed. Increasing strain leads to an increase in dislocation annihilation and hence a reduction in the work hardening rate. As the combined effect of dynamic recovery and dynamic recrystallisation progresses, peak stress is reached and then the flow softening begins until a steady state of work hardening and flow softening is reached. An equilibrium between the strain hardening and dynamic recovery is reached in stage III. Despite the flow softening observed in stage II, it's crucial to note that work hardening continues to occur [136]. The

dominance of dynamic recovery and recrystallisation, however, results in a more pronounced impact during this stage. The work done to characterise the different sections of the flow curves was to better select the most appropriate constitutive model to predict the flow behaviour over the mentioned strain rate and temperature range. Two constitutive equations were then developed to be compared.

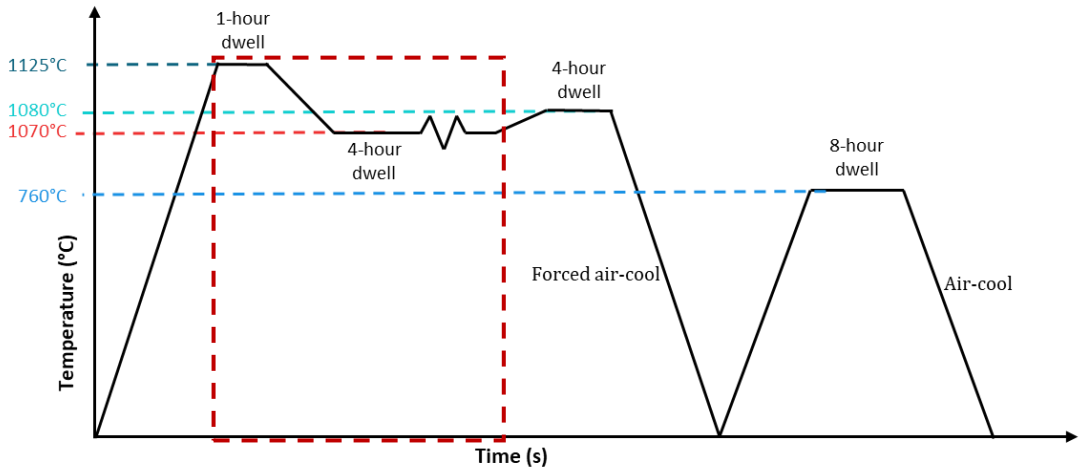

Figure 7.1: Thermo-mechanical processing route of AD730 investigated in this thesis, emphasising the forging stage which is explored in this chapter.

The first model developed was an empirical-based constitutive model based on the hyperbolic-sine Arrhenius equation originally developed for this application by Sellars -Tegart's [133] and hereby referred to as simply the Arrhenius equation. This constitutive equation was selected as it has shown to be accurate and reliable when used to predict the flow stress of many materials as shown in the literature review of this thesis in section 2.5.3 [132], [134], [143], [144], [145], [146].

The next was a physical based model based on the combined Estrin – Mecking [204] and Avrami [149] equations (hereby referred to as the EM+Avrami model). The choice of this combined equation stems from its promising performance in prior studies, as previously highlighted in the literature review chapter (section 2.5.3) [132], [135], [147]. However, its coverage in existing literature is comparatively limited, offering an opportunity for further exploration. A thorough examination of available literature underscores a significant gap in the utilisation of this equation for predicting the flow stresses of Ni-based superalloys. A constitutive artificial neural network was also trained, validated, and tested for predicting flow stresses over the same temperature and strain rate ranges.

Next, the predicted stress values from all three models were compared to the stress values obtained from the hot isothermal compression tests, and the error between the predicted flow curves and experimentally obtained flow curves was quantified. Lastly, both constitutive material models were implemented into user created sub-routines for FE simulations carried out in DEFORM. The hot forging of a double truncated cone (DTC) was simulated and the results of which were compared against the experimental results obtained from the high temperature forging of two DTC's.

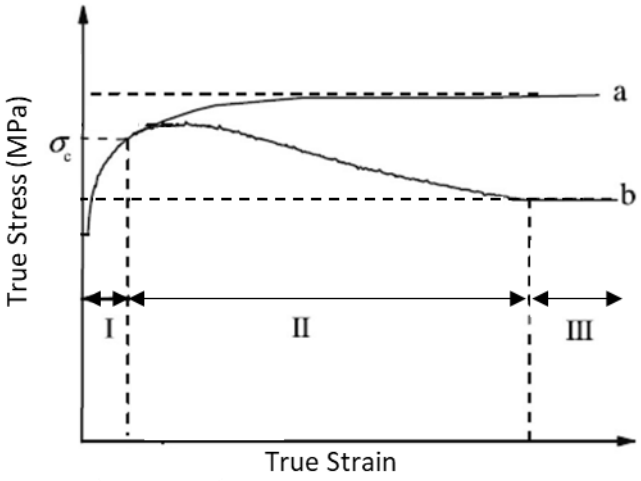

Figure 7.2: Example true stress-true strain curves showing sectioning for characterisation [136].

7.2 Methodology

7.2.1 Material

The AD730 material was sourced from the same billet, possessing identical chemical composition and initial microstructure, as the material discussed in Chapter 6. The chemical composition of the material is provided in Table 6.1 and microstructural characteristics illustrated in Figure 6.7.

7.2.2 Compression Tests

To overcome the challenge of higher loads from tests at lower temperatures potentially damaging the tooling, three different sizes of cylindrical compression samples were extracted using a wire electrical-discharge machining (EDM) from the as-received billet. A summary of the samples and the tests they were used for can be seen in Table 7.1. Tests carried out at 900 °C with strain rates ranging from 1 to 5 s^{-1} used a sample of 9 mm in height and 6 mm in

diameter. For tests carried out at 1000 °C with strain rates of 1 and 5 s^{-1}, a sample of 15 mm in height and 10 mm in diameter was used. For all other compression tests, a sample of 18 mm in height and 12 mm in diameter as recommended by the National Physical Laboratory's good practice guide number 3 was used [205]. As can be seen from the sizes used in Table 7.1, the ratio of 3:2 of height to diameter as recommended by the good practice guide was maintained for all samples.

Table 7.1: Summary of samples sizes used in each test.

Temperature (°C)	Strain rate (s^{-1})	Sample Dimension H × D (mm)
900	10^{-3}, 10^{-2}, & 0.1	$18 \times \varnothing 12$
900	1 & 5	$9 \times \varnothing 6$
1000	10^{-3}, 10^{-2}, & 0.1	$18 \times \varnothing 12$
1000	1 & 5	$15 \times \varnothing 10$
1080	10^{-3}, 10^{-2}, 0.1, 1, & 5	$18 \times \varnothing 12$
1125	10^{-3}, 10^{-2}, 0.1, 1, & 5	$18 \times \varnothing 12$

Before the compression tests, the samples were heated to 1125 °C, i.e., above the γ' solvus temperature of 1110 °C [63], and held for 2 hours and 20 minutes to normalise the microstructure by eliminating any work hardening effects and dissolving any γ' precipitates before being water quenched. The transfer time for water quenching was on average 12 seconds. Then in accordance with ASTM E209-18, samples were then subjected to hot isothermal compression testing at one of four critical test temperatures (T_c), including 900 °C, 1000 °C, 1080 °C, and 1125 °C. Each sample was heated to the target temperature and then soaked for 10 minutes before being compressed under one of the five strain rates of $0.001s^{-1}$, $0.01s^{-1}$, 0.1 s^{-1}, 1 s^{-1}, and 5 s^{-1}. A schematic diagram of the hot compression testing routine including the 2 hours and 20 minutes heat treatment carried out beforehand is provided in Figure 7.3. These test temperatures and strain rates were selected to match up with those experienced during supersolvus and subsolvus ingot-to-billet conversion by the AD730 alloy [65], [206]. The temperature of 900 °C is however too low for the ingot-to-billet conversion process of AD730, but this temperature was included to make an attempt at developing a constitutive model for the material flow behaviour which encompasses as wide a temperature range as possible.

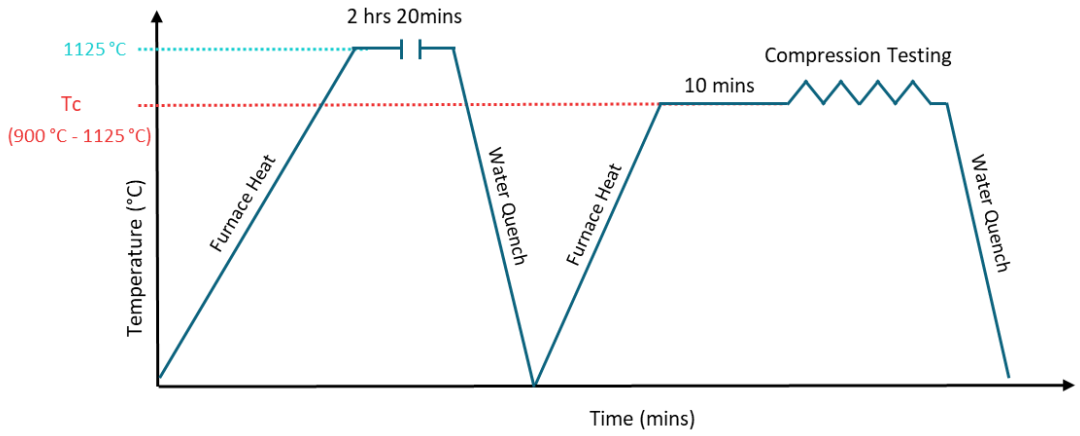

Figure 7.3: Schematic diagram of the hot compression testing routine.

Compression tests under 0.001 s^{-1}, 0.01 s^{-1}, and 0.1 s^{-1} strain rates were carried out using a Zwick Roell Z150 uniaxial screw-machine with a Severn Thermal Solutions split-convection furnace with three distinct controllable heating zones. Compression tests at under 1 s^{-1} and 5 s^{-1} strain rates were performed using a Zwick Roell HA250 uniaxial servo-hydraulic machine equipped with a similar furnace as that of Zwick Roell Z150. All tests were carried out at true strain rate and were compressed to a reduction of 60% in height. Boron Nitride was applied to the compression platens to act as a lubricant and to reduce the friction coefficient the compression sample and the platens. This is discussed in more details in section 7.2.4. Some tests at the lowest temperature of 900 °C began to shear before reaching the target 60% reduction and therefore only a section of those tests are included in the results, as illustrated in Figure 7.4 . After being compressed the samples were then water quenched immediately (i.e., with a 15 second transfer time) to minimise microstructural changes taking place after deformation had stopped. One repeat test was carried out at each temperature to check the validity of the set-up and the repeatability of the stress-strain curves.

Figure 7.4: Sheared **c**ompression sample from a test carried out at 900°C with a strain rate of $0.1s^{-1}$.

7.2.3 Post-Compression Test Characterisations

The compressed samples were then sectioned through the middle parallel to the axial direction, and following standard metallographic techniques, they were ground and polished to a mirror finished condition. They then underwent eight hours vibratory polishing, using 0.02 µm colloidal silica as a suspension. They were then characterised using a FEI Quanta 650 field-emission gun (FEG) scanning electron microscope (SEM) equipped with a back scatter electron detector (BSE). Electron backscatter diffraction (EBSD) was then carried out using an Oxford Instruments EBSD camera. Micrographs and EBSD maps were taken from the central cross-section of the compression samples, where the strain was maximum. An aperture of 100 µm diameter and an accelerating voltage of 25kV was used. The EBSD results were captured and post-processed according to E2627-13 [202]. A step size of 0.51 µm was selected, the scan area was 831 x 569 μm^2, and the resulting average indexing rate across all samples was greater than 98 %.

Characterisation of the microstructure immediately after the 2 hours 20 minutes heat treatment (hereby referred to as the solution-annealed microstructure) was carried out using EBSD with a large area stitched scan area of 6944 x 6881 μm^2. This was necessary due to the combination of the sample having a large grain size and ASTM E2627-13 specifying a minimum of 50 grains were needed for a robust grain size analysis. Average indexing for this map was 93%. Comparison of the solution-annealed microstructure was carried out with the

microstructure of a test compressed at 1125°C with a strain rate of 0.1 s^{-1} to demonstrate the impact of compression testing on the microstructure evolution.

7.2.4 Flow Stress Corrections

The true-stress vs. true-strain curves produced from the hot isothermal compression tests are subject to friction and adiabatic heating effects, as well as machine compliance. Machine compliance was corrected by implementing a standard method [205] . The friction between the compression platen surface and the surface of the sample prevents the unrestricted movement of the sample and causes it to barrel. The effect of this friction is that it causes energy to dissipate requiring more force to deform the sample [207]. There are two well documented methods used for correcting the flow stress for frictional effects, the first method developed by Dieter [208], and the other by Rowe [209]. Torrente et al. found both methods to be similar in terms of the corrected stress, particularly at true strain magnitudes of less than 1 [207], so for conciseness only the Dieter method was used for flow stress corrections in this work.

The friction correction equation from Dieter can be seen in Equation 7.1 where σ is axial stress with friction correction, σ_z is axial stress without friction correction and C_f is the coulomb stress distribution. The Coulomb stress distribution is given in Equation 7.2, where r is the instantaneous radius, μ is the friction coefficient, and h is the instantaneous height of the sample. These equations assume that the barrelling is negligible [207], [210]. It is possible to overcome this issue by assuming an average coefficient of friction value [210]. An average value of 0.3 was assumed for all tests carried out in this study as this was in line with other studies [207], [211].

$$\sigma = \frac{C_f^2 \sigma_z}{2[\exp(C_f) - C_f - 1]}$$

Equation 7.1

$$C_f = \frac{2\mu r}{h}$$

Equation 7.2

The increase in temperature of the sample during deformation is caused by adiabatic heating, which is when the energy used to deform the material turns into heat (i.e., no heat exchange occurs between the whole testing assembly and the environment). This results in the flow stress being reduced locally compared to that corrected for adiabatic heating. The amount of adiabatic heating which is generated in a sample is a function of the strain rate and temperature. Adiabatic heating increases with an increase in the strain rate, where the rate is less when the deformation temperature is increased [131]. Goetz et al. [212] showed that the effect of adiabatic heating can be calculated using Equation 7.3, where ΔT is the change in temperature due to adiabatic heating, ∫σdε is the area under the uncorrected stress-strain curve, ρ is the density, η is the adiabatic correction factor, and C_p is the specific heat capacity which when combined with density is the volumetric specific heat capacity.

$$\Delta T = \frac{\eta 0.95 \int \sigma d\varepsilon}{\rho C_p}$$

Equation 7.3

The value of 0.95 is the Taylor-Quinny factor, which is the fraction of mechanical work converted to heat energy [213]. This factor is usually taken to be between 0.9 and 0.95 [212]. The remaining fraction goes towards the microstructural changes (i.e., plastic deformation) which takes place within the sample. The governing equation for the adiabatic correction factor which is the amount of adiabatic heat retained in the sample after heat loss to the surrounding dies is given by Equation 7.4, the full derivation of which can be found in [212]; where Δε is the change in strain, x_w is one half of the sample height, $\dot{\varepsilon}$ is the strain rate, and h is an overall heat transfer coefficient (HTC) which is a function of the dies and the sample [212].

$$\eta = [1 + (h\Delta\varepsilon)/(x_w \rho C_p \dot{\varepsilon})]^{-1}$$

Equation 7.4

The changes in the flow stress at different strain rates were calculated with the gradient of the plot of true stress against deformation temperature (m) at a given strain value used as described by Equation 7.5. The corrected flow curves for tests carried out at 1125 ˚C and for various strain rates can be seen in Figure 7.12.

$$m = \Delta T \left(\partial\sigma/\partial T\right)|_{\varepsilon}$$

Equation 7.5

7.2.5 Forging Trials

To validate the constitutive material models, forging trials were carried out on two double truncated cones (DTC's) made of AD730. A drawing of the DTC's showing key dimensions can be seen in Figure 7.5. Double truncated cones (DTCs) were used in the forging trials for several reasons. Firstly, the material flow is more controlled compared to cube or cylindrical samples. DTCs also reduce the barrelling and end effects that are more pronounced in cylindrical samples. Additionally, DTCs provide a better representation of the forging process, offering a range of strain magnitudes for investigation when forged, in this case from approximately 0.2 to 2.5.

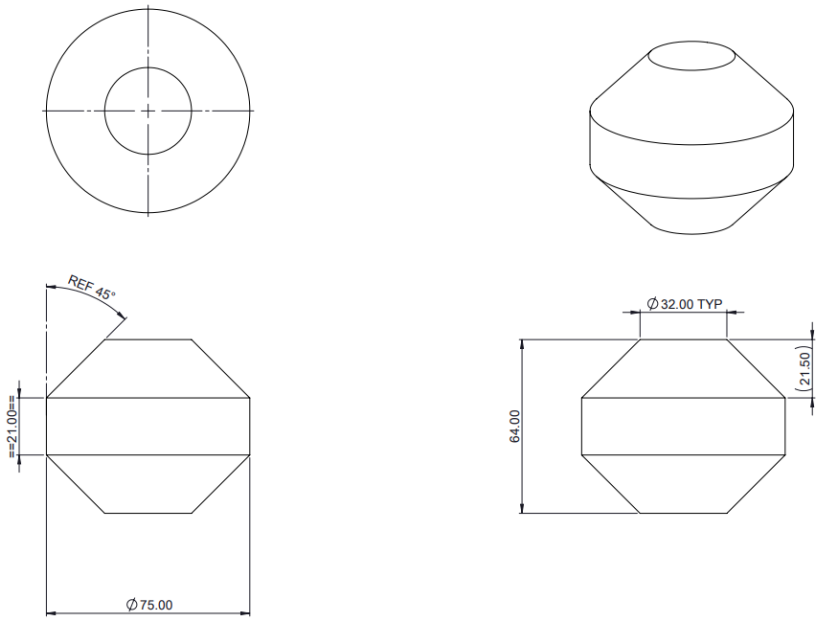

Figure 7.5: Drawing of DTC's showing the key dimensions in mm.

The forging schedule shown in Figure 7.6, was followed for the forging of the DTC samples, which is similar to the temperatures practiced in industry. This schedule is representative of the forging process, which is why the range of strain rates for forging are between 0.01 to $0.1s^{-1}$. The forced air-cooling at the end of the process involved directing room temperature air to

the forged DTCs placed on top of refractory bricks, facilitated by a large fan. A photograph taken from the setup during cooling is shown in Figure 7.27c in the results section. The DTC's were sandblasted and coated in glass before being put in the furnace, this was to help reduce friction and oxidation.

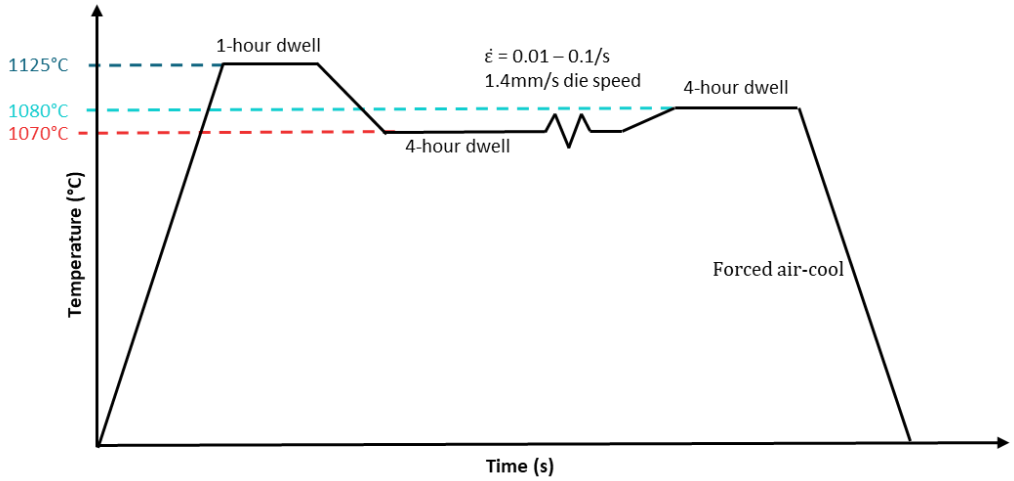

Figure 7.6: Forging schedule representing the forging process for AD730.

To determine the die velocity corresponding to the desired range of strain rates, a 2D axisymmetric FE simulation was conducted in DEFORM. The temperature of the DTC was set to 1070 °C, the environment temperature was set to 20 °C, and the temperature of the dies were set to 700 °C. The DTC was set as a plastic model and the dies were set as rigid bodies. The HTC at the interfaces between the DTC and the dies was set to 5 N/s/mm/°C and the shear friction coefficient at the same interfaces was set to 0.3, as was recommended by the software for hot forging with lubrication. The DTC was meshed using simple linear 2D quadrilateral elements. The minimum element size was 0.49 mm, the maximum element size was 1.48mm, and there was a total of 4000 elements. The simulation was solved using the MUMPS solver and the Newton-Raphson iteration method. This simulation utilised the flow stresses obtained from the hot isothermal compression tests as tabular inputs within the software, which the software used to establish a material model. DEFORM performs interpolation between the flow stresses at given temperatures and strain rates, thereby creating a comprehensive material model. For simplicity, this dataset will be referred to as tabular data. The remaining mechanical and thermo-physical properties needed to complete the material model was taken from the Aubert & Duval website and are listed in Table 7.2.

Table 7.2: Mechanical and thermo-physical properties for AD730 taken from the Aubert & Duval website [206].

Temp (°C)	Thermal conductivity ($Wm^{-1} K^{-1}$)	Density (g/cm^3)	Specific Heat Capacity (J/Kg °C)	Mean Thermal Expansion Coefficient ($x10^{-5}$)	Young's Modulus (GPa)
20	11.26	8.23	485.8	1.1	219
100	12.02		497.7		
200	13.13		515.0		
300			463		
316				1.28	
400	15.35		526.4		
427				1.34	
500	17.79		549.6		
538				1.4	
550					189
600	20.39		573		
650				1.48	
700	21.99		603.7		
760				1.54	
770					179
800	23.63		634.4		
871				1.64	
900	25.58		663.4		

An iterative process was then carried out whereby the velocity of the die was altered to achieve strain rates within the appropriate ranges. The maximum strain rate predicted by the final iterative solution slightly exceeded $0.1s^{-1}$, providing a margin of error in the simulation prediction. The results of the final iterative solution showing the range of strain rates and strain magnitude across the cross-section of the deformed DTC are provided in Figure 7.7. The optimal die velocity to achieve these range of strain rates was 1.4 mm/s.

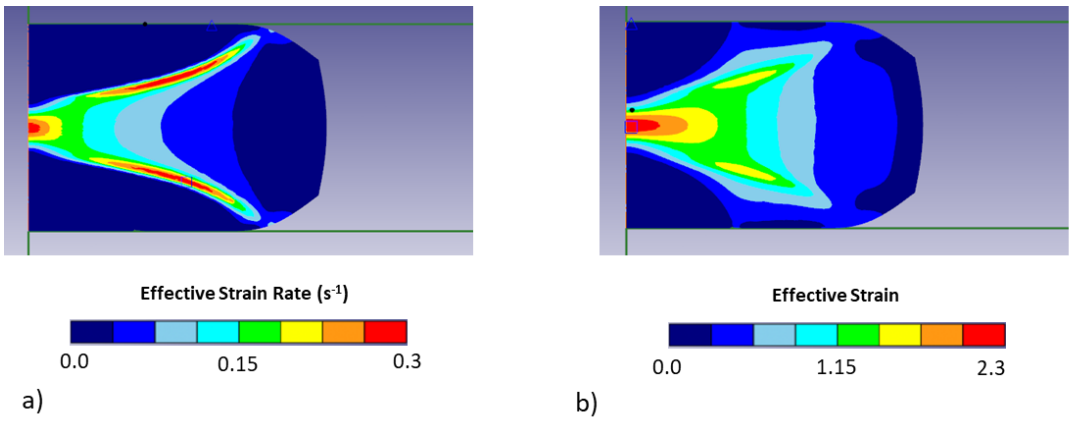

Figure 7.7: Simulation of DTC compressed to 50% of initial height showing a) effective strain rate, and b) effective strain distributions.

The two DTC's employed for forging trials were initially wire EDM cut and subsequently machined from the same billet used for the hot isothermal compression testing. Forging of the DTCs was carried out using a refurbished 500-tonnes hydraulic press at a die velocity of 1.4 mm/s. Waspalloy dies, pre-heated to their maximum temperature of 700 °C and lubricated with graphite, were employed to minimise the die-chilling effect. After the process it was noticed that the dies were not flat and parallel, this had a substantial effect on the forging and will be discussed more in the results section. A video of the process was recorded and used to approximate the transfer time between the furnace and the press, which was approximately 6 seconds. Subsequently, the DTCs rested on the dies for approximately 10 seconds before the compression process commenced. Both DTCs underwent deformation to 50% of their initial height. The press load required for this deformation was recorded using a high-speed data logger integrated into the press. This recorded load was then compared with the loads calculated from the FE simulations, which employed the two constitutive models developed as material models.

7.2.6 Constitutive Artificial Neural Network

The architecture of the neural network used in this chapter was a 3-5-5-1 model as shown schematically in Figure 7.8. This means the model consists of three inputs, true strain, strain rate, and temperature, two hidden layers each containing 5 neurons, and one output of true stress. The neural network was trained using MATLAB and the 'trainbr' function which uses Bayesian Regularisation backpropagation to reduce the objective function, in this case the mean square error, to a minimum. The data used for training, validation, and testing was split

up randomly in a 70-15-15% split, respectively. The model iterated 1,000 times. The coefficient of determination (R^2), RMSE, and AARE were also calculated to determine the accuracy of the model.

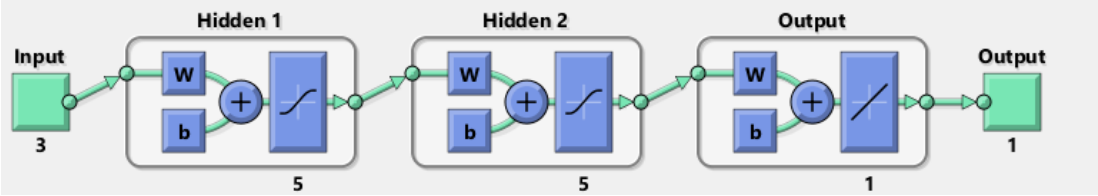

Figure 7.8: Schematic representation of the CANN architecture.

7.2.7 Finite Element Modelling of the Forging of DTC's

A comprehensive 3D FE model was constructed in DEFORM to replicate the forging process undergone by both DTC samples. The simulation comprised multiple steps, mimicking the actual forging process. The first step simulated the transfer from the furnace to the press dies, the second step accounted for the time the sample spent resting on the dies, and the third step simulated the forging itself.

For the first two steps, the DTC was configured as an elastic-plastic model, while for the forging step (third step), it was set up as a plastic model. This choice was made due to the capabilities of DEFORM's user-defined subroutine, which can accommodate both elastic and plastic behaviours. The material model used for the first two steps included tabular data for flow stresses, consistent with the 2D simulation. Tabular data was utilised for simplicity and computational efficiency, given the expected minimal deformation during this stage. For the forging step, a user-defined subroutine was employed for each of the two developed constitutive models.

The DTC was discretised with 40,429 tetrahedral elements, featuring a mesh density detailed in Figure 7.9a and b. Throughout all steps, the conjugate gradient iterative solver was employed alongside the direct iteration method. The transfer time from furnace to press and the time the sample rested on the dies matched the experimental conditions at 6 seconds and 10 seconds, respectively.

Due to issues with the experimental dies not being flat and parallel, the misalignment angle was determined by placing the forged pancakes on a flat, level surface and measuring the slope angle on the top surface using a digital protractor, as depicted in Figure 7.9c. Note the forged DTC has been sectioned in half in Figure 7.9c as further analysis was carried out on it which will be discussed in the following chapter. The misalignment angles were 4° for the first DTC and 6.4° for the second DTC. The 4° misalignment angle was incorporated into the model, as illustrated in Figure 7.9d.

The simulation results obtained using the Arrhenius model, the combined EM+Avrami model, and tabular data are systematically compared. Additionally, comparisons are made between these simulation outcomes and experimental results using two distinct approaches. Initially, the final dimensions of the simulated DTC samples are compared against the measured final dimensions of the experimentally forged DTCs, specifically those forged with a misalignment angle of 4°. Furthermore, comparisons are drawn between the force-stroke curves obtained from both the press during forging and the simulations.

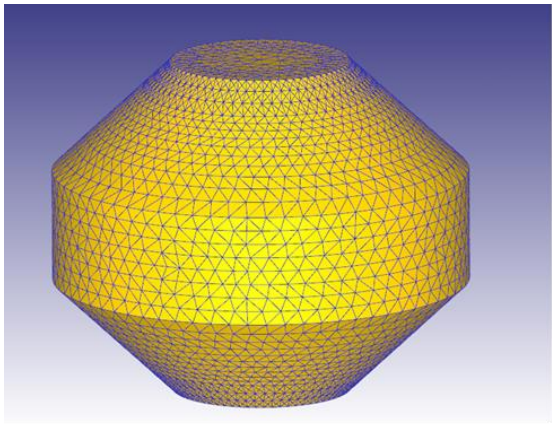

a)

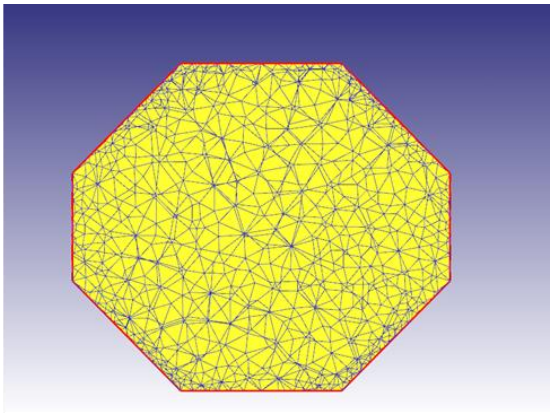

b)

c)

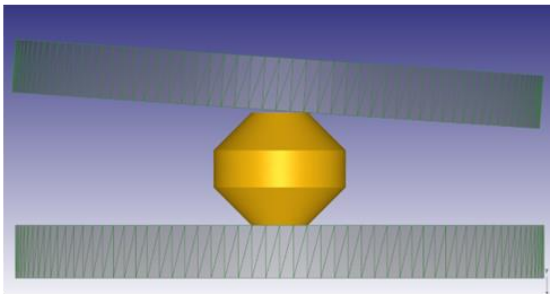

d)

Figure 7.9: a) Mesh Density of 3D DTC in 3D view in DEFORM, b) mesh density of DTC in 2D view, c) digital protractor for determining misalignment angle of dies on forged pancake, and d) implementation of misalignment angle in DEFORM simulation.

7.3 Results

7.3.1 Microstructural Characteristics

The microstructure after the initial solution annealing heat treatment at 1125 °C for 2 hours and 20 minutes are shown in Figure 7.10. The solution annealed sample has large, equiaxed grains; the grain size histogram shows a typical Gaussian distribution, and the average grain size determined by the equivalent circle diameter method is 323 ± 179.9µm. There is no visible γ' in the microstructure meaning that the solution heat treatment and subsequent water quench was successful in dissolving γ' into the γ matrix. Even with a fast-cooling rate like that experienced during water quenching, there will still be small tertiary γ' in the microstructure, however, these are not resolved with the SEM used for this study. The recrystallisation fraction determined by grains having a GOS of less than 2° which was 100% of the area fraction, as shown in Figure 7.10d, and the inverse polefigure map shows no preferential texture, as shown in Figure 7.10c.

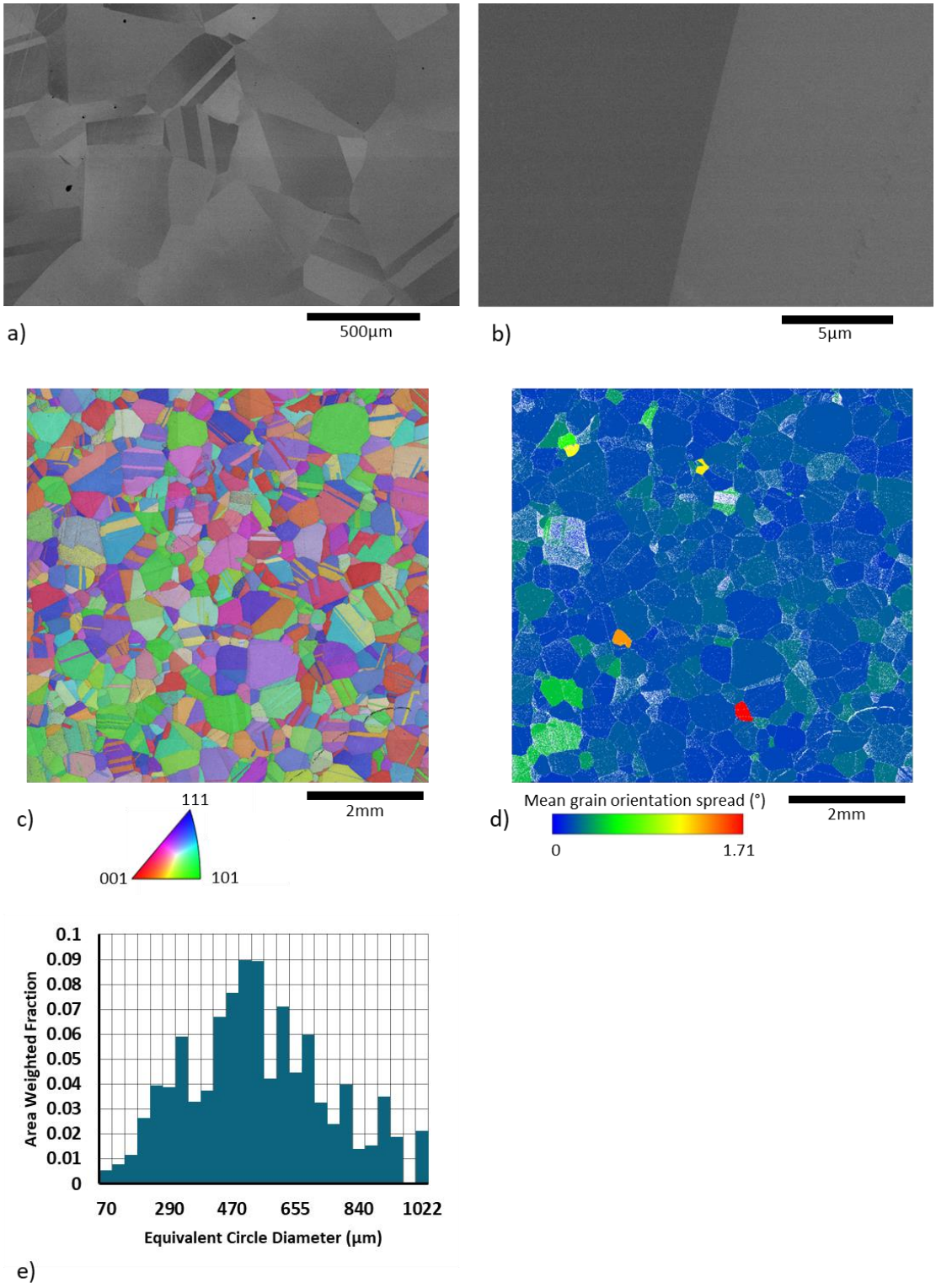

Figure 7.10: Microstructural characteristics of the solution heat-treated (2 hours and 20 mins at 1125°C) and water quenched material; a) and b) SEM BSE micrographs showing no perceivable γ' in the microstructure c) EBSD inverse polefigure map with respect to the out-of-plane direction, d) mean GOS map showing 100% recrystallisation for a 2° threshold, and e) grain size distribution histogram.

The microstructure of the sample compressed at 1125 °C under a strain rate of 0.1 s^{-1} is shown in Figure 7.11. The grains are seen to be equiaxed and the recrystallisation fraction determined by grains having a GOS of less than 2° was 99.48% of the area fraction (see Figure 7.11b). The average grain size using the equivalent circle diameter method is 32.8 ± 18.1 µm. It can therefore be said that the microstructure is fully recrystalised.

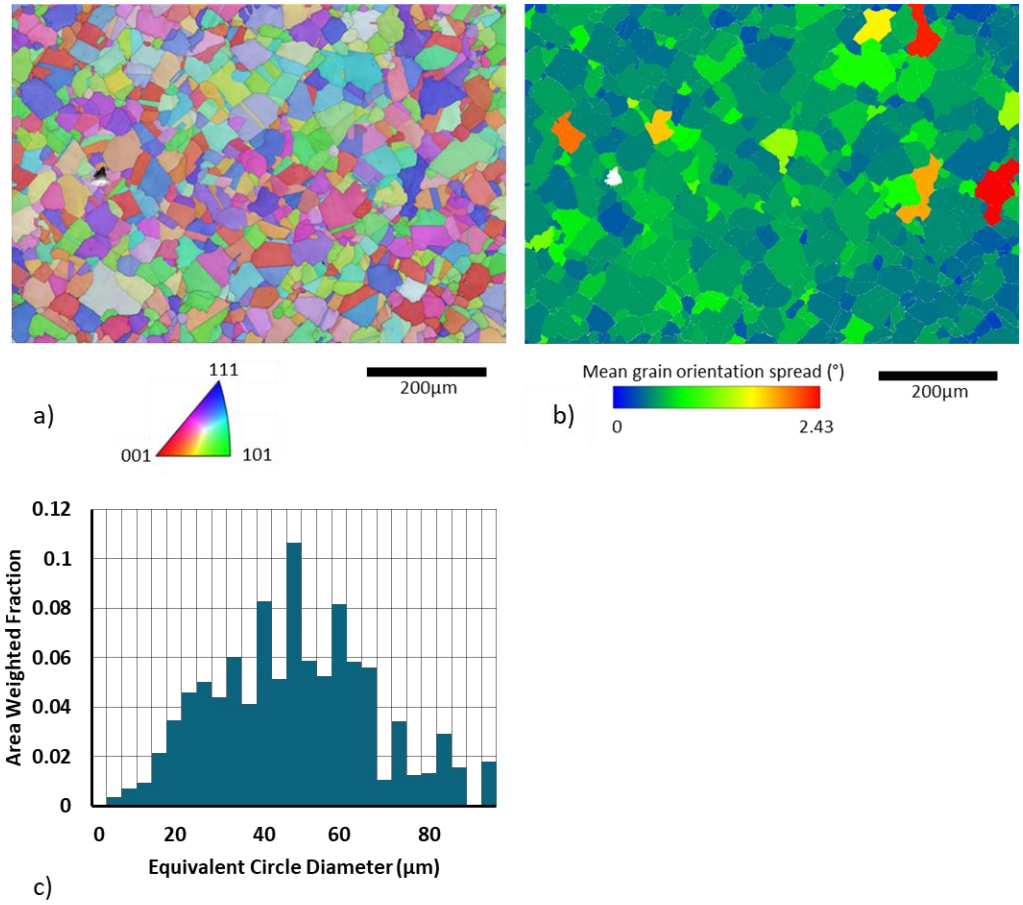

Figure 7.11: Microstructural characteristics of the sample tested at 1125 °C with a strain rate of 0.1 s^{-1}, a) EBSD inverse polefigure map with respect to the out-of-plane direction, b) mean GOS map showing amount of recrystallisation present for a 2° threshold, and c) grain size distribution histogram.

7.3.2 Flow Behaviours

The combined impact that friction and adiabatic heating has on the flow stress can be seen in Figure 7.12, where the flow stresses for tests carried out at 1125 ˚C under five different strain rates can be seen. Figure 7.12 shows that the combined effects of friction and adiabatic heating is more impactful at strain rates above 0.001 s^{-1}, and most impactful at the highest strain rate of 5 s^{-1}. This appeared to be similar for all temperatures.

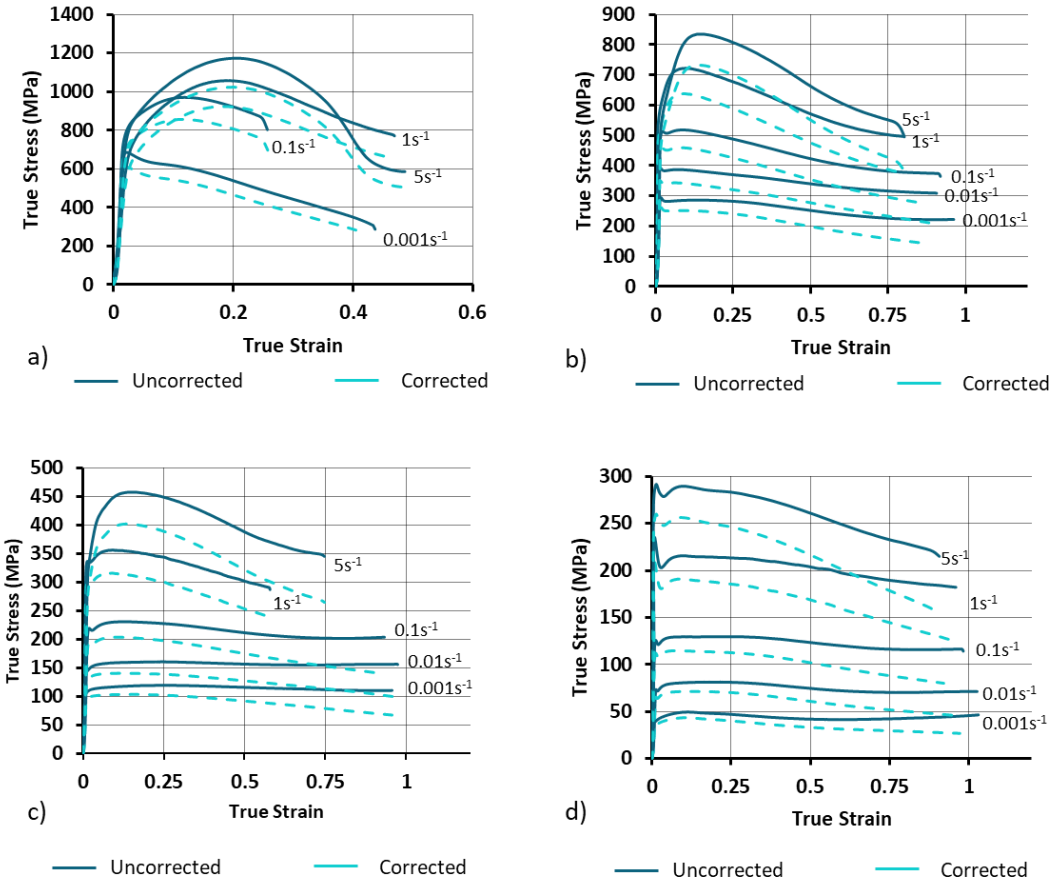

Figure 7.12: The measured True-Stress True-Strain curves showing uncorrected and corrected data for friction and adiabatic heating effects at a) 900˚C b) 1000˚C c) 1080˚C & d) 1125˚C.

Figure 7.13 shows the flow curves measured at various temperatures and under different strain rates, following corrections for friction and adiabatic heating. As can be seen in Figure 7.13, all flow curves showed a similar general behaviour of an increase in flow stress up until a peak stress, and then followed by flow softening behaviours. Work hardening occurs when the rate of dislocation generation (i.e., density) within grains increases with higher stress than the dislocation annihilation (i.e., recovery). Dynamic recovery, on the other hand, maintains the grain size while reducing the dislocation count through rearrangements, thereby decreasing the internal energy. Dynamic recrystallisation involves the nucleation and growth of new grains in a deformed microstructure after the total strain surpasses the critical strain (ε_C) [19].

The tests carried out at 900 ˚C are shorter in terms of total deformation level (i.e., lower ductility) as they began to shear after reaching certain strain values, so only the portion of the test which were confidently a uniaxial compression test were included. This is shown in Figure

7.13. In the early stage, all tests indicate concurrent work hardening and dynamic recovery, with the former exhibiting greater dominance. Higher strain rates (1 s^{-1} and 5 s^{-1} in particular) show higher levels of work hardening as can be seen in Figure 7.13. After peak stress, flow softening behaviour takes place which was determined by the microstructural deformation mechanisms such as work hardening, dynamic recovery and dynamic recrystallisation (dynamic recrystallisation being the dominant mechanism in this case). All samples experience an increase in the flow stress as the strain rate increased and as the temperature decreased.

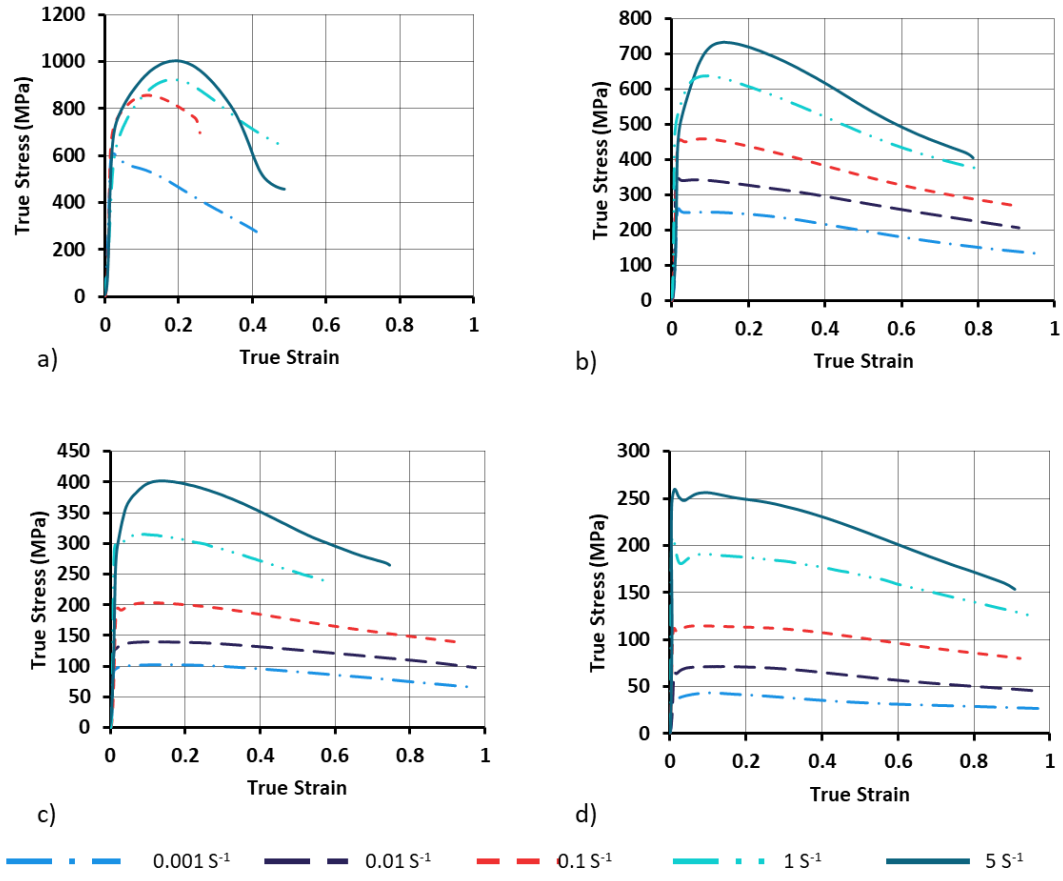

Figure 7.13: The measured True-Stress True-Strain curves for four different strain rates at a) 900˚C b) 1000˚C c) 1080˚C & d) 1125˚C.

7.3.3 Yield drop phenomenon

The flow stress curves obtained at 1125 ˚C, 1080 ˚C, and 1000˚C (see Figure 7.13) for specific strain rates, exhibit yield drop behaviour. Figure 7.14a provides a schematic representation of the yield drop phenomenon, highlighting the method and key measurements used for its characterisation. To determine the yield drop stress, Δσ, it is crucial to first characterise the

peak stress, σ_{max}, before the onset of the yield drop. This step is essential for understanding the magnitude of the yield drop with respect to the maximum stress ($\Delta\sigma/\sigma_{max}$), as depicted in Figure 7.14b. Characterising the yield drop also involves understanding the differential strain, $\Delta\varepsilon$, which represents the strain value from the peak stress to the lowest stress during the yield drop, as illustrated in Figure 7.14a. The differential strain is further characterised in relation to the maximum strain ($\Delta\varepsilon/\varepsilon_{max}$), as presented in Figure 7.14c.

Figure 7.14b does not reveal a clear trend; however, there seems to be a suggestive outline regarding the yield drop stress. With the exception of the results obtained under 0.1 s^{-1}, an increase in temperature seems to correlate with a higher yield drop stress in the material. Additionally, it is observed that the extent of strain over which the yield drop occurs tends to decrease with rising temperature. Consequently, the yield drop stress generally exhibits a more pronounced and sharper peak as the temperature of the test increases. This observation aligns well with the flow stresses depicted in Figure 7.13. In all instances where the stress curves exhibit the yield drop phenomenon, the stress recovers and continues towards peak stress. There have been several studies which have confirmed the presence of the yield drop phenomenon for superalloys such as Waspaloy [214], IN718 [214], [215], and Udimet 720 [216]. There have been several proposals as to the cause of the yield drop phenomenon in Ni-based superalloys. Roy et. al suggested when investigating Alloy 617 that the yield drop phenomenon could be directly linked to the formation of carbides, dislocation pile-ups, and pinned dislocations at grain boundaries [217]. Veyssière however suggested that the cause of the yield drop phenomenon in Ll_2 ordered alloys was due to the competition of the multiplication rate with the exhaustion rate of mobile dislocations heavily impacted by dislocation locking mechanism [218]. Short range order locking of dislocations was also cited as the likely reason for the yield drop phenomenon in Udimet 720 [216] as it was proposed that the dissolution of γ’ forming solutes at higher temperatures hinders dynamic dislocation movement and eventually locks them. This appears to be the contributing factor in this case. At 1125 ˚C, all flow curves exhibit the yield drop phenomenon for all strain rates, however as the temperature is decreased, the yield drop phenomenon becomes non-existent especially at higher strain rates.

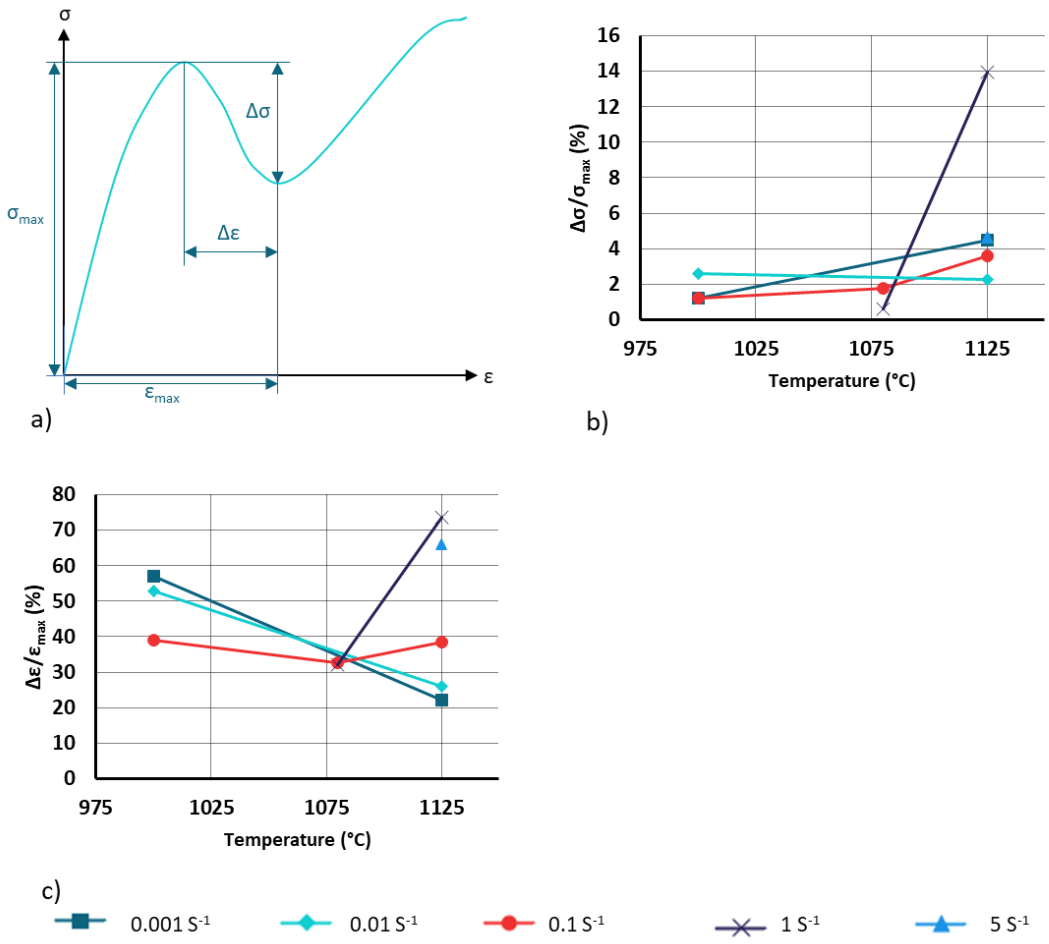

Figure 7.14: a) Schematic representation of the yield drop phenomenon observed in the measured flow stress curves for AD730, recreated from Monajati et. al [216] demonstrating key measurements, b) and c) yield drop measurements, $\Delta\sigma/\sigma_{max}$ and $\Delta\varepsilon/\varepsilon_{max}$ respectively, for flow stresses obtained under different strain rates and temperatures.

7.3.4 Arrhenius Model

Based on the experimental results of the isothermal compression tests, the material constants for the Arrhenius constitutive model can be developed. Because the flow stresses obtained from the hot isothermal compression tests at 900 °C showed signs of shearing, and lower deformation % than tests at the other temperatures, they were excluded in the development of the constitutive models. The Zener-Hollomon relationship is used to relate the changes in strain rate and temperature to the flow stress. The Zener-Hollomon relation is presented in Equation 7.6 where $\dot{\varepsilon}$ is the strain rate, Q is the thermal activation energy of the material, R is the gas constant (taken to be 8.3145 J/molK) and T is the temperature in Kelvin. The strain rate

is further defined in Equation 7.7 and Equation 7.8 where A, β, α, n_1, and n_2 are material constants [132], [143]. $F(\sigma^{n1})$ shown in Equation 7.8 represents the power law which breaks down at the higher stresses due to the variation of n_1 with the strain rate, and $F(\exp(\beta\sigma))$ is the exponential law which is preferred at higher stresses but breaks down at lower stresses for higher temperatures and strain rates of lower than 1 s^{-1} [219] . Sellars and Tegart's therefore proposed a hyperbolic sine equation which could be used to describe material's deformation behaviour over the entire stress range, in the form of the relationship presented by Equation 7.9 [220].

$$Z = \dot{\varepsilon} exp(Q/RT)$$

Equation 7.6

$$\dot{\varepsilon} = AF(\sigma) exp(-Q/RT)$$

Equation 7.7

$$F(\sigma) = \begin{cases} \sigma^{n_1} & for\ \alpha\sigma < 0.8 \\ \exp(\beta\sigma) & for\ \alpha\sigma > 1.2 \\ [\sinh(\alpha\sigma)]^{n2} & for\ all\ \sigma \end{cases}$$

Equation 7.8

$$\dot{\varepsilon} = A[\sinh(\alpha\sigma)]^{n_2} exp(-Q/RT)$$

Equation 7.9

By substituting Equation 7.6 into Equation 7.9, another form of the Zener-Hollomon parameter is established shown in Equation 7.10.

$$Z = A[\sinh(\alpha\sigma)]^{n_2}$$

Equation 7.10

Equation 7.10 can then be solved using the standard definition for the hyperbolic sine equation such that an expression for the flow stress is now given in Equation 7.11.

$$\sigma = \frac{1}{\alpha} ln \left\{ \left(\frac{Z}{A}\right)^{1/n_2} + \left[\left(\frac{Z}{A}\right)^{2/n_2} + 1\right]^{1/2} \right\}$$

Equation 7.11

Determining the Materials Constants

To solve Equation 7.11 and predict the flow stress, the material constants must be defined. These constants are derived from Equation 7.12, Equation 7.13, Equation 7.16, Equation 7.17, and Equation 7.18, and from the measured flow stress curves (see Figure 7.13). Firstly, a natural logarithm is taken from Equation 7.7 for both the power law and the exponential law which gives Equation 7.12 and Equation 7.13 [221].

$$ln\dot{\varepsilon} = lnA_1 + n1ln\sigma - \left(\frac{Q}{RT}\right)$$

Equation 7.12

$$ln\dot{\varepsilon} = lnA_2 + \beta\sigma - \left(\frac{Q}{RT}\right)$$

Equation 7.13

From Equation 7.12 the value of n_1 can be determined by plotting $ln\sigma_p$ vs $ln\dot{\varepsilon}$ for each temperature, where σ_p is the peak stress [131]. This can be seen in Figure 7.15a. The stress values were then fitted with a set of straight lines which showed reasonable agreement in most cases. The reciprocal of the slopes of each line was then averaged and an average value of 6.01 MPa^{-1} was obtained for n_1. A similar process was deployed to determine the value of β. From Equation 7.13 the material constant β was determined by plotting σ_p vs $ln\dot{\varepsilon}$ as seen in Figure 7.15b with the reciprocal of the slopes of each line averaged to obtain a β value of 0.0257 MPa^{-1}. Finally, α is calculated as described in Equation 7.14 to give a value of 0.004274 MPa^{-1}.

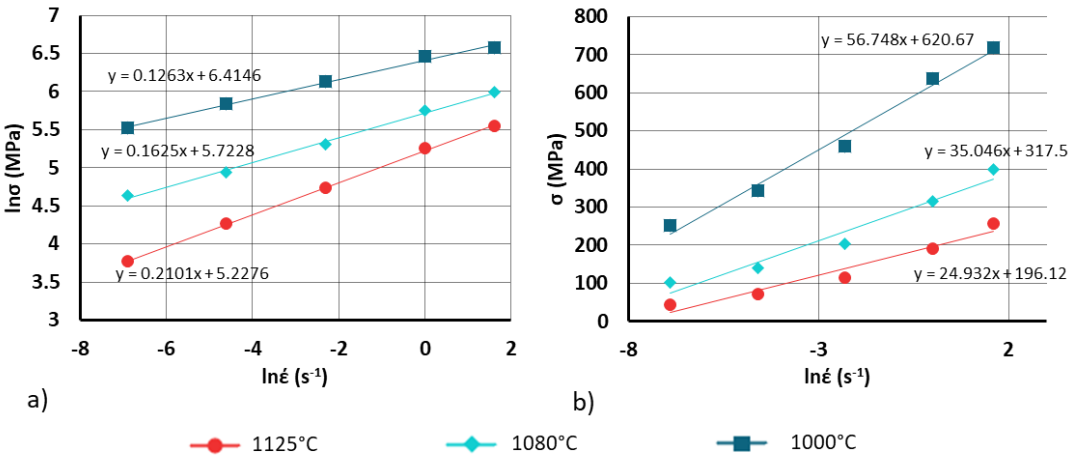

Figure 7.15: Linear plots for determining a) n_1 and b) β, at peak stress using Equation 7.12 and Equation 7.13.

$$\alpha = \beta/n_1$$

Equation 7.14

By taking the natural logarithm of the hyperbolic sine equation (Equation 7.9), Equation 7.15 is then obtained [216], [219].

$$ln\dot{\varepsilon} = lnA + n_2 ln[\sinh(\alpha\sigma)] - Q/RT)$$

Equation 7.15

From Equation 7.15, the partial derivative of $ln\dot{\varepsilon}$ with respect to $ln[\sinh(\alpha\sigma_p)]$ at a constant temperature can be used to determine n_2 as expressed in Equation 7.16. The material constant α, deformation temperatures, strain rates and peak stress values were substituted into Equation 7.16 and Figure 7.16a was then plotted. The reciprocal of the slopes of the straight lines were then averaged and a value of 4.234 MPa was calculated for n_2.

$$n_2 = \frac{\partial \ln \dot{\varepsilon}}{\partial \ln [\sinh(\alpha\sigma)]}\Big|_T$$

Equation 7.16

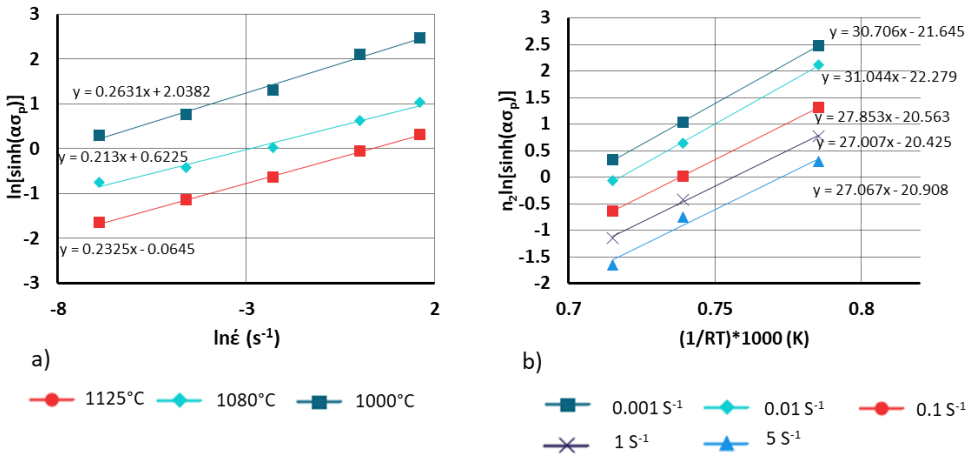

Figure 7.16: Linear plots for determining a) n_2, and b) the Activation Energy (Q) using Equation 7.16 and Equation 7.17.

From Equation 7.15, the partial derivative of $\ln[\sinh(\alpha\sigma_p)]$ with respect to 1/T at a constant strain rate can be used to determine the activation energy Q as expressed in Equation 7.17 [216], [219]. A plot of (1/RT)×1000 (K) vs. $n_2\ln[\sinh(\alpha\sigma p)]$ is shown in Figure 7.16b. The activation energy at each strain rate was calculated and then averaged to give an activation energy of Q = 1011 kJ/mol for all strain rates. While no comparable studies have been conducted on AD730 for direct comparison, investigations on other Ni-based superalloys, such as Udimet 720, have reported activation energies around 1552 kJ/ mol [216]. In the case of Udimet 520, activation energy has been observed to be as low as 780 kJ/mol under similar temperatures and strain rates [222]. Therefore, the value obtained in the course of this study seems reasonable and in line with literature.

$$Q = n_2 R \frac{\partial \ln[\sinh(\alpha\sigma)]}{\partial (1/T)}\bigg|_{\dot{\varepsilon}}$$

Equation 7.17

The equation which is used to derive the material constant, A, is obtained by taking the natural logarithm of Equation 7.10 to give Equation 7.18 [221]. The Zener-Hollomon parameter was calculated from Equation 7.6 for each temperature and strain rate and substituted into Equation 7.18 alongside the values of n_2, α, σ_p. This was then plotted as shown in Figure 7.17 with the y-intercept corresponding to the value of lnA which is 87.129.

$$ln = lnA + n_2 ln[\sinh(\alpha\sigma)]$$

Equation 7.18

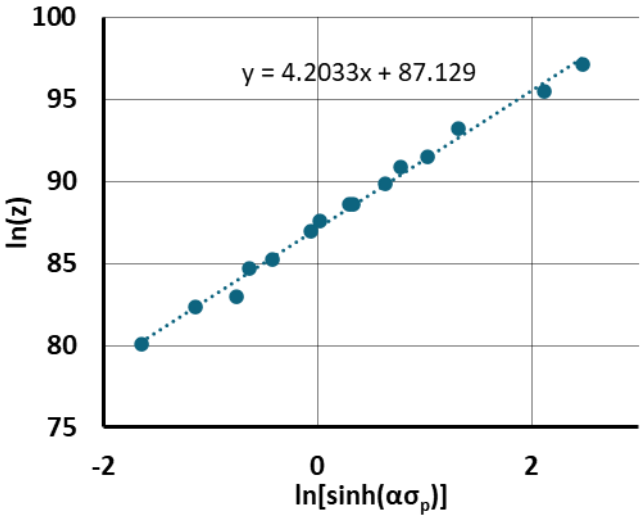

Figure 7.17: Linear plot for determining lnA.

The material constants A, α, β, n_2 and Q which have been determined for peak stress are then substituted into Equation 7.9 to give the constitutive equation for alloy AD730 as shown in Equation 7.19. The flow stress can be written as a function of the Zener-Hollomon parameter as was shown in Equation 7.11, to give Equation 7.20.

$$\dot{\varepsilon} = 6.91 \times 10^{37}[\sinh(0.004274\sigma)]^{4.234} exp(-1.011 * 10^6/RT)$$

Equation 7.19

$$\sigma = \frac{1}{0.004274} ln\left\{\left(\frac{Z}{6.91 \times 10\text{^}37}\right)^{1/4.234} + \left[\left(\frac{Z}{6.91 \times 10\text{^}37}\right)^{2/4.234} + 1\right]^{1/2}\right\}$$

Equation 7.20

The constitutive equations shown in Equation 7.19 and Equation 7.20 can now be used to predict the flow stress of alloy AD730, however these equations do not take into consideration the influence of strain. Currently these variables have only been calculated to obtain the peak stress. To increase the accuracy of this equation over the full range of stresses, the impact that the strain has on the material constants was then to be determined and introduced into the equations. This was done by determining the material constants in the same way as

demonstrated above but at strain values of 0.05, and then from 0.1 to 1 in intervals of 0.1. These values are summarised in Table 7.3.

Table 7.3: Material constants determined for each strain interval.

ε	n_1 (MPa^{-1})	β (MPa^{-1})	α (MPa^{-1})	n_2 (s^{-1} MPa^{-1})	Q (kJ/mol)	lnA (s^{-1})
0.05	6.24	0.029	0.004646	4.53	1032	89.10
0.1	6.01	0.026	0.004310	4.25	985	84.88
0.2	6.05	0.027	0.004492	4.33	955	82.24
0.3	6.10	0.029	0.004813	4.42	931	80.1
0.4	6.19	0.032	0.005238	4.51	917	78.88
0.5	6.24	0.036	0.005415	4.60	913	78.40
0.6	6.3	0.039	0.006172	4.64	907	77.78
0.7	6.33	0.042	0.006563	4.65	891	76.86
0.8	6.31	0.044	0.006901	4.57	891	76.22
0.9	6.26	0.045	0.007172	4.47	897	76.63
1.0	6.18	0.046	0.007394	4.37	920	78.67

The material constants were plotted as a function of strain as can be seen in Figure 7.18. The simplest equation which could accurately describe the behaviour of each constant as a function of strain was selected. For α, this was a 3rd order polynomial, and for n_2, Q and lnA this was a 4th order polynomial. These relationships can be seen in Equation 7.21. The calculated coefficients are provided in Table 7.4 for different orders of polynomial fits.

$$\alpha = B_0 + B_1\varepsilon + B_2\varepsilon^2 + B_3\varepsilon^3$$

$$n2 = C_0 + C_1\varepsilon + C_2\varepsilon^2 + C_3\varepsilon^3 + C_4\varepsilon^4$$

$$Q = D_0 + D_1\varepsilon + D_2\varepsilon^2 + D_3\varepsilon^3 + D_4\varepsilon^4$$

$$lnA = E_0 + E_1\varepsilon + E_2\varepsilon^2 + E_3\varepsilon^3 + E_4\varepsilon^4$$

Equation 7.21

Table 7.4: The material coefficients determined from fitting curves using different degrees of polynomial fitting.

	4th order coefficient	3rd order coefficient	2nd order coefficient	1st order coefficient	0 order coefficient
α	n/a	-0.004982	0.010238	-0.00215	0.0045859
Q	1.55E+03	-3.46E+03	2.81E+03	-1.06E+03	1.07E+03
n_2	1.03E+01	-2.51E+01	1.90E+01	-4.47E+00	4.60E+00
lnA	1.41E+02	-3.12E+02	2.51E+02	-9.38E+01	9.28E+01

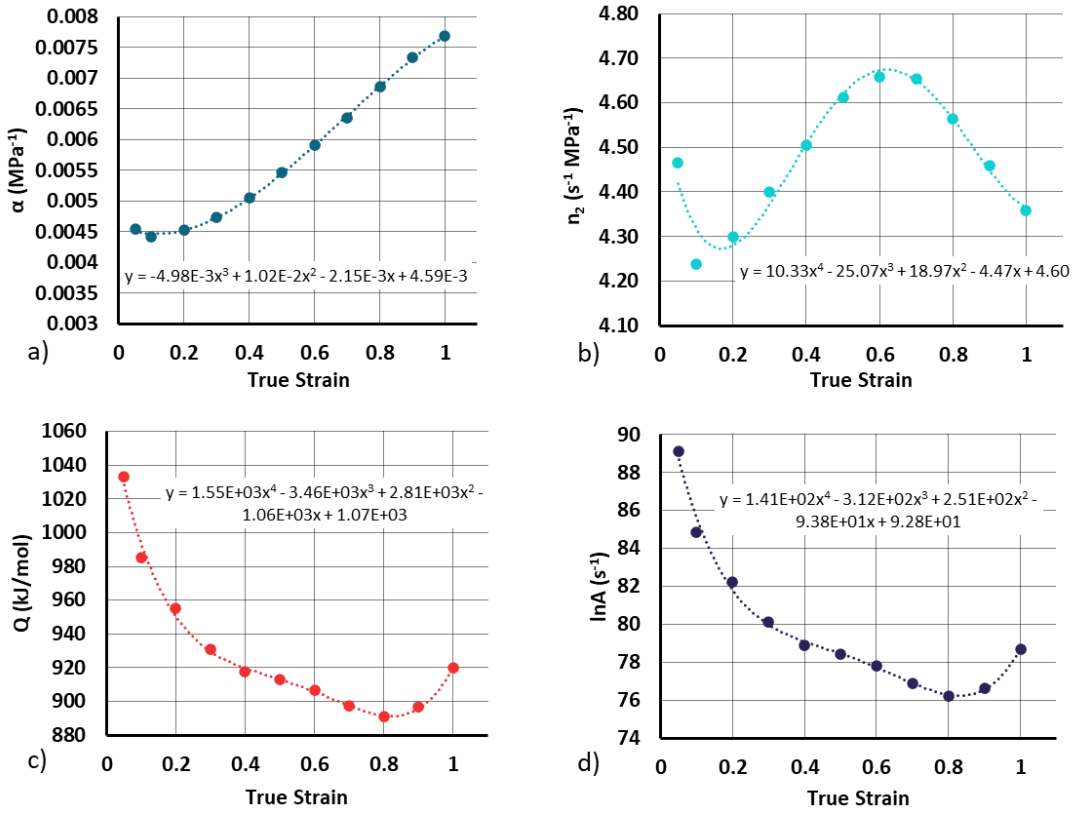

Figure 7.18: Material constants plotted as a function of strain, (a) α, (b) n_2, (c) Q, and (d) lnA.

The accuracy of the constitutive equation was then determined by calculating the root RMSE, the AARE, and the coefficient of determination (R^2). The AARE, RMSE, and R^2 values for the Arrhenius equation for alloy AD730 were calculated as 6.54%, 13.53 MPa, and 0.997, respectively. These are in line with similar works [131], [136], [223]. These metrics demonstrate a very good fit, as can be seen in Figure 7.19a. An attempt to further improve accuracy by using a generalised reduced gradient solver built into Microsoft Excel was made by altering the material constants such that the AARE was reduced to a minimum [143]. This involved setting the AARE as the objective function and solving for different permutations of coefficients shown in Equation 7.21 for α, n_2, Q and lnA. The reduced solver iterated 5 times before returning an error message that the original solution was optimal.

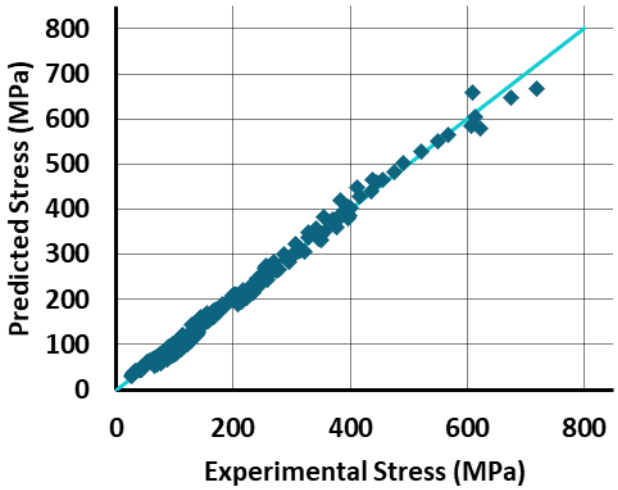

Figure 7.19: Correlation of experimental and predicted stress from Arrhenius model.

7.3.5 EM+Avrami Constitutive Material Model

Modelling Work Hardening and Dynamic Recovery using the Estrin and Mecking Model

At all temperatures, the work hardening rate decreases as the true stress increases up until a point known as the saturation stress (σ_s), where the generation and annihilation rates of dislocations are at an equilibrium. The work hardening rate then becomes negative because of flow softening (i.e., caused by dynamic recovery and dynamic recrystallisation) overcoming the work hardening. This can be seen schematically in Figure 7.20 [131]. The work hardening rate (θ) can be calculated by Equation 7.22. To further understand the work hardening rate, plots of work hardening rate vs. true stress at different temperatures, but constant strain rates, are used (see example in Figure 7.21).

$$\theta = \frac{\partial \sigma}{\partial \varepsilon}\bigg|_{\dot{\varepsilon}T}$$

Equation 7.22

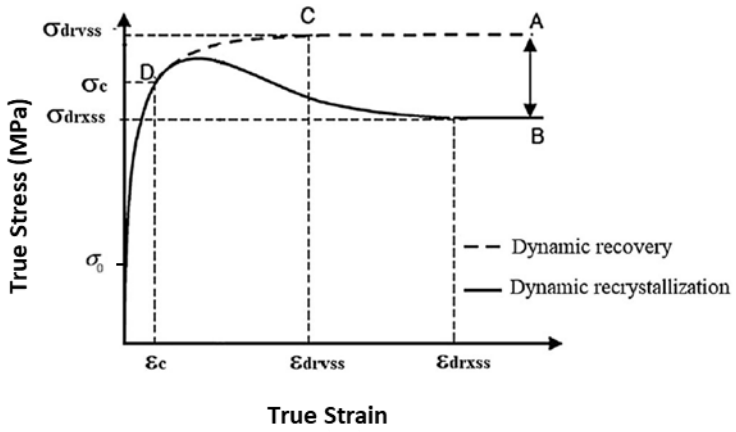

Figure 7.20: Schematic flow curve showing influence of dynamic recovery and dynamic recrystallisation where σ_{drvss} and ε_{drvss} are the dynamic recovery saturation stress and strain, σ_{drxss} and ε_{drxss} are the recrystallisation saturation stress and strain, and σ_c and ε_c are the critical stress and strain, respectively (Recreated from [131]).

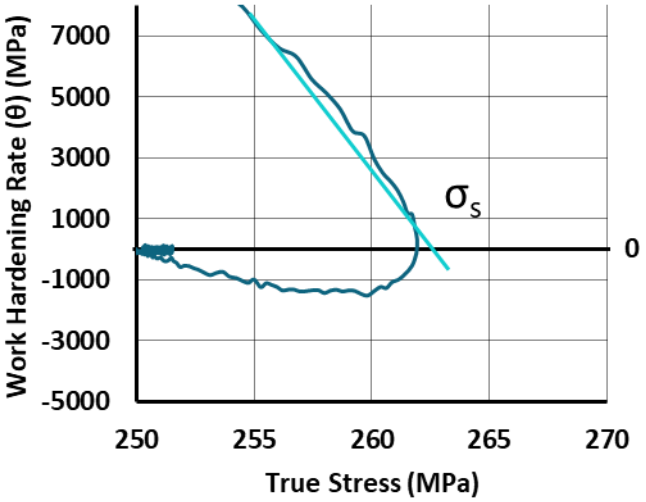

Figure 7.21: Plot of work hardening rate for 0.001 s^{-1} at 1000 °C demonstrating the process for determining σ_s.

The linear relationship between the work hardening rate and the flow stress is given in Equation 7.23 [204] where σ_s is the saturation stress shown in Equation 7.24, θ_0 is the initial work hardening rate shown in Equation 7.25, k_1 and k_2 are the constants related to the generation and annihilation of dislocations, α is a material constant, G is the shear modulus, and b is the magnitude of Burger's vector [131], [224]. The procedure for determining the saturation stress σ_s can be seen in Figure 7.21, where a straight line from the work hardening rate curve is extrapolated until it meets the x-axis. The x-intercept is the saturation stress (σ_s).

$$\theta = \theta_0 \left(1 - \frac{\sigma}{\sigma_s}\right)$$

Equation 7.23

$$\sigma_s = \left(\frac{k_1}{k_2}\right)$$

Equation 7.24

$$\theta_0 = \frac{\alpha G b k_1}{2}$$

Equation 7.25

Estrin and Mecking then assumed that the dislocation density rate was constant leading to a modification of the Kocks and Mecking method which yielded Equation 7.26 [223], [224], where A and B are constants.

$$\theta\sigma = A - B\sigma^2$$

Equation 7.26

Assuming a constant strain rate, the integration of Equation 7.26 means the flow stress in the dynamic recovery regime can be given by Equation 7.27 with the saturation stress given in Equation 7.28, and σ_0 being the stress at strain zero.

$$\sigma = [\sigma_s^2 + (\sigma_0^2 - \sigma_s^2)exp(-2B\varepsilon)]^{1/2}$$

Equation 7.27

$$\sigma_s = \sqrt{\frac{A}{B}}$$

Equation 7.28

Taking the natural logarithm of Equation 7.28 gives Equation 7.29. The constant B and the initial stress σ_0 are then obtained by plotting $\ln(\sigma_s^2 - \sigma^2)$ vs. ε for each strain rate and temperature with the gradient being the value of B and the y-intercept being σ_0. A plot for determining B and σ_0 at a range of temperatures and for a strain rate of 5 s^{-1} can be seen in Figure 7.22. As can be seen in Figure 7.22, points at different true strain values were plotted for each test. This was because some samples yielded before others, so only data from the elastic region was included. There was also some 'pick-up' at the beginning of the compression

tests where the true stress-true strain behaviour was not linear, data was not included from these instances. The values for B varied depending on the strain rate and temperature of the test. For the sake of simplicity in the model, the impact of temperature on B is taken to be negligible as is the impact of strain rate, and a value of 33.78 was averaged from all B values determined using the method described previously.

$$ln(\sigma_s^2 - \sigma^2) = ln(\sigma_s^2 - \sigma_0^2) - 2B\varepsilon$$

Equation 7.29

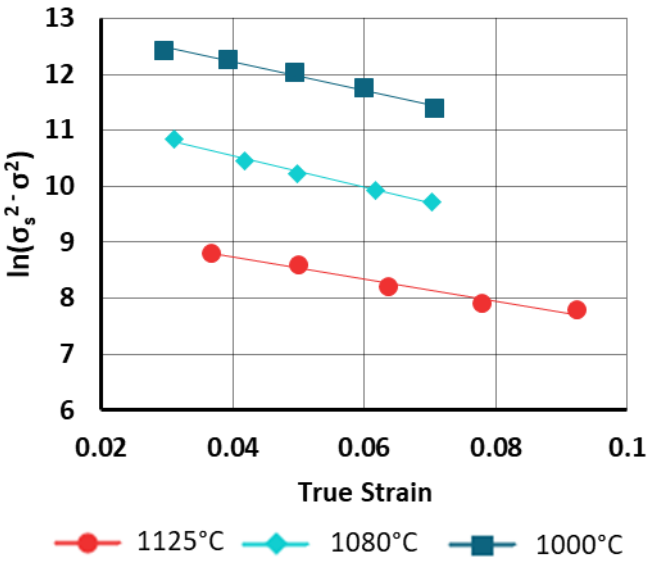

Figure 7.22: Linear plot to determine B value and σ_0 according to Equation 32 for a strain rate of 5 s^{-1}.

The flow curves up until the point of peak stress can be predicted using the Estrin-Mecking model shown in Equation 7.27, however after this, work hardening is no longer the dominant factor and flow softening becomes dominant. To incorporate the dynamic softening into the model, the Avrami model is further implemented to produce a combined model which is described in the following section.

Modelling Dynamic Recrystallisation using Avrami's approach

The Avrami approach is used to predict the effect of dynamic recrystallisation and introduces this into the constitutive model. Only after the point of critical strain is the effect of dynamic recrystallisation considered, and then it is evaluated for every strain value. X is the fraction of recrystallisation at a given strain value ($0 \leq X \leq 1$), an expression for which can be seen in

Equation 7.30, where σ_{EM} is the stress predicted by the Estrin-Mecking model, and σ_{ss} is the saturation stress.

$$X = \frac{\sigma_{EM} - \sigma}{\sigma_s - \sigma_{ss}}$$

Equation 7.30

X can also be determined using the Avrami equation as shown in Equation 7.31, where a and b are material constants, and ε_c is the critical strain. Accurate determination of the critical strain can be challenging and often adds an undue amount of uncertainty, therefore the peak strain ε_p is often used instead.

$$X = 1 - \exp\left(-a(\varepsilon - \varepsilon_c)^b\right.$$

Equation 7.31

Equation 7.31 can then be further derived to give Equation 7.32.

$$\ln\left(-(\ln(1 - X)\right) = lna + bln(\varepsilon - \varepsilon_c)$$

Equation 7.32

The values of constants *a* and *b* can be calculated using a plot of ln(-ln(1-X)) vs. ln (ε-ε_p) with the slope of the curve representing *a*, and the y-intercept representing *b*, as shown in Figure 7.23. In similar work by other authors these values have been shown to be constant [132], [223]; in this instance there was some variation although not significant, so an average value of 1.54 was evaluated for *a* and 0.864 for *b*. These values where an average of all *a* and *b* values calculated from the method described above for all temperatures and strain rates.

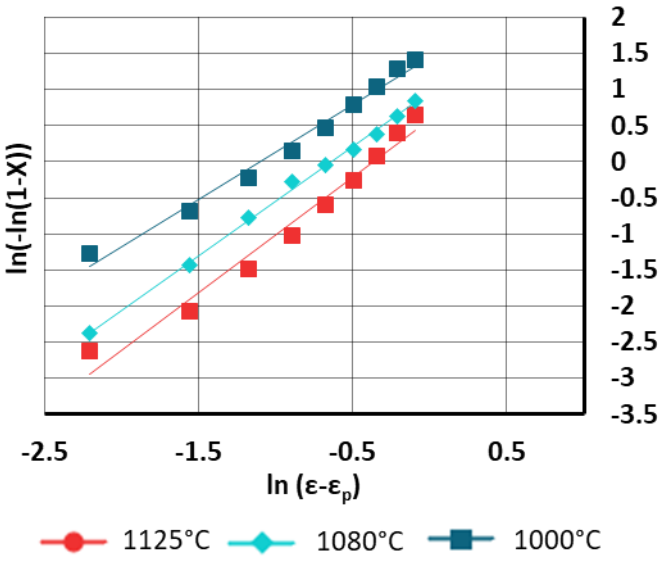

Figure 7.23: Plot for determining values of constants *a* and *b* based on Equation 7.32 at strain rate of 1 s^{-1}.

The values of ε_p, σ_s, σ_{ss}, and σ_0 were all calculated as a function of the Zener-Hollomon equation (Equation 7.6) in order to take into consideration, the effects of temperature and strain rate. This has been shown to increase the accuracy of the model [136] . A second order polynomial, as shown in Figure 7.24a-d, was selected to capture the behaviour of σ_s, σ_{ss}, and σ_0 with respect to the Zener-Hollomon parameter. The value of ε_p varied so little for each test that it was averaged giving a value of 0.94. The second order polynomial fit is described in Equation 7.33 and the calculated coefficients can be seen in Table 7.5. The AARE, RMSE and coefficient of determination (R^2) were all calculated to quantify the accuracy of the model.

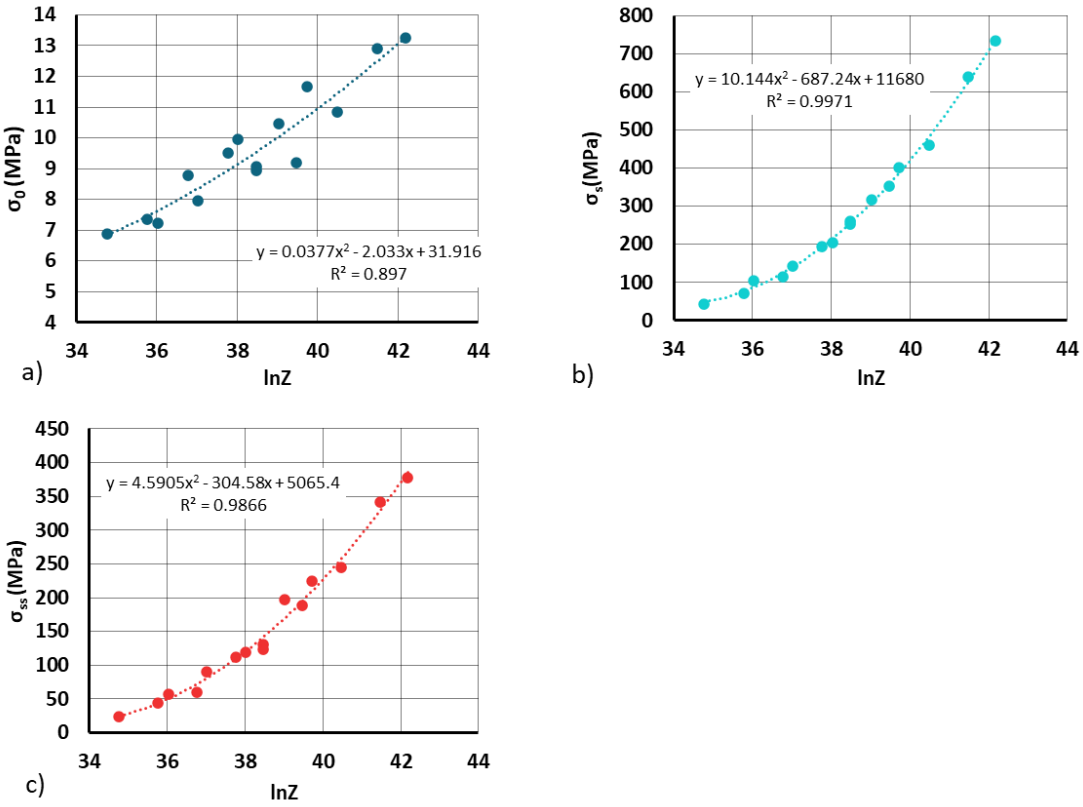

Figure 7.24: Variation as a function of the Zener-Hollomon parameter of a) Initial Stress (σ_0), b) Saturation Stress (σ_s), and c) Steady State Stress (σ_{ss}).

$$\sigma_0 = B_0 + B_1 Z + B_2 Z^2$$

$$\sigma_s = D_0 + D_1 Z + D_2 Z^2$$

$$\sigma_{ss} = E_0 + E_1 Z + E_2 Z^2$$

Equation 7.33

Table 7.5: The determined coefficients from fitting different polynomials to the Initial Stress (σ_0), Saturation Stress and Steady State Stress (σ_{ss}) curves as a function of the Zener Hollomon parameter in Figure 7.24.

	2nd order coefficient	1st order coefficient	0 order coefficient
σ_0	0.037	-2.032	31.91
σ_S	10.14	-687.23	11679.74
σ_{SS}	4.59	-304.58	5065.39

Finally, the combined EM+Avrami equation for predicting the flow behaviour of alloy AD730 over the temperature range of 1000 – 1125 ˚C for strain rates of 0.001 - 5 s^{-1} can be seen in Equation 7.34 (a) and (b).

$$\sigma^{EM} = [\sigma_s^2 + (\sigma_0^2 - \sigma_s^2)exp(-2B\varepsilon)]^{1/2} \quad for\ \varepsilon < \varepsilon_p \qquad \text{(a)}$$

$$\sigma = \sigma^{EM} - X(\sigma_s - \sigma_{ss}) \quad for\ \varepsilon \geq \varepsilon_p \qquad \text{(b)}$$

Equation 7.34

The AARE, RMSE, and R^2 values for the EM+Avrami constitutive equation for AD730 were calculated as 8.19%, 30.27 MPa, and 0.99, respectively. The accuracy of the fit can be seen in Figure 7.25. The EM+Avrami model does not have as accurate a fit at the higher stresses as it does at the lower stresses with a tendency to predict higher stresses than experimentally measured. These metrics demonstrate a reasonable amount of error when compared to similar works [131], [136], [223]. Given the physical significance of the constants established for this model, the generalised reduced gradient solver was not employed, as it has the potential to compromise the meaningful interpretation of the variables ε_p, σ_s, σ_{ss}, and σ_0.

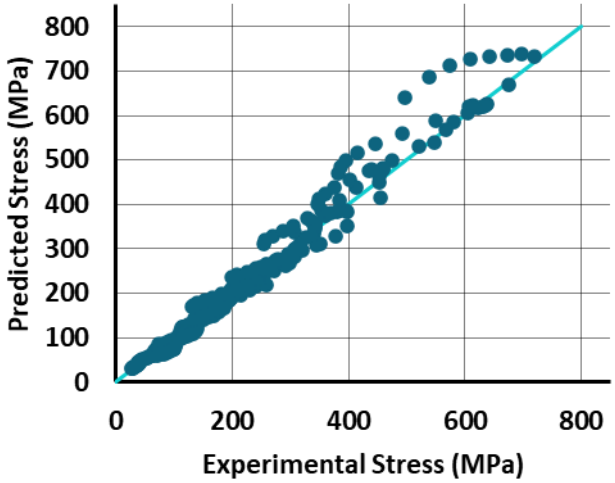

Figure 7.25: Correlation of experimental and predicted stress using the EM+Avrami constitutive equation.

7.3.6 Constitutive Artificial Neural Network

The coefficient of determination (R^2), RMSE, and AARE for the CANN results were calculated as 0.99, 13.64 MPa, and 1.45%, respectively. The accuracy of the fit can be seen in Figure 7.26.These results represent a high degree of accuracy when compared with results from

similar works using conventional constitutive equations [131], [136], [223]. Overtraining in a neural network occurs when it is trained on a specific dataset, capturing trends that do not accurately represent the dataset as a whole. This phenomenon can result in a precise fit for the training data but may lead to a less accurate fit for the validation and test data. In this study, the mean squared error for the training data was 7 MPa, and for the test data, it was 12 MPa. These values suggest that there was no significant overtraining, indicating that the network performed well in predicting data not included in the training set.

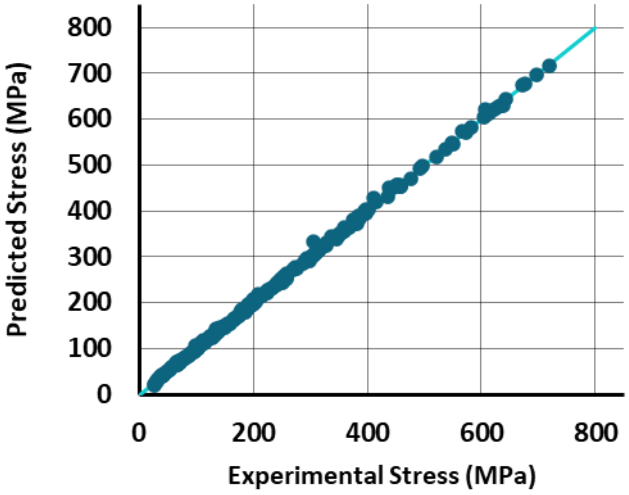

Figure 7.26: Correlation of experimental and predicted stress using CANN.

7.3.7 Forging Trials and FE simulations

Some images of the forging trials can be seen in Figure 7.27 *a*, *b* and *c* showing the forging and forced air-cooling of the DTC's. Figure 7.27d shows a top-down view of one of the forged DTC's demonstrating reasonably good circularity, indicating that even though the dies were not flat and parallel, the impact on circularity is not severe. In Figure 7.27e and f, the side-on views of both DTCs are presented, with a digital protractor placed on top to illustrate the misalignment angle. It is evident that the misalignment angle is inconsistent, signifying a worsening of the misalignment issue with the dies during forging. Hence, caution is necessary when interpreting the results. It is important to note that in Figure 7.27e and f, the forged DTC's have been sectioned in halves for further analysis which will be discussed in the following chapter. The sectioning strategy was such that the sample was cut in two through the middle such that each half of a disc could be treated as symmetrical with the other half. The markings visible on the left-hand side and near the centre of the forged DTCs in Figure 7.27e and f, originate from the

wire EDM process. It's important to note that these markings had no impact on the forging of the DTCs.

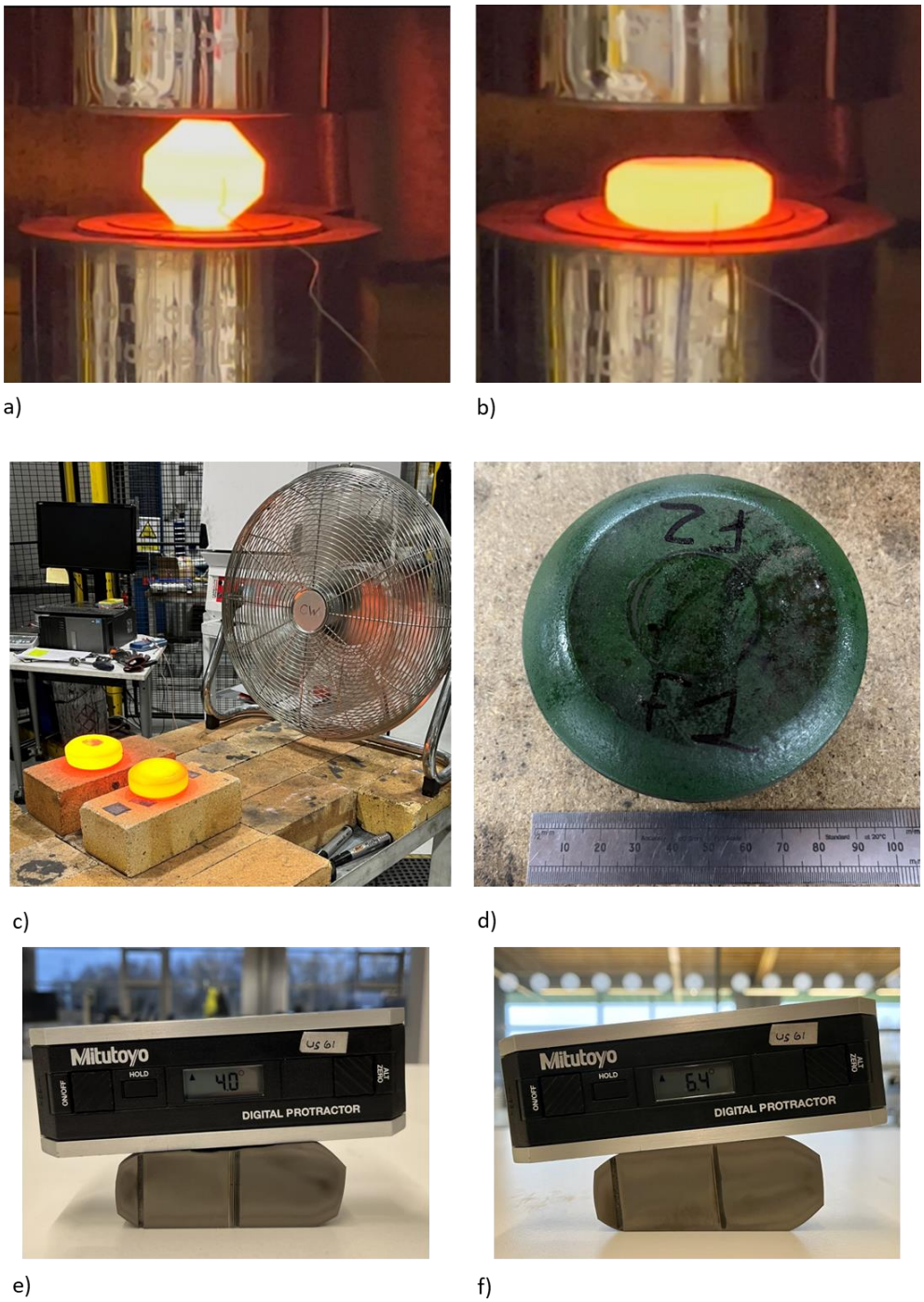

Figure 7.27: a) A photograph of a DTC at the commencement of forging (i.e., placed on the bottom die), b) The deformed DTC immediately after forging, c) force air-cooling of the forged DTC's, d) top-down view of a forged DTC demonstrating good circularity, e) half side of DTC 1 showing misalignment angle of 4°, and f) half side of DTC 2 showing misalignment angle of 6.4°.

The outline of the forged DTC's were measured after sectioning using a CMM to compare the final dimensions with the final predicted deformations from the simulation. The outlines measured using the CMM can be seen in Figure 7.28. Comparison of these outlines' lays bare the misalignment issue with the dies and the subsequent impact this has had on the dimensions of the final forged parts. Measurements were taken at locations A and B for DTC 1 and DTC 2. A summary of the measurements are provided in Table 7.6.

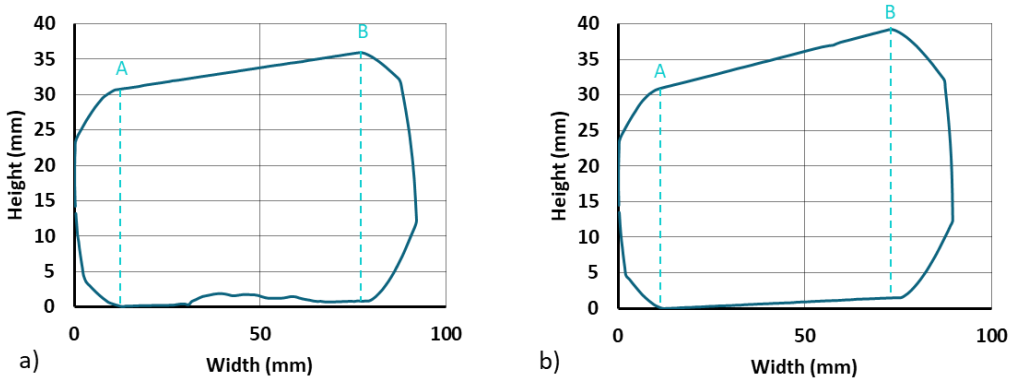

Figure 7.28: CMM measured outline for a) DTC 1 with 4° misalignment angle and, b) DTC 2 with 6.4° misalignment angle. Note: hatched cyan lines and annotations A and B indicate where measurements were taken for comparison with simulated data.

Table 7.6: Critical dimensions of the two forged DTC's.

Identifier	Misalignment angle (°)	Measurement A (mm)	Measurement B (mm)
DTC 1	4	30.75	35.11
DTC 2	6.4	31.3	37.74

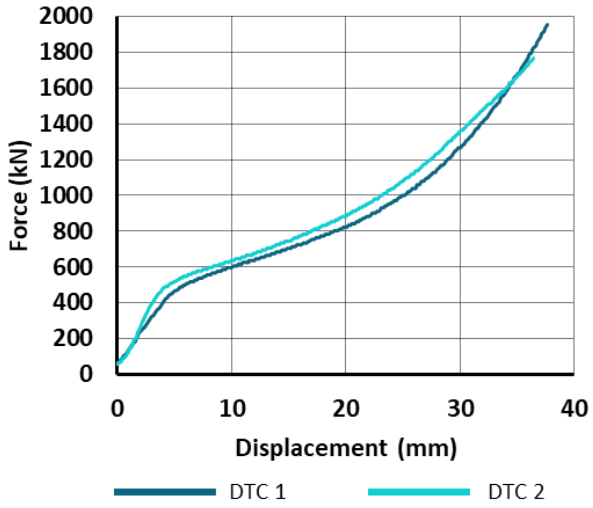

Figure 7.29: Comparison force-displacement curves from forging of both DTC's measured from the 500T press.

The force-displacement curves in Figure 7.29 depict the forging process for both DTCs. While both curves generally follow a similar path, DTC 1 exhibits higher displacement (1.4mm) and force (186kN) compared to DTC 2. Interestingly, in both cases, the total displacement exceeded the 32mm target for a 50% reduction in height. DTC 1 achieved 37.6mm reduction for a supposed final height of 26.4mm, while DTC 2 reached 36.4mm reduction for a final height of 27.6mm.

Understanding this requires insight into how the press measures displacement. Before the samples are put on the dies, the dies are brought together, and a small compressive force is applied to zero the displacement, assuming flat and parallel dies. At this point, the dies are believed to have been flat and parallel due to the small compressive force overcoming the misalignment issue. As the dies separate for forging preparation, the misalignment angle returns.

Assuming the misalignment rotation is centred on the middle of the die, this now means that depending on how far away from the centre of the dies the DTC is forged and in what direction, the DTC will undergo a different amount of displacement than the target value, as shown schematically in Figure 7.30. This partly explains the varied displacements and the deviation from the 32mm target displacement shown in Figure 7.29.

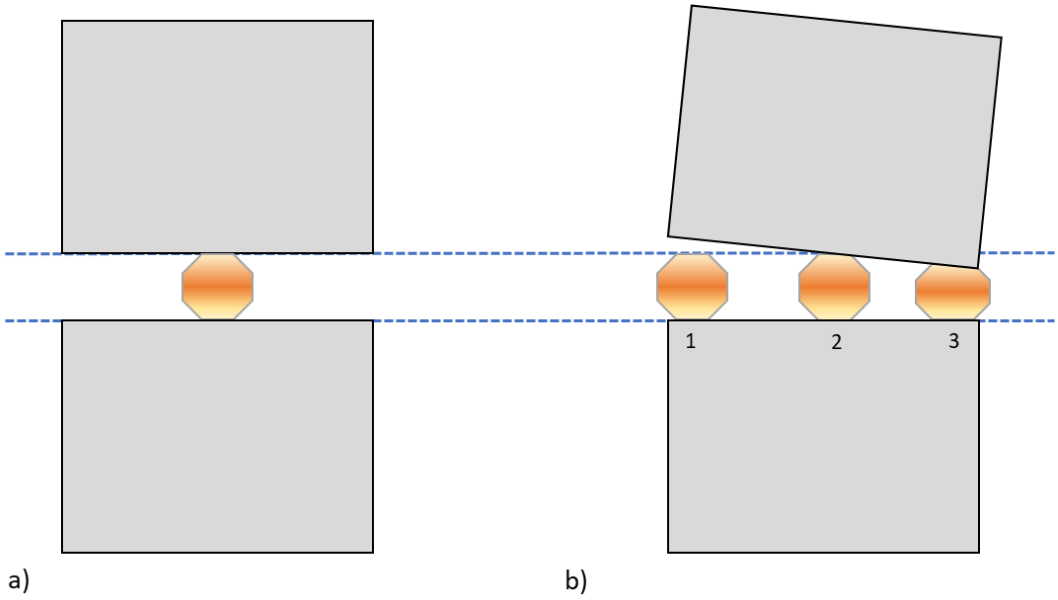

Figure 7.30: a) Ideal scenario with flat and aligned dies making initial contact with the DTC at the expected 64 mm height from the bottom die. b) Flat but misaligned dies at the same 64 mm height from the bottom die as in a); in the case of imaginary Sample 1, no contact has been made, leaving significant headroom. Sample 2 has partly made contact and started compression, while Sample 3 is already in the compression phase. Note that in b), from the point shown, all DTCs will undergo 32mm of compression, explaining the over compression in DTC 1 and 2.

An important point to note on the force-displacement curves shown in Figure 7.29 is that the beginning of the test was not taken as the point when the die reached 64 mm in height. As demonstrated in Figure 7.30, if this were to have been done, significant amounts of deformation could already have taken place, and valuable information would have been lost. Instead, the beginning of the test was taken as the point at which the force began to increase beyond what was deemed to be noise. In the case of the forging of both DTCs, this was before the expected first-touch point of 64mm was reached.

It is important to note that for DTC 1, Figure 7.28 and Table 7.6 show that at measurement location A (the shortest distance between where the top and bottom die deformed the sample), the measured height of the sample (at 30.75mm) is significantly greater than the height after deformation measured from the press (26.4mm in height). This means there is a discrepancy between the final measured height of the part and the measured displacement from the press, with the press suggesting the DTCs have been compressed more than the dimensions suggest. Two possible explanations could be compliance in the press, however this is found to be very small, or the part is sliding on the dies, likely due to the misalignment. This

means that the displacement measurement from the press is likely an over-estimation of the total reduction of the DTC's.

Adding further complexity, the misalignment angles differ for both DTCs, potentially occurring during the second DTC forging. This has likely impacted the correlation of the force-displacement curves.

In summary, three factors significantly impact the forging of the DTCs:

1. The misalignment of the dies causes the DTCs to begin being compressed before the dies have reached the expected point of first-touch at 64 mm in height, leading to over-compression.
2. The disagreement between the final DTC dimensions and the total compression measured by the press, with the press suggesting the DTC's have been forged more significantly than what the measured dimensions indicate, implies that the DTCs must be sliding during the forging, likely due to misalignment. This means the displacement measurement from the press is an over-estimation of the reduction in height of the DTC's.
3. The misalignment angle differs for the DTCs, suggesting that the angle increases during the forging of the second DTC.

Inspection of the dies post-forging showed that in both forging trials, the DTC's were not centred in the middle of the die, as shown in Figure 7.31a. Figure 7.31b shows evidence that the DTC has slid during forging. The smaller, circular, beige coloured marking is where the original geometry of the DTC rested on the die as forging commenced. The red lines shown in Figure 7.31b are equidistant lines taken from the central point of this smaller circle. If the dies were flat and parallel, the forged DTC would be circular in shape centred around this centre-point, and the outline of the forged markings would line up with the red equidistant lines. But because the DTC has slid, the forged markings have lost their circularity, and they are not centred on the central point indicated by the red lines. Instead, the forging has slid from left to the right, which is towards the centre of the die. This makes sense when recalling from earlier that the force-displacement curves indicated that the DTC's were being loaded before the first-touch point of 32 mm was reached, meaning the dies were in the situation of sample 3 in Figure 7.30b, before sliding towards the central point of the dies.

a) b)

Figure 7.31: The bottom die post-forging displays forging marks from both DTCs. Image a) reveals the forging marks on the dies, indicating the location of forging relative to the centre point of the die. In image b), a higher magnification focuses on the forging markings left by one of the DTCs. Equidistant red lines illustrate the outer axis of a perfect circle cantered on the DTC's original position within the die, based on post-forging markings. The blue circular outline represents a non-perfect circle, outlining the actual forged DTC based on the post-forging markings and indicating that the DTC slid during forging from left to right, i.e. towards the centre.

As was discussed in 7.3.7, the misalignment angle was accounted for in the simulation by tilting the top die angle in DEFORM as shown in Figure 7.9d. Given the impossibility of accurately predicting changes in the misalignment angle during forging, a fixed angle of 4° was set for the entire simulation. To mitigate the impact of the DTC's sliding during the forging trials, the DTC's dimensions measured by CMM were used as the reference stopping point for the dies. Since only one DTC (DTC 1) was simulated, a total die travel of 32mm was selected to observe the final dimensions of the simulated part and compare them with the experimentally measured part. Figure 7.32d, Figure 7.33d, and Figure 7.34d illustrate the close match between the final dimensions in all three simulations conducted with the Arrhenius material model, EM+Avrami model, and tabular data, respectively. The complete results of the simulations using the Arrhenius model, EM+Avrami model, and tabular data are presented Figure 7.32, Figure 7.33, and Figure 7.34, respectively.

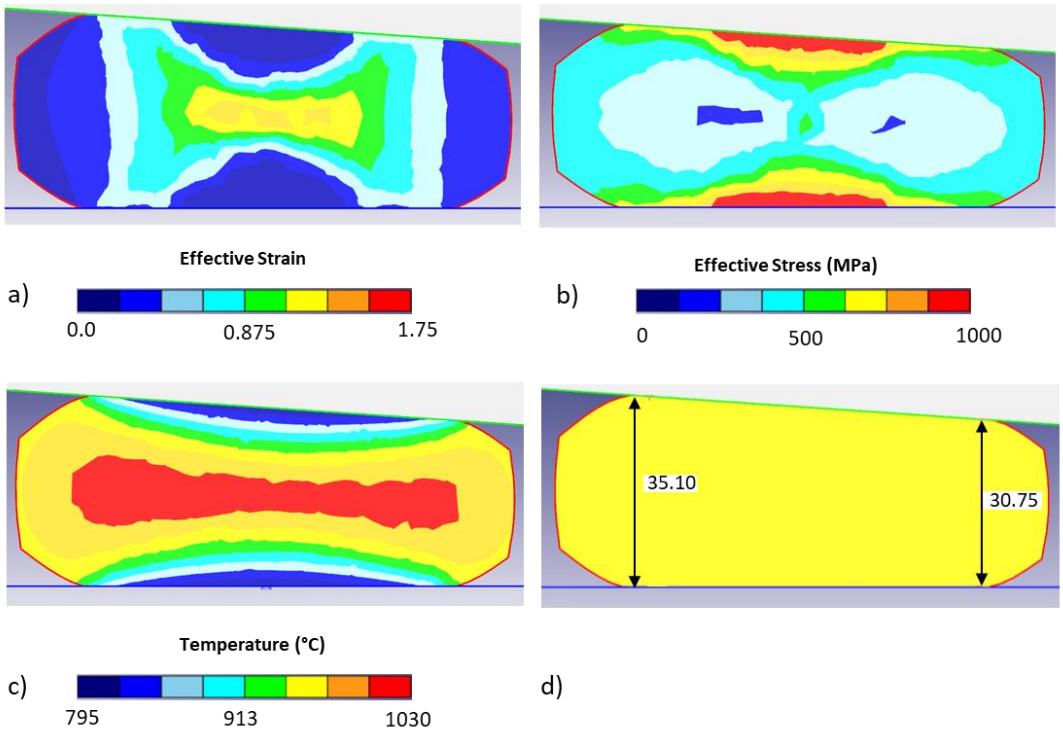

Figure 7.32: Simulation results obtained in DEFORM using the developed Arrhenius constitutive model for predicting flow stress. Results shown are immediately after the completion of forging with panel a) showing effective strain, b) displaying effective stress, c) illustrating temperature, and d) presenting final dimensions at the end of forging.

A comparison of temperature maps across all three simulations reveals similar distributions. The models consistently predict similar magnitudes of effective strain after maximum compression, as demonstrated in panels a) of Figure 7.32, Figure 7.33, and Figure 7.34.

In the effective strain map generated by the Arrhenius material model (Figure 7.32a), a slightly blocky distribution is observed. This blockiness, seen in the effective strain map, stress map, and to a smaller extent in the temperature map for the Arrhenius model, is an artefact resulting from the material model. Despite having identical mesh and element size across all simulations, this blocky feature is specific to the material model employed.

While the effective stress distributions in all three simulations are generally similar, some variations are noteworthy. Notably, the results for effective stress derived from tabular data exhibit fewer tensile stresses near the die-part interface compared to the other two simulations. Furthermore, compressive stresses in the tabular data are comparatively lower than those obtained from the other equations developed using the constitutive models. This

discrepancy underscores the significant impact of the chosen material model on the predicted flow stress.

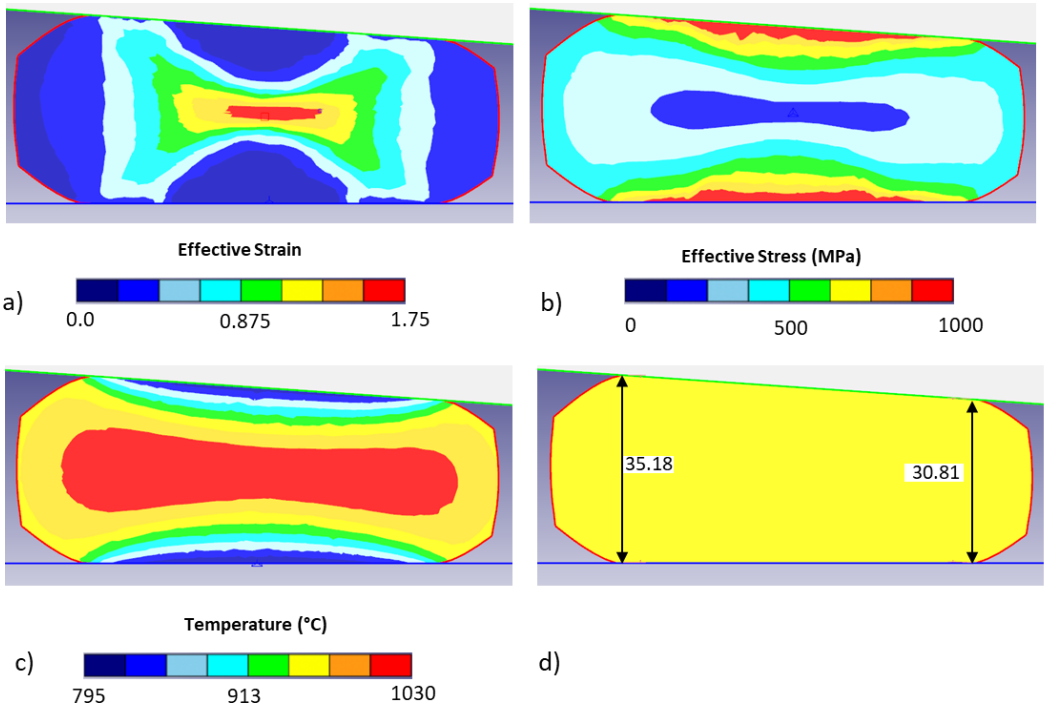

Figure 7.33: Simulation results obtained in DEFORM using the developed EM+Avrami constitutive model for predicting flow stress. Results shown are immediately after the completion of forging with panel a) showing effective strain, b) displaying effective stress, c) illustrating temperature, and d) presenting final dimensions at the end of forging.

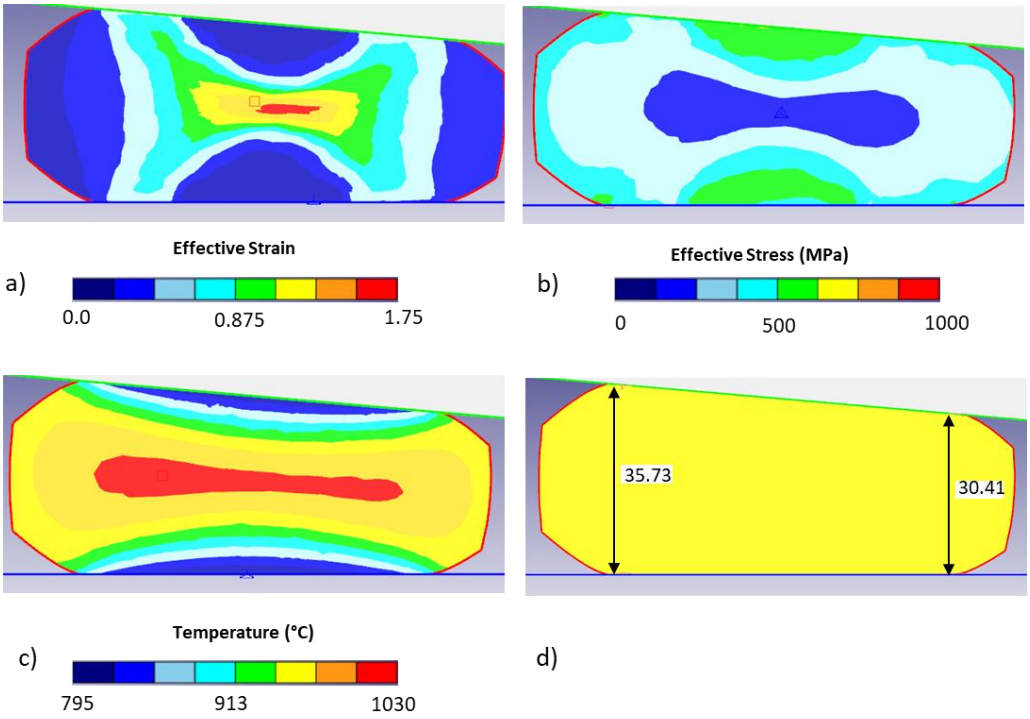

Figure 7.34: Simulation results obtained in DEFORM using the developed tabular data for predicting flow stress. Results shown are immediately after the completion of forging with panel a) showing effective strain, b) displaying effective stress, c) illustrating temperature, and d) presenting final dimensions at the end of forging.

Force-displacement curves from all three simulated models and experimentally obtained curves from the press are compared in Figure 7.35. The simulation curves align well with the experimental curves for DTC1 up to 20mm of displacement, after which a divergence is observed. Possible reasons include: 1) a drop in part temperature below the model's development range (minimum 1000°C), 2) exceeding strain limits in the DTC centre, impacting model reliability, and 3) potential sliding effects affecting displacement measurements. Despite the unreliability of experimentally obtained curves, final force measurements for DTC1 and simulated curves are reasonably close, as shown in Figure 7.35. This is because despite the error in the displacement measurement from the forging of DTC 1, the simulation and the experimentally fogged DTC have the same final dimensions.

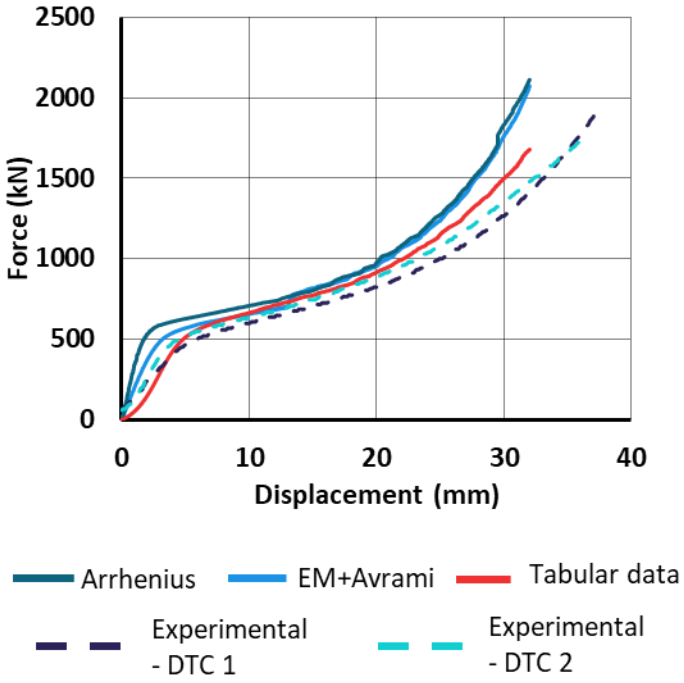

Figure 7.35: Comparison of force-displacement curves: Forging trials of DTCs 1 and 2 alongside simulated forging of DTC 1 using material models developed with the Arrhenius constitutive equation, the EM+Avrami constitutive equation, and tabular data.

7.4 Discussion

In Figure 7.36, the AARE for each strain rate is presented as a function of temperature. The Arrhenius model performs better in predicting flow stress at higher strain rates (0.1, 1, and 5 s^{-1}) compared to lower strain rates (0.001 and 0.01 s^{-1}). The EM+Avrami equation exhibits consistent performance across all strain rates and temperatures, generally maintaining an AARE below 10%. However, similar to the Arrhenius model, does not give accurate predictions at 0.001 s^{-1} and shows an AARE > 10% at 1 s^{-1} and 1000°C. In contrast, the CANN method consistently yields lower AARE values at every temperature and strain rate, suggesting it is not only a viable option but also the most accurate method for predicting the flow stress of AD730.

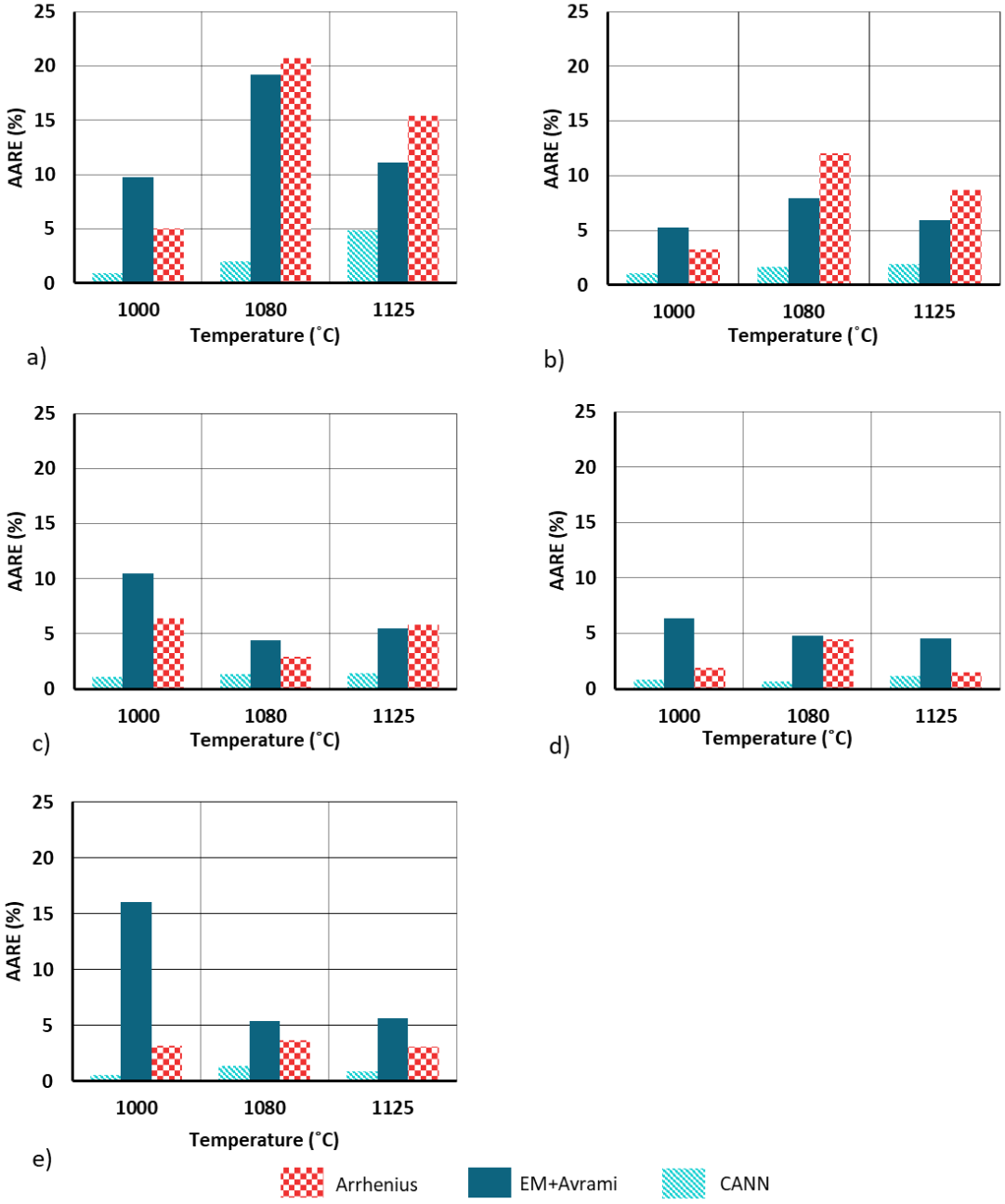

Figure 7.36: Comparison of AARE at differing temperatures for strain rates of a) 0.001 s^{-1}, b) 0.01 s^{-1}, c) 0.1 s^{-1}, d) 1 s^{-1}, and e) 5 s^{-1}

In Figure 7.37, the correlation of each predicted curve compared to the experimental curves is illustrated. Figure 7.37a and b demonstrate that all models effectively track experimentally measured stresses at lower strain rates (0.001, 0.01, and 0.1 s^{-1}), but their performance diminishes at higher strain rates (1 and 5 s^{-1}). Notably, the CANN results are at their least accurate under these conditions. Figure 7.37c and d show average correlations between

predicted and experimentally measured flow stresses under lower strain rates (0.001 and 0.01 s-1) at 1080 °C for both the Arrhenius and EM+Avrami material models. Figure 7.37e and f reveal that all models reasonably track experimental stress at 1125 °C, with the Arrhenius model exhibiting slightly poorer results than the other models.

The combined EM+Avrami equation generally performs well, especially at strain rates greater than 0.01 s^{-1}, as supported by the lower AARE in Figure 7.36 for higher strain rates. The Arrhenius equation excels at strain rates greater than 0.01 s^{-1}, surpassing the EM+Avrami model in most cases, except for lower strain rates (0.001 and 0.01 s^{-1}).

Notably, the CANN exhibits superior tracking compared to other models in Figure 7.37. However, the CANN has certain disadvantages, particularly its 'black box' nature in terms of output, making its implementation into FE software like ABAQUS or DEFORM challenging. This limitation highlights a potential area for improvement and future work.

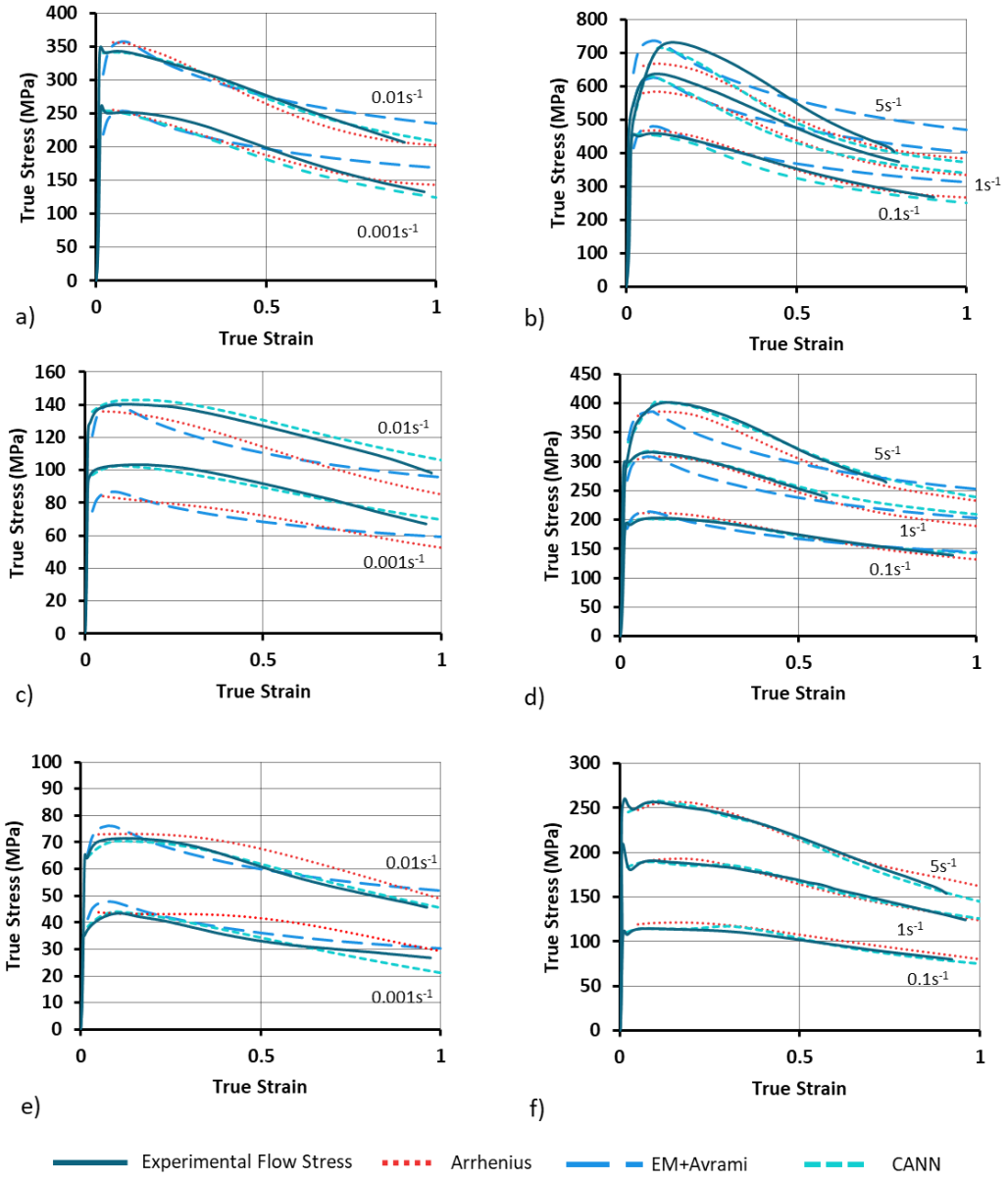

Figure 7.37: Comparison between experimental and predicted stress values for tests conducted at: a) 1000 ˚C with strain rates of 0.001 s^{-1} and 0.01 s^{-1}, b) 1000 ˚C with strain rates of 0.01 s^{-1}, 1 s^{-1}, and 5 s^{-1}, c) 1080 ˚C with strain rates of 0.001 s^{-1} and 0.01 s^{-1}, d) 1080 ˚C with strain rates of 0.01 s^{-1}, s^{-1}, and 5 s^{-1}, e) 1125 ˚C with strain rates of 0.001 s^{-1} and 0.01 s^{-1}, and f) 1125 ˚C with strain rates of 0.01 s^{-1}, 1 s^{-1}, and s^{-1}.

Overall, it can be seen that all three models have a good degree of accuracy and success in predicting the flow stress at the given strain rate range and temperature range. There are several key takeaways from the experimental data which is likely to have had an impact on the flow stress predictions using the three models.

1. The data collected at 1125 °C is above the γ' solvus. This means there should be no γ' precipitates in the microstructure and this should affect the mechanics of deformation. In all cases though, the constitutive models and CANN were able to include this data and predict it reasonably well without compromising the accuracy of the models at lower temperatures.

2. In cases where the curves exhibited the yield drop phenomenon, for the sake of modelling, this was ignored. It would have been impractical to apply these models to accurately predict this. In cases where the peak stress was the stress before the yield drop phenomenon, as is the case in Figure 7.37f (i.e., at 1125 °C under a strain rate of $1s^{-1}$), the peak stress for developing the models was taken to be the peak stress after the flow stress rebounds from the yield drop.

3. The data collected at 900 °C was presented in Figure 7.13a and was originally included to increase the capability of the model over a larger temperature range, however the compression tests at this temperature were very challenging to successfully complete. The compression samples often began to shear during the uniaxial compression testing making a substantial proportion of the data unreliable. The data was not used to determine the coefficient of the constitutive models, nor was it used to train the CANN. Had this data been included, it would have undoubtedly changed the coefficient values for the models.

While the forging trials did not play out as planned for (i.e., due to die misalignment), analyses were conducted through both force-displacement curves from the press and measurements of the final dimensions of the forged DTCs. Die misalignment introduced two significant phenomena: over-compression of the DTCs and sliding of the DTCs on the dies. The misalignment angle of the die is also believed to increase during the forging of DTC 2, making it an inconsistent variable. Despite these challenges, a FE model was constructed in DEFORM, and user-defined subroutines were employed to implement the Arrhenius and EM+Avrami constitutive models, solving successfully. The unexpected die misalignment further stress tested the FE model and the integrated material sub-routines (i.e., flow stress models). Generally, the distribution of effective strain and effective stress was similar for both these models and the FE model developed using the tabular data, instilling confidence in their accuracy. The final predicted force of the models, when compared to the final force obtained

from the forging of DTC 1, showed reasonable agreement. However, due to the aforementioned die damage which resulted in misalignment, correlating the simulated force-displacement curves with the experimentally obtained curves was impossible in terms of displacement, despite of the same load magnitude (see Figure 7.35).

7.5 Conclusions

The hot deformation behaviours of AD730 for the hot isothermal compression testing between temperatures of 900 °C to 1125 °C and strain rates of 0.001 s^{-1} to 5 s^{-1} were investigated. Two constitutive models, the Arrhenius equation and the EM+Avrami equations were used to model and predict the flow stress along with a CANN. The accuracy of prediction was analysed in each of the three cases, and the following conclusions were drawn:

- The accuracy of the Arrhenius constitutive model was quantified using the AARE, RMSE, and R^2 values which were determined as 6.54%, 13.53 MPa, and 0.997, respectively. This model demonstrated better accuracy at predicting the flow stress when compared to experimentally measured flow stress at higher strain rates of 0.1, 1, and 5 s^{-1}, than the lower strain rates of 0.001, and 0.01 s^{-1}.
- The accuracy of the EM+Avrami constitutive model also had better accuracy at predicting the flow stress at higher strain rates of 0.1, 1, and 5 s^{-1}, than the lower strain rates of 0.001, and 0.01 s^{-1}. Strain rates of the constitutive model was optimised using a generalised reduced gradient solver with the AARE as the objective function. The AARE, RMSE, and R^2 values for the EM+Avrami model was determined as 8.19%, 30.27 MPa, and 0.99, respectively.
- When directly compared to the Arrhenius model, the EM+Avrami model is more accurate at lower strain rates of 0.001 and 0.01 s^{-1}, than at higher strain rates of 0.1, 1, and 5 s^{-1} where the Arrhenius model is more accurate.
- The CANN demonstrated the best accuracy of all three methods evaluated in this chapter of work, with the R^2, RMSE, and AARE calculated as 0.99, 13.64 MPa, and 1.45%, respectively.
- The transferability of the "black box" trained artificial neural network into a subroutine for implementation in FE software such as ABAQUS or DEFORM raises questions,

which is a research topic to be explored in Chapter 8 of this thesis. Currently, it is considered a potential significant disadvantage of this method.

- The forging trials involving two DTCs encountered substantial challenges due to misaligned dies; however, they successfully yielded valuable data for benchmarking a FE simulation with the developed constitutive models.
- Both constitutive models developed in this chapter were incorporated into a user-defined subroutine and implemented into an FE solver. The simulation results were validated against the forging trials, demonstrating good agreement in the final forged dimensions of the DTC between the simulation and experimental data, as well as in the final values of the force-displacement curves.

The FE model created in this chapter will play a central role in a larger multi-step, multi-process FE model. This comprehensive model will be utilised to predict the behaviour of AD730 throughout its thermo-mechanical processing route, as explored in Chapter 8.

8

The Multi-step, Multi-process Finite Element Model of AD730 Describing the Thermo-Mechanical Processing Behaviour

8.1 Introduction

This chapter aims to integrate the methodology established in Chapter 4, which focused on determining HTC values for a Ni-based superalloy during air-cooling from the solution-annealing temperature, with the developed constitutive stress relaxation model and constitutive material model for AD730. This integration involves creating a comprehensive multi-step multi-process FE model based on the thermo-mechanical processing route outlined in Figure 8.1. In this chapter, residual stress analyses using the contour method was conducted on the two forged DTC's at the stages denoted by the letters A and B in Figure 8.1, respectively. The results of which were compared to the FE model results to validate the simulation.

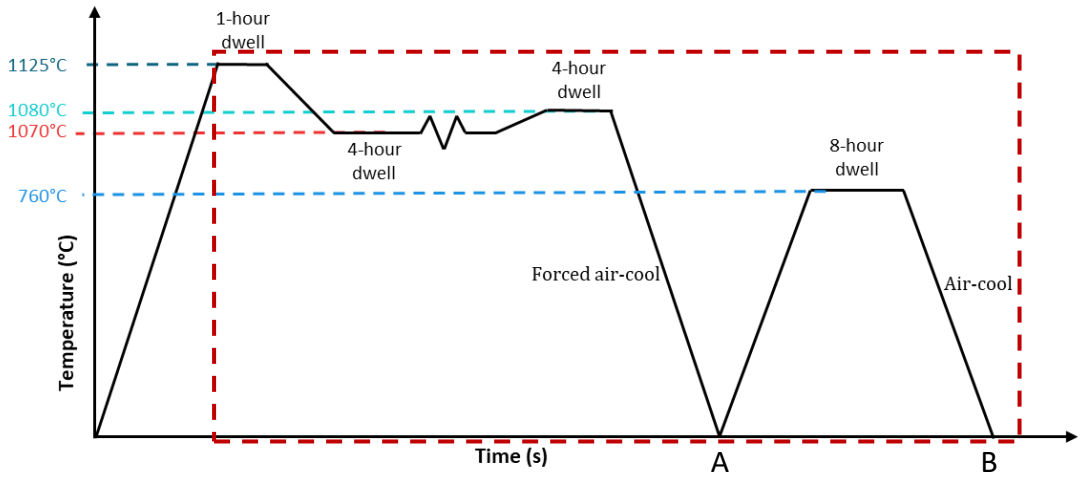

Figure 8.1: Thermo-mechanical processing route of AD730 investigated in this thesis, emphasising the steps included in the multi-step multi-process model explored in this chapter. Stages denoted by letters A and B involve conducting residual stress measurements using the contour method on DTC 1 and DTC 2, respectively.

8.2 Methodology

8.2.1 Material

The DTC's mentioned in Chapter 7 were the same DTC's which had further analysis performed on them in this chapter. Information on chemical composition and the microstructure characteristics of the material in the pre-forged as-received condition can be found in section 7.2.1 and section 7.3.1.

8.2.2 Forging Trials and Heat Treatments

Further analyses were done on the results of forging trials carried out and discussed in Chapter 8. In this Chapter, only the additional follow-on analyses are discussed. As discussed in Chapter 7, the forging trials were carried out on AD730. Following the forging trials, DTC 1 underwent residual stress measurement using the contour method, while DTC 2 underwent an additional ageing heat treatment, as outlined in the forging schedule presented in Figure 8.1 . During the ageing heat treatment, the sample was positioned inside a pre-heated convection furnace set to 760 °C. A thermocouple was placed inside the furnace and pressed against DTC 2 (i.e., referred to as the controlling thermocouple) to ensure precise temperature monitoring. The 8-hour heat treatment commenced once the controlling thermocouple reached 760 °C after which the DTC was air-cooled. Subsequently, DTC 2 underwent residual stress measurement

using the contour method, after air-cooling, and the results were compared to those of DTC 1, which was not aged following forging (i.e., no stress relaxation).

8.2.3 Residual Stress Measurement

The residual stress measurement with the contour method followed the same process as was described in detail in Section 4.2.3 of Chapter 4 for the scaled-disc components. This included (i) cutting with the wire EDM, (ii) surface profile measurements with CMM, (iii) data cleaning and surface fitting, and (iv) FE modelling to determine residual stress by using the surface fitting data as boundary condition.

The cuts on both DTCs were conducted radially. Initially, a hole was wire EDM drilled through the sample in the axial direction, 15mm from the edge, as depicted in Figure 8.2. The cut then commenced from this point, went through the midpoint, and extended to the opposite edge. The purpose of drilling the pilot hole first was to preserve a small ligament in-line with the cut line to prevent the cut from collapsing inwards. This ensures that the faces of both halves of the DTCs do not touch during or after cutting, thereby preserving the accuracy of the final residual stress data. Given that the DTCs were asymmetric due to the misalignment angle of the dies, the location of the smallest height was identified. The cut line was then determined from this point, passing through the midpoint, and extending to the opposite side. This approach aimed to maximise the symmetry in both halves of the DTCs.

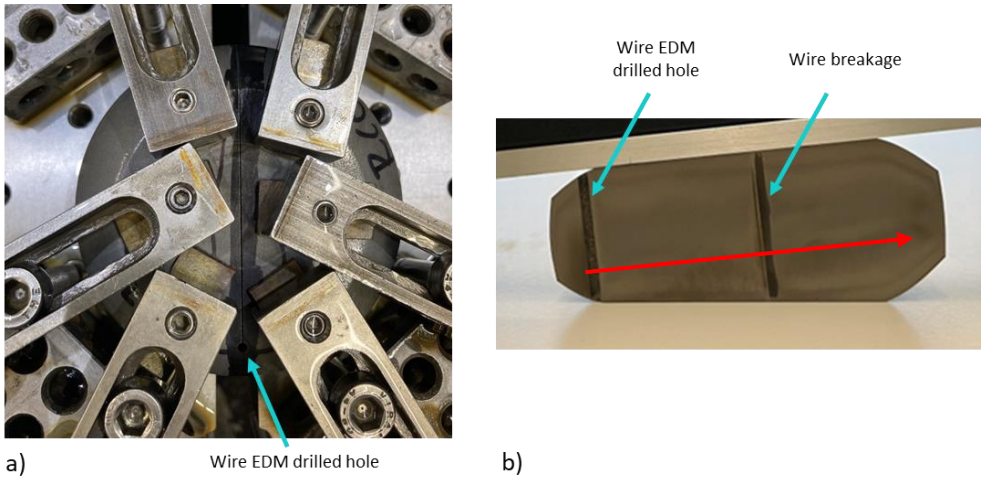

Figure 8.2: a) A photograph of DTC 2 during sectioning, starting from the section of shortest height; the pilot hole was wire-EDM drilled, and the cut was started from the hole to the other side of the cut (i.e., the largest section), b) A photograph of the cross-section of one of the cut halves of DTC 2 displaying the location and direction of the wire EDM drilled pilot hole, along with artefacts from wire breakage. Red arrow indicates cut direction.

A GF AgieCharmilles Cut 400 SP wire EDM was utilised with "skim cut" settings for sectioning the DTC's. The DTC's were securely clamped as close as possible to the cut line and on both sides of the cut to prevent any movement, as shown in Figure 8.2a. As shown in Figure 8.2b, a second artefact is visible on the cut surface near the centre of the DTC. This artefact was present on both cut surfaces of the DTC's and was caused by EDM wire breakage during the cut. Efforts were made during the cleaning of the CMM data to minimise the impact of this artefact.

After the completion of the cuts, both halves of each DTC's had their outline and surface profiles measured using a Mitutoyo Crysta Apex C CMM with a 1 mm ruby interfaced to a Renishaw PH10T touch probe. The pitch size for all DTC measurements was 500 µm in both in plane directions.

The raw surface profile data obtained from the CMM were carefully cleaned and analysed, using an in-house developed software in Matlab. Surface profile data from both halves of the same part were aligned onto the same grid in a common coordinate system. Subsequently, the data from one half of the part, referred to as the "floating half," was mirrored and superimposed onto the data from the corresponding other half, termed the "reference half." A linear interpolation was then performed, followed by averaging of the two datasets in the common coordinate system.

Bivariate cubic splines were then fitted to the averaged datasets for different knot intensities. Determining a suitable knot intensity requires some degree of iteration. A knot intensity of 7 mm was selected as the most suitable as it provided an appropriate level of detail without oversimplifying the fit and losing detail.

The final step involves calculating residual stress using a 3D model in Abaqus CAE, utilising processed surface profile data as a boundary condition. The original outline geometry of the reference half was extruded to 80 mm in length. Mesh density is determined by nodes on the outline, serving as mesh seeds. Given the significance of the top face (i.e., representing the cut surface), a biased meshing approach is employed, ranging from 0.5mm to 7.5mm, with higher density at the top compared to the bottom surface. This is shown in Figure 8.3. All components are meshed using 20-noded quadratic hexahedral (C3D20R) elements. Material elastic properties, including the Young's modulus of 219 GPa and a Poisson's ratio of 0.3, were

assigned. Residual stress was then computed by deforming the half-cut part surface to match the average surface profile data, inverted in the out-of-plane direction.

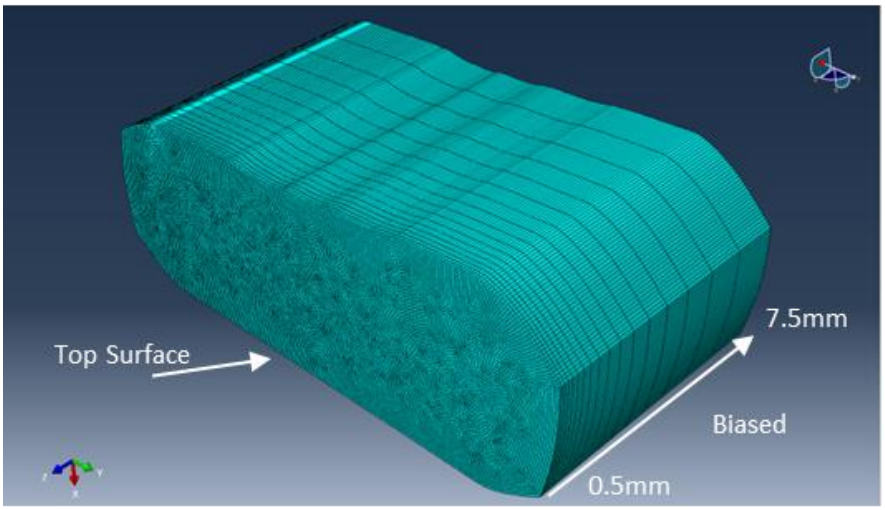

Figure 8.3: Extruded reference outline of one of the DTC showing uniform seeding around cut surface with biased seeding of 0.5 to 7.5mm from top surface (i.e., the cut surface) to bottom surface.

8.2.4 Finite Element Modelling of the Forging of DTC's

A detailed 3D FE model was developed in DEFORM to replicate the forging procedure underwent by both DTC samples. The simulation involved multiple stages, closely resembling the real forging process. Only the forging process for AD730 was simulated. A summary of the simulated steps is presented in Figure 8.4. It's worth noting that some of the forging process had already been simulated in Chapter 7, as indicated by the different coloured blocks depicted in Figure 8.4. Subsequently, all post-forging operations, including forced air-cooling, ageing, and air-cooling after ageing were simulated as part of this chapter.

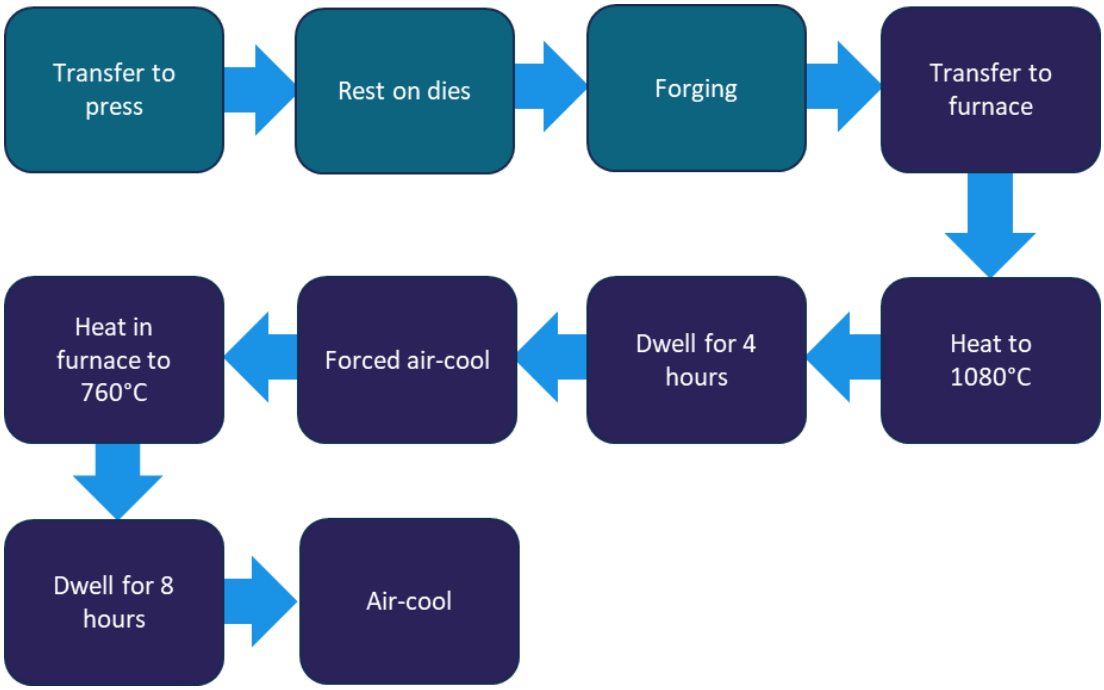

Figure 8.4: Summary of the simulated operations for the forging and ageing schedule for AD730.

Each subsequent step following the forging operation utilised the preceding results from the previous Chapters as input. The simulation settings for the forging trials were extensively detailed in Section 7.2.7. There were some initial changes made from these settings in the *transfer to furnace* operation. Specifically, the model type was switched to an elastic-plastic model, deemed more suitable for simulating thermally induced stresses. This model type persisted for the remainder of the process. The transfer time between the press and the furnace was set at 15 seconds, and the default convection coefficient of 0.02 kW/m^{2}K was chosen for transfer through air. Subsequently, *heating to 1080 °C* was simulated for a 2-hour duration. No stress relaxation data was obtained at 1080°C, so a creep model wasn't employed meaning the hold duration for the *dwell for 4-hours* operation could be reduced to 10 minutes, considering no changes to the stress profile within the DTC where expected. For *forced air-cooling*, HTC values were taken from Chapter 4 for the air-cooling of IN718, as illustrated in Figure 4.22d. As the residual stress after the post-forging forced air-cooling was measured by the aid of contour method, the HTC curve in Figure 4.22d was therefore iteratively modified to give residual stress which matched up with the measured residual stress. The optimised HTC values are plotted in Figure 8.5. The overall shape of the curve was relatively unchanged; however, the values were increased. The HTC values obtained from Chapter 4 for the air-

cooling of IN718 then utilised for *air-cooling* from 760 °C (see Figure 8.1). Heating to 760 °C was simulated for a 2-hour duration. Tabular data was employed for flow stress behaviours (see Chapter 7) in all post-forging operations, as it significantly expedited the simulation, with minor discrepancies compared to the developed EM+Avrami and Arrhenius material models, as evidenced in Chapter 7. For the 8 hours ageing (see Figure 8.1), a creep model was implemented. As the DTC was simply undergoing an isothermal hold at 760 °C for 8 hours, tabular data was used to implement the data obtained from the stress relaxation tests (Chapter 6). The creep strain rates were calculated from the stress relaxation rates using the methodology described in Section 2.5.3 whereby the creep strain rate was determined using Equation 2.18. As the effect of volumetric contraction had to be included in the stress relaxation behaviour, the uncorrected stress relaxation plots and not the stress relaxation plots corrected for volumetric contraction were used to determine the creep strain rates. The data used in the Creep model implemented into the FE simulation in DEFORM are provided in Table 8.1.

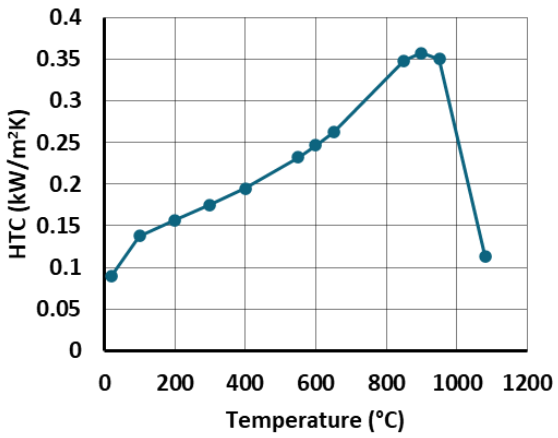

Figure 8.5: A plot of an iteratively modified HTC curve used for the FE simulation of forced air-cooling of AD730.

Table 8.1: Creep strain rates converted from stress relaxation rates used in the FE simulation for an isothermal ageing of a DTC at 3 different initial stress values and an ageing temperature of 760°C.

Time	Creep Strain rate 300 MPa (s^{-1})	Creep Strain rate 500 MPa (s^{-1})	Creep Strain rate 650 MPa (s^{-1})
5	1.79×10^{-7}	1.80×10^{-6}	2.68×10^{-6}
100	2.07×10^{-9}	8.10×10^{-8}	3.54×10^{-7}
250	4.31×10^{-9}	3.10×10^{-9}	7.86×10^{-8}
1000	4.94×10^{-9}	1.37×10^{-9}	6.15×10^{-9}
2000	7.12×10^{-9}	2.51×10^{-9}	1.49×10^{-8}
3000	3.32×10^{-9}	3.30×10^{-9}	5.46×10^{-8}
3600	8.70×10^{-9}	2.20×10^{-9}	4.60×10^{-8}

8.3 Results

8.3.1 Residual Stress Measurement

Figure 8.6 and Figure 8.7 depict contour maps illustrating surface height and stress distribution for the out-of-plane residual stress profiles of both DTC 1 and 2.

The stress distribution exhibits characteristics similar to those of water-quenched parts, with central regions experiencing tensile stress and edges exhibiting compressive stress. However, asymmetry is evident, likely influenced by misalignment of the dies during forging. DTC 1, subjected to forging and forced air-cooling, displays slightly higher tensile stress near the centre (280 MPa) compared to DTC 2, which underwent the same process plus an additional ageing heat treatment at 760 °C for 8 hours, showing 245 MPa tensile stress near the centre. This indicates a relaxation of approximately 35 MPa, a relatively modest amount. Initial comparisons with the stress relaxation curve for AD730 at an initial stress of 300 MPa (Figure 6.14b) suggest this relaxation aligns well.

Compressive stress distribution around the periphery of both DTC's is consistent in magnitude (approximately 385 MPa), with minimal relaxation during ageing. Overall, the ageing heat treatment appears to have only a modest impact on the residual stress profile, with no significant alterations observed.

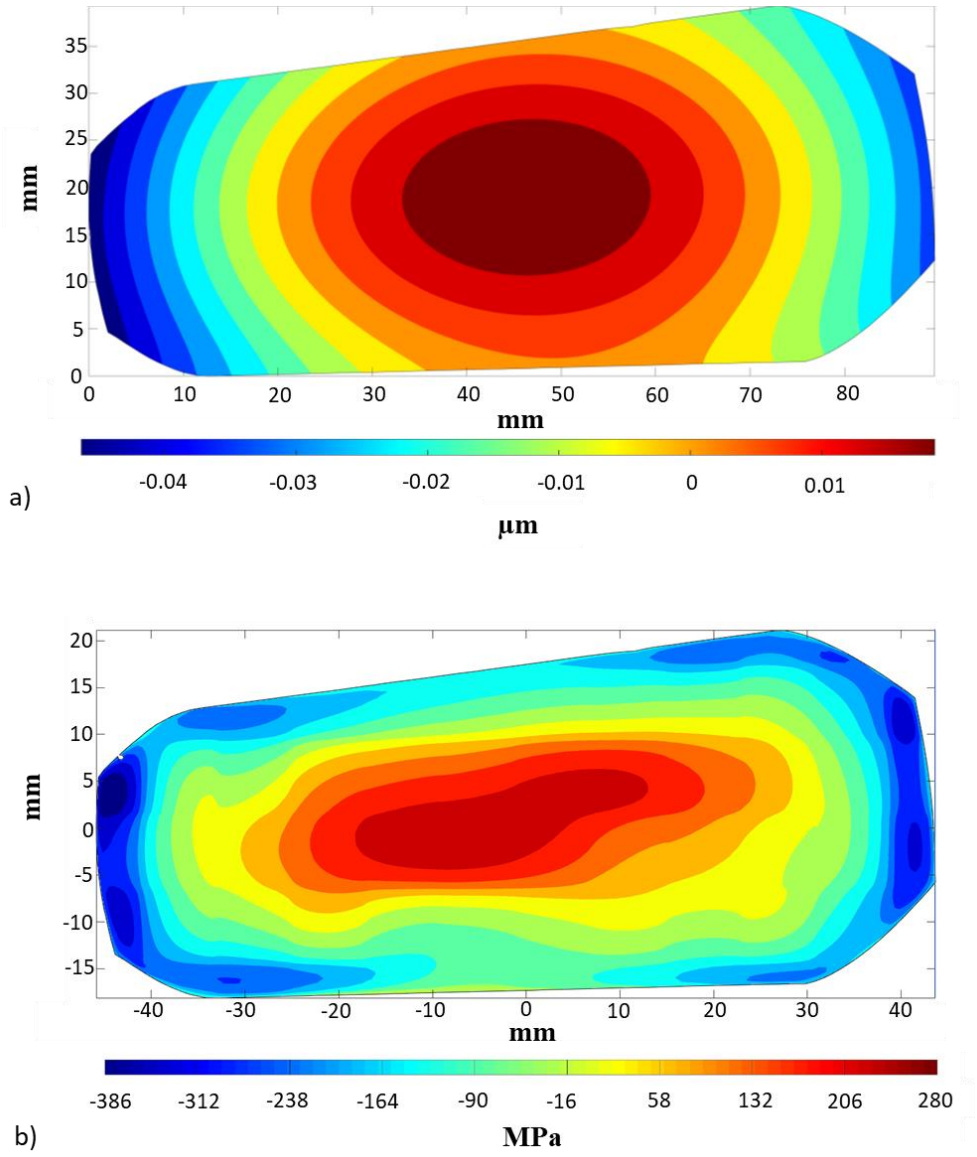

Figure 8.6: a) 2-D contour map of surface height for the forged and forced air-cooled DTC 1, and b) 2-D map of residual stress distribution in the out-of-plane direction for DTC 1.

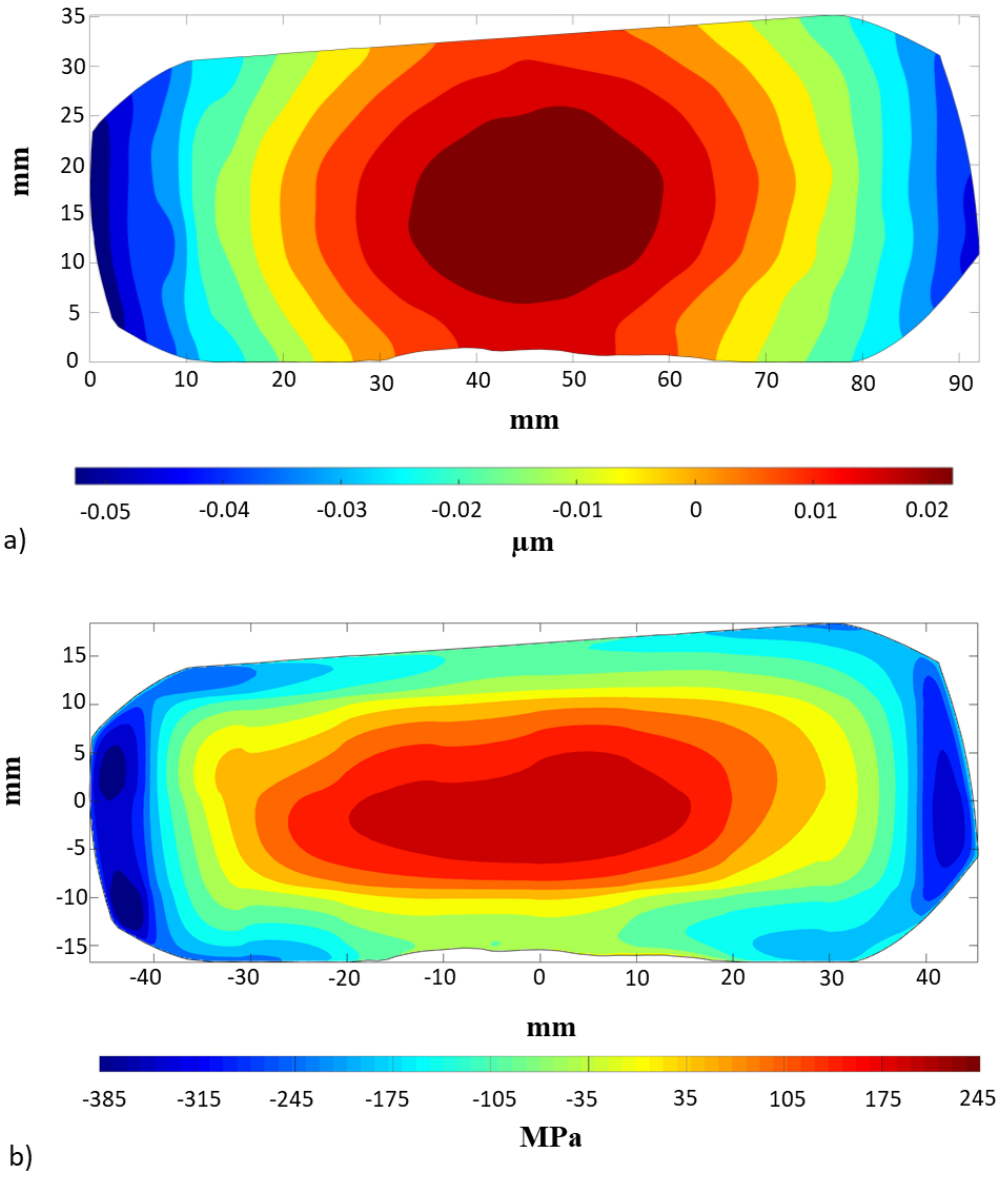

Figure 8.7: a) 2-D contour map of surface height for the forged, forced air-cooled and aged DTC 2, and b) 2-D residual stress map in the out-of-plane direction for DTC 2.

8.3.2 FE Simulation

A comprehensive 3D FE model was constructed in DEFORM to simulate the post-forging cooling and subsequent heat treatments of AD730. The results of FE predictions of the forged and forced air-cooled DTC from the post-forging heat treatment at 1080 °C are presented in Figure 8.8a and b. The same results after the subsequent re-heating, ageing, and subsequent air-cooling are shown in Figure 8.8c and d. Figure 8.8b, illustrates the result of the iterative

determination of HTC values necessary to cool from 1080 °C to room temperature, successfully aligning the out-of-plane stress results obtained from the FE model with those measured experimentally using the contour method, as depicted in Figure 8.8b. The stress distribution in the FE results shown in Figure 8.8b resembles a ripple pattern, akin to what one might observe when a stone is dropped in a pond, with tensile stress near the centre transitioning to compressive stress towards the edges. However, at the farthest sections, particularly on the left and right sides of the part, the ripple pattern breaks down, resulting in elongated or widened regions at the extremities. This is slightly different to the stress distribution experimentally measured and shown in Figure 8.6b, although overall, there is substantial agreement between the two.

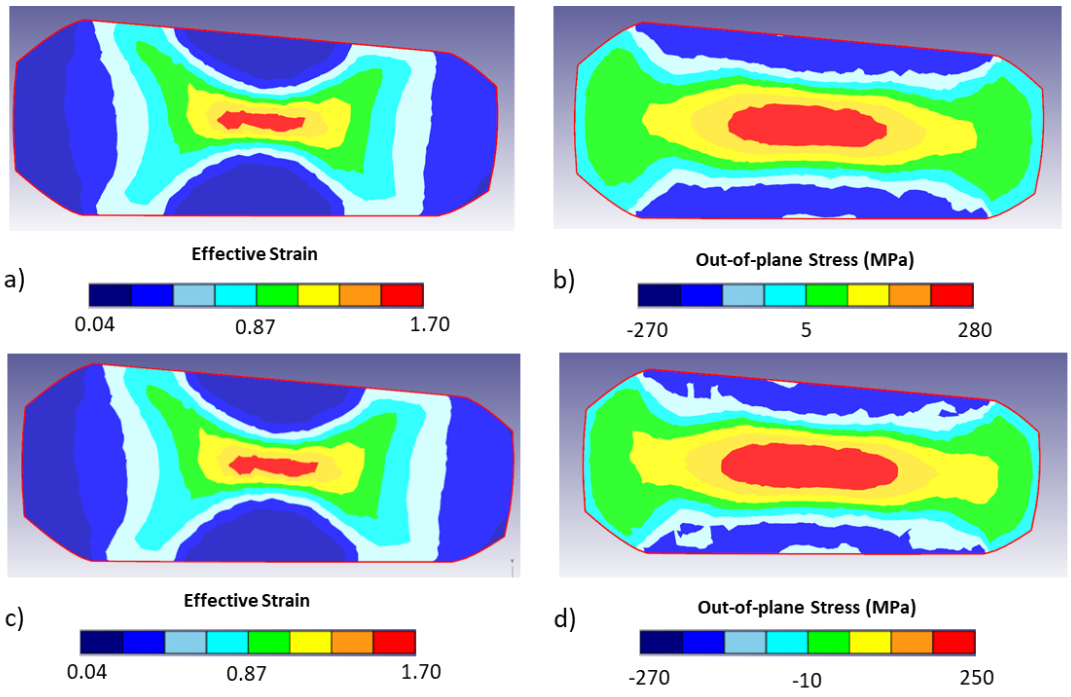

Figure 8.8: Simulation results obtained in DEFORM a) Effective strain after forced air-cooling from 1080 °C, b) effective stress after forced air-cooling from 1080 °C, c) effective strain after ageing heat treatment and forced air-cooling from 760°C, and d) effective stress after ageing heat treatment and forced air-cooling from 760°C.

Figure 8.8d depicts the out-of-plane stress prediction from DEFORM for the aged and air-cooled DTC. The stress distribution closely resembles that of the DTC subjected to forced air-cooling from 1080°C before ageing (Figure 8.8b) and the experimentally measured stress depicted in Figure 8.7. Notably, the discrepancies between the measured stress and the FE solver-predicted stress for the aged and force air-cooled DTC occur in the same areas as

observed for the DTC force air-cooled from 1080 °C, particularly towards the edges on the left and right sides of the part.

The magnitude of relaxation in the central tensile region for the FE-predicted stress after ageing and air-cooling is approximately 30 MPa, consistent with the relaxation measured (approximately 35MPa) in a similar region measured with the contour method. Moreover, the magnitudes of the measured and predicted compressive stresses exhibit consistent behaviour during the ageing process in both the model and experimental results, indicating good agreement. This underscores the capability of the FE model to accurately capture the stress relaxation behaviour of AD730 during ageing, confirming the successful development of a model for the final forging and subsequent heat treatments.

8.4 Discussion

A multi-step multi-process predictive FE model for forging and heat treatments of AD730 has been developed in Chapters 4 to 8 of this thesis for the steps outlined in Figure 8.4. In this Chapter, the post-forging heat treatments steps of the FE model, including ageing, were developed and showed a good correlation with the experimentally measured residual stress values using the contour method. Integration of the model developed in Chapter 7, which predicted deformation behaviour during forging, with the stress obtained from forced air-cooling of forged DTC 1 and aged DTC 2 enhanced the model's applicability. This model could be made more robust by obtaining flow stress data for temperatures below 1000 °C. Currently the model is interpolating for these temperatures. Furthermore, the HTC's values used for forced air-cooling were determined using a best first guess and then an iterative approach of solving for a known experimentally measured stress profile. Whilst this was successful in overcoming the hurdle of determining the HTC values for forced air-cooling, future research could focus on employing the methodology outlined in Chapter 4 to determine residual stress in parts calculated from inverse HTC analyses.

It can be seen in Figure 8.6 and Figure 8.7 that a stress profile which is similar to those of water quenched parts, is typical for both samples. This demonstrates the effect of the forging and subsequent cooling and heat treatments on the stress profile. In Chapter 4, when left to air-cool without the addition of a fan, one of the IN718 discs showed a relatively homogenous stress distribution. This was not the case in the post-aged, air-cooled DTC, indicating that the

previous forging and heat treatments play a more significant role in the stress profile persisting after forging and being forced air-cooled. Of course, there is a difference in the size and shape of the parts, so care must be taken when making this comparison. Care must also be taken when comparing the results of the contour method from DTC 1 with DTC 2, as it was noticed and highlighted in Chapter 7 that the misalignment angle was not consistent during forging, meaning part of the reason for the different stress profiles comes from a slightly different forging conditions.

In summary, the methodologies outlined in Chapters 4 to 8 of this thesis have demonstrated their efficacy in predicting the thermo-mechanical behaviour of AD730 during forging and subsequent heat treatments. Through experimental validation, a multi-step multi-process FE model has proven capable of accurately capturing the stress evolution and dimensional changes of the part during processing. These findings underscore the robustness and applicability of the methods employed, consolidating their value in advancing the understanding and optimisation of thermo-mechanical processing of Ni-based superalloys.

8.5 Conclusions

In this chapter, the integration of the methodology to determine the HTC values essential for understanding thermally induced residual stresses during cooling, along with the developed constitutive stress relaxation model and constitutive material model for AD730, was successfully implemented into a multi-step multi-process FE model. The validation of the results obtained from this model was conducted through residual stress measurements on two forged DTC's. From these findings, the following conclusion can be drawn:

- The residual stress profile of the aged and air-cooled DTC was very similar to the post-forged and forced air-cooled DTC, showing only a modest (≈35MPa) reduction in peak tensile stress. This is in line with the stress relaxation results for AD730 captured in Chapter 6, which generally showed a sluggish stress relaxation response for this material at ageing temperatures.
- The out-of-plane residual stress profile was similar to the distribution seen in water quenched parts (see Chapter 4), with peak tensile stresses near the centre of the sample transitioning towards compressive stresses near the edges.

- The developed FE model predicting the impact of ageing and the subsequent air-cooling on the stress evolution was compared to the experimentally measured stresses using the contour method and showed good correlation.
- A multi-process predictive FE model of the forging and heat treatments of AD730 has been successfully developed and validated against experimental trials.

9

Conclusions

The work presented in this PhD thesis began by developing a micro-mechanical testing method for Ni-based superalloys, combined with DIC, providing a solid foundation for leveraging the advantages of micro-mechanical testing and the rapid heating rates achievable through the Joule effect. This new approach ensured the reliability of stress relaxation tests, which were essential for accurately modelling the thermo-mechanical behaviour of these alloys.

A novel sample geometry, designed specifically for high-temperature tensile testing, was developed using thermal data from an infrared camera and strain data from DIC. This ensured the geometry's effectiveness during testing. The Young's modulus values obtained from these tensile tests were validated against similar results in the literature, confirming the success of the geometry's design. It is hoped that this geometry can be adopted for future testing of precipitation-hardenable materials, enhancing their characterisation.

The research investigating the influence of quenching configuration and media on thermally induced residual stress has revealed their significant roles in residual stress development. Essential to modelling this phenomenon is the acquisition of accurate HTC values. Challenges arose when employing experimentally obtained cooling curves as boundary conditions for inverse HTC analysis via an FE solver, primarily due to the suboptimal placement of embedded thermocouples in the part, as identified during the study. Consequently, the accuracy of subsequent residual stress predictions, reliant on these results, was compromised. Nonetheless, the FE solver's predictions of residual stresses demonstrated reasonable

agreement with experimental results obtained using the contour method, highlighting the capability of the developed model.

This work is poised to benefit industry by providing insights into optimising quenching processes to mitigate residual stress in manufactured components. Furthermore, it sheds light on the challenges associated with obtaining accurate HTC values, emphasising the need for improved methodologies in measuring and incorporating HTC data into FE simulations. Addressing these challenges has the potential to yield more robust predictive models for residual stress, ultimately enhancing the accuracy and reliability of manufacturing processes.

The final part of research, covered across two chapters, focused on developing a predictive multi-process FE model for the thermo-mechanical processing of AD730 during forging and the subsequent heat treatments. The hot deformation behaviour of AD730 was then simulated using both physical-based and empirical-based constitutive plasticity models, developed based on hot compression tests conducted between 1000°C and 1125°C. Following successful model development, both approaches were integrated into the FE solver via a subroutine, and the forging behaviour was simulated. Comparative analysis was conducted between the models and tabular data, demonstrating good correlation between the Arrhenius and EM+Avrami models, while slight variations were observed in the tabular data. Accounting for die misalignment effects observed during experimental forging trials, the modelling results aligned well with the experimental outcomes.

The FE model, initially used to predict the forging behaviour of the DTCs made from AD730, was expanded to incorporate forced air-cooling and ageing heat treatments of the same material. The measured relaxation of tensile stresses was approximately 35MPa, while the relaxation of compressive stresses was minimal. Two constitutive stress relaxation models were developed and successfully predicted the stress relaxation of AD730 during ageing. Stress relaxation tests, following the ASTM E328-21 standard, were conducted, revealing unconventional relaxation behaviour previously documented in literature [128], [129]. This phenomenon was attributed to volumetric contraction associated with the precipitation of γ’ and γ’’ phases. Attempts were made to mitigate these effects using stress-free isothermal dilatometry data from literature, yielding partial success. The developed constitutive stress relaxation models demonstrated effectiveness in predicting relaxation behaviour within specified ranges of temperature and initial stress. Given the isothermal nature of ageing of

AD730, tabular data was incorporated into the FE solver to represent relaxation behaviour. Predicted out-of-plane stresses from the FE model exhibited strong agreement with experimental results, confirming the model's validity and accuracy. The constitutive stress relaxation models developed for IN718, remain unvalidated as the experimental work required to do so, was out of the scope of this PhD.

The applicability of the developed predictive FE model for AD730 is apparent, with the thermo-mechanical processing route being provided by an industrial supporter Aubert & Duval. Prediction of the hot deformation behaviour of AD730 during forging, as well as the stress relaxation behaviour during ageing, offer crucial insights into the material's response to processing. This understanding allows for more precise control over the thermo-mechanical processing parameters, leading to enhanced manufacturing efficiency and ultimately, component performance.

In industry, where the optimisation of manufacturing processes is paramount, these models provide a valuable tool for streamlining production workflows. By incorporating the predicted relaxation behaviour into FE simulations, manufacturers can anticipate and mitigate potential issues related to residual stress, leading to improved component quality and reliability. Moreover, the ability to accurately predict stress relaxation facilitates the development of tailored heat treatment protocols, optimising material properties for specific applications while minimizing manufacturing costs.

Overall, the impact of these developed models extends beyond the laboratory, offering tangible benefits to industrial processes. Through their application, manufacturers can achieve greater precision, efficiency, and reliability in the thermo-mechanical processing of AD730, IN718, and similar materials, ultimately driving innovation and competitiveness in the manufacturing sector.

10

Future Work

There are a number of avenues of investigation which could be pursued to further the work laid out in this thesis. Further testing using the geometry designed for micro-mechanical tensile testing could be conducted with other precipitation-hardenable materials to assess its suitability for use with materials within the same class besides AD730 and IN718. Additionally, research efforts could focus on modelling the thermo-mechanical behaviour of the newly designed sample geometry for testing precipitation-hardenable materials using the ETMT. This approach would provide deeper insights into strain distribution and temperature variations across the sample gauge length during testing, potentially improving the stress prediction equation without relying on DIC. The simulation results could be easily validated using data obtained from DIC.

Exploring alternative quenching media like polymer or brine, along with investigating the effects of sample scale and complex geometries, could provide further insights into the generation of thermally induced residual stresses during quenching. Additionally, conducting XRD analyses to examine in-plane stresses in conjunction with the contour method, which provides out-of-plane stress results, would offer additional data for validating the model used for determination of thermally induced residual stresses during quenching.

A natural continuation of the work in this thesis is to enhance the robustness and accuracy of the multi-step process FE model for AD730. This can be done by incorporating the method

outlined in Chapter 4 for determining HTC's, and applying to the cooling phase from both 1080°C and 760°C. Furthermore, the model could be improved by conducting stress relaxation tests at 1080°C to comprehensively understand stress evolution during the initial post-forging heat treatment. By integrating these methods, the model's reliability and precision can be significantly improved. Implementation of the constitutive stress relaxation models developed for IN718 into a FE solver, and then the results compared to experimental trials such as was done for AD730, is the next step for the work on IN718.

Continuation work on the development of a comprehensive through-life predictive model for the entire thermo-mechanical processing route of AD730, spanning from the as-cast stage to the final part would be a natural progression of this work. This entails incorporating all relevant processing steps, including forging, heat treatments, and cooling processes, into a unified predictive model. Such a model would provide invaluable insights into the material's behaviour throughout its processing stages, enabling more informed decision-making and process optimisation.

11

Bibliography

[1] Rolls Royce, *The Jet Engine*, 5th ed. Derby, 1996.

[2] R. C. Reed, *The Superalloys fundamentals and applications*, 1st ed. 2006. doi: 10.1017/CBO9780511541285.

[3] A. Devaux and P. Heritier, 'Nickel-Based Superalloy and Parts Made From said Superalloy', US20120183432A1, 2010

[4] A. L. Marsh, 'Electric Resistance Element', 1906

[5] S. Kamal, R. Jayaganthan, and S. Prakash, 'High temperature cyclic oxidation and hot corrosion behaviours of superalloys at 900 ° C', vol. 33, no. 3, pp. 299–306, 2010.

[6] A. Kracke, 'Superalloys, the most successful alloy system of modern times - Past, present and future', *7th International Symposium on Superalloy 718 and Derivatives 2010*, vol. 1, pp. 13–50, 2010, doi: 10.1002/9781118495223.ch2.

[7] B. Geddes, H. Leon, and X. Huang, *Superalloys: Alloying and Performance*. 2010.

[8] C. T. Sims, 'A History of Superalloy Metallurgy for Superalloy Metallurgists', in *Superalloys 1984: Proceedings*, 1984, pp. 399–419. doi: 10.7449/1984/superalloys_1984_399_419.

[9] A. D. Cetel and D. N. Duhl, 'Second-Generation Nickel-Base Single Crystal Superalloy', in *Superalloys 1988 Symposium*, 1988, pp. 235–244. doi: 10.7449/1988/superalloys_1988_235_244.

[10] R. Schafrik and R. Sprague, 'Superalloy Technology - A Perspective on Critical Innovations for Turbine Engines', *Key Eng Mater*, vol. 380, no. March, pp. 113–134, 2008, doi: 10.4028/www.scientific.net/kem.380.113.

[11] R. Brunetaud, D. Coutsouradis, T. B. Gibbons, Y. Lindblom, D. B. Meadowcroft, and R. Stickler, *High Temperature Alloys for Gas Turbines 1982: Proceedings of a Conference held in Liège, Belgium, 4--6 October 1982*. Springer Netherlands, 1982.

[12] L. B. Pfeil, 'Improvements relating to heat-resisting alloys', GB583162A, 1940

[13] B. Graybill, M. Li, D. Malawey, C. Ma, J. M. Alvarado-Orozco, and E. Martinez-Franco, 'Additive manufacturing of nickel-based superalloys', *ASME 2018 13th International Manufacturing Science and Engineering Conference, MSEC 2018*, vol. 1, no. June, 2018, doi: 10.1115/MSEC2018-6666.

[14] A. Kulkarni, 'Additive Manufacturing of Nickel Based Superalloys', Michigan Technological University, Houghton 49931USA.

[15] A. Devaux *et al.*, 'Effect of Aging Heat-Treatment on Mechanical Properties of AD730™ Superalloy', *8th International Symposium on Superalloy 718 and Derivatives*, no. August 2016, pp. 521–535, 2014, doi: 10.1002/9781119016854.ch41.

[16] F. Hugo *et al.*, 'Isothermal Forging System for the production of large rotating components from titanium alloys or superalloys', in *World Titanium Conference Proceedings*, 1984, pp. 741–744.

[17] G. H. Gessinger and M. J. Bomford, *Powder metallurgy of superalloys*, vol. 19, no. 1. Butterworths Monographs in Materials, 1974. doi: 10.1179/imtlr.1974.19.1.51.

[18] E. Akca, A. Gursel, and A. Gürsel, 'A Review on Superalloys and IN718 Nickel-Based INCONEL Superalloy', *Periodicals of Engineering and Natural Sciences (PEN)*, vol. 3, no. 1, Jun. 2015, doi: 10.21533/pen.v3i1.43.

[19] C. Meher-Homji, 'The Historical Evolution of Turbomachinery', in *29th Turbomachinery Symposium*, 2000, pp. 281–322. doi: 10.21423/R1X948.

[20] J. G. Hoag, 'The Evolution of Nickel-Base Precipitation-Hardening Superalloys', 1961.

[21] V. Tvergaard, 'Influence of grain boundary sliding on material failure in the tertiary creep range', *Int J Solids Struct*, vol. 21, no. 3, pp. 279–293, 1985, doi: 10.1016/0020-7683(85)90024-1.

[22] D. N. DUHL, '5 - Single Crystal Superalloys', in *Superalloys Supercomposites Superceramics*, J. K. TIEN and T. CAULFIELD, Eds., Academic Press, 1989, pp. 149–182. doi: https://doi.org/10.1016/B978-0-12-690845-9.50011-7.

[23] P. Caron and T. Khan, 'Evolution of Ni-based superalloys for single crystal gas turbine blade applications', *Aerosp Sci Technol*, vol. 3, no. 8, pp. 513–523, 1999, doi: 10.1016/S1270-9638(99)00108-X.

[24] H. Long, S. Mao, Y. Liu, Z. Zhang, and X. Han, 'Microstructural and compositional design of Ni-based single crystalline superalloys — A review', *J Alloys Compd*, vol. 743, no. April, pp. 203–220, 2018, doi: 10.1016/j.jallcom.2018.01.224.

[25] A. Sato *et al.*, 'A 5th generation SC superalloy with balanced high temperature properties and processability', *Proceedings of the International Symposium on Superalloys*, pp. 131–138, 2008, doi: 10.7449/2008/superalloys_2008_131_138.

[26] H. Rouault-Rogez, M. Dupeux, and M. Ignat, 'High temperature tensile creep of CMSX-2 Nickel base superalloy single crystals', *Acta Metallurgica et Materialia*, vol. 42, no. 9, pp. 3137–3148, 1994, doi: https://doi.org/10.1016/0956-7151(94)90411-1.

[27] J. A. Heaney, M. L. Lasonde, A. M. Powell, B. J. Bond, and C. M. O'Brien, 'Development of a new cast and wrought alloy (René 65) for high temperature disk applications', *8th International Symposium on Superalloy 718 and Derivatives 2014*, no. Rene 65, pp. 67–77, 2014, doi: 10.1002/9781119016854.ch6.

[28] F. R. Caliari, N. M. Guimarães, D. A. P. Reis, A. A. Couto, C. de Moura Neto, and K. C. G. Candioto, 'Study of the Secondary Phases in Inconel 718 Aged Superalloy Using Thermodynamics Modeling', *Key Eng Mater*, vol. 553, pp. 23–28, 2013, doi: 10.4028/www.scientific.net/KEM.553.23.

[29] F. Pettinari-Sturmel *et al.*, 'Creep behavior in the new AD730 TM nickel-based disk superalloy – Influence of aging heat treatment and local chemical fluctuations', *Materials Science and Engineering A*, vol. 754, no. February, pp. 9–17, 2019, doi: 10.1016/j.msea.2019.02.088.

[30] C. T. Sims, N. S. Stoloff, and W. C. Hagel, *Superalloys II: High-Temperature Materials for Aerospace and Industrial Power*. in Wiley-Interscience publication. Wiley, 1987.

[31] G.A. L´opez, S. Sommadossi, W. Gust, E. J. Mittemeijer, and and P. Zieba, 'Phase Characterization of Diffusion Soldered Ni/Al/Ni Interconnections', *Interface Science*, pp. 13–19, 2002, doi: 10.1023/A.

[32] Y. M. Wang-Koh, 'Understanding the yield behaviour of L12-ordered alloys', *Materials Science and Technology (United Kingdom)*, vol. 33, no. 8, pp. 934–943, 2017, doi: 10.1080/02670836.2016.1215961.

[33] R. J. Mitchell, M. Hardy, M. Preuss, and S. Tin, 'Development of γ ' Morphology in P / M Rotor Disc Alloys During Heat Treatment', in *Superalloys 2004 (Tenth International Symposium)*, 2004. doi: 10.7449/2004/Superalloys.

[34] J. W. Brooks and P. J. Bridges, 'Metallurgical Stability of Inconel 718', *Superalloys 1988 Symposium*, pp. 33–42, 1988, doi: 10.7449/1988/Superalloys_1988_33_42.

[35] F. Masoumi, M. Jahazi, D. Shahriari, and J. Cormier, 'Coarsening and dissolution of γ' precipitates during solution treatment of AD730^{TM} Ni-based superalloy: Mechanisms and kinetics models', *J Alloys Compd*, vol. 658, pp. 981–995, 2016, doi: 10.1016/j.jallcom.2015.11.002.

[36] A. Jafari, S. M. Abbasi, A. Rahimi, M. Morakabati, and M. Seifollahi, 'The Effects of Solution Treatment on the Microstructure of the Case Ni-Based IN100 Superalloy', *Metallurgical and Materials Engineering*, vol. 21 (3), pp. 167–181, 2015.

[37] G. Lvov, V. I. Levit, and M. J. Kaufman, 'Mechanism of Primary MC Carbide Decomposition in Ni-Base Superalloys', *Metallurgical and Materials Transactions*, vol. 35A, pp. 1669–1679, 2004.

[38] X. B. Hu *et al.*, 'Interfacial precipitation of the M 5 B 3 -type boride in Ni-based superalloys', *Philos Mag Lett*, vol. 96, no. 7, pp. 273–279, 2016, doi: 10.1080/09500839.2016.1200756.

[39] J. R. Davis and A. S. M. I. H. Committee, *Nickel, Cobalt, and Their Alloys*. in ASM specialty handbook. ASM International, 2000.

[40] A. K. Jena and M. C. Chaturvedi, 'The role of alloying elements in the design of nickel based superalloys', *Journal of Material Science*, vol. 19, no. 10, pp. 3121–3139, 1984.

[41] R. W. Kozar, A. Suzuki, W. W. Milligan, J. J. Schirra, M. F. Savage, and T. M. Pollock, 'Strengthening Mechanisms in Polycrystalline Multimodal Nickel-Base superalloys', *Metallurgical and Materials Transactions*, vol. 40A, no. 7, 2009.

[42] Z. Yao, C. C. Degnan, M. A. E. Jepson, and R. C. Thomson, 'Microstructural and Chemical Rejuvenation of a Ni-Based Superalloy', *Metall Mater Trans A Phys Metall Mater Sci*, vol. 47, no. 12, pp. 6330–6338, 2016, doi: 10.1007/s11661-016-3790-2.

[43] E. Nembach, K. Suzuki, M. Ichihara, and S. Takeuchi, 'In situ deformation of the γ' hardened superalloy Nimonic PE16 in high-voltage electron microscopes', *Philosophical Magazine A*, vol. 51, no. 4, pp. 607–618, 1985, doi: 10.1080/01418618508237581.

[44] E. Sjölander and S. Seifeddine, 'The heat treatment of Al-Si-Cu-Mg casting alloys', *J Mater Process Technol*, vol. 210, no. 10, pp. 1249–1259, 2010, doi: 10.1016/j.jmatprotec.2010.03.020.

[45] V. Gerold and H.-M. Pham, 'Precipitation hardening by misfitting particles and its comparison with experiments', *Scripta Metallurgica*, vol. 13, pp. 895–898, 1979.

[46] I. Polmear, Dr. D. St. John, and V. Ravi, *Light Alloys: From Traditional Alloys to Nanocrystals*. Oxford: Elsevier Science & Technology, 2005.

[47] L. Grabowski and J. E. King, 'Modelling Short Crack Growth Behaviour in Nickel-Base Superalloys', *Fatigue Fract Eng Mater Struct*, vol. 15, no. 6, pp. 595–606, 1992, doi: 10.1111/j.1460-2695.1992.tb01298.x.

[48] D. Hull and D. J. Bacon, *Introduction to dislocations*, vol. 10, no. 6. 2011. doi: 10.1016/0022-5088(66)90102-0.

[49] A. International. H. Committee, S. Lampman, C. Moosbrugger, E. DeGuire, and A. S. for Metals, *ASM Handbook Volume 15: Casting*. in ASM Handbook. ASM International, 2008.

[50] E. Pod, L. Pregled, B. Arh, B. Podgornik, and J. Burja, 'Electroslag Remelting: A Process Overview', *Materials and technology*, vol. 50, no. 6, pp. 971–979, 2016, doi: 10.17222/mit.2016.108.

[51] C. R. Woodside, P. E. King, and C. Nordlund, 'Arc distribution during the vacuum arc remelting of Ti-6Al-4V', *Metallurgical and Materials Transactions B: Process Metallurgy and Materials Processing Science*, vol. 44, no. 1, pp. 154–165, 2013, doi: 10.1007/s11663-012-9760-1.

[52] M. J. Donachie and S. J. Donachie, *Superalloys: A Technical Guide, 2nd Edition*. in Ingenieria de minas. ASM International, 2002.

[53] C. A. Dandre, C. A. Walsh, R. W. Evans, R. C. Reed, and S. M. Roberts, 'Microstructural Evolution of Nickel-Base Superalloy Forgings during Ingot-to-Billet Conversion: Process Modeling and Validation', in *Superalloys 2000*, 2000, pp. 85–94. doi: 10.7449/2000/superalloys_2000_85_94.

[54] ASM International. Handbook Committee, *ASM Handbook Volume 7: Powder Metallurgy*, no. v. 7. in ASM Handbook. ASM International, 1998.

[55] 'The Library of Manufacturing'. Accessed: Dec. 01, 2018. [Online]. Available: http://thelibraryofmanufacturing.com/investment_casting.html

[56] K. Hoshikawa, J. Osada, Y. Saitou, E. Ohba, and C. Miyagawa, 'Vertical Bridgman Growth of Sapphire — Seed crystal shapes and seeding characteristics —', *J Cryst Growth*, vol. 401, pp. 149–149, 2014.

[57] A. D. Cetel and D. N. Duhl, 'Second Generation Columnar Grain Nickel Base Superalloy', *Superalloys 1992*, pp. 287–296, 1992, doi: 10.7449/1992/Superalloys_1992_287_296.

[58] R. L. Zhang, L. N. Chen, C. H. Li, N. Wang, X. G. Lu, and Z. M. Ren, 'Influence of spiral crystal selector on crystal orientation of single crystal superalloy', *Transactions of Nonferrous Metals Society of China (English Edition)*, vol. 22, no. 5, pp. 1092–1095, 2012, doi: 10.1016/S1003-6326(11)61288-0.

[59] A. Onyszko, K. Kubiak, and J. Sieniawski, 'Turbine blades of the single crystal nickel based CMSX-6 superalloy', *Journal of Achievements in Materials and Manufacturing Engineering*, vol. 32, no. 1, pp. 66–69, 2009, doi: 10.1016/j.colsurfa.2017.03.046.

[60] E. Rzyankina, M. Pytel, N. Mahomed, and A. Nowotnik, 'Solution Heat Treatment of Single Crystal Castings of CMSX-4 Nickel-base Solution Heat Treatment of Single Crystal Castings of CMSX-4 Nickel-base Superalloy', in *International Conference on Competitive Manufacturing*, 2016.

[61] Y. Koizumi *et al.*, 'Development of Next-Generation Ni-Base Single Crystal Superalloys', in *Superalloys 2004 (Tenth International Symposium)*, 2008, pp. 35–44. doi: 10.7449/2004/Superalloys_2004_35_43.

[62] H. T. Michel *et al.*, 'Mechanical properties of cast & wrought hybrid disks', *Proceedings of the International Symposium on Superalloys*, vol. 2016-Janua, no. September, pp. 539–548, 2016.

[63] S. Vernier, J. M. Franchet, C. Dumont, and N. Bozzolo, 'A Mechanism Leading to γ' Precipitates with {111} Facets and Unusual Orientation Relationships to the Matrix in γ–γ' Nickel-Based Superalloys', *Metall Mater Trans A Phys Metall Mater Sci*, vol. 49, no. 9, pp. 4308–4323, 2018, doi: 10.1007/s11661-018-4734-9.

[64] A. Devaux, L. Berglin, L. Thebaud, R. Delattre, C. Crozet, and O. Nodin, 'Mechanical properties and development of supersolvus heat treated new nickel base superalloy

AD730 TM', *MATEC Web of Conferences*, vol. 14, 2014, doi: 10.1051/matecconf/20141401004.

[65] A. Devaux, B. Picqué, M. F. Gervais, E. Georges, T. Poulain, and P. Héritier, 'AD730 ™ - A New Nickel-Based Superalloy for High Temperature Engine Rotative Parts', in *Superalloys 2012*, 2012, pp. 911–919. doi: 10.1002/9781118516430.ch100.

[66] K. L. Xiao-Xiao Li, Mei-Qiong Ou, Min Wang, Xian-Chao Hao, Ying-Che Ma, 'Effect of Co on Microstructure and Stress Rupture Properties of K4750 Alloy', *Acta Metallurgica Sinica(English Letters)*, vol. 32, no. 12, pp. 1501–1510, 2019.

[67] A. Coyne-Grell *et al.*, 'Recrystallization mechanisms and associated microstructure evolution during billet conversion of a gamma-gamma' nickel based superalloy', *J Alloys Compd*, vol. 916, p. 165465, 2022, doi: 10.1016/j.jallcom.2022.165465.

[68] A. Coyne-Grell *et al.*, 'Evolution of γ' Precipitation During the Early Stages of Industrial Forging of a Nickel-Based Superalloy', *Metall Mater Trans A Phys Metall Mater Sci*, vol. 54, no. 5, pp. 2022–2036, 2023, doi: 10.1007/s11661-022-06878-w.

[69] P. J. Withers and H. K. D. H. Bhadeshia, 'Residual stress part 1 - Measurement techniques', *Materials Science and Technology*, vol. 17, no. 4, pp. 355–365, 2001, doi: 10.1179/026708301101509980.

[70] J. J. Zhu, W. H. Yuan, F. Peng, and Q. Fu, 'Interaction of stress relaxation aging behavior and microstructural evolution in Inconel 718 alloy with different initial stress status', *J Mater Sci*, vol. 56, no. 24, pp. 13814–13826, 2021, doi: 10.1007/s10853-021-06144-1.

[71] H. Qin *et al.*, 'Study of precipitation-assisted stress relaxation and creep behavior during the ageing of a nickel-iron superalloy', 2019. doi: 10.1016/j.msea.2018.11.028.

[72] H. L. Eiselstein, 'Age-Hardenable Nickel Alloy', 1962

[73] T. Fedorova and J. Rosier, 'Microstructure and Strength of Alloy 718', in *Materials for Advanced Power Engineering*, 2010, pp. 749–758.

[74] P. M. Mignanelli *et al.*, 'Gamma-gamma prime-gamma double prime dual-superlattice superalloys', *Scr Mater*, vol. 136, pp. 136–140, 2017, doi: 10.1016/j.scriptamat.2017.04.029.

[75] J. Lacaze, M. Dehmas, A. Niang, and B. Viguier, 'TEM study of high-temperature precipitation of delta phase in inconel 718 alloy', *Advances in Materials Science and Engineering*, vol. 2011, 2011, doi: 10.1155/2011/940634.

[76] S. Azadian, 'Aspects of Precipitation in the Alloy Inconel 718', *Thesis*, p. 129, 2004.

[77] A. Oradei-Basile and J. F. Radavich, 'A Current T-T-T Diagram for Wrought Alloy 718', pp. 325–335, 2012, doi: 10.7449/1991/superalloys_1991_325_335.

[78] P. J. P. Kañetas, L. A. R. Osorio, M. P. G. Mata, M. D. La Garza, and V. P. López, 'Influence of the Delta Phase in the Microstructure of the Inconel 718 subjected to "Delta-processing" Heat Treatment and Hot Deformed', *Procedia Materials Science*, vol. 8, pp. 1160–1165, 2015, doi: 10.1016/j.mspro.2015.04.180.

[79] S. Azadian, L. Y. Wei, and R. Warren, 'Delta phase precipitation in inconel 718', *Mater Charact*, vol. 53, no. 1, pp. 7–16, 2004, doi: 10.1016/j.matchar.2004.07.004.

[80] P. J. P. Kañetas, J. Calvo, P. Rodriguez-Calvillo, J. M. C. Marrero, M. A. Z. Antuñano, and M. P. Guerrero-Mata, 'Ebsd study of delta-processed ni-based superalloy', *Metals (Basel)*, vol. 10, no. 11, pp. 1–14, 2020, doi: 10.3390/met10111466.

[81] C. M. Kuo, Y. T. Yang, H. Y. Bor, C. N. Wei, and C. C. Tai, 'Aging effects on the microstructure and creep behavior of Inconel 718 superalloy', *Materials Science and Engineering A*, vol. 510–511, no. C, pp. 289–294, 2009, doi: 10.1016/j.msea.2008.04.097.

[82] J. J. Schirra, R. H. Caless, and R. W. Hatala, 'The Effect of Laves Phase on the Mechanical Properties of Wrought and Cast + HIP Inconel 718', pp. 375–388, 2012, doi: 10.7449/1991/superalloys_1991_375_388.

[83] A. Lingenfelter, 'Welding of Inconel Alloy 718: A Historical Overview', pp. 673–683, 2012, doi: 10.7449/1989/superalloys_1989_673_683.

[84] K.-M. Chang, H.-J. Lai, and J.-Y. Hwang, 'Existence of Laves Phase in Nb-Hardened Superalloys', pp. 683–694, 2012, doi: 10.7449/1994/superalloys_1994_683_694.

[85] N. K. Park, J. T. Yeom, J. H. Kim, and X. X. Cui, 'Characteristics of VIM/VAR-processed alloy 718 ingot and the evolution of microstructure during cogging', *Proceedings of the International Symposium on Superalloys and Various Derivative*, pp. 253–260, 2005, doi: 10.7449/2005/superalloys_2005_253_260.

[86] P. Petit and J. P. Fesland, 'Manufacturing of Large IN706 and IN718 Forging Parts', *Superalloys*, pp. 153–162, 1997, doi: 10.7449/1997/superalloys_1997_153_162.

[87] L. Zhao *et al.*, 'Homogenization behavior of IN 718 superalloy prepared by electron beam layered solidification technology', *Journal of Materials Research and Technology*, vol. 13, pp. 1567–1575, 2021, doi: 10.1016/j.jmrt.2021.05.109.

[88] H. Y. Bor, C. N. Wei, H. T. Nguyen, A. C. Yeh, and C. M. Kuo, 'Aging effects on the γ' and γ" precipitates of Inconel 718 superalloy', *7th International Symposium on Superalloy 718 and Derivatives 2010*, vol. 2, pp. 679–688, 2010, doi: 10.1002/9781118495223.ch52.

[89] S. Rahimi, M. King, and C. Dumont, 'Stress relaxation behaviour in IN718 nickel based superalloy during ageing heat treatments', *Materials Science and Engineering A*, vol. 708, no. November, pp. 563–573, 2017, doi: 10.1016/j.msea.2017.09.116.

[90] L. Renhof, C. Krempaszky, E. Werner, and M. Stockinger, 'Analysis of microstructural properties of in 718 after high speed forging', *Proceedings of the International Symposium on Superalloys and Various Derivatives*, pp. 261–270, 2005, doi: 10.7449/2005/superalloys_2005_261_270.

[91] D. Dye, B. A. Roder, S. Tin, M. A. Rist, J. A. James, and M. R. Daymond, 'Modeling and measurement of residual stresses in a forged IN718 superalloy disc', *Proceedings of the*

International Symposium on Superalloys, pp. 315–322, 2004, doi: 10.7449/2004/superalloys_2004_315_322.

[92] B. Smoljan, 'Numerical Simulation of Steel Quenching', *ASM International*, vol. 11, no. May 2001, pp. 75–79, 2002, doi: 10.1361/105994902770344420.

[93] Y. Nagasaka, J. K. Brimacombe, E. B. Hawbolt, I. V Samarasekera, B. Hernandez-Morales, and S. E. Chidiac, 'Mathematical model of phase transformations and elastoplastic stress in the water spray quenching of steel bars', *Metallurgical Transactions A*, vol. 24, no. 4, pp. 795–808, 1993.

[94] M. T. Todinov, 'Influence of some parameters on the residual stresses from quenching', *Model Simul Mat Sci Eng*, vol. 25, no. 41, 1999.

[95] P. J. Withers and H. K. D. H. Bhadeshia, 'Residual stress part 2 - Nature and origins', *Materials Science and Technology*, vol. 17, no. 4, pp. 366–375, 2001, doi: 10.1179/026708301101510087.

[96] D. Dye, K. T. Conlon, and R. C. Reed, 'Characterization and modeling of quenching-induced residual stresses in the nickel-based superalloy IN718', *Metall Mater Trans A Phys Metall Mater Sci*, vol. 35 A, no. 6, pp. 1703–1713, 2004, doi: 10.1007/s11661-004-0079-7.

[97] S. Kwofie, 'Relaxation of residual stress under fatigue load described in terms of cyclic-plastic deformation model', *SDHM Structural Durability and Health Monitoring*, vol. 8, no. 4, pp. 295–305, 2012, doi: 10.32604/sdhm.2012.008.295.

[98] H. R. Manjoine, M.J. Voorhees, *Compilation of Stress-Relaxation Data for Engineering Alloys*. 1982.

[99] J. Rolph *et al.*, 'Residual Stress Evolution during Manufacture of Aerospace Forgings', in *Superalloys 2012*, 2012, pp. 881–891. doi: 10.1002/9781118516430.ch97.

[100] M. E. Kassner, 'Chapter 1 - Fundamentals of Creep in Materials', in *Fundamentals of Creep in Metals and Alloys (Third Edition)*, Third Edit., M. E. Kassner, Ed., Boston: Butterworth-Heinemann, 2015, pp. 1–6. doi: https://doi.org/10.1016/B978-0-08-099427-7.00001-3.

[101] D. M. Shah, S. Vega, S. Woodard, and A. D. Cetel, 'Primary creep in nickel-base superalloys', *Proceedings of the International Symposium on Superalloys*, pp. 197–206, 2004, doi: 10.7449/2004/superalloys_2004_197_206.

[102] T. G. Langdon, 'Creep', in *Concise Encyclopedia of Advanced Ceramic Materials*, Oxford: Pergamon, 1991, pp. 92–96. doi: https://doi.org/10.1016/B978-0-08-034720-2.50034-4.

[103] K. Linga Murty, S. Gollapudi, and I. Charit, 'Newtonian viscous creep in metals', *Transactions of the Indian Institute of Metals*, vol. 63, no. 2–3, pp. 85–91, 2010, doi: 10.1007/s12666-010-0012-2.

[104] E. Arzt and J. Rösler, 'The kinetics of dislocation climb over hard particles-II. Effects of an attractive particle-dislocation interaction', *Acta Metallurgica*, vol. 36, no. 4, pp. 1053–1060, 1988, doi: 10.1016/0001-6160(88)90159-9.

[105] M. S. Blantner, I. S. Golovin, H. Neuhauser, and H. R. Sinning, *Internal Friction in Metallic Materials*, vol. 3, no. 6. 2001.

[106] D. Mari and R. Schaller, 'Elastic and Inelastic Behavior of Ceramics', in *Encyclopedia of Materials: Technical Ceramics and Glasses*, M. Pomeroy, Ed., Oxford: Elsevier, 2021, pp. 705–717. doi: https://doi.org/10.1016/B978-0-12-818542-1.00018-7.

[107] P.-E. Aba-Perea, 'in-Situ Stress Relaxation Studies in Nickel-Base Superalloy Forgings', 2016.

[108] H. J. Frost and M. F. Ashby, *Deformation-mechanism Maps: The Plasticity and Creep of Metals and Ceramics*. Franklin Book Company, Incorporated, 1982.

[109] V. F. Cormier, M. I. Bergman, and P. L. Olson, *Inner core dynamics*. 2022. doi: 10.1016/b978-0-12-811400-1.00008-2.

[110] J. Gong and A. J. Wilkinson, 'Sample size effects on grain boundary sliding', *Scr Mater*, vol. 114, pp. 17–20, 2016, doi: 10.1016/j.scriptamat.2015.11.029.

[111] K. H. J. Buschow, *The Encyclopedia of Materials : Science and Technology*. Place of publication not identified: Pergamon Imprint, 2001.

[112] R. H. Leggat, D. J. Smith, S. D. Smith, and F. Faure, 'Development and Experimental Validation of the Deep Hole Drilling Method for Residual Stress Measurement', *Journal of Strain Analysis*, vol. 31, no. 3, 1996.

[113] A. T. DeWald and M. R. Hill, 'Improved data reduction for the deep-hole method of residual stress measurement', *Journal of Strain Analysis for Engineering Design*, vol. 38, no. 1, pp. 65–78, 2003, doi: 10.1243/030932403762671908.

[114] J. Schwaighofer, 'Determination of residual stresses on the surface of structural parts', *Exp Mech*, vol. 4, no. 2, pp. 54–56, 1964, doi: 10.1007/BF02323965.

[115] G. G. Stoney, 'The Tension of Metallic Films Deposited by Electrolysis', *Proceedings of The Royal Society A: Mathematical, Physical and Engineering Sciences*, vol. 82, pp. 172–175, 1909, [Online]. Available: https://api.semanticscholar.org/CorpusID:135506127

[116] M. B. Prime, 'Residual Stress Measurement By Succesive Extension of a slot: a literature review', University of California, 1997.

[117] N. S. Rossinia, M. Dassisti, K. Y. Benyounis, and A. G. Olabi, 'Methods of Measuring Residual Stresses in Components', *Mater Des*, pp. 572–588, 2012, doi: doi.org/10.1016/j.matdes.2011.08.022.

[118] M. B. Prime, 'Cross-sectional mapping of residual stresses by measuring the surface contour after a cut', *J Eng Mater Technol*, vol. 123, no. 2, pp. 162–168, 2001, doi: 10.1115/1.1345526.

[119] G. Johnson, 'Residual stress measurements using the contour method', 2008.

[120] J. Rohde and A. Jeppsson, 'Literature review of heat treatment simulations with respect to phase transformation, residual stresses and distortion', *Scandinavian Journal of Metallurgy*, vol. 29, no. 2, pp. 47–62, 2000, doi: 10.1034/j.1600-0692.2000.d01-6.x.

[121] J. Ahn, 'Experimental characterisation and numerical simulation of fibre laser welding of AA 2024-T3 and Ti-6Al-4V', 2024. doi: 10.13140/RG.2.2.26191.07848.

[122] W. Rae, 'Thermo-metallo-mechanical modelling of heat treatment induced residual stress in Ti–6Al–4V alloy', *Materials Science and Technology (United Kingdom)*, vol. 35, no. 7, pp. 747–766, 2019, doi: 10.1080/02670836.2019.1591031.

[123] H. S. Hasan, 'Evaluation of Heat Transfer Coefficient during Quenching of Steels', 2009.

[124] E. A. Wilson and S. F. Medina, 'Application of Koistinen and Marburger's athermal equation for volume fraction of martensite to diffusional transformations obtained on continuous cooling 0-13%C high strength low alloy steel', *Materials Science and Technology*, vol. 16, no. 6, pp. 630–633, 2000, doi: 10.1179/026708300101508397.

[125] T. Sakai, A. Belyakov, R. Kaibyshev, H. Miura, and J. J. Jonas, 'Dynamic and post-dynamic recrystallization under hot, cold and severe plastic deformation conditions', *Prog Mater Sci*, vol. 60, no. 1, pp. 130–207, 2014, doi: 10.1016/j.pmatsci.2013.09.002.

[126] J. Irwin, E. W. Reutzel, P. Michaleris, J. Keist, and A. R. Nassar, 'Predicting Microstructure from Thermal History during Additive Manufacturing for Ti-6Al-4V', *Journal of Manufacturing Science and Engineering, Transactions of the ASME*, vol. 138, no. 11, pp. 1–11, 2016, doi: 10.1115/1.4033525.

[127] L. Taleb, 'Transformation-Induced Plasticity (TRIP)', in *Encyclopedia of Thermal Stresses*, R. B. Hetnarski, Ed., Dordrecht: Springer Netherlands, 2014, pp. 6153–6163. doi: 10.1007/978-94-007-2739-7_858.

[128] M. Durand *et al.*, 'Chemical redistribution and change in crystal lattice parameters during stress relaxation annealing of the AD730TM superalloy', *Acta Mater*, vol. 237, Sep. 2022, doi: 10.1016/j.actamat.2022.118141.

[129] M. Durand, J. Cormier, P. Villechaise, J. M. Franchet, C. Dumont, and N. Bozzolo, 'Metallurgical Mechanisms upon Stress Relaxation Annealing of the AD730TM Superalloy', in *Minerals, Metals and Materials Series*, Springer Science and Business Media Deutschland GmbH, 2020, pp. 546–558. doi: 10.1007/978-3-030-51834-9_53.

[130] C. H. Gür, and A. E. Tekkaya, 'Numerical and Experimental Analysis of Quench Induced Stresses and Microstructures', *J Mech Behav Mater*, vol. 9, no. 4, pp. 237–256, 1998, doi: 10.1515/jmbm.1998.9.4.237.

[131] P. M. Souza, H. Beladi, R. P. Singh, P. D. Hodgson, and B. Rolfe, 'An Analysis on the Constitutive Models for Forging of Ti6Al4V Alloy Considering the Softening Behavior', *J Mater Eng Perform*, vol. 27, no. 7, pp. 3545–3558, 2018, doi: 10.1007/s11665-018-3402-y.

[132] P. M. Souza, G. Sivaswamy, L. Bradley, A. Barrow, and S. Rahimi, 'An innovative constitutive material model for predicting high temperature flow behaviour of inconel 625 alloy', *J Mater Sci*, vol. 57, no. 44, pp. 20794–20814, 2022, doi: 10.1007/s10853-022-07906-1.

[133] S. Solhjoo, 'Revisiting the Common Practice of Sellars and Tegart's Hyperbolic Sine Constitutive Model', *Modelling*, vol. 3, no. 3, pp. 359–373, 2022, doi: 10.3390/modelling3030023.

[134] J. Wu, Y. Jiang, W. Deng, and G. Yao, 'The hot deformation behaviors and constitutive modeling of Hastelloy C276 The hot deformation behaviors and constitutive modeling of Hastelloy C276'.

[135] G. Tan *et al.*, 'Physical-Based Constitutive Modeling of Hot Deformation in a Hot-Extruded Powder Metallurgy Nickel-Based Superalloy', *J Mater Eng Perform*, vol. 30, no. 1, pp. 794–804, 2021, doi: 10.1007/s11665-020-05291-x.

[136] P. M. Souza, H. Beladi, R. Singh, B. Rolfe, and P. D. Hodgson, 'Constitutive analysis of hot deformation behavior of a Ti6Al4V alloy using physical based model', *Materials Science and Engineering A*, vol. 648, pp. 265–273, 2015, doi: 10.1016/j.msea.2015.09.055.

[137] D. S. Svyetlichnyy, 'A coupled model of flow stress and microstructure evolution', *AIP Conf Proc*, vol. 908, no. May, pp. 1307–1312, 2007, doi: 10.1063/1.2740990.

[138] F. J. Zerilli, 'Dislocation mechanics-based constitutive equations', *Metall Mater Trans A Phys Metall Mater Sci*, vol. 35 A, no. 9, pp. 2547–2555, 2004, doi: 10.1007/s11661-004-0201-x.

[139] G. Z. Voyiadjis and A. H. Almasri, 'A physically based constitutive model for fcc metals with applications to dynamic hardness', *Mechanics of Materials*, vol. 40, no. 6, pp. 549–563, 2008, doi: 10.1016/j.mechmat.2007.11.008.

[140] G. R. Johnson and W. H. Cook, 'Fracture characteristics of three metals subjected to various strains, strain rates, temperatures and pressures', *Eng Fract Mech*, vol. 21, no. 1, pp. 31–48, 1985, doi: 10.1016/0013-7944(85)90052-9.

[141] A. S. Khan and S. Huang, 'Experimental and theoretical study of mechanical behavior of 1100 aluminum in the strain rate range 10-5-104s-1', *Int J Plast*, vol. 8, no. 4, pp. 397–424, 1992, doi: 10.1016/0749-6419(92)90057-J.

[142] G. Varela-Castro, J. M. Cabrera, and J. M. Prado, 'Critical strain for dynamic recrystallisation. The particular case of steels', *Metals (Basel)*, vol. 10, no. 1, 2020, doi: 10.3390/met10010135.

[143] M. O. Bodunrin, 'Flow stress prediction using hyperbolic-sine Arrhenius constants optimised by simple generalised reduced gradient refinement', *Journal of Materials Research and Technology*, vol. 9, no. 2, pp. 2376–2386, 2020, doi: 10.1016/j.jmrt.2019.12.070.

[144] H. Mirzadeh, 'Developing constitutive equations of flow stress for hot deformation of AZ31 magnesium alloy under compression, torsion, and tension', *International Journal*

of Material Forming, vol. 12, no. 4, pp. 643–648, 2019, doi: 10.1007/s12289-018-1440-5.

[145] H. Monajati, F. Zarandi, M. Jahazi, and S. Yue, 'Strain induced γ' precipitation in nickel base superalloy Udimet 720 using a stress relaxation based technique', *Scr Mater*, vol. 52, no. 8, pp. 771–776, 2005, doi: 10.1016/j.scriptamat.2004.12.006.

[146] A. Chamanfar, M. Jahazi, J. Gholipour, P. Wanjara, and S. Yue, 'Evolution of flow stress and microstructure during isothermal compression of Waspaloy', *Materials Science and Engineering A*, vol. 615, pp. 497–510, 2014, doi: 10.1016/j.msea.2014.07.093.

[147] Y. Zhang, Q. Fan, X. Zhang, Z. Zhou, Z. Xia, and Z. Qian, 'Avrami kinetic-based constitutive relationship for armco-type pure iron in hot deformation', *Metals (Basel)*, vol. 9, no. 3, 2019, doi: 10.3390/met9030365.

[148] Y. C. Lin, X. M. Chen, D. X. Wen, and M. S. Chen, 'A physically-based constitutive model for a typical nickel-based superalloy', *Comput Mater Sci*, vol. 83, pp. 282–289, 2014, doi: 10.1016/j.commatsci.2013.11.003.

[149] J. J. Jonas, X. Quelennec, L. Jiang, and É. Martin, 'The Avrami kinetics of dynamic recrystallization', *Acta Mater*, vol. 57, no. 9, pp. 2748–2756, 2009, doi: 10.1016/j.actamat.2009.02.033.

[150] D. Cai, P. Nie, J. Shan, W. Liu, Y. Gao, and M. Yao, 'Precipitation and residual stress relaxation kinetics in shot-peened inconel 718', *J Mater Eng Perform*, vol. 15, no. 5, pp. 614–617, 2006, doi: 10.1361/105994906X124613.

[151] Z. Zhou *et al.*, 'A finite element study of thermal relaxation of residual stress in laser shock peened IN718 superalloy', *Int J Impact Eng*, vol. 38, no. 7, pp. 590–596, 2011, doi: 10.1016/j.ijimpeng.2011.02.006.

[152] I. Torrano, O. Barbero, A. Kortabarria, and P. J. Arrazola, 'Prediction of residual stresses in turning of inconel 718', *Adv Mat Res*, vol. 223, pp. 421–430, 2011, doi: 10.4028/www.scientific.net/AMR.223.421.

[153] K. S. Prasad, S. K. Panda, S. K. Kar, S. V. S. N. Murty, and S. C. Sharma, 'Prediction capability of constitutive models for Inconel 718 sheets deformed at various elevated temperatures and strain rates', *Mater Perform Charact*, vol. 8, no. 5, pp. 869–891, 2019, doi: 10.1520/MPC20190004.

[154] J. S. Park, S. W. Kim, H. C. Lim, and J. H. Kang, 'Flow Stress Optimization of Inconel 718 Based on a Coupled Simulation of Material-Forming Analysis and Joule Heating Analysis', *Metals (Basel)*, vol. 12, no. 12, 2022, doi: 10.3390/met12122024.

[155] Y. Zhou, X.-M. Chen, and S. Qin, 'A Strain-Compensated Constitutive Model for Describing the Hot Compressive Deformation Behaviors of an Aged Inconel 718 Superalloy', *High Temperature Materials and Processes*, vol. 38, no. 2019, pp. 436–443, 2019, doi: doi:10.1515/htmp-2018-0108.

[156] G. Mahalle, O. Salunke, N. Kotkunde, A. Kumar Gupta, and S. K. Singh, 'Study of Khan-Huang-Liang (KHL) Anisotropic Deformation Model for Deep Drawing Behaviour of

Inconel 718 Alloy', *IOP Conf Ser Mater Sci Eng*, vol. 967, no. 1, 2020, doi: 10.1088/1757-899X/967/1/012054.

[157] J. Goldak, M. Bibby, J. Moore, R. House, and B. Patel, 'Computer modeling of heat flow in welds', *Metallurgical Transactions B*, vol. 17, no. 3, pp. 587–600, 1986, doi: 10.1007/BF02670226.

[158] M. P. Jackson and R. C. Reed, 'Heat treatment of UDIMET 720Li: The effect of microstructure on properties', *Materials Science and Engineering A*, vol. 259, no. 1, pp. 85–97, 1999, doi: 10.1016/S0921-5093(98)00867-3.

[159] M. Sattar *et al.*, 'Curve fitting for damage evolution through regression analysis for the kachanov–rabotnov model to the norton–bailey creep law of ss-316 material', *Materials*, vol. 14, no. 19, 2021, doi: 10.3390/ma14195518.

[160] F. C. Monkman, 'An empirical relationship between rupture life and minimum creep rate in creep-rupture tests', in *Proc of the ASTM*, 1956, pp. 593–620.

[161] F. Masoumi *et al.*, 'High temperature creep properties of a linear friction welded newly developed wrought Ni-based superalloy', *Materials Science and Engineering A*, vol. 710, no. June 2017, pp. 214–226, 2018, doi: 10.1016/j.msea.2017.10.091.

[162] J. Moverare, 'Testing Methods for High Temperature Materials', in *Encyclopedia of Materials: Metals and Alloys*, F. G. Caballero, Ed., Oxford: Elsevier, 2022, pp. 277–286. doi: https://doi.org/10.1016/B978-0-12-803581-8.12106-X.

[163] Y. C. Lin, J. S. Zhu, J. Y. Chen, and J. Q. Wang, 'Residual-stress relaxation mechanism and model description of 5052H32 Al alloy spun ellipsoidal heads during annealing treatment', *Adv Manuf*, vol. 10, no. 1, pp. 87–100, 2022, doi: 10.1007/s40436-021-00367-w.

[164] S. C. Tjong and Z. Y. Ma, 'Creep behaviour of precipitation-hardened ferritic Fe – 19Cr – 4Ni – 2Al alloy', vol. 56, no. September, pp. 59–64, 2002.

[165] Y. Yang, X. Deng, and W. Shi, 'Numerical simulation of stress evolutions in 2A14 aluminum alloy components during solution and aging process', *Heat Treatment and Surface Engineering*, vol. 4, no. 1, pp. 1–12, 2022, doi: 10.1080/25787616.2022.2031550.

[166] A. Madariaga *et al.*, 'Effect of Thermal Annealing on Machining-Induced Residual Stresses in Inconel 718', *J Mater Eng Perform*, vol. 26, no. 8, pp. 3728–3738, 2017, doi: 10.1007/s11665-017-2824-2.

[167] K. Linka, M. Hillgärtner, K. P. Abdolazizi, R. C. Aydin, M. Itskov, and C. J. Cyron, 'Constitutive artificial neural networks: A fast and general approach to predictive data-driven constitutive modeling by deep learning', *J Comput Phys*, vol. 429, 2021, doi: 10.1016/j.jcp.2020.110010.

[168] X. Liu, S. Tian, F. Tao, and W. Yu, 'A review of artificial neural networks in the constitutive modeling of composite materials', *Compos B Eng*, vol. 224, no. March, p. 109152, 2021, doi: 10.1016/j.compositesb.2021.109152.

[169] A. Tyagunov, O. Milder, and D. Tarasov, 'Application of artificial neural networks for prediction of nickel-based superalloys service properties based on the chemical composition', *WSEAS Transactions on Environment and Development*, vol. 15, pp. 113–119, 2019.

[170] Y. Zhu, W. Zeng, Y. Sun, F. Feng, and Y. Zhou, 'Artificial neural network approach to predict the flow stress in the isothermal compression of as-cast TC21 titanium alloy', *Comput Mater Sci*, vol. 50, no. 5, pp. 1785–1790, 2011, doi: 10.1016/j.commatsci.2011.01.015.

[171] I. Y. Moon *et al.*, 'Predicting High Temperature Flow Stress of Nickel Alloy A230 Based on an Artificial Neural Network', *Metals (Basel)*, vol. 12, no. 2, 2022, doi: 10.3390/met12020223.

[172] H. Yang, H. Bu, M. Li, and X. Lu, 'Prediction of flow stress of annealed 7075 al alloy in hot deformation using strain-compensated arrhenius and neural network models', *Materials*, vol. 14, no. 20, 2021, doi: 10.3390/ma14205986.

[173] J. P. B. A. Sembiring, A. Amanov, and Y. S. Pyun, 'Artificial neural network-based prediction model of residual stress and hardness of nickel-based alloys for UNSM parameters optimization', *Mater Today Commun*, vol. 25, no. April, p. 101391, 2020, doi: 10.1016/j.mtcomm.2020.101391.

[174] ASTM International, *ASTM E328-21 Standard Test Methods for Stress Relaxation for Materials and Structures*, vol. 02, no. Reapproved 2021. 2022, pp. 1–15. doi: 10.1520/E0328-21.2.

[175] Y. Desvallees, M. Bouzidi, F. Bois, and N. Beaude, 'Delta Phase in INCONEL 718: Mechanical Properties and Forging Process Requirements', in *Sixth International Symposium on Superalloys 718, 625, 706 and Derivatives*, 1994, pp. 281–291. doi: 10.7449/1994/superalloys_1994_281_291.

[176] M. Sundararaman, P. Mukhopadhyay, and S. K. Banerjee, 'Precipitation of the $δ$-Ni3Nb phase in two nickel base superalloys', *Metallurgical Transactions A*, vol. 19, pp. 453–465, 1988.

[177] K. N. Prabhu and A. A. Ashish, 'Inverse modeling of heat transfer with application to solidification and quenching', *Materials and Manufacturing Processes*, vol. 17, no. 4, pp. 469–481, 2002, doi: 10.1081/AMP-120014230.

[178] B. Liščić and S. Singer, '12.05 - Calculation of the Heat Transfer Coefficient Based on Experiments by the Liscic Probes', in *Comprehensive Materials Processing*, vol. 12, S. Hashmi, G. F. Batalha, C. J. Van Tyne, and B. Yilbas, Eds., Oxford: Elsevier, 2014, pp. 123–176. doi: https://doi.org/10.1016/B978-0-08-096532-1.01205-X.

[179] R. I. Ramakrishnan and T. E. Howson, 'Modeling the heat treatment of superalloys', *JOM*, vol. 44, no. 6, pp. 29–32, 1992, doi: 10.1007/BF03222251.

[180] S. G. Chen, C. I. Weng, and J. Lin, 'Inverse estimation of transient temperature distribution in the end quenching test', *J Mater Process Technol*, vol. 86, no. 1–3, pp. 257–263, 1998, doi: 10.1016/S0924-0136(98)00322-7.

[181] D. Fernández, V. García Navas, A. Sandá, and I. Bengoetxea, 'Comparison of machining inconel 718 with conventional and sustainable coolant', *MM Science Journal*, no. December 2014, pp. 506–510, 2014, doi: 10.17973/mmsj.2014_12_201415.

[182] Special Metals, 'Special Metals Inconel Alloy 718', 2007. doi: 10.31399/asm.ad.ni0774.

[183] F. Masoumi, M. Jahazi, J. Cormier, and D. Shahriari, 'Dissolution kinetics and morphological changes of γ ' in AD730TM superalloy', *MATEC Web of Conferences*, vol. 14, 2014, doi: 10.1051/matecconf/20141413005.

[184] A. Samuel and K. N. Prabhu, 'Residual Stress and Distortion during Quench Hardening of Steels: A Review', *J Mater Eng Perform*, vol. 31, no. 7, pp. 5161–5188, 2022, doi: 10.1007/s11665-022-06667-x.

[185] ASTM International, *ASTM E8/E8M standard test methods for tension testing of metallic materials*, no. 21. 2021, pp. 1–27. doi: 10.1520/E0008_E0008M-21.

[186] ASTM and ASTM International, *ASTM E21 Standard Test Methods for Elevated Temperature Tension Tests of Metallic Materials*, vol. 03. 2020, pp. 1–8. doi: 10.1520/E0021-20.2.

[187] B. Roebuck, M. Brooks, and A. Pearce, *Good Practice Guide for Miniature ETMT Tests*, 1st ed. London: National Physical Laboratory, 2016.

[188] B. Roebuck, D. C. Cox, and R. C. Reed, *An Innovative Device for the Mechanical Testing of Miniature Specimens of Superalloys*. 2004. doi: 10.7449/2004/Superalloys_2004_523_528.

[189] B. Roebuck, M. G. Gee, J. D. Lord, and L. N. McCartney, 'Miniature thermal cycling tests on aluminium alloy metal matrix composites', *Materials Science and Technology*, vol. 14, no. 9–10, pp. 1001–1008, 1998.

[190] E. a Kardoulaki, J. a Lin, D. a Balint, and D. b Farrugia, 'Investigation of the effects of thermal gradients present in Gleeble high-temperature tensile tests on the strain state for free cutting steel', *Journal of Strain Analysis for Engineering Design*, vol. 49, no. 7, pp. 521–532, 2014, doi: 10.1177/0309324714531950.

[191] T. Konkova, S. Rahimi, S. Mironov, and T. N. Baker, 'Effect of strain level on the evolution of microstructure in a recently developed AD730 nickel based superalloy during hot forging', *Mater Charact*, vol. 139, pp. 437–445, 2018, doi: 10.1016/j.matchar.2018.03.027.

[192] S. Sulzer, E. Alabort, A. Németh, B. Roebuck, and R. Reed, 'On the Rapid Assessment of Mechanical Behavior of a Prototype Nickel-Based Superalloy using Small-Scale Testing', *Metall Mater Trans A Phys Metall Mater Sci*, vol. 49, no. 9, pp. 4214–4235, 2018, doi: 10.1007/s11661-018-4673-5.

[193] M. Ganapathy, N. Li, J. Lin, M. Abspoel, and H. Guido, 'Analysis of new Gleeble tensile specimen design for hot', vol. 05013, pp. 0–6, 2015.

[194] C. Ma, Z. Zeng, H. Zhang, and X. Rui, 'A correction method for heatwave distortion in digital image correlation measurements based on background-oriented schlieren', *Applied Sciences (Switzerland)*, vol. 9, no. 18, 2019, doi: 10.3390/app9183851.

[195] E. M. C. Jones and P. L. Reu, 'Distortion of Digital Image Correlation (DIC) Displacements and Strains from Heat Waves', *Exp Mech*, vol. 58, no. 7, pp. 1133–1156, 2018, doi: 10.1007/s11340-017-0354-3.

[196] G. Valeri, B. Koohbor, A. Kidane, and M. A. Sutton, 'Determining the tensile response of materials at high temperature using DIC and the Virtual Fields Method', *Opt Lasers Eng*, vol. 91, no. August 2016, pp. 53–61, 2017, doi: 10.1016/j.optlaseng.2016.11.004.

[197] M. A. (Eds.) International Digital Image Correlation Society, Jones, E.M.C. and Iadicola, 'A Good Practices Guide for Digital Image Correlation', *International Digital Image Correlation Society*, p. 94, 2018.

[198] J. F. Barker, E. W. Ross, and J. F. Radavich, 'Long Time Stability of Inconel 718', *Journal of Metals*, vol. 22, no. 1, pp. 31–41, 1970, doi: 10.1007/bf03355624.

[199] S. Azadian, L.-Y. Wei, F. Niklasson, and R. Warren, 'Precipitation in Spray-Formed in 718', 2001, pp. 617–626. doi: 10.7449/2001/Superalloys_2001_617_626.

[200] B. M. B. Grant, H. J. Stone, P. J. Withers, and M. Preuss, 'High-temperature strain field measurement using digital image correlation', *Journal of Strain Analysis for Engineering Design*, vol. 44, no. 4, pp. 263–271, 2009, doi: 10.1243/03093247JSA478.

[201] P. E. Aba-Perea, T. Pirling, P. J. Withers, J. Kelleher, S. Kabra, and M. Preuss, 'Determination of the high temperature elastic properties and diffraction elastic constants of Ni-base superalloys', *Mater Des*, vol. 89, pp. 856–863, 2016, doi: 10.1016/j.matdes.2015.09.152.

[202] A. International, 'Standard Practice for Determining Average Grain Size Using Electron Backscatter Diffraction (EBSD) in Fully Recrystallized Polycrystalline Materials', vol. i, no. Reapproved, pp. 10–13, 2010, doi: 10.1520/E2627.

[203] A. Seret, C. Moussa, M. Bernacki, and N. Bozzolo, 'On the Coupling between Recrystallization and Precipitation Following Hot Deformation in a γ-γ' Nickel-Based Superalloy', *Metall Mater Trans A Phys Metall Mater Sci*, vol. 49, no. 9, pp. 4199–4213, 2018, doi: 10.1007/s11661-018-4707-z.

[204] H. Mecking and U. F. Kocks, 'Kinetics of flow and strain-hardening', *Acta Metallurgica*, vol. 29, no. 11, pp. 1865–1875, 1981, doi: https://doi.org/10.1016/0001-6160(81)90112-7.

[205] B. Roebuck, J. D. Lord, M. Brooks, M. S. Loveday, C. M. Sellars, and R. W. Evans, 'Measuring flow stress in hot axisymmetric compression tests', *Measurement Good Practice Guide Number 3*, no. 3, p. 56, 2002.

[206] Aubert & Duval Company, 'AD730 for High Temperature Applications'. Accessed: Jan. 07, 2019. [Online]. Available: https://www.aubertduval.com/wp-media/uploads/sites/2/2018/03/2017_Brochure_AD730.pdf

[207] G. Torrente, 'Numerical and experimental studies of compression-tested copper: Proposal for a new friction correction', *Materials Research*, vol. 21, no. 4, 2018, doi: 10.1590/1980-5373-mr-2017-0905.

[208] P. Paupler, 'G. E. Dieter. Mechanical Metallurgy. 3rd ed., Mc Graw-Hill Book Co., New York 1986. XXIII + 751 p., DM 138.50, ISBN 0–07–016893–8', *Crystal Research and Technology*, vol. 23, no. 2, p. 194, 1988, doi: https://doi.org/10.1002/crat.2170230211.

[209] G. W. Rowe, *Introduction to the Principles of Metalworking*. St. Martin's Press, 1969.

[210] Y. C. Lin, Y. C. Xia, X. M. Chen, and M. S. Chen, 'Constitutive descriptions for hot compressed 2124-T851 aluminum alloy over a wide range of temperature and strain rate', *Comput Mater Sci*, vol. 50, no. 1, pp. 227–233, 2010, doi: 10.1016/j.commatsci.2010.08.003.

[211] H. Sofuoglu, H. Gedikli, and J. Rasty, 'Determination of Friction Coefficient by Employing the Ring Compression Test ', *J Eng Mater Technol*, vol. 123, no. 3, pp. 338–348, 2000, doi: 10.1115/1.1369601.

[212] R. L. Goetz and S. L. Semiatin, 'The adiabatic correction factor for deformation heating during the uniaxial compression test', *J Mater Eng Perform*, vol. 10, no. 6, pp. 710–717, 2001, doi: 10.1361/105994901770344593.

[213] M. Kulakov, S. Rahimi, and S. L. Semiatin, 'Effect of Deformation Heating on Microstructure Evolution During Hot Forging of Ti-6Al-4V', *Metallurgical and Materials Transactions A*, vol. 53, no. 2, pp. 407–419, 2022, doi: 10.1007/s11661-021-06493-1.

[214] A. A. Guimaraes and J. J. Jonas, 'Recrystallization and aging effects associated with the high temperature deformation of waspaloy and inconel 718', *Metallurgical Transactions A*, vol. 12, no. 9, pp. 1655–1666, 1981, doi: 10.1007/BF02643571.

[215] S. C. Medeiros, Y. V. R. K. Prasad, W. G. Frazier, and R. Srinivasan, 'Microstructural modeling of metadynamic recrystallization in hot working of IN 718 superalloy', *Materials Science and Engineering A*, vol. 293, no. 1, pp. 198–207, 2000, doi: 10.1016/S0921-5093(00)01053-4.

[216] H. Monajati, M. Jahazi, S. Yue, and A. K. Taheri, 'Deformation characteristics of isothermally forged UDIMET 720 nickel-base superalloy', *Metall Mater Trans A Phys Metall Mater Sci*, vol. 36, no. 4, pp. 895–905, 2005, doi: 10.1007/s11661-005-0284-z.

[217] A. K. Roy and V. Marthandam, 'Mechanism of yield strength anomaly of Alloy 617', *Materials Science and Engineering A*, vol. 517, no. 1–2, pp. 276–280, 2009, doi: 10.1016/j.msea.2009.03.090.

[218] P. Veyssière, 'Yield stress anomalies in ordered alloys: A review of microstructural findings and hypotheses', *Materials Science and Engineering A*, vol. 309–310, pp. 44–48, 2001, doi: 10.1016/S0921-5093(00)01662-2.

[219] H. J. McQueen and N. D. Ryan, 'Constitutive analysis in hot working', *Materials Science and Engineering A*, vol. 322, no. 1–2, pp. 43–63, 2002, doi: 10.1016/S0921-5093(01)01117-0.

[220] Cm. Sellars and W. J. McTegart, 'On the mechanism of hot deformation', *Acta Metallurgica*, vol. 14, pp. 1136–1138, 1966.

[221] L. Chen, G. Zhao, J. Yu, and W. Zhang, 'Constitutive analysis of homogenized 7005 aluminum alloy at evaluated temperature for extrusion process', *Mater Des*, vol. 66, no. PA, pp. 129–136, 2015, doi: 10.1016/j.matdes.2014.10.045.

[222] A. R. Mashreghi, H. Monajatizadeh, M. Jahazi, and S. Yue, 'High temperature deformation of nickel base superalloy Udimet 520', *Materials Science and Technology*, vol. 20, no. 2, pp. 161–166, 2004, doi: 10.1179/026708304225010343.

[223] N. Haghdadi, D. Martin, and P. Hodgson, 'Physically-based constitutive modelling of hot deformation behavior in a LDX 2101 duplex stainless steel', *Mater Des*, vol. 106, pp. 420–427, 2016, doi: 10.1016/j.matdes.2016.05.118.

[224] Y. Estrin and H. Mecking, 'A unified phenomenological description of work hardening based on one-parameter models', *Acta Metallurgica*, vol. 32, pp. 57–70, 1984, doi: 10.1016/0001-6160(84)90202-5.

Appendix

Table 2: Crystal Structure, Lattice Parameters, and Formulas for Different Phases.

Phase	Crystal Structure	Lattice Parameters (nm)	Formula
γ'	FCC (ordered $L1_2$)	0.3561 for pure Ni_3Al	Ni_3Al, $Ni_3(Al, Ti)$
γ''	BCT (ordered $D0_{22}$)	α = 0.3624, c = 0.7406	Ni_3Nb
δ	Orthorhombic (Ordered Cu_3Ti)	α_0 = 0.5106 - 0.511, b_0 = 0.421 - 0.4251, c_0 = 0.451 – 0.4556	Ni_3Nb
σ	Tetragonal	α_0 =0.88 – 0.91, c_0 = 0.45 – 0.48	FeCr, FeCrMo, CrFeMoNi, CrCo, CrNiMo
α-Cr	BCC	Diameter =~ 300nm	Cr (Cr>80wt%)
Laves	Hexagonal	α_0 =0.475-0.495 c_0 = 0.77-0.815	Fe_2Nb, Fe_2Ti, Fe_2Mo, Co_2Ta, Co_2Ti
MC	Cubic	α_0 =0.43-0.47	TiC, NbC
$M_{23}C_6$	FCC	α_0 =1.05-1.07	$Cr_{23}C_6$(Cr, Fe, W, Mo)$_{23}C_6$
MN	Cubic	α_0 =0.424	TiN, NbN